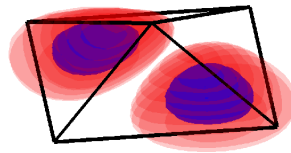

Electronic and Optical Properties of Quantum Dots: A Tight-Binding Approach

by Stefan Schulz

May, 2007



University of Bremen



FB 1

Institute for Theoretical Physics

Electronic and Optical Properties of Quantum Dots: A Tight-Binding Approach

Dem Fachbereich für Physik und Elektrotechnik
der Universität Bremen

zur Erlangung des akademischen Grades
Doktor der Naturwissenschaften (Dr. rer. nat.)
genehmigte Dissertation

von

Dipl. Phys. Stefan Schulz
aus Delmenhorst

1. Gutachter: Prof. Dr. rer. nat. G. Czycholl
2. Gutachter: Prof. Dr. rer. nat. F. Jahnke

Eingereicht am: 29.05.2007
Tag des Promotionskolloquiums: 17.07.2007

Persönlichkeiten werden nicht durch schöne Reden geformt,
sondern durch Arbeit und eigene Leistung.

Albert Einstein

Abstract

In this thesis the electronic and optical properties of semiconductor quantum dots are investigated by means of tight-binding (TB) models combined with configuration interaction calculations.

In the first part, an empirical TB model is used to investigate the electronic states of group II-VI semiconductor quantum dots with a zinc blende structure. TB matrix elements up to second nearest neighbors and spin-orbit coupling are included. Within this approach we study pyramidal-shaped CdSe quantum dots embedded in a ZnSe matrix as well as spherical CdSe nanocrystals. Lattice distortions are included by an appropriate model strain field. Within the TB model, the influence of strain on the bound electronic states, in particular their spatial orientation, are investigated. The theoretical results for spherical nanocrystals are compared with data from tunneling and optical spectroscopy.

Additionally to the quantum dots based on II-VI materials, we investigate the electronic and optical properties of self-assembled nitride quantum dots. Coulomb and dipole matrix elements are calculated from the single-particle wave functions, which fully include the atomistic wurtzite structure. These matrix elements serve as an input for the calculation of optical spectra. For the investigated InN/GaN material system, the optical selection rules are found to be strongly affected by band-mixing effects. Within this framework, excitonic absorption and emission as well as multi-exciton emission spectra are analyzed for different lens-shaped quantum dots. A dark exciton and biexciton ground state for small quantum dots is found. For larger structures, the strong electrostatic built-in fields lead to a level reordering for the hole states, which results in a bright exciton ground state.

Furthermore the electronic and optical properties of truncated pyramidal GaN/AlN QDs with zinc blende structure are studied. The influence of the strain field on the single-particle states and energies is discussed. Coulomb and dipole matrix elements are calculated from the single-particle wave functions and the excitonic absorption spectrum is analyzed. This analysis reveals a strong anisotropy in the polarization of the energetically lowest inter-band transition. In addition, the results of our atomistic TB description are compared with approaches based on continuum models.

Contents

1 Prologue	v
-------------------	----------

Part I Basic Considerations

2 Modeling Semiconductor Quantum Dots	1
2.1 Quantum Dots	2
2.2 Theoretical Approaches for the Calculation of Electronic Properties . .	5
2.2.1 Effective-Mass Approximation and $\mathbf{k} \cdot \mathbf{p}$ -Models	5
2.2.2 Pseudopotential Model	6
2.2.3 Tight-Binding Model	7
3 Tight-Binding Models	9
3.1 Tight-Binding Model for Bulk Materials	9
3.1.1 Spin-Orbit Coupling	17
3.2 Tight-Binding Model for Semiconductor Quantum Dots	19
3.2.1 Strain fields	22
3.2.2 Piezoelectricity	24
3.2.3 Numerical Determination of Eigenvalues: The Folded Spectrum Method	26
4 Short Introduction in Group Theory	29
4.1 General Considerations	29
4.2 Symmetry Properties of Energy Bands	36
4.3 Time Reversal Symmetry	40
4.3.1 Degeneracies due to Time Reversal Symmetry	43

**Part II Electronic Properties of CdSe Nanostructures with
Zinc Blende Structure**

5	Introduction to Part II	49
6	Crystals with a Zinc Blende Structure	51
6.1	Crystal Structure	51
6.2	Symmetry Considerations and Bulk Band Structure for Zinc Blende Semiconductors	52
6.3	Tight-binding Model with $s_c p_a^3$ Basis	54
7	Results for CdSe Nanostructures	59
7.1	Results for a Pyramidal CdSe QDs Embedded in ZnSe	59
7.1.1	Quantum Dot Geometry and strain	59
7.1.2	Single-Particle Properties	61
7.2	Results for CdSe Nanocrystals	69
7.2.1	Quantum Dot Geometry and Strain	69
7.2.2	Single-particle Properties and Comparison with Experimental Results	69

**Part III Electronic and Optical Properties of Nitride
Quantum Dots with a Wurtzite Structure**

8	Introduction to Part III	77
9	Crystals with a Wurtzite Structure	79
9.1	Crystal Structure	79
9.2	Symmetry Considerations and Bulk Band Structure for Wurtzite Semiconductors	81
9.3	Spontaneous Polarization	84
9.4	Tight-binding Model with sp^3 Basis	85
10	Results for InN/GaN Quantum Dots	89
10.1	Single-Particle Properties	89
10.1.1	Quantum Dot Geometry and Strain	89
10.1.2	The Electrostatic Built-In Field	91
10.1.3	Single-Particle States and Energies	93
10.1.4	Influence of Crystal Field Splitting and Spin-Orbit Coupling	97
10.2	Many-Particle Properties	101
10.2.1	Many-Body Hamiltonian and Light-Matter Interaction	102

10.2.2	Matrix Elements	103
10.2.3	Excitonic Spectra	110
10.2.4	Multi-Exciton Emission Spectra	112

**Part IV Electronic and Optical Properties of Zinc Blende
GaN/AlN Quantum Dots**

11	Introduction to Part IV	119
12	Electronic and Optical Properties of GaN/AlN QDs	121
12.1	Electronic Structure	121
12.1.1	Geometry of the Quantum Dot Structure	121
12.1.2	Strain Field Calculation	122
12.1.3	Tight-Binding Model	126
12.2	Optical Properties	129
12.2.1	Many-Body Hamiltonian, Coulomb and Dipole Matrix Elements	129
13	Results for Truncated Pyramidal GaN Quantum Dots	133
13.1	Electron Single-Particle States and Energies	133
13.2	Hole Single-Particle States and Energies	135
13.3	Excitonic Absorption Spectra	136

Part V

	Summary and Outlook	143
	Appendix	146
A	Parameters for CdSe and ZnSe	149
B	Parameters for InN and GaN	150
C	Coulomb Matrix Elements	152
C.1	Orthogonalized Slater orbitals	154
D	Strain Field Equations	157
E	Parameters for Cubic GaN and AlN	159
	List of Figures	161
	List of Tables	165
	Bibliography	167

1 Prologue

The invention of the transistor and integrated circuits was the start of a rapid development towards smaller and faster electronic devices. These components are the building-blocks of complex electronic systems. The driving force behind these developments is the economical benefit from packing more and more wiring, transistors and functionality on a single chip. Nowadays our life is hardly imaginable without the use of semiconductors. Products based on these devices such as computers, optical storage media and communication infrastructure are commonplace. Clearly, semiconductor materials have changed the way we work, communicate and entertain.

In the pursuit of further miniaturization of semiconductor devices, the nanometer technology made the confinement of the carriers from three to lower dimensions possible. In this progress, one is currently reaching the regime where the quantum mechanical description of the system is of major importance. Confining electrons in all three spatial dimensions denotes the ultimate miniaturization in semiconductor technology. According to the quantum mechanical laws, and in similarity to atoms, the electrons occupy discrete energy levels. These low-dimensional structures are called *quantum dots* (QDs) [1].

Semiconductor QDs can experimentally be realized by modern epitaxial growth procedures, such as molecular beam epitaxy (MBE) or metal organic vapor phase epitaxy (MOVPE). These techniques allow for the formation of crystal layers with atomic precision. With these methods the realization of QD structures can be achieved by growing on top of a smooth substrate a material with a different lattice constant. Due to the lattice mismatch a strain field develops in the system. For a certain critical film thickness the formation of three dimensional nano-islands on top of a thin two dimensional layer can be observed. Such a process has been described as early as 1938 by Stranski and Krastanow [2], and is therefore called the Stranski-Krastanow growth mode. Interestingly, the first successful self-organized realizations of such low-dimensional systems have been reported only about two decades ago [3, 4]. For many applications these nanostructures are overgrown with the substrate material. The resulting QD structures have a size, from a few up to several tens of nanometers, are of regular shape and may be grown with very high surface densities.

The last decade witnessed revolutionary breakthroughs both in synthesis of quantum dots, leading to nearly defect-free nanostructures, and in characterization of such systems, revealing ultra narrow spectroscopic lines having linewidth smaller than 1 meV. In these optimized structures one discovered new intriguing effects, such as multiple exciton generation, fine-structure splitting, quantum entanglement and multi-exciton

recombination. These discoveries have led to new technological applications including quantum information [5,6] and ultra-high efficiency solar cells [7].

For all kinds of new applications the detailed understanding of the electronic structure is of essential importance, since this provides the link between the structural and optical properties of these systems. To achieve a comprehensive understanding of the available experimental data on QDs, complex numerical models are required to investigate the influence of the shape, strain, and electrostatic built-in fields on the electronic and optical properties. Such quantitative accurate predictions also provide guidance to tailor the properties of optoelectronic devices at will. A detailed understanding of these structures requires the study of large, up to million-atom systems composed of the QD and the WL embedded in the surrounding material. First-principles computational techniques based on density functional theory are not applicable to such large structures. At the same time the continuum-based techniques cannot provide insights on atomistic related phenomena, which are revealed by experiments. Thus, methods are required that use an atomistic resolution and utilize single-particle and many-body techniques that are scalable to nanostructures systems containing $10^3 - 10^6$ atoms.

A framework which allows an atomistic description of the electronic and optical properties of large nanostructures, is composed of a series of different steps. Starting from the input geometry of the QD, which is obtained by experimental data or geometrical considerations, the positions of the different atoms have to be determined from a strain field calculation. Once the atomic positions are known, one has to choose a basis in which the single-particle Schrödinger equation will be solved. The prerequisite of this basis set is that the calculated band structure within this ansatz must reproduce the band structure known from the literature. This ensures that the characteristic bulk properties, e.g., the energy gap and the effective masses of different bands, are included accurately in the calculation. Starting from this basis set, the Schrödinger equation for the nanostructure has to be solved as an interior eigenvalue problem, i.e., only a few eigenstates near the band gap of the QD material are of interest. Once the single-particle wave functions and energies have been obtained, the next step is to calculate the optical properties of the QD. This task requires the evaluation of Coulomb and dipole matrix elements. Based on these matrix elements, one can calculate different properties such as absorption and emission spectra.

Outline of this Thesis

In this thesis different tight-binding models including strain and electrostatic built-in fields are applied to the calculations of the electronic and optical properties of arbitrarily shaped QDs. The electronic structure, excitonic absorption and multi-exciton emission spectra are calculated in a coherent framework. As it is mandatory to accurately reproduce the realistic bulk properties of the semiconductor materials under consideration, we make sure that the complicated electronic band structures in the region of the Brillouin zone center are described by our tight-binding models. The intention of this work

is to establish and validate a method that allows a flexible modeling of a variety of low-dimensional nanostructures.

The present thesis has been divided into four parts. In the first part we give a general introduction into the topic of semiconductor QDs, followed by a closer look at the different theoretical models used for the description of electronic states in such systems. Subsequently, the basic ideas of the tight-binding formalism are given, followed by an introduction to group theory, which is very useful for the analysis of electronic and optical properties. The second part of this thesis deals with the electronic properties of CdSe QDs. After the discussion of CdSe QDs, we focus on the nitride systems. In part three the electronic and optical properties of InN/GaN QDs with a wurtzite structure are investigated, while the properties of GaN/AlN nanostructures in the zinc blende phase are studied in part four. Finally a summary and an outlook is given.

Basic Considerations

2 Modeling Semiconductor Quantum Dots

Semiconductor quantum dots (QDs) [1] have been a central research topic for several years. Due to the progress in QD growth technology, relatively uniform dot layers can be obtained by using the so-called Stranski-Krastanow growth mode. Strong interest lies in semiconductor QDs for both basic research and possible device applications. From a fundamental perspective, QDs represent an intermediate stage between single molecules and the condensed phase, and consequently enable the study of the evolution of optical and electrical properties with sample size. Due to the discrete level structure of these objects, QDs are often called “artificial atoms”. From a more technological point of view, QDs are important because of potential device applications, particularly in the field of optoelectronics. Owing to the rapid progress in nanostructure growth technology, the theoretical study of self-organized QDs is of major interest both for the interpretation of present experiments and to guide and stimulate future developments. A key requirement is the calculation of the electron and hole energy levels and wave functions in an arbitrarily-shaped QD structure. This task is considerably more difficult and computationally more intensive than for a quantum well structure, where quantization only occurs along one direction, and the theorem of Bloch can be used for the other two. For QDs, the calculation of the energy spectra must include the full three-dimensional quantization and the shape of the QD.

A widely used approximation for the theoretical analysis of semiconductor nanostructures is the one-band effective-mass approximation for the conduction and valence band. However, most of the semiconductor materials do not have such a simple band structure. Consequently, the real multi-band structure of the materials must be taken into account. This can, for example, be done in a multi-band effective-mass approach, the so-called $\mathbf{k} \cdot \mathbf{p}$ -model. However, this model cannot account for an atomistic description of low-dimensional systems. Especially for small nanostructures a proper treatment of the underlying microscopic structure is of particular importance. Suitable for an atomistic multi-band description are empirical pseudopotential methods [8] as well as an empirical tight-binding approach [9].

In the following section, the general properties of QDs and their fabrication techniques will be outlined. After this short introduction, a brief discussion of the different empirical models, which are primarily used to calculate the electronic structure of such low dimensional systems, will be given.

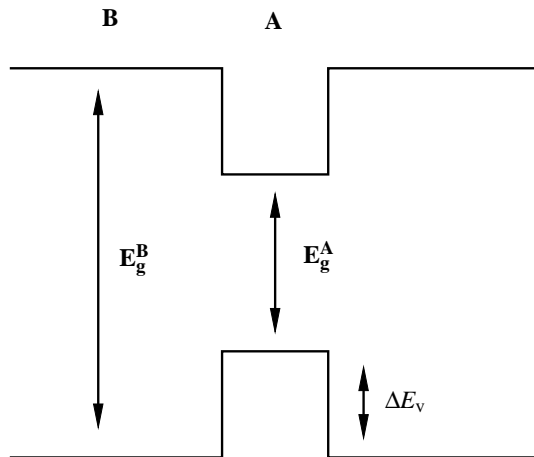


Figure 2.1: Schematic energy diagram for conduction and valence band-edge between the materials B and A . The energy gaps of the two materials are denoted by E_g^B and E_g^A . ΔE_v indicates the valence band offset.

2.1 Quantum Dots

Quantum dots (QDs) are systems which are spatially confined on a nanometer scale in all three spatial dimensions. With respect to the energy spectrum and the system size, QDs are intermediate between molecules and bulk materials. Therefore, these structures show both molecular and bulk features. The crystal structure inside the QD resembles the lattice structure of the bulk system. However, the periodicity of the underlying crystal lattice is spoiled at the QD surface.

The nanostructure is often embedded in different materials, whose band edges vary from those of the QD material. If the conduction and valence band edge of the surrounding materials are higher and lower, respectively, the nanostructure confines both, electrons and holes.¹ A schematic representation of the band alignment is shown in Figure 2.1. The relative position of conduction and valence band edge of the different materials is determined by the band gaps E_g^A and E_g^B of the dot and barrier semiconductor material as well as the valence band offset ΔE_v between the materials.

The three-dimensional spatial confinement of the QD leads to a discrete energy spectrum. In Figure 2.2 the evolution of the density of states $D(E)$ is depicted as the dimensionality is reduced. As more dimensions are confined the density of states $D(E)$ becomes less continuous, and finally becomes δ -function-like in case of the zero-dimensional QD. Due to their discrete level structure, QDs are often referred to as “artificial atoms”. However, these systems exhibit also features, for example *non*-exponential photoluminescence decay, which cannot be understood in a simple atomic-like (two-level) approach [10].

¹ This is the so-called type I heterostructure, whereas in type II systems only one type of carrier is confined. In this thesis only type I structures will be discussed.

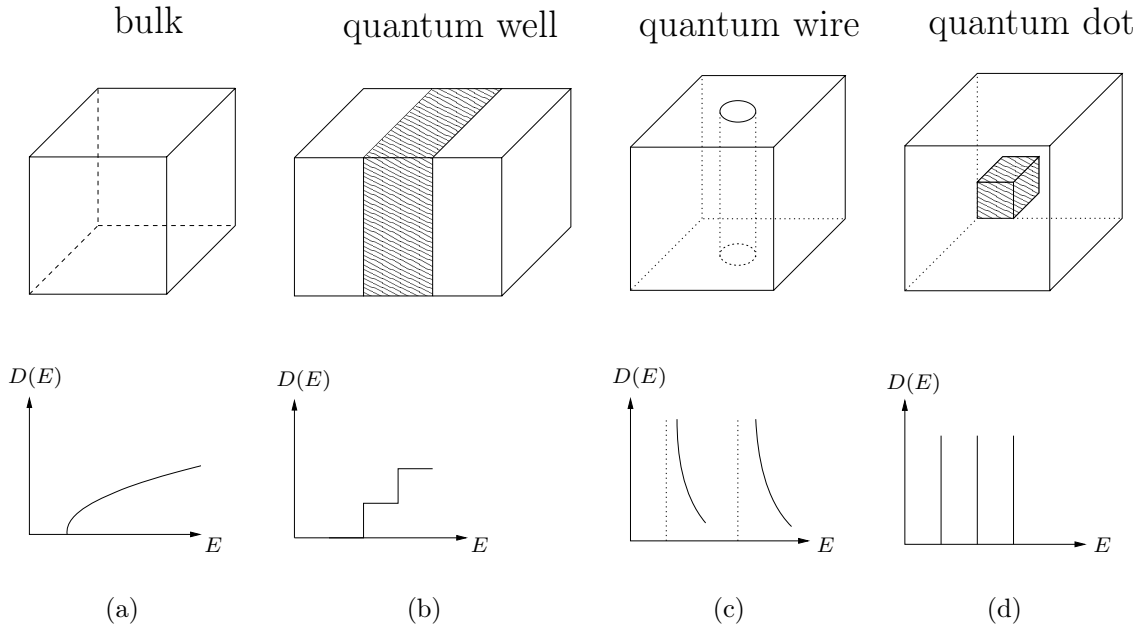


Figure 2.2: Evolution of the density of states $D(E)$ as the dimensionality of the structure is reduced from three dimensional bulk systems a) to zero-dimensional quantum dots d). As more dimensions are confined, the density of states becomes sharper and pronouncedly discrete.

The electronic and optical properties of QDs differ strongly from those of the higher dimensional systems such as bulk, quantum well and quantum wire systems. For example the optical properties as well as the electronic transport features depend strongly on the system size. As the dot size is reduced, the electronic energy is increased due to the increased kinetic energy. This behavior is already expected from a naive particle-in-a-box picture. As a consequence of the altered kinetic energy the excitonic absorption spectrum of QDs varies strongly with the system size. In a nice experiment the absorption was measured for spherical CdSe nanocrystals as function of the diameter [11]. The authors find, that by increasing the system size, the absorption edge can be shifted from the visible region to the near infrared region of the spectrum. Thanks to their size tunable properties, QDs are proposed as the building blocks of various optoelectronic devices, like low threshold lasers, quantum computers and memory devices.

Different fabrication techniques for the realization of these low dimensional systems are available. Semiconductor QDs can, for example, be produced by means of metallic gates providing external (electrostatic) confinement potentials [12], by means of self-organized clustering in the Stranski-Krastanow growth mode [13–15], or chemically by stopping the crystallographic growth using suitable surfactant materials [16–19]. In the present thesis we deal only with the latter two types of QDs. The QDs created in the Stranski-Krastanow growth mode emerge self-assembled in the epitaxial growth process because of the preferential deposition of material in regions of intrinsic strain or along certain crystallographic directions, due to the lattice mismatch between the

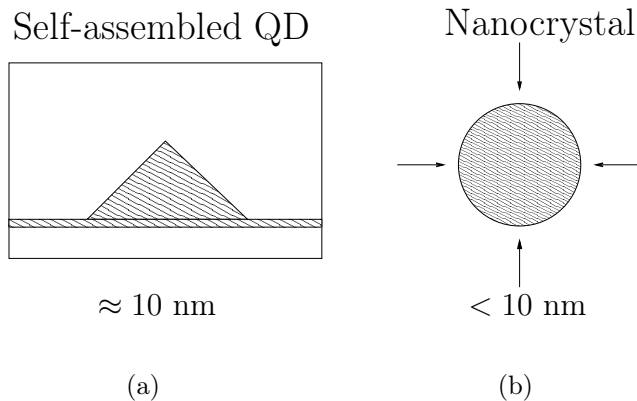


Figure 2.3: Schematically illustration of the two different types of QDs and sizes produced by different techniques. The Stranski-Krastanow growth mode leads to the formation of QDs, on top of a thin wetting layer. Spherical nanocrystals surrounded by a flexible glass matrix can be produced by chemical synthesis.

semiconductors A and B . In the epitaxial growth of a semiconductor material A on top of a semiconductor material B at most a few monolayers of A material may be deposited homogeneously as a quasi-two-dimensional A layer on top of the B surface forming the so-called wetting layer (WL). Further deposited A atoms will not form a further homogeneous layer but they will cluster and form islands of A material because this may lower the elastic energy due to the lattice mismatch of the A and B material. When the growth process is then stopped, free standing QDs of material A on top of an WL of material A on the B material are produced. If one continues the epitaxial growth process with B material, one obtains embedded QDs, i.e., QDs of A -material on top of an A -material WL embedded within B material.

The chemically realized QDs emerge by means of colloidal chemical synthesis [16, 17]. Thereby the crystal growth of semiconductor material in the surrounding of soap-like films, called surfactants, is stopped when the surface is covered by a monolayer of surfactant material. Thus one obtains tiny crystallites with their typical size being in the nanometer region. This is why these QDs are also called “nanocrystals”. The size and the shape of the grown nanocrystals can be controlled by external parameters such as growth time, temperature, concentration and the surfactant material [18, 19]. Due to the flexibility of the surrounding ligands, these structures exhibit the crystal structure of the bulk-materials and are nearly unstrained and spherical in shape. Certain physical properties like the band gap (and thus the color) depend crucially on the size of the nanocrystals. Typical diameters for both, embedded QDs and nanocrystals, are between 3 and 30 nm, i.e., they contain about 10^3 to 10^5 atoms. Therefore, they can be considered to be a new, artificial kind of condensed matter in between molecules and solids. For QDs grown in the Stranski-Krastanow growth modus, lens-shaped dots [20, 21], dome shaped and pyramidal dots [13, 22, 23], prismatic structures [24], and also truncated cones [25] have been found experimentally. Figure 2.3 gives a schematic illustration of the two different nanostructures.

After this brief overview of QDs and the growth mechanisms, we will turn our attention to the calculation of the electronic structure of these low dimensional systems. In the remainder of this chapter we present a short discussion of the three empirical models frequently used for QD studies.

2.2 Theoretical Approaches for the Calculation of Electronic Properties

One of the fundamental tasks is the calculation of the electronic properties of embedded QDs and nanocrystals. A major difficulty one encounters is that these systems are much larger than conventional molecules and at the same time lack a fundamental symmetry of solid state physics, namely translational invariance, which makes the calculation of bulk properties feasible. Therefore, neither the standard methods of theoretical chemistry nor those of solid state theory can immediately be applied. Conventional ab-initio methods of solid state theory based on density functional theory (DFT) and local density approximation (LDA) would require supercell calculations. However, as the size of a supercell must be larger than the embedded QD, such calculations are still beyond the possibility of present day computational equipment. To date, only systems with up to a few hundred atoms can be investigated in the framework of the standard ab-initio DFT methods [26–28]. Due to the generally high computationally demand of first principle studies, empirical models are widely used for the investigation of QDs. Three empirical models are mainly used for these studies: (i) single and multi-band effective-mass approximations [20, 29, 30], (ii) pseudopotential models [8, 31] and (iii) tight-binding approaches [9, 32]. In the following, we compare the different models and discuss their advantages and disadvantages.

2.2.1 Effective-Mass Approximation and $\mathbf{k} \cdot \mathbf{p}$ -Models

In the effective-mass approach the energy dispersion relations $E_n(\mathbf{k})$ of the bulk bands, in the vicinity of the band edge, are approximated to be parabolic. The kinetic part of the single-particle Hamiltonian is described by replacing the “bare” electron mass m_0 by an effective one, denoted m^* . In the simplest case, the coupling of different bands is neglected. Then, the effective single-particle Hamiltonian for electrons, H_e , and holes, H_h , can be written in the following form:

$$\begin{aligned} H_e &= -\frac{\hbar^2}{2m_e^*} \Delta + V_e(\mathbf{r}) + E_g , \\ H_h &= -\frac{\hbar^2}{2m_h^*} \Delta + V_h(\mathbf{r}) . \end{aligned}$$

Here m_e^* and m_h^* are the effective masses for electrons and holes, respectively. The band gap of the bulk material, which builds the QD, is given by E_g . The confinement

of the carriers is described by the potentials $V_e(\mathbf{r})$ and $V_h(\mathbf{r})$, for electrons and holes, respectively. As an example, the confinement potential $V(\mathbf{r})$ for electrons and holes of a spherical QD can be written in the following way:

$$V(\mathbf{r}) = V_0\Theta(r - R) \quad ,$$

where Θ is the step function, R is the radius of the QD. The constant V_0 is defined by the band offset between the dot and the surrounding material.

To improve the single-band effective-mass approximation, one can include more bands and allow the coupling between the different bands. These models are referred to as $\mathbf{k} \cdot \mathbf{p}$ -models. For example, the Kohn-Luttinger Hamiltonian for a zinc blende structure includes also the contributions of the second- and third highest valence bands to the hole Hamiltonian H_h [33]. This operator contains also the coupling between these three different valence bands, which are referred to as the *heavy-*, *light-* and *split-off* hole band.

The Luttinger-Kohn Hamiltonian can further be improved by including the couplings between the conduction and valence bands [34]. This leads to the so-called 8-band- $\mathbf{k} \cdot \mathbf{p}$ model. Due to these couplings, the single-particle Hamiltonian can no longer be divided into a part that describes the electrons and one that describes only the holes. The inclusion of the coupling between the conduction and valence bands is important especially for the investigation of nanostructures with narrow band gap [35].

The accuracy and applicability of both the single-band effective mass-approximation and the $\mathbf{k} \cdot \mathbf{p}$ -model has inherent restrictions caused by the non-parabolic dispersion of the bands away from the center of the first Brillouin zone, the so-called Γ point, and the lack of an atomistic description of the single-particle Hamiltonian. Since the construction of the Hamiltonian is based on the parabolic behavior of the bands in the vicinity of the Γ -point, this approximation is only valid, if the relevant properties of the nanostructure can be attributed to the single-particle states near the Γ point. Furthermore the $\mathbf{k} \cdot \mathbf{p}$ -model does not contain an atomistic description of ionic potentials. In such a continuum description only the global shape of the QD enters and the detailed atomistic symmetry is not described. Therefore, it cannot provide an accurate description of low-dimensional systems with complicated surface structures. Hence, the $\mathbf{k} \cdot \mathbf{p}$ -model is only applicable for relatively large QDs, where the properties of the low-dimensional system are dominated by the crystal structure inside the nanostructure, and the influence of the surface properties is negligible.

2.2.2 Pseudopotential Model

The general idea of the pseudopotential method is to replace the real potential due to the ion and the core electrons by a so-called pseudopotential, such that both potentials provide a similar behavior of the electron wave function in the region between the ions and away from the core-region. In such an approach the nodal features of the wave

functions in the core region are neglected by the choice of the pseudopotential. This is a reasonable approximation, if the relevant properties are dominated by contributions that stem from the variation of the wave function outside the core-region. In a pseudopotential approach plane waves are the typical basis states. The pseudopotential Hamiltonian H_{pp} and wave functions $\psi_{pp}(\mathbf{r})$ can be written as:

$$H_{pp} = -\frac{\hbar^2}{2m}\Delta + \sum_i V_{pp}(\mathbf{r} - \mathbf{R}_i)$$

$$\psi_{pp} = \sum_{\mathbf{k}} c_{\mathbf{k}} e^{i\mathbf{k}\mathbf{r}} ,$$

where \mathbf{R}_i denotes the lattice vector, and $V_{pp}(\mathbf{r})$ is the pseudopotential.

To study the electronic structure of a QD, the potential $V_{pp}(\mathbf{r} - \mathbf{R}_i)$ is given by the pseudopotential of the dot if \mathbf{R}_i is inside the QD and by the surrounding material otherwise. The confinement potential, which is treated in the effective-mass approximation by a step function, is in the pseudopotential approach atomistically described by the difference between the pseudopotentials of the dot and the barrier material. Since the single-particle Hamiltonian consists of the atomistic pseudopotentials, a single-particle wave function contains a detailed description of the variation between different sites. Due to the microscopic detail included in the pseudopotential model, the determination of single-particle states and energies is computationally extremely demanding.

2.2.3 Tight-Binding Model

Another powerful atomistic description for the investigation of single-particle states and energies of semiconductor QDs is the tight-binding (TB) model. This approximation is based on the assumption that the electrons in a solid are tightly bound to their ions. Therefore the TB single-particle Hamiltonian consists of the overlap between different localized states in the presence of the ionic potentials. The basis states of the TB model are localized orbitals of the valence electrons, which are not necessarily the same as the atomic orbitals of the corresponding valence electrons of an isolated atom. The matrix elements between various orbitals localized at different sites that determine the TB Hamiltonian can be evaluated by either ab-initio or empirical methods. In the ab-initio approach, the Hamiltonian matrix elements are calculated with the atomic orbitals and ionic potentials. In contrast, empirical models treat the matrix elements as fitting parameters which are adjusted to characteristic properties of the bulk band structure.

In summary, the effective-mass and $\mathbf{k} \cdot \mathbf{p}$ -model treat the QDs as confined continuum systems, whereas pseudopotential and TB models take into account the atomistic potentials. The difference between the latter two approaches lies in the degree to which the atomic details are included. In case of a TB model the atomic details are restricted

to a small basis set. The pseudopotential approach takes into account the local variation of the wave functions within a large basis set. However, the large number of plane waves needed to accurately describe the bulk system, does not guarantee that such an approach can be efficiently extended to nanostructures [36,37]. In such cases, new approaches based on the so-called *linear combination of bulk bands* (LCBB) [38] have to be applied to overcome these problems. With standard techniques, plane wave methods can hardly afford the study of nanostructures with more than a few hundreds of atoms. Since the size of the TB basis set is linear in the number of atoms, the TB approach is computationally less demanding than the standard pseudopotential method. To study relatively large and complicated systems, for which both the computational efficiency and atomistic treatment is required, the TB approach is particularly suitable. An example for such a system are vertically stacked QDs, which not only contain millions of atoms but also sharp edges and thin barriers [39,40]. In order to benefit from both the numerical efficiency and the atomistic description of low-dimensional nanostructures we use the TB model to study the electronic structure of semiconductor QDs. General aspects of the construction of the single-particle Hamiltonian for bulk-systems and nanostructures are discussed in detail in the following chapter.

3 Tight-Binding Models

A tight-binding (TB) model provides a microscopic description of the electronic properties in solids [41,42]. It is based on the assumption that electrons in solids, similar to atoms, are tightly bound to their respective atoms. This approach is the opposite limit to the free electron model which assumes that the electrons in a solid move freely so that their wave functions can be described by plane waves [41]. In the free electron model, the basic assumption is that the interaction between the conduction electrons and the atomic cores can be modeled by using a weak and perturbing potential. Even though the assumption of tightly bound electrons seems to limit the applicability of the TB model mainly to insulating materials and may be to the valence bands of semiconductors, it has been shown that the approach can also successfully describe the electronic structure of transition metals [43] and conduction bands of semiconductors. This is achieved by taking into account overlap matrix elements to more distant neighbor sites, and by increasing the basis set [44]. Therefore, the TB model provides a suitable atomistic approach to construct the single-particle Hamiltonian and to calculate the single-particle wave functions of a QD. The TB matrix elements can be obtained either by first-principle or empirical methods. In the first principle or ab-initio approach the Hamiltonian matrix elements are calculated using the atomic orbitals and the ionic potential. Such an approach is realized, for example, in the Density Functional based Tight Binding (DFTB) method [45]. In contrast to this approach, the empirical TB model treats the different matrix elements as parameters, and has the advantage of simplicity and computational efficiency, while reproducing all physical quantities accurately.

In the following section the theoretical basis of the TB model for the description of the electronic structure of bulk materials is explained. Furthermore the spin-orbit coupling will be addressed. The subsequent section deals with the implementation of tight binding models for semiconductor QDs. After this we introduce different approaches for the calculation of strain fields in these structures. The last section is dedicated to the calculation of a piezoelectric field that can occur in these low-dimensional systems.

3.1 Tight-Binding Model for Bulk Materials

Contrary to the free-electron picture, the TB model describes the electronic band structure starting from the limit of isolated-atoms. The basis states correspond to the localized orbitals of the different atoms. In this way, one obtains a description of the

electronic properties, which simultaneously takes into account the microscopic structure of the solid and offers a transparent approach. Unlike the artificial pseudopotentials the matrix elements in the TB approach have a simple physical interpretation as they represent couplings between electrons on adjacent atoms.

The localized basis states $|\mathbf{R}, \alpha, \nu, \sigma\rangle$ are classified according to their unit cell \mathbf{R} , the type of atom α at which they are centered, the orbital type ν , and the spin σ . The basic assumptions of the TB model are that (i) a small number of basis states per unit cell is already sufficient to describe the bulk band structure and (ii) that the overlap of the strongly localized atomic orbitals decreases rapidly with increasing distance of the atomic sites.

Since the inner electronic shells are only slightly affected by the field of all the other atoms, for the description of the bulk band structure it is sufficient to take into account the states of the outer shells. These orbitals then form the highest valence- and lowest conduction bands. We start from electron wave functions of an isolated atom. The Schrödinger equation for an atom located at the position \mathbf{R}_l is

$$H^{\text{at}}|\mathbf{R}_l, \alpha, \nu, \sigma\rangle = E_{\alpha, \nu}^{\text{at}}|\mathbf{R}_l, \alpha, \nu, \sigma\rangle ,$$

with

$$H^{\text{at}} = \frac{p^2}{2m_0} + V^0(\mathbf{R}_l, \alpha) ,$$

where $V^0(\mathbf{R}_l, \alpha)$ denotes the atomic potential of the atom at the position \mathbf{R}_l . Due to the presence of all other atoms in the crystal, the wave functions are modified. The single-particle Hamiltonian of the periodic system can be written in the following way:

$$H^{\text{bulk}} = H^{\text{at}}(\mathbf{R}_l, \alpha) + \underbrace{\sum_{\substack{n \neq l \\ \alpha'}} V(\mathbf{R}_n, \alpha')}_{\Delta V(\mathbf{R}_l)} .$$

Here, the Hamilton operator of the isolated atom α at the position \mathbf{R}_l is denoted by $H^{\text{at}}(\mathbf{R}_l, \alpha)$ and $\Delta V(\mathbf{R}_l)$ is the potential generated by all other ions in the lattice. The full problem of the periodic solid is then

$$H^{\text{bulk}}|\mathbf{k}\rangle = E(\mathbf{k})|\mathbf{k}\rangle , \quad (3.1)$$

where \mathbf{k} denotes the crystal wave vector. To solve the Schrödinger equation (3.1), the electronic wave functions $|\mathbf{k}\rangle$ are approximated by linear combinations of the atomic orbitals. Because of the translation symmetry of the crystal, the wave functions can be expressed in terms of Bloch functions:

$$|\mathbf{k}\rangle = \sqrt{\frac{V_0}{V}} \sum_n e^{i\mathbf{k}\mathbf{R}_n} \sum_{\alpha, \nu, \sigma} e^{i\mathbf{k}\Delta_\alpha} u_{\alpha, \nu, \sigma}(\mathbf{k}) |\mathbf{R}_n, \alpha, \nu, \sigma\rangle \quad \text{with} \quad \mathbf{k} \in 1. \text{ BZ} . \quad (3.2)$$

The position of the atom α in the unit cell \mathbf{R}_n is given by Δ_α . The volume of the unit cell is denoted by V_0 and the volume of the system by V . Due to the periodicity of

the crystal, it is sufficient to restrict \mathbf{k} to the first Brillouin zone (1. BZ). This ansatz fulfills the Bloch theorem [41].¹ By plugging the wave function of Eq. (3.2) into the Schrödinger equation

$$H^{\text{bulk}}|\mathbf{k}\rangle = [H^{\text{at}}(\mathbf{R}_l, \alpha) + \Delta V(\mathbf{R}_l)]|\mathbf{k}\rangle = E(\mathbf{k})|\mathbf{k}\rangle, \quad (3.3)$$

and applying the bra-vector $\langle \mathbf{k}, \alpha', \nu', \sigma' |$, one is left with a matrix equation

$$\sum_{\alpha, \nu, \sigma} H_{\alpha', \nu', \sigma'; \alpha, \nu, \sigma}^{\text{bulk}}(\mathbf{k}) u_{\alpha, \nu, \sigma}(\mathbf{k}) = E(\mathbf{k}) \sum_{\alpha, \nu, \sigma} S_{\alpha', \nu', \sigma'; \alpha, \nu, \sigma}(\mathbf{k}) u_{\alpha, \nu, \sigma}(\mathbf{k}), \quad (3.4)$$

instead of differential equation (3.3). For each \mathbf{k} , this constitutes a generalized eigenvalue problem for the matrix $\underline{\mathbf{H}}^{\text{bulk}}(\mathbf{k})$, with a matrix $\underline{\mathbf{S}}$ instead of the identity that occurs in an ordinary eigenvalue problem. $E(\mathbf{k})$ represents the eigenvalue, corresponding to the eigenvector $\mathbf{u}(\mathbf{k})$. The elements of the Hamiltonian-matrix read:

$$H_{\alpha', \nu', \sigma'; \alpha, \nu, \sigma}^{\text{bulk}}(\mathbf{k}) = \frac{V_0}{V} \sum_{n, m} e^{i\mathbf{k}(\mathbf{R}_m + \Delta_\alpha - \mathbf{R}_n - \Delta_{\alpha'})} \langle \mathbf{R}_m, \alpha', \nu', \sigma' | H^{\text{bulk}} | \mathbf{R}_n, \alpha, \nu, \sigma \rangle, \quad (3.5)$$

and the overlap-matrix elements $S_{\alpha', \nu', \sigma'; \alpha, \nu, \sigma}(\mathbf{k})$:

$$S_{\alpha', \nu', \sigma'; \alpha, \nu, \sigma}(\mathbf{k}) = \frac{V_0}{V} \sum_{n, m} e^{i\mathbf{k}(\mathbf{R}_m + \Delta_\alpha - \mathbf{R}_n - \Delta_{\alpha'})} \langle \mathbf{R}_m, \alpha', \nu', \sigma' | \mathbf{R}_n, \alpha, \nu, \sigma \rangle. \quad (3.6)$$

According to the basic assumptions of a TB model the electrons stay close to the atomic sites and the electronic wave functions centered around neighboring sites have little overlap. Consequently, there is almost no overlap between wave functions for electrons that are separated by two or more atoms (second-nearest neighbors, third nearest neighbors, etc.). Nevertheless, the basis orbitals, and thus the Bloch sums, are in general not fully orthogonal to one another.

It turns out, however, that if the localized TB basis \mathcal{B} is not orthogonal, one can use a so-called *Löwdin*-transformation, to transform it into an orthogonal one [46]. These Löwdin orbitals are also localized and preserve the symmetry of the orbital from which they are derived. The only prerequisite is that: The matrix of the overlap-integrals $S_{\alpha', \alpha, \nu', \nu, \sigma', \sigma}$ between the basis states of \mathcal{B} must be positive definite. However, this is

¹ In spatial representation, the wave function for a given (α, ν, σ) is

$$\langle \mathbf{r} | \mathbf{k}, \alpha, \nu, \sigma \rangle = \psi_{\alpha, \nu, \sigma, \mathbf{k}}(\mathbf{r}) = \sqrt{\frac{V_0}{V}} e^{i\mathbf{k}\Delta_\alpha} \sum_{\mathbf{R}} e^{i\mathbf{k}\mathbf{R}} \phi_{\alpha, \nu, \sigma}(\mathbf{r} - \mathbf{R}).$$

This wave function $\psi_{\alpha, \nu, \sigma, \mathbf{k}}(\mathbf{r})$ fulfills for any lattice vector \mathbf{R} the condition

$$\psi_{\alpha, \nu, \sigma, \mathbf{k}}(\mathbf{r} + \mathbf{R}) = e^{i\mathbf{k}\mathbf{R}} \psi_{\alpha, \nu, \sigma, \mathbf{k}}(\mathbf{r})$$

and therefore has the elementary properties of a Bloch function.

fulfilled in most cases for the strongly localized basis states which enter the matrix $\underline{\underline{S}}$. Therefore we assume in the following an orthogonal basis set, so that the overlap-matrix elements, Eq. (3.6), are given simply by:

$$S_{\alpha',\alpha,\nu',\nu,\sigma',\sigma} = \delta_{\mathbf{R}_m,\mathbf{R}_n} \delta_{\alpha',\alpha} \delta_{\nu',\nu} \delta_{\sigma',\sigma} , \quad (3.7)$$

and the Schrödinger equation, Eq. (3.4), is reduced to:

$$\sum_{\alpha,\nu,\sigma} H_{\alpha',\nu',\sigma';\alpha,\nu,\sigma}^{\text{bulk}}(\mathbf{k}) u_{\alpha,\nu,\sigma}(\mathbf{k}) = E(\mathbf{k}) u_{\alpha',\nu',\sigma'}(\mathbf{k}) . \quad (3.8)$$

For the sake of a simplified illustration only, we assume for the next couple of paragraphs a system with one atom per unit cell and one orbital per site. Furthermore, we assume a spin-independent Hamiltonian H^{bulk} , so that $\sigma' = \sigma$. In this case, the matrix elements $H_{\alpha',\nu',\sigma';\alpha,\nu,\sigma}^{\text{bulk}}(\mathbf{k})$ are given by:

$$\begin{aligned} \langle \mathbf{k}, \alpha, \nu, \sigma | H^{\text{bulk}} | \mathbf{k}, \alpha, \nu, \sigma \rangle &= \frac{V_0}{V} \sum_{m,n} e^{i\mathbf{k}(\mathbf{R}_n - \mathbf{R}_m)} \langle \mathbf{R}_m, \alpha, \nu, \sigma | H^{\text{bulk}} | \mathbf{R}_n, \alpha, \nu, \sigma \rangle \\ &= \frac{V_0}{V} \sum_{m,n} e^{i\mathbf{k}(\mathbf{R}_n - \mathbf{R}_m)} I_{mn} . \end{aligned} \quad (3.9)$$

Due to the localized structure of the atomic wave functions, the integrals I_{mn} become exponentially small for large $R = |(\mathbf{R}_m - \mathbf{R}_n)|$. It is therefore reasonable to ignore all integrals outside some R_{max} , as they would bring only negligible corrections to the band structure $E(\mathbf{k})$. The leading contribution is $n = m$, the so-called on-site contributions, then nearest neighbor contributions which we denote simply by $n = m \pm 1$, etc. Keeping only the leading order of the expression of Eq. (3.9), the matrix elements I_{mn} can be approximated as follows:

$$\begin{aligned} I_{mn} &= \delta_{n,m} \left[\langle \mathbf{R}_m, \alpha, \nu, \sigma | H^{\text{at}} | \mathbf{R}_n, \alpha, \nu, \sigma \rangle \right. \\ &\quad \left. + \sum_{l \neq n} \langle \mathbf{R}_m, \alpha, \nu, \sigma | V(\mathbf{R}_l, \alpha) | \mathbf{R}_n, \alpha, \nu, \sigma \rangle \right] \\ &\quad + \delta_{n \pm 1, m} \sum_l \langle \mathbf{R}_m, \alpha, \nu, \sigma | V(\mathbf{R}_l, \alpha) | \mathbf{R}_n, \alpha, \nu, \sigma \rangle + \dots \\ &\equiv \delta_{n,m} \tilde{E} + \delta_{n \pm 1, m} \lambda + \dots . \end{aligned} \quad (3.10)$$

where \tilde{E} can be interpreted as the renormalized atomic energy level in the presence of all the other atoms in the lattice. The matrix elements containing orbitals from different atomic sites are denoted by λ . Finally, one obtains from Eq. (3.9):

$$\langle \mathbf{k}, \alpha, \nu, \sigma | H^{\text{bulk}} | \mathbf{k}, \alpha, \nu, \sigma \rangle = \frac{V_0}{V} \sum_{m,n} e^{i\mathbf{k}(\mathbf{R}_n - \mathbf{R}_m)} (\delta_{n,m} \tilde{E} + \delta_{n \pm 1, m} \lambda + \dots) . \quad (3.11)$$

The symmetry properties of the crystal together with the symmetries of the basis states determine which matrix elements vanish and which are equal. For the calculation of the

TB matrix elements two different approaches are possible: From the knowledge of the atomic potential V^0 and the atomic orbitals, one could calculate the matrix elements of $\underline{\mathbf{H}}^{\text{bulk}}$ as well as the overlap matrix elements $S_{\alpha',\alpha,\nu',\nu,\sigma',\sigma}$. A different way to obtain these matrix elements is to treat them as parameters. This approach leads to the so-called *empirical* TB model. These parameters are fitted to characteristic properties of the bulk band structure, like band gaps and effective masses. With both methods a microscopic description of the solid arises. This approach can then be used to model semiconductor nanostructures, which consist of different semiconductor materials. In this work empirical TB models are employed.

As already discussed we assume that the basis states are Löwdin orbitals. Therefore the different TB-matrix elements can be symbolized by:

$$\langle \mathbf{R}', \alpha', \nu', \sigma' | H^{\text{bulk}} | \mathbf{R}, \alpha, \nu, \sigma \rangle = \underbrace{E_{\nu',\nu}(\mathbf{R} - \mathbf{R}')_{\alpha',\alpha} \delta_{\sigma,\sigma'}}_{\text{TB-parameter}} . \quad (3.12)$$

Here, the translation invariance of the crystal is already used. In addition, we have assumed that H^{bulk} is spin-independent. A spin-dependent component of H^{bulk} , the spin-orbit coupling, will be introduced in the following section. In this section, we drop the spin index σ , and denote the Hamiltonian by H_0^{bulk} .

The on-site matrix elements, $E_{\nu,\nu}(\mathbf{0})_{\alpha,\alpha}$, which are the expectation values of the Hamiltonian H^{bulk} between two identical atomic orbitals at the same site, correspond to the *orbital energies* which are renormalized and shifted due to the other atoms in the crystal. The matrix element $E_{\nu,\nu}(\mathbf{0})_{\alpha,\alpha}$ equals \tilde{E} in Eq. (3.10). The off-diagonal matrix elements, which describe the coupling between different orbitals at different sites are called *hopping matrix elements*, because they give the probability amplitude of an electron moving from one site to another [41].

To further reduce the number of relevant TB-matrix elements, one can use the so-called *two-center approximation* of Slater and Koster [47]. Slater and Koster proposed to neglect the so-called three-center integrals which are considerably smaller than the so-called two-center integrals. The three-center integrals involve two orbitals located at different atoms, and a potential part at a third atom. This corresponds to contributions in Eq. (3.10) where $l \neq n \neq m$. Thus, in the Slater and Koster approach, only the potential due to the two atoms at which the orbitals are located is taken into account. Therefore, the (effective) potential is symmetric around the axis $\mathbf{d} = \mathbf{R}' + \mathbf{\Delta}_{\alpha'} - (\mathbf{R} + \mathbf{\Delta}_{\alpha})$ between the two atoms. In this approximation, all hopping matrix elements vanish, if the two involved orbitals are eigenstates of the angular momentum $L_{\mathbf{d}} = \mathbf{L} \frac{\mathbf{d}}{d}$ in \mathbf{d} -direction with different eigenvalues $\hbar m_{\mathbf{d}} \neq \hbar m'_{\mathbf{d}}$. Since the (effective) Hamiltonian H , which contains the axially symmetric potential of the two atoms, commutes with $L_{\mathbf{d}}$, this statement follows from the simple consideration

$$0 = \langle i | [H, L_{\mathbf{d}}] | i' \rangle = \langle i | H L_{\mathbf{d}} | i' \rangle - \langle i | L_{\mathbf{d}} H | i' \rangle = \hbar (m'_{\mathbf{d}} - m_{\mathbf{d}}) \langle i | H | i' \rangle . \quad (3.13)$$

For an *sp*-bonding, there are only four nonzero hopping integrals as indicated in Figure 3.1, in which σ ($m_{\mathbf{d}} = 0$) and π ($m_{\mathbf{d}} = \pm 1$) bondings are defined such that the

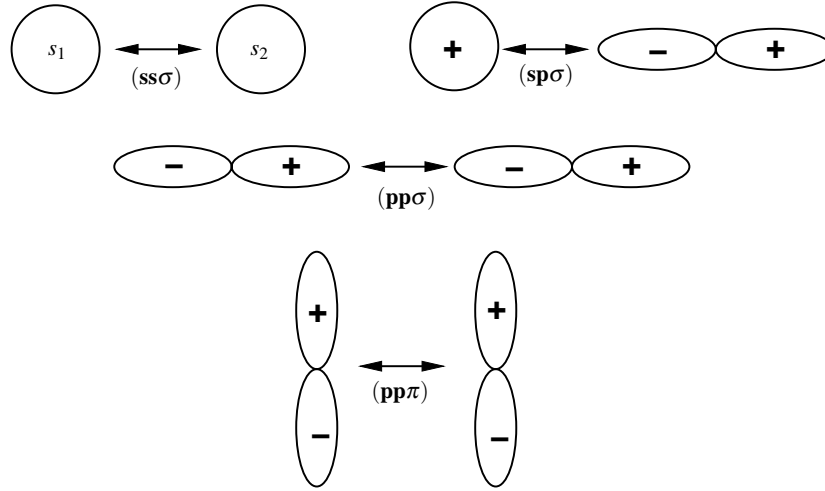


Figure 3.1: Nonzero hopping matrix elements $V_{ll'm}$ in case of an sp -bonding. The indices l and l' , denotes the orbital type and m the z component of the orbital angular momentum for rotation around the interaction vector.

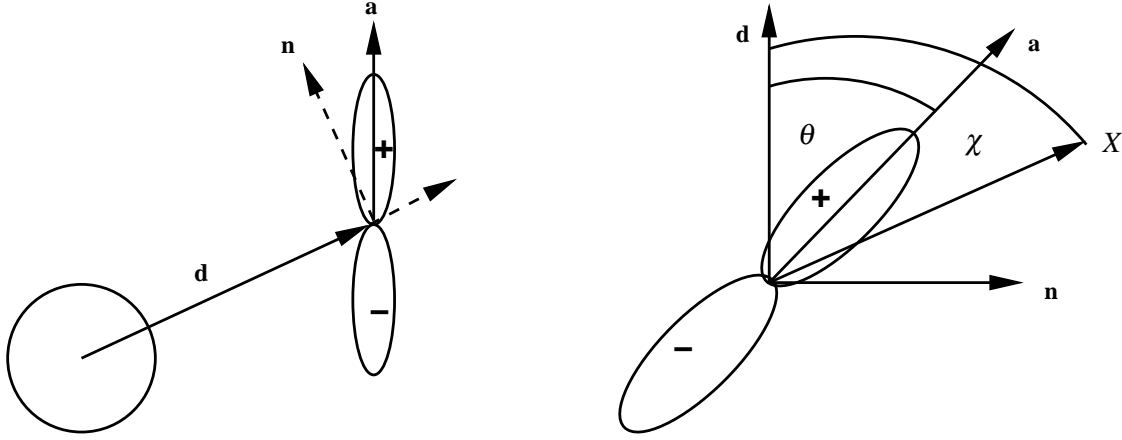
axes of the involved p orbitals are parallel and normal to the interatomic vector \mathbf{d} , respectively. So far, the electronic wave functions are expanded in terms of the p orbitals along the Cartesian x , y and z axis, whereas the hopping integrals are parameterized for p -orbitals that are parallel or normal to the bonding directions. To construct the Hamiltonian matrix elements, in the general case it is fruitful to decompose the Cartesian p orbitals into the bond-parallel and bond-normal p orbitals.

As an example of this procedure, we consider the Hamiltonian matrix element $\langle s|H|p_i\rangle$, between the s orbital, $|s\rangle$, and one of the p orbitals, $|p_i\rangle$ ($i = x, y, z$), localized at different atoms. Let \mathbf{d} be the vector along the bond from the first atom to the second and \mathbf{a} the unit vector along one of the Cartesian (x , y or z) axes, as shown in Figure 3.2(a). We first decompose the p orbital along \mathbf{a} , $|p_a\rangle$, into two p -orbitals that are parallel and normal to \mathbf{d} , respectively:

$$|p_a\rangle = \mathbf{ad}|p_\sigma\rangle + \mathbf{an}|p_\pi\rangle ,$$

where \mathbf{n} is the unit vector normal to \mathbf{d} within the plane spanned by \mathbf{d} and \mathbf{a} . Let θ be the angle between the vectors \mathbf{d} and \mathbf{a} . Consider an arbitrary point X in the three-dimensional space, whose polar angle from the \mathbf{d} axis is χ . This situation is depicted in Figure 3.2(b). At the point X , the value of the function $|p_a\rangle$ around the \mathbf{a} axis is given by

$$\begin{aligned} |p_a\rangle &= \cos(\theta - \chi) \\ &= \cos(\theta) \cos \chi + \sin(\theta) \sin(\chi) \\ &= \mathbf{ad} \cos(\chi) + \mathbf{an} \sin(\chi) \\ &= \mathbf{ad}|p_\sigma\rangle + \mathbf{an}|p_\pi\rangle . \end{aligned}$$



(a) Schematic illustration of the overlap between s and p_i orbital along the vector d joining the two atoms.

(b) Plane spanned by the unit vector \mathbf{n} and the vector \mathbf{d} . An arbitrary point X with the polar angle χ relative to \mathbf{d} is considered.

The Hamiltonian matrix element is then given by

$$\begin{aligned} \langle s_1 | H | p_{2,a} \rangle &= \mathbf{ad} \langle s | H | p_\sigma \rangle + \mathbf{an} \langle s | H | p_\pi \rangle \\ &= \mathbf{ad} \langle s | H | p_\sigma \rangle \\ &= \mathbf{ad} V_{sp\sigma} . \end{aligned}$$

The s -orbital centered around atom one is labeled by $|s_1\rangle$ and the p -orbital localized at atom two by $|p_{2,a}\rangle$. The matrix element $V_{sp\pi} = \langle s | H | p_\pi \rangle$ vanishes according to Eq. (3.13). To obtain an explicit formula in terms of p_x , p_y and p_z , let us introduce the directional cosines (d_x, d_y, d_z) along the x , y and z axes via $\mathbf{d} = |\mathbf{d}|(d_x, d_y, d_z)$. Then we obtain from the previous equation with $\mathbf{a} = \mathbf{e}_i$

$$\begin{pmatrix} \langle s_1 | H | p_{2,x} \rangle \\ \langle s_1 | H | p_{2,y} \rangle \\ \langle s_1 | H | p_{2,z} \rangle \end{pmatrix} = \begin{pmatrix} d_x V_{sp\sigma} \\ d_y V_{sp\sigma} \\ d_z V_{sp\sigma} \end{pmatrix} . \quad (3.14)$$

A similar analysis can be carried out for the matrix elements $\langle p_{1,i} | H | p_{2,j} \rangle$ and leads to

$$\begin{aligned} \langle p_{1,x} | H | p_{2,x} \rangle &= d_x^2 V_{pp\sigma} + (1 - d_x^2) V_{pp\pi} , \\ \langle p_{1,x} | H | p_{2,y} \rangle &= d_x d_y V_{pp\sigma} - d_x d_y V_{pp\pi} , \\ \langle p_{1,z} | H | p_{2,y} \rangle &= d_z d_y V_{pp\sigma} - d_z d_y V_{pp\pi} . \end{aligned} \quad (3.15)$$

The other hopping matrix elements can be obtained by cyclical permutation of the coordinates and direction cosines.

Therefore, by constructing the basis orbitals $|\mathbf{R}, \alpha, \nu\rangle$ as linear combinations of the basis states $|\mathbf{R}, \alpha, \{l, m\}\rangle$, the hopping parameters $E_{\nu', \nu}(\mathbf{R} - \mathbf{R}')_{\alpha', \alpha}$ can be described in terms of the parameters $V_{ll'm}$ and the directional cosines of \mathbf{d} :

$$\begin{aligned} E_{ss}(\mathbf{d})_{\alpha', \alpha} &= V_{ss\sigma}(d, \alpha', \alpha) , \\ E_{sx}(\mathbf{d})_{\alpha', \alpha} &= d_x V_{sp\sigma}(d, \alpha', \alpha) , \\ E_{xx}(\mathbf{d})_{\alpha', \alpha} &= d_x^2 V_{pp\sigma}(d, \alpha', \alpha) + (1 - d_x^2) V_{pp\pi}(d, \alpha', \alpha) , \\ E_{xy}(\mathbf{d})_{\alpha', \alpha} &= d_x d_y V_{pp\sigma}(d, \alpha', \alpha) - d_x d_y V_{pp\pi}(d, \alpha', \alpha) , \end{aligned}$$

with $\mathbf{d} = |\mathbf{d}|(d_x, d_y, d_z)$. Note that interchanging the order of the indices l and l' of $V_{ll'm}$ has no effect if the sum of the parities of the two orbitals is even, but changes sign if the sum of the parities is odd [47]. Similar formulas can be worked out for each combination of the localized orbitals, and are listed for example in Ref. [47]. Furthermore, one can deduce from the above considerations that the hopping matrix elements in two-center approximation depend only on the orbital type and the distance between the two sites.

Because of the translation invariance of the bulk system the Hamiltonian matrix $\underline{\underline{\mathbf{H}_0^{\text{bulk}}}}$ can be divided into sub-blocks which are diagonal in \mathbf{k} :

$$\underline{\underline{\mathbf{H}_0^{\text{bulk}}}}(\mathbf{k}) = (\langle \mathbf{k}, \alpha', \nu', \sigma' | H_0^{\text{bulk}} | \mathbf{k}, \alpha, \nu, \sigma \rangle) . \quad (3.16)$$

The dimension of this matrix depends on the number of basis states within one unit cell. From the diagonalization of this matrix, one obtains the energy dispersion $E(\mathbf{k})$ as a function of the TB parameters. The energy eigenstates $|n\mathbf{k}\rangle$ are related to the eigenvector $(\mathbf{u}_{n\mathbf{k}})_{\alpha, \nu, \sigma} = u_{n, \alpha, \nu, \sigma}(\mathbf{k})$ via

$$|n\mathbf{k}\rangle = \sum_{\alpha, \nu, \sigma} u_{n, \alpha, \nu, \sigma}(\mathbf{k}) |\mathbf{k}, \alpha, \nu, \sigma\rangle , \quad (3.17)$$

where n denotes the different bands.

In order to obtain an accurate description of the bulk band structure of semiconductor materials containing heavier atoms such as CdSe and InSb, relativistic effects on the electronic states in crystals have to be considered. In semiconductors containing lighter atoms such as AlP and InN, these effects are negligible for many purposes [48]. This is due to the fact that the potential is very strong near the nuclei and the kinetic energy is consequently very large, so that the electron velocity is comparable to the velocity of light. Therefore, the relativistic corrections become more important for heavy elements. One can include these contributions for the motion of an electron in a potential $V(\mathbf{r})$ by considering the *Dirac equation* [49]. From a *Foldy-Wouthuysen transformation* of the Dirac equation one obtains relativistic corrections to the Schrödinger equation. These additional terms are related to (i) relativistic corrections to the kinetic energy, (ii) relativistic contributions to the potential $V(\mathbf{r})$, known as the Darwin corrections and (iii) the spin-orbit interaction. The spin-orbit coupling originates from the interaction of the electron spin magnetic moment with the magnetic field “seen” by the electron. The first two components (i) and (ii) do not depend on the spin of the electron. Therefore

these terms do not change the symmetry properties of the non-relativistic Hamiltonian. However, the term corresponding to spin-orbit interaction, as we will see, couples the operators in spin space and ordinary spatial space, thus reducing the symmetry. The effect of the spin-orbit coupling in removing degeneracies of the non-relativistic results can be found using group theory [50].

Therefore, for certain semiconductor materials, it is essential for an accurate bulk band structure description in the framework of a TB model to include the contributions of the spin-orbit coupling. This issue will be discussed in the following section.

3.1.1 Spin-Orbit Coupling

In this section, we discuss the inclusion of the spin-orbit coupling in the TB band structure formalism. Here, the approach of Chadi [51] is employed to the TB scheme. An advantage of the technique presented is, that it allows the spin-orbit effect to be included without increasing the size of the basis. This is particularly significant for the calculation of QD states.

The TB approximation in its usual formulation does not include the spin-orbit interaction. For II-VI or III-V semiconductors, the basis for the eigensolution of the energy band equation, Eq. (3.8), normally consists of the s state and three p states for each atom in the unit cell. These four states are considered to be of the same spin. Of course, for a lattice structure where there are two or more atoms per unit cell the basis will be larger than the basis for crystals with one atom per unit cell as each atom contains s and p orbitals. The spin-orbit interaction is here considered to couple only p orbitals at the same atom. An s state with $l = 0$ is not split, since the angular part is constant. One can then apply this technique to each atom in the unit cell. This scheme can also be extended to include nearest neighbor spin-orbit interactions [52]. However, for the semiconductor materials under investigation in this work, e.g. CdSe, ZnSe, InN, GaN and AlN, it turns out that the interaction among the p -like orbitals at the same site is already sufficient to reproduce the valence band structure known from the literature at the Brillouin zone center.

We add the spin-orbit energy to the TB Hamiltonian H_0^{bulk} of the previous section. Therefore, the bulk Hamiltonian of a perfect crystal is given by:

$$H^{\text{bulk}} = H_0^{\text{bulk}} + H_{\text{so}} \quad (3.18)$$

where H_0^{bulk} is the spin-independent part and H_{so} denotes the operator of the spin-orbit coupling. Assuming only s - and p -orbitals, one has to investigate the action of this operator on the basis states of the previous section. The part H_0^{bulk} yields only non-zero interactions between states of the same spin. The matrix elements arising from the spin-orbit component H_{so} of the Hamiltonian H^{bulk} have the potential to connect states of different spins. To calculate these terms, we assume here that the operator

H_{so} acts on the TB basis states like the atomic spin-orbit operator [49]

$$H_{\text{so}}^{\text{atom}} = \frac{1}{2m^2c^2} \frac{1}{r} \frac{\partial V_{\text{atom}}}{\partial r} \mathbf{L} \mathbf{s} \quad (3.19)$$

on atomic orbitals. Here, V_{atom} is the atomic potential, \mathbf{s} the spin operator and \mathbf{L} denotes the operator of the angular momentum. As we will see in the following, the spin-orbit interaction can be described by a single parameter:

$$\lambda = \langle p_x | \frac{\hbar^2}{4m^2c^2} \frac{1}{r} \frac{\partial V_{\text{atom}}}{\partial r} | p_x \rangle . \quad (3.20)$$

All matrix elements $\langle p_i \sigma' | H_{\text{so}} | p_j \sigma \rangle$ can be determined in the following way: The operators s_x and s_y can be described by the flip/flop operators s_{\pm} :

$$\begin{aligned} s_x &= \frac{s_+ + s_-}{2} \\ s_y &= -i \frac{s_+ - s_-}{2} . \end{aligned}$$

The operators s_x , s_y and s_z act on the spin states $|\uparrow\rangle$ and $|\downarrow\rangle$ in the following way

$$\begin{aligned} s_x |\uparrow\rangle &= \frac{\hbar}{2} |\downarrow\rangle \quad ; \quad s_x |\downarrow\rangle = \frac{\hbar}{2} |\uparrow\rangle \\ s_y |\uparrow\rangle &= i \frac{\hbar}{2} |\downarrow\rangle \quad ; \quad s_y |\downarrow\rangle = -i \frac{\hbar}{2} |\uparrow\rangle \\ s_z |\uparrow\rangle &= \frac{\hbar}{2} |\uparrow\rangle \quad ; \quad s_z |\downarrow\rangle = -\frac{\hbar}{2} |\downarrow\rangle . \end{aligned} \quad (3.21)$$

Furthermore, we have to define the action of the angular momentum operator \mathbf{L} on the states $|p_x\rangle$, $|p_y\rangle$ and $|p_z\rangle$. The states can be written in terms of the *spherical harmonics* Y_{lm} :

$$\begin{aligned} |p_z\rangle &= Y_{10} = \sqrt{\frac{3}{4\pi}} \cos \theta = \sqrt{\frac{3}{4\pi}} \frac{z}{r} \\ |p_y\rangle &= \frac{i}{\sqrt{2}} (Y_{11} + Y_{1-1}) = \sqrt{\frac{3}{4\pi}} \frac{y}{r} \\ |p_x\rangle &= \frac{1}{\sqrt{2}} (Y_{1-1} - Y_{11}) = \sqrt{\frac{3}{4\pi}} \frac{x}{r} , \end{aligned} \quad (3.22)$$

which fulfill:

$$\begin{aligned} \mathbf{L}^2 Y_{lm} &= \hbar^2 l(l+1) Y_{lm} \\ L_z Y_{lm} &= \hbar m Y_{lm} . \end{aligned} \quad (3.23)$$

The calculation of the matrix elements shall exemplarily be demonstrated for the two matrix elements $\langle p_x \uparrow | H_{\text{so}} | p_y \uparrow \rangle$ and $\langle p_z \downarrow | H_{\text{so}} | p_x \uparrow \rangle$. For $\langle p_x \uparrow | H_{\text{so}} | p_y \uparrow \rangle$ we obtain:

$$\begin{aligned} \langle p_x \uparrow | H_{\text{so}} | p_y \uparrow \rangle &= \langle p_x \uparrow | C L_x s_x | p_y \uparrow \rangle + \langle p_x \uparrow | C L_y s_y | p_y \uparrow \rangle + \langle p_x \uparrow | C L_z s_z | p_y \uparrow \rangle \\ &= \frac{\hbar}{2} \langle p_x | C L_z | p_y \rangle = \frac{1}{i} \langle p_x | \frac{\hbar^2}{2} C | p_x \rangle , \end{aligned}$$

with C given by:

$$C = \frac{1}{2m^2c^2} \frac{1}{r} \frac{\partial V_{\text{atom}}}{\partial r}.$$

Here, we have used the Eqs. (3.21) and that the states $|\uparrow\rangle$ and $|\downarrow\rangle$ are orthogonal to each other to derive the second line from the first. The last line is obtained from Eq. (3.22). For the matrix element $\langle p_z \downarrow | H_{\text{so}} | p_x \uparrow \rangle$ we obtain:

$$\begin{aligned} \langle p_z \downarrow | H_{\text{so}} | p_x \uparrow \rangle &= \langle p_z \downarrow | CL_x s_x | p_x \uparrow \rangle + \langle p_z \downarrow | CL_y s_y | p_x \uparrow \rangle \\ &\quad + \langle p_z \downarrow | CL_z s_z | p_x \uparrow \rangle \\ &= \frac{\hbar}{2} \langle p_z | CL_x | p_x \rangle + i \frac{\hbar}{2} \langle p_z | CL_y | p_x \rangle \\ &= \underbrace{\frac{i\hbar^2}{2} \langle p_y | C | p_x \rangle}_{=0} + \langle p_x | \frac{\hbar^2}{2} C | p_x \rangle. \end{aligned}$$

Due to the symmetry of the wave functions, the matrix element $\langle y | C | x \rangle$ vanishes. This analysis shows that both matrix elements can be expressed in terms of

$$\langle p_x | \frac{\hbar^2}{4m^2c^2} \frac{1}{r} \frac{\partial V_{\text{atom}}}{\partial r} | p_x \rangle = \lambda.$$

Along the same line all the other elements can be deduced. Since the different states $|p_i \pm\rangle$ are orthogonal, many of the matrix elements will be zero. Evaluation of all possible terms gives non-zero results in case of

$$\begin{aligned} \langle p_x \pm | H_{\text{so}} | p_z \mp \rangle &= \pm \lambda \\ \langle p_x \pm | H_{\text{so}} | p_y \pm \rangle &= \mp i \lambda \\ \langle p_y \pm | H_{\text{so}} | p_z \mp \rangle &= -i \lambda, \end{aligned} \tag{3.24}$$

and their complex conjugates. To obtain a compact notation, we denote the states $|\uparrow\rangle$ and $|\downarrow\rangle$ by $|+\rangle$ and $|-\rangle$, respectively. The additional parameter λ is used to reproduce the splitting of the different valence bands in the vicinity of the Brillouin zone center.

To summarize this section, we have presented a technique which allows us to include the spin-orbit coupling in the TB formalism. The presented approach is particularly advantageous since it does not increase the size of the basis. In semiconductor materials with a large spin-orbit splitting at the Brillouin zone center, the inclusion of the spin-orbit coupling is important for a more accurate calculation of the bulk band structure and therefore a more realistic description of the single-particle states in semiconductor nanostructures.

3.2 Tight-Binding Model for Semiconductor Quantum Dots

Starting from the bulk tight-binding (TB) parameters, the embedded QD and the nanocrystal are modeled on an atomistic level. To this end one sets the matrix ele-

ments for each lattice site according to the occupying atom. For the matrix elements we use the TB parameters of the corresponding bulk materials. The resulting i^{th} TB wave function $|\psi_i\rangle$ of the nanostructures, is expressed in terms of the localized orbitals $|\nu, \alpha, \sigma, \mathbf{R}\rangle$:

$$|\psi_i\rangle = \sum_{\alpha, \nu, \sigma, \mathbf{R}} c_{\nu, \alpha, \sigma, \mathbf{R}}^i |\nu, \alpha, \sigma, \mathbf{R}\rangle. \quad (3.25)$$

As before \mathbf{R} denotes the unit cell, α the orbital type, σ the spin and ν an anion or cation. Then the Schrödinger equation leads to the following finite matrix eigenvalue problem:

$$\sum_{\alpha, \nu, \sigma, \mathbf{R}} \langle \nu', \alpha', \sigma', \mathbf{R}' | H | \nu, \alpha, \sigma, \mathbf{R} \rangle c_{\nu, \alpha, \sigma, \mathbf{R}}^i - E^i c_{\nu', \alpha', \sigma', \mathbf{R}'}^i = 0, \quad (3.26)$$

where E^i is the corresponding eigenvalue. The abbreviation $\langle \nu', \alpha', \sigma', \mathbf{R}' | H | \nu, \alpha, \sigma, \mathbf{R} \rangle = H_{l\mathbf{R}', m\mathbf{R}}$ is used in the following for the matrix elements with $l = \nu', \alpha', \sigma'$ and $m = \nu, \alpha, \sigma$.

To model a QD of material A embedded in a matrix of material B , a supercell with a crystal lattice is chosen. For the treatment of the surfaces of the nanocrystal or of the boundaries of the supercell there are different possibilities. One can use fixed boundary conditions, i.e., use a value of zero for the hopping matrix elements from a surface atom to its fictitious neighbors, or (for the embedded QDs) one can use periodic boundary conditions to avoid surface effects, which may arise artificially from the finite cell size. For the investigation of embedded structures we choose fixed boundary conditions, in order to reduce the number of non-zero matrix elements. To avoid numerical artifacts in the localized QD states, a sufficiently large supercell is required. As mentioned already, the abrupt termination of the supercell in an atomistic approach results in the creation of dangling bonds that will form surface states. These states often appear in the central energy region of the fundamental band gap. These surface effects in the finite-size supercell are removed according to Ref. [53], by a layer of atoms that passivates the surface of the supercell. Thus, we raise both the orbital energies of the passivating atoms and the hopping between the surface atoms and the passivating ones. In this method the electrons are inhibited from populating surface atom orbitals. By this means, one can remove the nonphysical surface states in the region of the energy gap.

In this thesis we will deal with CdSe/ZnSe, InN/GaN and GaN/AlN QDs, respectively. At the interfaces averages of the TB parameters are used to take into account that the nitrogen (selen) atoms cannot unambiguously be attributed to one of the constituting materials. Note that, we are using Löwdin transformed basis states and not pure atomic orbitals. The Löwdin basis states depend also on the neighboring atoms. Since in the investigated heterostructure semiconductors with different band gaps are combined, one has to take into account also the relative position of the conduction and valence band edge. The quantity that measures these discontinuities, is referred to as the valence band offset ΔE_v and conduction band offset ΔE_c , respectively. The relative position of conduction and valence band edge is determined by the electron affinities of the different materials [54]. The valence band offset ΔE_v between the two materials is included in

the model by shifting the diagonal matrix elements of the dot material:

$$\begin{aligned} \langle \mathbf{R}', \alpha', \nu', \sigma' | H | \mathbf{R}, \alpha, \nu, \sigma \rangle &= {}_A \langle \mathbf{R}', \alpha', \nu', \sigma' | H_A^{\text{bulk}} | \mathbf{R}, \alpha, \nu, \sigma \rangle_A \\ &+ \Delta E_v \delta_{\mathbf{R}, \mathbf{R}'} \delta_{\alpha, \alpha'} \delta_{\nu, \nu'} \delta_{\sigma, \sigma'} \end{aligned}$$

if (\mathbf{R}, α) and (\mathbf{R}', α') are in the region of the QD of material A and

$$\langle \mathbf{R}', \alpha', \nu', \sigma' | H | \mathbf{R}, \alpha, \nu, \sigma \rangle = {}_B \langle \mathbf{R}', \alpha', \nu', \sigma' | H_B^{\text{bulk}} | \mathbf{R}, \alpha, \nu, \sigma \rangle_B ,$$

if (\mathbf{R}, α) and (\mathbf{R}', α') are within the region of material B . There are different experimental techniques [55, 56] as well as theoretical approaches [57–59] to determine the valence band offsets ΔE_v between different materials.

Furthermore, in a heterostructure of two materials with different lattice constants strain effects have to be included in general for a realistic description of the electronic structure, because the distance between two lattice sites \mathbf{R} and \mathbf{R}' in the heterostructure is not the same as the corresponding value in the bulk system. Additionally the bond angles will be affected by the strain field in the nanostructure. This means that the TB matrix elements $H_{l\mathbf{R}', m\mathbf{R}}$ in the QD differ from those of the unstrained bulk material. In the following the bulk matrix elements without taking strain into account are denoted by $H_{l\mathbf{R}', m\mathbf{R}}^0$. We consider here only scaling of the inter-site matrix elements, for which, in general, a relation

$$H_{l\mathbf{R}', m\mathbf{R}} = H_{l\mathbf{R}', m\mathbf{R}}^0 f(\mathbf{d}_{\mathbf{R}'-\mathbf{R}}^0, \mathbf{d}_{\mathbf{R}'-\mathbf{R}}) \quad (3.27)$$

is expected, where $\mathbf{d}_{\mathbf{R}'-\mathbf{R}}^0$ and $\mathbf{d}_{\mathbf{R}'-\mathbf{R}}$ are the bond vectors between the atomic positions of the unstrained and strained material, respectively. Since the atomic-like orbitals of TB models are typically orthogonalized Löwdin orbitals, it might be that the diagonal matrix elements, too, vary in response to displacements of neighboring atoms. [60, 61] However, Priester *et al.* [62] achieved a very accurate band structure description in the framework of a spin-orbit dependent sp^3s^* TB model without adjusting the diagonal matrix elements. Therefore, we consider here only scaling of the inter-site matrix elements. The function $f(\mathbf{d}_{\mathbf{R}'-\mathbf{R}}^0, \mathbf{d}_{\mathbf{R}'-\mathbf{R}})$ describes, in general, the influence of the bond length and the bond angle on the inter-site (hopping) matrix elements. Here we use the relation $f(\mathbf{d}_{\mathbf{R}'-\mathbf{R}}^0, \mathbf{d}_{\mathbf{R}'-\mathbf{R}}) = (d_{\mathbf{R}'-\mathbf{R}}^0/d_{\mathbf{R}'-\mathbf{R}})^2$. This corresponds to Harrison's [63] d^{-2} rule, the validity of which has been demonstrated for II-VI-materials and nearest neighbors by Sapiro *et al.* [64]. Furthermore the results of Bertho *et al.* [65] for the calculations of hydrostatic and uniaxial deformation potentials in case of ZnSe show that the d^{-2} rule should be a reasonable approximation. Our model assumption for the function $f(\mathbf{d}_{\mathbf{R}'-\mathbf{R}}^0, \mathbf{d}_{\mathbf{R}'-\mathbf{R}})$ means that we have neglected so far the influence of bond angle distortion. In the Slater-Koster-formalism [47] which has been discussed in Section 3.1, the bond angle distortions can exactly be included in a TB model. This means that the directional cosines between the different atomic orbitals, see Eqs. (3.14) and (3.15), are calculated according to the strain-induced displacements of the different atoms. With this so-called d^{-2} ansatz, the interatomic matrix elements $H_{l\mathbf{R}', m\mathbf{R}}$, with $\mathbf{R}' \neq \mathbf{R}$, are given by

$$H_{l\mathbf{R}', m\mathbf{R}} = H_{l\mathbf{R}', m\mathbf{R}}^0 \left(\frac{d_{\mathbf{R}'-\mathbf{R}}^0}{d_{\mathbf{R}'-\mathbf{R}}} \right)^2 . \quad (3.28)$$

We use this power-law scaling also for the second nearest neighbors. It should be noted that the scaling of more distant matrix elements is not nearly as well understood as that of nearest neighbor matrix elements. More sophisticated ways to treat the scaling of the interatomic matrix elements, e.g. by calculating the dependence of energy bands on volume deformation effects, and different exponents for different orbitals can be found in the literature [9, 60, 66].

Another feature which stems from the crystal deformation of a semiconductor are electrostatic fields, the so-called *piezoelectric effect* [67]. This effect is caused by the displacements of the ions in response to the mechanical deformations, leading to the occurrence of charges on some of the crystal surfaces.²

After setting up the TB model for a nanostructure, one has to deal with the following three problems. First we have to calculate the strain field which is present in the nanostructure. In the following section, we will discuss two different approaches for the calculation of the strain field. Second, we have to introduce a piezoelectric field in the TB approach. This is detailed in Section 3.2.2. Third, after the TB Hamiltonian, including strain effects and piezoelectricity, is generated, the calculation of the single-particle states and energies is now reduced to the diagonalization of a finite but very large matrix. To calculate the eigenvalues of this matrix, in particular the bound electronic states in the QD, the *folded spectrum method* [36] is applied. In contrast to conventional diagonalization methods, this approach has the advantage that it scales linearly with the number of atoms in the system. The basic ideas of the folded spectrum method will be outlined in Section 3.2.3.

3.2.1 Strain fields

For the calculation of strain fields there are different theoretical approaches available: (i) Continuum elasticity approaches, (ii) atomistic approaches based on the so-called valence force field method or (iii) methods based on a Green's function approach. In the following we will briefly introduce the continuum mechanical model and the valence force field approach. For the Green function scheme, we refer the reader to Ref. [70].

Continuum mechanical model

In the continuum mechanical model the total strain energy is given by [71]

$$E_{\text{CM}} = \frac{1}{2} \sum_{i,j,k,l}^3 C_{ijkl}(\mathbf{r}) \epsilon_{ij}(\mathbf{r}) \epsilon_{kl}(\mathbf{r}) . \quad (3.29)$$

² Of course, the contribution introduced by the displacement of the ionic displacements tends to be counterbalanced by an electronic response. Therefore, this leads to a complicated interplay between ionic and electronic contributions [68, 69].

Here, the elastic moduli are denoted by $C_{ijkl}(\mathbf{r})$ and the components of the strain tensor are given by $\epsilon_{ij}(\mathbf{r})$. When \mathbf{r} is inside the QD, C_{ijkl} corresponds to the tensor of the elastic moduli of the dot material, otherwise to the elastic moduli of the barrier material. The tensor of the elastic moduli is different for materials with zinc blende or wurtzite crystal structure and is explicitly given for both structures in Ref. [72]. Since the strain tensor is symmetric, it can be represented in the following form:

$$\underline{\underline{\epsilon}} = \begin{pmatrix} \epsilon_{11} & \epsilon_{12} & \epsilon_{13} \\ \epsilon_{12} & \epsilon_{22} & \epsilon_{23} \\ \epsilon_{13} & \epsilon_{23} & \epsilon_{33} \end{pmatrix}. \quad (3.30)$$

The six components of the strain tensor $\underline{\underline{\epsilon}}$ are related to the displacement vector field $\mathbf{u}(\mathbf{r})$ of the atoms. The displacement $\mathbf{u}(\mathbf{r})$ describes the movement of the atom located at the point \mathbf{r}_0 to the spatial point \mathbf{r} by the relation $\mathbf{r}_0 + \mathbf{u}(\mathbf{r}) = \mathbf{r}$. For a given QD structure E_{CM} is minimized, using finite differences for the strain tensor $\epsilon_{ij} \propto \partial u_i / \partial x_j$. A detailed discussion of this approach can be found in Ref. [73].

Valence force field method

The continuum mechanical model can describe elastic properties and therefore strain effects only on a mesoscopic scale. Such an approach is only suitable for systems with small strain contributions. In particular, problems arise for regions where the strain changes extremely rapidly, e.g., at the edges and corners of embedded structures. Thus, for very small QD structures a microscopic, atomistic approach is required for the strain field calculation. Such a treatment is provided by the valence force field approach [74], which uses a Keating potential [74, 75] for the interatomic interactions. In that case, the strain energy E_{VFF} is expressed as a function of the bond length and the bond angle distortion

$$E_{VFF} = \overbrace{\frac{1}{4} \sum_i \left[3 \frac{\alpha_{ij}}{4} \sum_j \frac{(|\mathbf{R}_i - \mathbf{R}_j|^2 - (d_{ij}^0)^2)^2}{(d_{ij}^0)^2} \right]}^{E_{\text{stretch}}} + \underbrace{\frac{1}{4} \sum_i \left[\sum_{j,k>j} \frac{3\beta_{ijk}}{2d_{ij}^0 d_{ik}^0} [(\mathbf{R}_j - \mathbf{R}_i)(\mathbf{R}_k - \mathbf{R}_i) - \cos \theta_0 d_{ij}^0 d_{ik}^0]^2 \right]}_{E_{\text{bend}}}.$$

Here, d_{ij}^0 denotes the bulk equilibrium bond length between nearest neighbor atoms i and j in the corresponding material. The position of the i^{th} -atom is given by \mathbf{R}_i . The ideal bond angle is denoted by θ_0 . The first term E_{stretch} is a sum over all atoms i and, in case of zinc blende or wurtzite structures, over its four nearest neighbors j . The term E_{stretch} is non-zero when the bond *length* is changed compared to the system without strain and is therefore called *bond-stretching* interaction. The second term E_{bend} is a

sum over all atoms i and all pairs of their neighbors (i, j) . E_{bend} is non-zero when the *angle* between bonds is altered and thus it is the so-called *bond – bending* interaction. The local-environment-dependent coefficients α_{ij} and β_{ikj} are the bond-stretching and bond-bending force constants, respectively.

A comparison between the valence force field method and continuum mechanical model has been given by Pryor *et al.* [73]. They compare the strain distribution of pyramidal InAs QDs embedded in a GaAs matrix obtained by the two approaches. A significant difference was found in the strain around the dot interfaces and inside the QD. The deviation in the barrier material was found to be very small. This discrepancy originates from the fact that the strain contributions are clearly outside the linearity regime of the continuum mechanical model, and can also be attributed to the loss of the correct atomic symmetry the continuum mechanical approach is based on.

3.2.2 Piezoelectricity

After the discussion of strain effects, we turn our attention to the piezoelectric effect. The strain in the nanostructure causes atoms in the unit cell to shift relative to each other. In certain directions, such a shift can lead to a polarization. For example in a zinc blende semiconductor, the polarization is due to shear strains only and can be written in the following way [72]:

$$\mathbf{P}_{\text{piezo}} \propto \begin{pmatrix} \epsilon_{23} \\ \epsilon_{13} \\ \epsilon_{12} \end{pmatrix}$$

This means, that the strain in pseudomorphically grown heterostructures can cause piezoelectric polarization in a semiconductor. Therefore the main effect is expected when the growth direction is along the [111]-direction and the strain has purely shear character. For the [001] growth direction, no piezoelectric polarization is expected [76, 77].

How can such a piezoelectric polarization be included in an electronic structure calculation? A self-consistent calculation of the electronic structure of a deformed solid naturally includes the field generated by piezoelectric displacements. Of course, such a self-consistent evaluation requires the inclusion of all occupied states and their response to strain effects. Therefore such an approach is limited to very small systems. For larger systems ($\gg 10^3$ atoms) it is often impractical to calculate all occupied states, and one has to concentrate oneself to only a few states in the energy range of interest. In such cases the calculation is no longer self-consistent and the piezoelectricity does not arise naturally. Instead it has to be introduced as an external potential V_{piezo} in the Schrödinger equation.

The evaluation of the external piezoelectric potential V_{piezo} can be divided into four steps. In a first step one has to determine the so-called piezoelectric coefficients for the

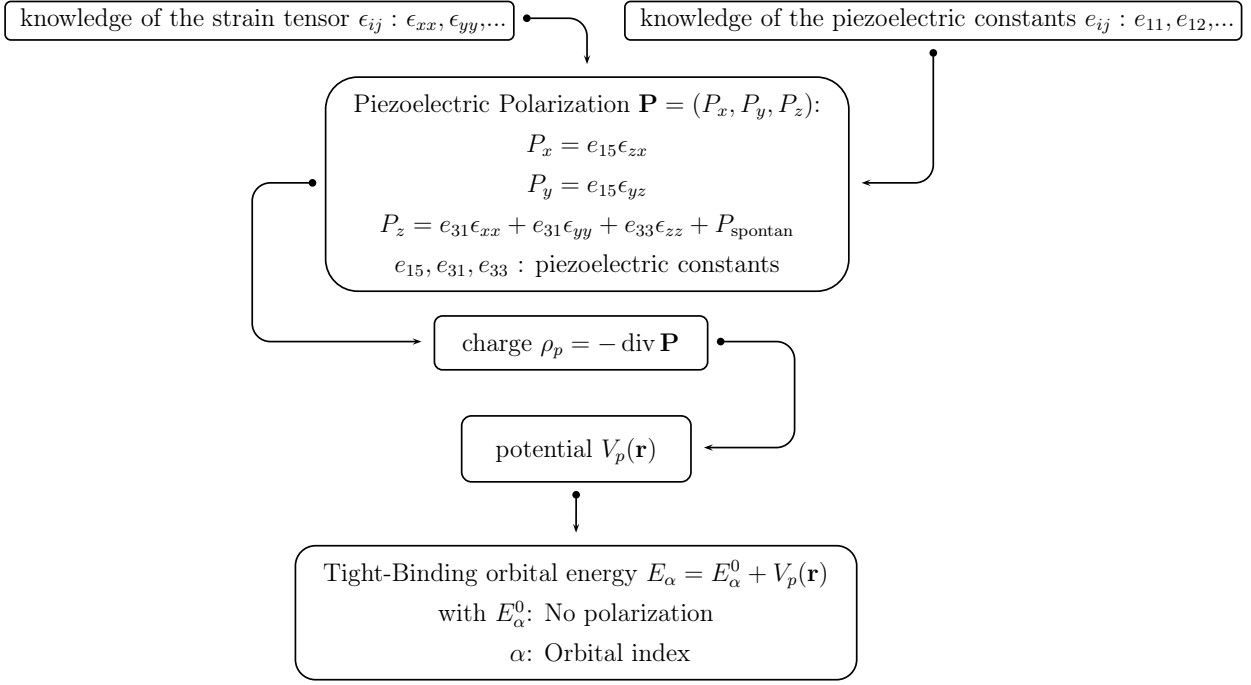


Figure 3.2: Flowchart for the calculation of the piezoelectric potential and its inclusion in a tight-binding model. The explicit formulas are given for a wurtzite structure.

strained bulk materials. This can either be done theoretically using, for example, linear response density functional theory [78] or experimentally by interpreting the measured electrostatic fields and assuming a linear relationship between polarization and strain [79, 80].³

In the second step the piezoelectric polarization $\mathbf{P}_{\text{piezo}}$ is calculated from the strain field in the following way

$$P_i^{\text{piezo}} = \sum_j^6 e_{ij} \epsilon_j ,$$

with the notations

$$(\epsilon_{11}, \epsilon_{22}, \epsilon_{33}, \epsilon_{23}, \epsilon_{13}, \epsilon_{12}) = (\epsilon_1, \epsilon_2, \epsilon_3, \epsilon_4, \epsilon_5, \epsilon_6) .$$

The matrix $\underline{\underline{e}}$ of the piezoelectric coefficients depends on the material system and is given for zinc blende and wurtzite structures explicitly in Ref. [72].

In step three, one has to calculate the piezoelectric charge density ρ_{piezo} from the divergence of the polarization $\mathbf{P}_{\text{piezo}}$

$$\rho_{\text{piezo}} = -\text{div } \mathbf{P}_{\text{piezo}} .$$

³ However, second order effects are hardly to detect, because the measurements are restricted to systems with small lattice mismatch, like $\text{In}_x\text{Ga}_{1-x}\text{As}$ QWs with low In-content. Heterostructures with large lattice mismatch were avoided because they tend to exhibit dislocations and defects.

In the final step, the electrostatic potential ϕ_{piezo} can be obtained from the solution of the Poisson equation:

$$\rho_{\text{piezo}} = \epsilon_0 \nabla [\epsilon_r(\mathbf{r}) \nabla \phi_{\text{piezo}}] \quad (3.31)$$

$$\Rightarrow \Delta \phi_{\text{piezo}}(\mathbf{r}) = \frac{\rho_{\text{piezo}}}{\epsilon_0 \epsilon_r} - \frac{1}{\epsilon_r(\mathbf{r})} \nabla \phi_{\text{piezo}}(\mathbf{r}) \nabla \epsilon_r(\mathbf{r}) \quad (3.32)$$

where $\epsilon_r(\mathbf{r})$ is the static dielectric constant of the respective material at the position \mathbf{r} . The first term on the right-hand side of Eq. (3.32) refers to the true three-dimensional charge density while the second term is connected with the polarization surface charge densities caused by the discontinuity of the dielectric constant $\epsilon_r(\mathbf{r})$. The latter one is often discussed as image charge contribution [81, 82].

The resulting electrostatic potential is included in the TB model as a site-diagonal potential energy $V_{\text{piezo}} = -e\phi_{\text{piezo}}$. This method has successfully been applied to quantum well [83] and QD [84] structures. A schematic representation of the whole procedure is depicted in Figure 3.2.

3.2.3 Numerical Determination of Eigenvalues: The Folded Spectrum Method

As already discussed in Section 3.2, the single-particle TB-Hamiltonian H of the whole supercell corresponds to a very large matrix. Therefore, the eigenstates and eigenenergies must be determined by efficient diagonalization algorithms. For the electronic structure and optical properties of a nanostructure, quantities of particular interest are the electronic states near the band gap, that are states near the valence band maximum and conduction band minimum. Therefore, the knowledge of all the eigenstates of the matrix is neither required nor feasible even with modern supercomputers. If valence and conduction band would decouple, the states of interest would be the eigenfunctions with the largest and smallest eigenvalue in valence and conduction band, respectively. For such special cases extremely efficient algorithms exist. Due to the coupling between conduction and valence band the states of interest are energetically somewhat in the interior of the spectrum of the Hamiltonian H . Therefore, the single-particle Schrödinger equation, Eq. (3.26), has to be solved as an *interior* eigenvalue problem and only a few eigenvalues near the band gap region must be computed. For this purpose we employ the *folded spectrum method* [36].

The folded spectrum method was developed by Wang and Zunger in 1993 for large scale non-selfconsistent calculations of mesoscopic systems (> 1000 atoms). The conventional approach to the eigenvalue problem defined by

$$H|\psi_i\rangle = \epsilon_i|\psi_i\rangle, \quad (3.33)$$

is to minimize the expectation value $\langle \psi_i | H | \psi_i \rangle$. The first wave function obtained by this approach is then the lowest energy eigenstate of H . To find a higher state $|\psi_i\rangle$,

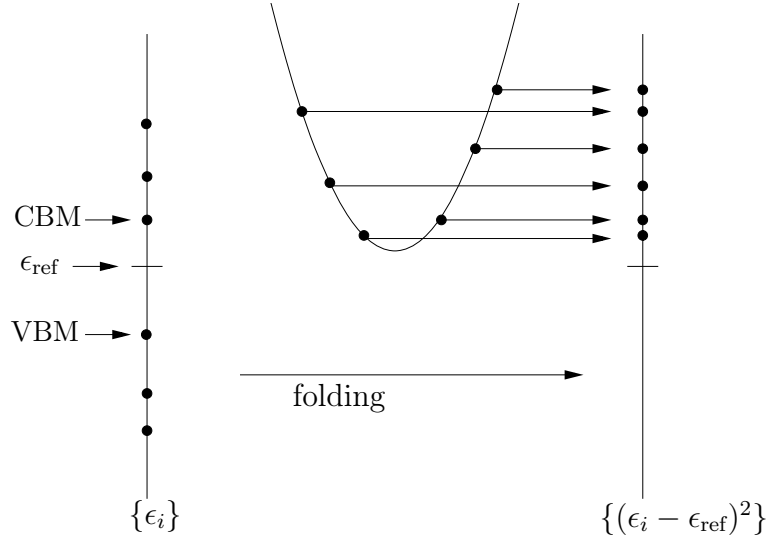


Figure 3.3: Schematic illustration of the folded spectrum method. Left hand side: Eigenvalue spectrum of the Hamiltonian H . Right hand side: Folded spectrum of $(H - \epsilon_{\text{ref}}\mathbb{1})^2$. The conduction band maximum and valence band minimum are denoted by CBM and VBM, respectively.

one has to orthogonalize $|\psi_i\rangle$ to the previously converged eigenstates $\{|\psi_j\rangle\}_{j=1}^i$ with lower energies. The effort which is required for this orthogonalization procedure scales as N^3 , where N is the number of atoms in the system. Consequently, this conventional approach is only applicable to small systems ($N \lesssim 1000$ atoms). Therefore to study QD structures that contain several thousand atoms, one needs a technique which enables the calculation of eigensolutions in the vicinity of a given reference energy ϵ_{ref} without the requirement to calculate all the solutions energetically below it. This idea leads to the folded spectrum method. A schematic representation of the folded spectrum method is given in Figure 3.2. The central point is, that the solutions of Eq. (3.33) also satisfy the following equation

$$(H - \epsilon_{\text{ref}}\mathbb{1})^2 |\psi_i\rangle = (\epsilon_i - \epsilon_{\text{ref}})^2 |\psi_i\rangle \quad (3.34)$$

This means that the original spectrum $\{\epsilon_i\}$ of H has been folded around the point ϵ_{ref} into the spectrum $\{\epsilon_i - \epsilon_{\text{ref}}\}$. Thus, the lowest eigensolution of the new, *folded* spectrum is the eigenstate with ϵ_i closest to ϵ_{ref} . Within this approach, one can transform an arbitrarily high eigensolution into the lowest one, just by placing the reference energy ϵ_{ref} close to the energy of interest. This avoids the manifold orthogonalization process. If ϵ_{ref} is placed in the band gap region of the dot material, the solution of Eq. (3.34) with the lowest energy results either in a state near the valence band maximum or a state near the conduction band minimum, depending on which is closer to ϵ_{ref} . By changing ϵ_{ref} in the band gap region, one can find both the states near the valence band maximum and those near conduction band minimum. The effort involved in this method scales linearly with the system size [36].

The solution of Eq. (3.34) is numerically achieved by the PARPACK (Parallel ARPACK)

routines [85]. **PARPACK** is an extension of the **ARPACK** libraries used for large-scale eigenvalue problems on distributed memory parallel architectures. Such an architecture is provided by the Forschungszentrum Jülich with the supercomputer ‘JUMP’ [86]. The **PARPACK** package is designed to compute a few eigenvalues, e.g., those with smallest real-part or smallest magnitude, and corresponding eigenvectors of a general n by n matrix. It is most appropriate for large sparse matrices.

4 Short Introduction in Group Theory

The symmetry of the atomic arrangement is the basis for the classification of the various crystal structures. Using group theory, important conclusions can be drawn about the physical properties of the crystal, such as its elastic and electronic properties. Furthermore, it makes it possible to classify states, and, more importantly, to determine selection rules without the need for any numerical calculations. The application of symmetry arguments to atoms and molecules has its origin in group theory developed by mathematicians in the 19th century. This subject is often presented in a rigorous mathematical formulation. However, it is possible to progress quite a long way in understanding symmetry without a detailed mathematical knowledge of the theory of groups, and only a simple introduction to the subject will be outlined here. Detailed discussions are given for example in Refs. [50, 87, 88].

4.1 General Considerations

A set of elements $G = \{g_1, g_2, g_3, \dots\}$ with an operation denoted by “.” is a group if the following axioms are obeyed:

- A1** *Closure.* If g_1 and g_2 are two members of the group, then their product $g_3 = g_1 \cdot g_2$ must also be a member of the group.
- A2** *Associativity.* The rule of combination must be such that the associativity property holds. This means, if $g_1, g_2,$ and g_3 are any three elements of the group, then $(g_1 \cdot g_2) \cdot g_3 = g_1 \cdot (g_2 \cdot g_3)$.
- A3** *Identity.* The group must contain a unique element E such that for any element g_1 of the group, $g_1 \cdot E = E \cdot g_1 = g_1$. Therefore, E is called the identity element.
- A4** *Inverse.* Each element g_1 of the group must have an inverse g_1^{-1} that is also a member of the group. By the term inverse we mean that $g_1 \cdot g_1^{-1} = g_1^{-1} \cdot g_1 = E$.

Each molecule or crystal lattice has a number of so-called *symmetry elements*, which leave the system unchanged. These operations, in addition to the identity operation, are normally considered to include rotation around an axis, reflection at a plane, inversion through a point, translation or a combination of these operations. All symmetry operations that leave a crystal unchanged constitute a so-called *space group*. Besides

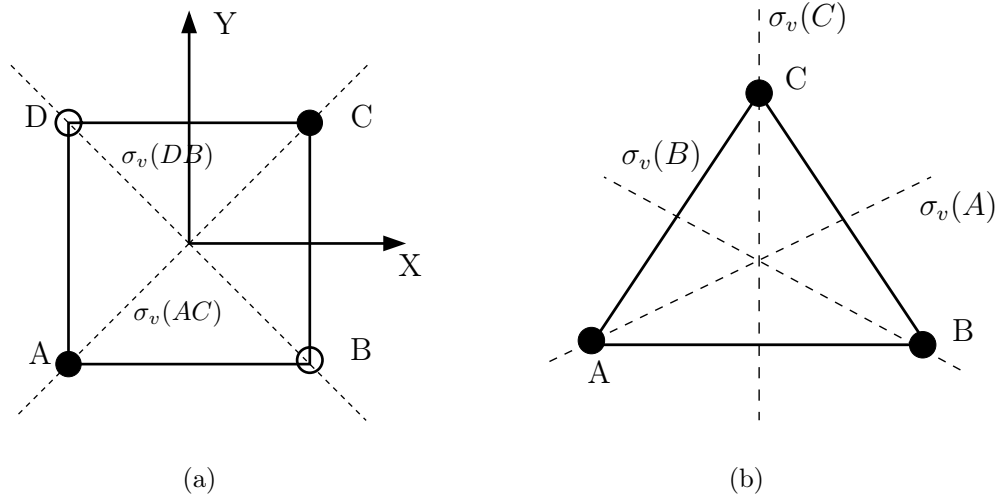


Figure 4.1: Schematic representation of (a) C_{2v} and (b) C_{3v} symmetry. The dashed lines indicate the mirror planes.

the translation symmetry operations, a space group contains rotations and reflections, followed by an appropriate displacement. The elements of a space group can be denoted by $\{\underline{\mathbf{R}}|\mathbf{a}\}$, where $\underline{\mathbf{R}}$ is a matrix indicating the rotational part (rotations, rotations followed by inversion), \mathbf{a} is an appropriate space displacement vector. All possible vectors \mathbf{a} associated with $\underline{\mathbf{R}}$ have the form $\mathbf{a} = \mathbf{t}_n + \mathbf{f}$ where \mathbf{t}_n is a translation defined by $\mathbf{t}_n = n_1\mathbf{b}_1 + n_2\mathbf{b}_2 + n_3\mathbf{b}_3$ with a collection of three integers and the three basic lattice vectors \mathbf{b}_1 , \mathbf{b}_2 and \mathbf{b}_3 . The vector \mathbf{f} is a fractional translation required for some rotations. The set of operations $\{\underline{\mathbf{R}}|\mathbf{0}\}$, where $\underline{\mathbf{R}}$ ranges over the different rotational parts of the space group elements, constitute a group which is called the *point group* of the lattice. Only 32 point groups are possible because of the limitations imposed by translational symmetry [87].

As a first example of an object with a distinct point group, we consider a square consisting of two different types of atoms as depicted in Figure 4.1(a). The two different types of atoms are indicated by white and black circles, respectively. The symmetries of such a system will play an important role for the discussion of the electronic states of QDs with a zinc blende structure. As one can infer from Figure 4.1(a), the following symmetry elements are present:

1. The *identity* element E : the symmetry operation E requires no action to the square, so that it may seem too trivial to be of importance. However, as noted above it is a crucial element for any group.
2. A *two-fold axis of symmetry* C_{2z} : rotation of the square by $2\pi/n$, with $n = 2$, around the z -axis produces a configuration which is indistinguishable from the initial one.

C_{2v}	E	C_{2z}	$\sigma_v(AC)$	$\sigma_v(DB)$
E	E	C_{2z}	$\sigma_v(AC)$	$\sigma_v(DB)$
C_{2z}	C_{2z}	E	$\sigma_v(DB)$	$\sigma_v(AC)$
$\sigma_v(AC)$	$\sigma_v(AC)$	$\sigma_v(DB)$	E	C_{2z}
$\sigma_v(DB)$	$\sigma_v(DB)$	$\sigma_v(AC)$	C_{2z}	E

Table 4.1: Multiplication table for the C_{2v} group.

3. A *symmetry plane* $\sigma_v(AC)$ perpendicular to the plane of the square: Reflection on this plane produces a configuration indistinguishable from the initial one. The subscript “ v ” stands for vertical and implies that the plane contains the highest-fold symmetry axis, which is C_{2z} in this case. Planes that are perpendicular to the highest-fold symmetry axis are called horizontal, or σ_h , planes.
4. A second symmetry plane: $\sigma_v(DB)$.

A system with these four particular symmetry elements is called to have C_{2v} symmetry. A useful device for thinking about groups is what is called the multiplication or *group table*. This is a table, where the symmetry operations displayed horizontally and vertically are combined and their product reported in the corresponding table entry. For instance, the result $\sigma_v(DB)$ of the operation $C_{2z}\sigma_v(AC)$ is placed in the row of C_{2z} and the column of $\sigma_v(AC)$. The order in which the symmetry operations are applied is important since the law of combination is not necessarily commutative. We will note symbolically the product of two operations g and h , gh . In this convention, the operation h is carried out first and g second. According to the axiom A1, the elements of the multiplication table must also be elements in the group. For the C_{2v} group, the multiplication table is given in Table 4.1. Following the discussion above, another feature which can be deduced from the group table, is whether the group is *abelian* (commutative) or *non-abelian*. Since the group table of the C_{2v} is symmetric with respect to its main diagonal, every element commutes with the others. Therefore, the group C_{2v} is abelian.

Before going further, one needs to explain the important concept of *classes* and for that, to define the term *similarity transformation*. If Q and X are elements of a group, then the element P such that $P = X^{-1}QX$ is known as the similarity transform of Q by X . One also says that Q and P are *conjugate*. Each set of mutually conjugate elements is called a *class*. By using the multiplication table, one obtains that for the C_{2v} group each element is conjugate only to itself, so it founds its own class. This is typical for abelian groups where $P = X^{-1}QX = QX^{-1}X = Q$.

At this point we introduce another group which will be of major importance for the discussion of nitride QDs, the C_{3v} group. This group turns out to be a *non-abelian* group. For the C_{3v} group, appropriate for systems with a wurtzite structure, the number of symmetry elements is six (the identity E , C_{3z} , C_{3z}^2 , and three σ_v elements). An

C_{3v}	E	C_{3z}	C_{3z}^2	$\sigma_v(A)$	$\sigma_v(B)$	$\sigma_v(C)$
E	E	C_{3z}	C_{3z}^2	$\sigma_v(A)$	$\sigma_v(B)$	$\sigma_v(C)$
C_{3z}	C_{3z}	C_{3z}^2	E	$\sigma_v(C)$	$\sigma_v(A)$	$\sigma_v(B)$
C_{3z}^2	C_{3z}^2	E	C_{3z}	$\sigma_v(B)$	$\sigma_v(C)$	$\sigma_v(A)$
$\sigma_v(A)$	$\sigma_v(A)$	$\sigma_v(B)$	$\sigma_v(C)$	E	C_{3z}	C_{3z}^2
$\sigma_v(B)$	$\sigma_v(B)$	$\sigma_v(C)$	$\sigma_v(A)$	C_{3z}^2	E	C_{3z}^2
$\sigma_v(C)$	$\sigma_v(C)$	$\sigma_v(A)$	$\sigma_v(B)$	C_{3z}	C_{3z}^2	E

Table 4.2: Multiplication table for the C_{3v} group.

illustrative example for an object with C_{3v} symmetry is an equilateral triangle, shown in Figure 4.1(b). The dashed lines denote the three mirror planes σ_v . The corresponding group table is given in Table 4.2. Since the multiplication table is not symmetric, one can conclude that the group C_{3v} is non-abelian. For example, the elements of the rotation C_{3z} and C_{3z}^2 do not commute with mirroring σ_v . For the C_{3v} group the elements C_{3z} and C_{3z}^2 form a class, as do the three vertical reflection planes σ_v .

From the multiplication table of a group \mathcal{G} with the symmetry elements $\{R_1, R_2, \dots, R_n\}$ it is possible to find a variety of matrices $\{\underline{\underline{D}}(R) \forall R \in \mathcal{G}\}$ that multiply in the same way as the abstract symmetry elements do:

$$R_1 R_2 = R_3 \rightarrow \underline{\underline{D}}(R_1) \underline{\underline{D}}(R_2) = \underline{\underline{D}}(R_3)$$

Any set of non-zero square matrices that multiply in the same way as the elements of a group is said to form a *representation* of that group. Given a representation D of a group \mathcal{G} , and a set of associated matrices $\{\underline{\underline{D}}(R) \forall R \in \mathcal{G}\}$ the representation is said to be *reducible* if one can find a similarity transformation, that reduces all the matrices $\underline{\underline{D}}(R)$ to block-diagonal form. Otherwise the representation is called to be *irreducible*. As an illustrative example let us discuss the point group C_{3v} . We choose rectangular coordinates x, y, z with z along the symmetry axis C_3 and x along one of the symmetry planes σ_v , with y making a right-hand system. Then a point X is expressed as (x, y, z) . Any symmetry operation of the group C_{3v} will take these coordinates into (x', y', z') that are linear functions of the original coordinates. Explicitly, the transformations can be expressed by 3×3 matrices, acting on three-dimensional column vectors. Since the group contains six symmetry operations, there will be six matrices. The identity operator E corresponds to the identity matrix. The other five matrices are found from the formulas for rotation of coordinates [89]. As an example we choose the symmetry operation C_{3z} , which corresponds to a rotation around the z axis by an angle of $2\pi/3$:

$$\underline{\underline{D}}(C_{3z})\mathbf{r} = \begin{pmatrix} -\frac{1}{2} & -\frac{1}{2}\sqrt{3} & 0 \\ \frac{1}{2}\sqrt{3} & -\frac{1}{2} & 0 \\ 0 & 0 & 1 \end{pmatrix} \begin{pmatrix} x \\ y \\ z \end{pmatrix} = \begin{pmatrix} -\frac{1}{2}x - (\frac{1}{2}\sqrt{3})y \\ (\frac{1}{2}\sqrt{3})x - \frac{1}{2}y \\ z \end{pmatrix} = \begin{pmatrix} x' \\ y' \\ z' \end{pmatrix} = \mathbf{r}' .$$

	$\{E\}$	$\{C_{2z}\}$	$\{\sigma_v(AC)\}$	$\{\sigma_v(DB)\}$
A_1	1	1	1	1
A_2	1	1	-1	-1
B_1	1	-1	1	-1
B_2	1	-1	-1	1

(a)

	$\{E\}$	$\{2C_{3z}\}$	$\{3\sigma_v\}$
A_1	1	1	1
A_2	1	1	-1
E	2	-1	0

(b)

Table 4.3: Character table of the group (a) C_{2v} and (b) C_{3v}

It turns out, that z is not affected under the action of any of the symmetry operations. It is multiplied by one in each transformation and the values x and y are never mixed in. Therefore z is a basis of a representation all by itself, the unit representation where each member corresponds to one. The values of x and y do get mixed under the symmetry operations of group C_{3v} , and no choice of coordinates could change this. They form a basis of a two dimensional matrix representation. The representation in terms of (x, y, z) is said to be reducible to the two smaller representations and each of these is irreducible to smaller representations. In physical applications it is the irreducible representation that gives the essential information. In this case, it was easy to find the reducibility of the representations because we chose the coordinates wisely. If we had taken the coordinate axes in some arbitrary position, we would have obtained six rather full matrices and reducibility would not be at all obvious.

In the following, we will explain that entire matrices are often not required. In many cases, the traces of matrices alone can provide sufficient information. For the construction of the irreducible representations, we refer to Ref. [88]. If, in a certain representation, the matrix $\underline{\mathbf{D}}(R)$ corresponds to the symmetry operation R , then the trace of $\underline{\mathbf{D}}(R)$ is called the *character* $\chi(R)$ of R for that representation. The trace is not changed by a similarity transformation and therefore conjugate elements have the same character. The character is thus the same for the whole class of elements. Tabulations of the characters of the various representations for a group are called, *character tables*. The character tables for the groups C_{2v} and C_{3v} are given in Table 4.3(a) and Tab. 4.3(b), respectively. By construction, the classes are listed on the horizontal header of the table, while the irreducible representations are listed on the vertical header to the left. The classes are denoted by an identifying operation symbol preceded by the number of operations in the class. Assume that a group has N elements and these elements are divided into i classes. The number of elements in each class will be denoted by N_1, \dots, N_i . The identity operator E forms a class with only one element. For example, the group C_{3v} has six symmetry elements: The identity E , C_{3z} , C_{3z}^2 , and three vertical reflection planes σ_v . Since the elements C_{3z} and C_{3z}^2 form a class, as do the three reflection planes σ_v , the three classes including the identity operation E are denoted by $\{E\}$, $\{2C_{3z}\}$ and $\{3\sigma_v\}$. For the group C_{2v} , each element is its own class. In the

case of C_{2v} , the different irreducible representations are denoted by A_1 , A_2 , B_1 , and B_2 . Representations which are symmetric with respect to the principal rotation axis C_n are always denoted with the letter A , whereas those that are antisymmetric with respect to C_n are denoted with the letter B . The subscripts 1 or 2 then follow from the behavior under action of the other elements σ_v . The representation A_1 is called the *totally symmetric* representation, and must always be present, and is always listed first in character tables. For groups, such as C_{3v} , with irreducible representations that are degenerate, the letter E refers to those that are two dimensional, while three, four, and five dimensional irreducible representations are labeled by T , G , H . By convention, the identity operator E is always listed first in the header row of the character table. Since the identity operation leaves any basis function invariant, the character $\chi_i(E)$ within the first column of the character table itself provides the dimensionality of the irreducible representation.

Three important theorems are very useful for constructing the character table of a group

- T1** The number of irreducible representations of a group is equal to the number of classes in that group.
- T2** The sum of the squares of the dimensions d_i of all the irreducible representations of a group is equal to the order, denoted by $|G|$ of the group \mathcal{G} :

$$\sum_i d_i^2 = |G| \quad (4.1)$$

The order of the group $|G|$ is by definition the number of elements in the group.

- T3** The characters of two irreducible representations i and j satisfy

$$\sum_R \chi_i^*(R)\chi_j(R) = |G|\delta_{ij} \quad (4.2)$$

where $\chi_i(R)$ and $\chi_j(R)$ are the characters of the symmetry operation R in the representations i and j , respectively, and the sum runs over all symmetry operations of the group. From this we conclude that the sum of the squares of the absolute values of the characters in any irreducible representation is equal to the order of the group. This results in the so-called *Great Orthogonality Theorem*, which is extremely helpful for the reduction of reducible representations into irreducible ones and for the construction of character tables. Equation (4.2) implies that two irreducible representations cannot have the same set of characters.

Since the group C_{2v} contains four symmetry elements, the order $|G|$ of the group is four. According to theorems T1 and T2, each of the four irreducible representations must be one-dimensional. For the C_{3v} group, as already discussed, the number of symmetry elements is six. Hence, the order $|G|$ of this group is six. Furthermore, one has three

different classes $\{E\}$, $\{2C_3\}$ and $\{3\sigma_v\}$. Therefore we are left with three irreducible representations, and according to Eq. (4.1), the following relation must be fulfilled:

$$d_1^2 + d_2^2 + d_3^2 \stackrel{!}{=} |G| = 6 \quad (4.3)$$

The only set of three integers which satisfies Eq. (4.3) is 1, 1, 2, and so the C_{3v} group must have two one-dimensional and one two-dimensional irreducible representations.

So far we have considered the mathematical treatment of the representations of a group. In the following, we will make the connection between the representation theory and an eigenvalue problem. Consider, for a moment, the electronic wave functions of an atom or a QD. We know that they must satisfy the Schrödinger equation:

$$H|\psi_{j,v}\rangle = E_v|\psi_{j,v}\rangle, \quad (4.4)$$

where H , $|\psi_{j,v}\rangle$, and E_v are the electronic Hamiltonian, wave functions, and energies, respectively. The subscript v labels the energy levels and j distinguishes the different wave functions belonging to each level E_v . Furthermore, let \mathcal{G} denote the symmetry group of the operator H . An operation of symmetry in respect of an operator $H(\mathbf{r})$ is defined as linear transformation of coordinates $\mathbf{r}' = \underline{\mathbf{R}}\mathbf{r}$ that does not change the form of the operator, i.e. $H(\mathbf{r}') = H(\mathbf{r})$.¹ We suppose that the Hamiltonian is defined with respect to a set of Cartesian axes. In general this operator is a function of the derivatives with respect to the coordinates x , y and z as well as of the coordinates themselves, so that writing the Hamiltonian as $H(\mathbf{r})$ merely expresses the dependence on the coordinate system, and does not imply that $H(\mathbf{r})$ is only function of coordinates. The ensemble of operations associated with every element R of the group \mathcal{G} is given by O_R . If O_R is an operator corresponding to one of the symmetry operations in the group \mathcal{G} of the system, it can be shown that

$$[O_R, H] = 0. \quad (4.5)$$

This means that $|\psi_{j,v}\rangle$ and $O_R|\psi_{j,v}\rangle$ are both eigenfunctions belonging to the same eigenvalue. If the v^{th} level is n -fold degenerate, the index j ranges from 1 to n . In other words, a set of linearly independent eigenfunctions ($|\psi_{1,v}\rangle, |\psi_{2,v}\rangle, \dots, |\psi_{n,v}\rangle$) is associated with an eigenvalue E_v of degeneracy n . The functions $O_R|\psi_{j,v}\rangle$ are also eigenfunctions belonging to the eigenvalue E_v and can thus be expressed as linear combinations of ($|\psi_{1,v}\rangle, |\psi_{2,v}\rangle, \dots, |\psi_{n,v}\rangle$):

$$O_R|\psi_{j,v}\rangle = \sum_i \mathbf{D}_{ij}(R)|\psi_{j,v}\rangle \quad \text{with } (i, j = 1, 2, \dots, n) \quad (4.6)$$

The matrices $\underline{\mathbf{D}}(R)$ exhibit the multiplication rules of the group, and thus constitute the matrices for a representation D of the symmetry group. The representation D so

¹ The more general case of linear transformations of the type $\mathbf{r}' = \underline{\mathbf{R}}\mathbf{r} + \mathbf{a}$, which appear in crystals and the case in which spin-coordinates are included, are discussed for example in Ref. [87], though the general concepts of this section apply to those cases also.

obtained is said to have the $(|\psi_{1,v}\rangle, |\psi_{2,v}\rangle, \dots, |\psi_{n,v}\rangle)$ as basis functions. Instead of using such basis functions, one can consider a new set $(|\psi'_{1,v}\rangle, |\psi'_{2,v}\rangle, \dots, |\psi'_{n,v}\rangle)$ made up of n independent linear combinations of $(|\psi_{1,v}\rangle, |\psi_{2,v}\rangle, \dots, |\psi_{n,v}\rangle)$. It can be proved [88] that the representation D' of basis functions $(|\psi'_{1,v}\rangle, |\psi'_{2,v}\rangle, \dots, |\psi'_{n,v}\rangle)$ is related to the representation D of basis functions by a similarity transformation $\underline{D}'(R) = \underline{M}^{-1}\underline{D}(R)\underline{M}$, where \underline{M} is the matrix that transforms the set $|\psi_{j,v}\rangle$ into $|\psi'_{j,v}\rangle$. Two representations which are related to one another by a similarity transformation are called *equivalent*. These equivalent representations differ only in the choice of basis functions used to express them explicitly, otherwise they are essentially the same. Therefore we treat them as not distinct. Thus, the representation D is equivalent to D' , i.e., only one distinct representation of the symmetry group \mathcal{G} is associated with a given eigenstate. The space of the functions $(|\psi_{1,v}\rangle, |\psi_{2,v}\rangle, \dots, |\psi_{n,v}\rangle)$ is therefore said to be irreducible (reducible) if the representation is irreducible (reducible). In other words, if the D is irreducible and has the dimension n it is impossible to choose a number $< n$ of functions, that transform only among themselves under the operations of the group. The results so far obtained provide a classification of the eigenvalues of an operator. In conclusion we deduced two critical implications:

1. The wave functions of each electronic level of, for example, a QD transform according to an irreducible representation of the QD point group.
2. The degree of degeneracy of an energy level, barring “accidental degeneracies”, is equal to the dimension of the irreducible representation to which its wave function belongs. Therefore the irreducible representations determine *essential degeneracies* of the eigenvalues.

Thus, even without solving the Schrödinger equation, we know the possible degeneracies from the very beginning! Since the group C_{2v} contains only one-dimensional representations, every electronic level of a QD with C_{2v} symmetry must be non-degenerate. In systems with C_{3v} symmetry, one could also obtain double degenerate levels, since this group contains a two-dimensional representation.

So far we have discussed only point group symmetry operations, such as rotation and mirroring. For the investigation of bulk band structures space groups have to be introduced, which are formed by the combination of the elements of the point group with translations. In the next section symmetry properties of the electronic energy bands will be studied by means of group theory.

4.2 Symmetry Properties of Energy Bands

To find an appropriate TB model for the description of the bulk band structure, it is essential to know the symmetry properties of the different bands at high-symmetry points in the first Brillouin zone. Considerable information for a qualitative understanding of

the energy bands maxima and minima can be deduced by means of a combination of symmetry arguments, perturbation theory, and experimental information [90]. Here, we determine important properties of the energy bands from symmetry arguments alone. In order to illustrate this procedure we focus the discussion on the group-theoretic character tables associated with the zinc blende structure. Of course, a similar analysis can be carried out for other crystal structures.

As we have already seen in the previous section, character tables are the basic quantities from which many symmetry properties can be deduced. In addition to crystallographic symmetries, the so-called *time reversal symmetry*, which will be discussed in Section 4.3, is present. Since time reversal symmetry is distinct from the symmetries related to the space group, it will be necessary to include the influence of the effects of the former after having constructed the character tables for a given space group. First, we consider the symmetry problem without spin. Since the spin-orbit coupling is included in our TB model for systems having zinc blende structure, the spin is introduced in the discussion in a second step.

The elements of a space group $\mathcal{G}_{\text{space}}$ are combinations of the translational symmetry of an unit cell and an element of a point group. Every element of the latter is either a rotation or the product of a rotation and an inversion. For example, the zinc blende structure has the space group T_d^2 associated with the fcc translation group and the tetrahedral point group T_d [87].

As a consequence of the translation symmetry of the lattice, every energy eigenfunction can be written in form of a Bloch function $\psi_{\mathbf{k}}(\mathbf{r}) = \exp(i\mathbf{k}\mathbf{r})u_{\mathbf{k}}(\mathbf{r})$, where \mathbf{k} is the wave vector in the Brillouin zone and $u_{\mathbf{k}}(\mathbf{r})$ is a function that has the periodicity of the lattice. For a given wave vector \mathbf{k} associated with some symmetry point in reciprocal space, one finds those operations of the point group associated with the space group which transforms \mathbf{k} into itself plus a reciprocal-lattice vector [87]. Such a set of symmetry operations forms a group called the group of the wave vector \mathbf{k} . There is a distinct wave vector group for each type of symmetry line and point in the Brillouin zone [87]. All the wave vector groups are subgroups of the point group connected with the space group.

As an illustrative example we will now discuss the character table of a zinc blende crystal with $\mathbf{k} = \mathbf{0}$. The tetrahedral point group T_d consists of 24 symmetry elements which can be divided into five classes:

- $\{E\}$: Identity
- $\{8C_3\}$: Eight clockwise and counterclockwise rotations by $2\pi/3$ around the $[111], [\bar{1}\bar{1}\bar{1}], [1\bar{1}\bar{1}], [11\bar{1}]$ axes, respectively.
- $\{3C_2\}$: Three rotations by π around the $[100]$, $[010]$ and $[001]$ axes, respectively.
- $\{6IC_4\}$: Six clockwise and counterclockwise improper rotations by $\pi/2$ around $[100]$, $[010]$ and $[001]$ axes, respectively.
- $\{6\sigma\}$: Six reflections at the (110) , $(1\bar{1}0)$, (101) , $(10\bar{1})$, (011) , and $(01\bar{1})$ planes, respectively.

Notations			Classes				
Koster	BSW	Molecular	$\{E\}$	$\{3C_2\}$	$\{8C_3\}$	$\{6IC_4\}$	$\{6\sigma\}$
Γ_1	Γ_1	A_1	1	1	1	1	1
Γ_2	Γ_2	A_2	1	1	1	-1	-1
Γ_3	Γ_{12}	E	2	2	-1	0	0
Γ_4	Γ_{15}	T_2	3	-1	0	-1	1
Γ_5	Γ_{25}	T_1	3	-1	0	1	-1

Table 4.4: Character table and commonly used notations for the irreducible representations of the T_d point group.

Here, I is the inversion element and rotations followed by inversions are referred to as improper rotations. Since the number of irreducible representations is equal to the number of classes, the point group T_d has five irreducible representations. Note again, that the character of the class containing the identity operation $\{E\}$ is equal to the dimension of the representation. Since the order of the group T_d is $|G| = 24$, we obtain from Eq. (4.1):

$$\sum_i d_i^2 = |G| = 24 \quad (4.7)$$

The only possible combination of five squares which add to 24 is: $1^2 + 1^2 + 2^2 + 3^2 + 3^2$. This means, the point group T_d consists of two irreducible representations of the dimension one, one irreducible representation of dimension two, and two irreducible representations of dimension three. According to the discussion above, these representations are usually denoted by A_1 , A_2 , E , T_1 and T_2 . The character table of the T_d group is given in Table 4.4. Similar considerations can also be made for other symmetry points or lines of the first Brillouin zone [87].

The notation A_1 , A_2 , E etc. we introduced here so far, is more commonly found in the literature on molecular physics. In articles on semiconductor physics, different notations are frequently used. It can be shown [50, 87], that the wave functions of a crystal with the wave vector \mathbf{k} transform at the Γ point always like the irreducible representations of the point group of the crystal, and therefore the Bloch functions at $\mathbf{k} = \mathbf{0}$ can be classified according to the irreducible representations. Hence in semiconductor physics one uses, Γ plus a subscript i to denote the irreducible representations. There are two different conventions in the literature to choose the subscript i : One introduced by Koster while the other was proposed by Bouckaert, Smoluchowski and Wigner (BSW). The correspondence between the different notations for the T_d point group is also given in Table 4.4.

So far we have neglected the spin in our discussion. Without taking into account the spin, an electronic wave function is a scalar function of position \mathbf{r} . Therefore, the wave function always transforms into itself under a rotation by 2π . However, with spin

	$\{E\}$	$\{\bar{E}\}$	$\{3C_2/3\bar{E}C_2\}$	$\{8C_3\}$	$\{6IC_4\}$	$\{6\sigma/6\bar{E}\sigma\}$	$\{6\bar{E}(IC_4)\}$	$\{8\bar{E}C_3\}$
Γ_1	1	1	1	1	1	1	1	1
Γ_2	1	1	1	1	-1	-1	-1	1
Γ_3	2	2	2	-1	0	0	0	-1
Γ_4	3	3	-1	0	-1	1	-1	0
Γ_5	3	3	-1	0	1	-1	1	0
Γ_6	2	-2	0	1	$\sqrt{2}$	0	$-\sqrt{2}$	-1
Γ_7	2	-2	0	1	$-\sqrt{2}$	0	$\sqrt{2}$	-1
Γ_8	4	-4	0	-1	0	0	0	1

Table 4.5: Character table of the double group \bar{T}_d [48].

included, the wave function is a spinor and transforms into the negative of itself under any 2π rotation [49]. Without the spin, the point group contains n elements C_i . If one takes the spin into account, the point group will contain $2n$ elements, namely n elements C_i and n elements \bar{C}_i , where \bar{C}_i is defined by

$$\bar{C}_i = \bar{E}C_i, \quad (4.8)$$

and \bar{E} is a rotation by 2π . The operations C_i and \bar{C}_i are of course identical in their action on a point in space. Groups containing symmetry operations of spin wave functions are known as *double groups*. It is beyond the scope of this thesis to treat double groups in detail. The reader is referred to Refs. [50,87]. For our purposes, it is already sufficient to know the irreducible representation at $\mathbf{k} = \mathbf{0}$. Again, we focus the following discussion on a system with zinc blende structure. Since the single group T_d contains 24 elements, the double group \bar{T}_d contains 48 elements. However, the number of classes in the double group is not necessarily twice that of the corresponding single group. The reason is, that a class C in the single group may or may not belong to the same class with $\bar{E}C$. For example, at Γ in a zinc blende crystal, the elements in $\{3C_2\}$ and $\{3\bar{E}C_2\}$ belong to the same class in the double group. Therefore, the 48 elements in the double group of Γ in zinc blende crystals are divided into eight classes. In the character table 4.5 of the double group of Γ the eight classes and the eight irreducible representations are listed. In this case, the double group has two irreducible representations of the dimension one, three of the dimension two, two of the dimension three and one irreducible representation of the dimension four. From these considerations one can deduce properties of the valence band structure as well as for the conduction band minimum at $\mathbf{k} = \mathbf{0}$. Similar considerations can also be made for crystals with a wurtzite structure. These discussions will be extended in Part II for systems with a zinc blende structure, and in Part III for the wurtzite crystal structure.

In conclusion, this section was dedicated to introduce the terminology and notations of group theory, but no effort was made to prove the statements and theorems mentioned.

For a rigorous treatment the reader is referred to books on group theory. Note, that so far extra degeneracies due to the time reversal symmetry are not considered. These can be found, for example, by the techniques of Herring [91] and Elliott [92]. This will be subject of the following section.

4.3 Time Reversal Symmetry

So far we have mainly investigated geometrical symmetries of a system. In addition there are also non-geometrical symmetries like rotations in spin-space treated in the previous section and the time reversal invariance. This section is dedicated to the problem of additional degeneracies, which arise from the so-called *time reversal symmetry*. In a first step, we will introduce some properties of the time-reversal operator that will lead to the famous Kramers theorem. In a second step we will turn our attention to the extra degeneracies.

In quantum mechanics the state of a system is specified by a wave function ψ , and the evolution of a particle is governed by time dependent Schrödinger equation with a specific Hamiltonian H . To start with, let us suppose $|\psi(t)\rangle$ is a solution of the Schrödinger equation

$$H|\psi(t)\rangle = i\hbar\frac{\partial}{\partial t}|\psi(t)\rangle, \quad (4.9)$$

with a time-independent Hamiltonian H . Time reversal invariance is symmetry under the simple transformation $T : t \rightarrow -t$ alone. If we replace t by $-t$ this equation becomes:

$$H|\psi(-t)\rangle = -i\hbar\frac{\partial}{\partial t}|\psi(-t)\rangle,$$

showing that the Schrödinger equation is not invariant under the transformation $t \rightarrow -t$. However, for spinless particles and with real potentials (no magnetic field), the presence of i in Eq. (4.9), enables the original form to be restored by taking its complex conjugate:

$$H|\psi(-t)\rangle^* = i\hbar\frac{\partial}{\partial t}|\psi(-t)\rangle^*,$$

and $|\psi(-t)\rangle^*$ satisfies the same Schrödinger equation as $|\psi(t)\rangle$. In other words, defining K as the complex conjugation $K\psi(\mathbf{r}) = \psi^*(\mathbf{r})$ one sees that $K|\psi(t)\rangle$ is the solution of the original Eq. (4.9) but evolving backwards in time. This is why, for spinless particles K is the *time reversal operator* T . Note that it has the properties $K^2 = 1$ ($K^{-1} = K$) and $KH(\mathbf{r}, \mathbf{p})K = H(\mathbf{r}, -\mathbf{p}) = H(\mathbf{r}, \mathbf{p})$. The last equality holds because, in the absence of a magnetic field, H is quadratic in \mathbf{p} and therefore H commutes with T . Note also that the angular momentum $\mathbf{L} = \mathbf{r} \times \mathbf{p}$ changes sign under the time reversal.

The time reversal problem is more complicated in the presence of spin. To be more specific, in the following we consider half-spin particles. In this case, one has to deal

with the Pauli equation [50]

$$H(\mathbf{r}, \mathbf{p}, \boldsymbol{\sigma}) \begin{pmatrix} \psi_1(\mathbf{r}, t) \\ \psi_2(\mathbf{r}, t) \end{pmatrix} = i\hbar \frac{\partial}{\partial t} \begin{pmatrix} \psi_1(\mathbf{r}, t) \\ \psi_2(\mathbf{r}, t) \end{pmatrix}, \quad (4.10)$$

where $\boldsymbol{\sigma} = (\underline{\underline{\sigma}}_x, \underline{\underline{\sigma}}_y, \underline{\underline{\sigma}}_z)$ are the Pauli matrices

$$\underline{\underline{\sigma}}_x = \begin{pmatrix} 0 & 1 \\ 1 & 0 \end{pmatrix}, \quad \underline{\underline{\sigma}}_y = \begin{pmatrix} 0 & -i \\ i & 0 \end{pmatrix}, \quad \underline{\underline{\sigma}}_z = \begin{pmatrix} 1 & 0 \\ 0 & -1 \end{pmatrix}. \quad (4.11)$$

The dependence of the Hamiltonian H on the spin operators $\underline{\underline{\sigma}}_x, \underline{\underline{\sigma}}_y, \underline{\underline{\sigma}}_z$ is a way to write a system of two differential equations corresponding to the two spin components in compact form.

It can be shown that for half-spin particles the *time reversal operator* T is defined by [88]:

$$T = UK = (i\sigma_y)K. \quad (4.12)$$

The reason for this choice is that now the spin angular momentum $\mathbf{s} = \frac{\hbar}{2}\boldsymbol{\sigma}$, should change sign under time reversal, like the orbital angular momentum \mathbf{L} . Indeed with Eq. (4.12) one has [50]

$$T\mathbf{r}T^{-1} = \mathbf{r}, \quad T\mathbf{p}T^{-1} = -\mathbf{p}, \quad T\boldsymbol{\sigma}T^{-1} = -\boldsymbol{\sigma}, \quad (4.13)$$

and therefore, again in the absence of a magnetic field:

$$TH(\mathbf{r}, -\mathbf{p}, -\boldsymbol{\sigma})T^{-1} = H(\mathbf{r}, -\mathbf{p}, -\boldsymbol{\sigma}) = H(\mathbf{r}, \mathbf{p}, \boldsymbol{\sigma}). \quad (4.14)$$

The last equality holds again because H is quadratic in $(\mathbf{p}, \boldsymbol{\sigma})$.

From Eq. (4.13) we obtain that the expectation values of the coordinates in a state $|\psi\rangle$ and its time reversed conjugate $|T\psi\rangle$ are equal, while the expectation values of momenta and spin for state $|\psi\rangle$ and $|T\psi\rangle$ are opposite. According to the discussion above, we

conclude that, if $\psi = \begin{pmatrix} \psi_1(\mathbf{r}, t) \\ \psi_2(\mathbf{r}, t) \end{pmatrix}$ represents a succession of states, the succession of

states $\Psi = (i\sigma_y) \begin{pmatrix} \psi_1^*(\mathbf{r}, -t) \\ \psi_2^*(\mathbf{r}, -t) \end{pmatrix}$ in reversed chronological order constitutes a possible

succession of states. Therefore, one calls Ψ the *time reversed conjugate* of ψ .

From its definition, Eq. (4.12), the operator T is antilinear, i.e.,

$$T(a|\psi_1\rangle + b|\psi_2\rangle) = a^*T|\psi_1\rangle + b^*T|\psi_2\rangle$$

and anti-unitary, i.e.,

$$\langle\psi|\phi\rangle = \langle T\phi|T\psi\rangle. \quad (4.15)$$

Also:

$$T^2\Psi = (i\sigma_y K)(i\sigma_y K) \begin{pmatrix} \psi_1 \\ \psi_2 \end{pmatrix} = (i\sigma_y K) \begin{pmatrix} \psi_2^* \\ -\psi_1^* \end{pmatrix} = i^2 \begin{pmatrix} \psi_2 \\ \psi_1 \end{pmatrix} = -\Psi . \quad (4.16)$$

Let us now establish for which systems the time reversal operator T commutes with the Hamiltonian H , so that Eq. (4.14) is satisfied. Because of Eq. (4.13), the time reversal operator commutes with the potential energy terms and the kinetic energy term, which is quadratic in \mathbf{p} . It also commutes with terms which contain spin-orbit and spin-spin interactions. However, the operator T does not commute with the Hamiltonian of a charged particle in an external magnetic field because in such a case the Hamiltonian is linear in the operators \mathbf{p} and $\boldsymbol{\sigma}$ [49].

From the above considerations one can deduce the famous *Kramers theorem* [93]. For this, we consider a solution of the eigenvalue problem

$$H|\psi\rangle = E|\psi\rangle .$$

If the Hamiltonian H is invariant under time reversal symmetry, one obtains from the state $|\phi\rangle = T|\psi\rangle$

$$H|\phi\rangle = H(T|\psi\rangle) = TH|\psi\rangle = TE|\psi\rangle = ET|\psi\rangle = E|\phi\rangle , \quad (4.17)$$

which shows that $|\phi\rangle = T|\psi\rangle$ is also an eigenfunction of H with the same eigenvalue as $|\psi\rangle$. If the functions $|\phi\rangle$ and $|\psi\rangle$ are linearly independent, there will be a degeneracy due to the time reversal symmetry. Therefore, in a quantum mechanical system with time reversal symmetry, additional systematic degeneracies may be expected.

As an example of a systematic degeneracy introduced by the time reversal operator, we consider the case of half-spin particles and note that the spinor eigenfunctions $|\psi\rangle$ and $|\phi\rangle = T|\psi\rangle$ cannot be linearly dependent. This can be seen from the following simple example

$$\langle\psi|\phi\rangle \stackrel{\text{Eq. (4.15)}}{=} \langle T\phi|T\psi\rangle = \langle TT\psi|T\psi\rangle \stackrel{\text{Eq. (4.16)}}{=} -\langle\psi|T\psi\rangle = -\langle\psi|\phi\rangle$$

Thus $|\phi\rangle = T|\psi\rangle$ and $|\psi\rangle$ are orthogonal, and therefore there exists at least a double degeneracy for half-spin particles if the Hamiltonian is invariant under time reversal symmetry. This *essential* degeneracy is the so-called *Kramers degeneracy* of quantum mechanics. The Kramers degeneracy does of course not apply to quantum systems for which the time reversal operator is not a symmetry operator. For instance, an atomic state with total angular momentum \mathbf{J} is split by an external magnetic field into $2j + 1$ non-degenerate levels.

From these considerations, we can also conclude, that in the absence of an external magnetic field, all single-particle energy levels are at least twofold degenerate due to the time reversal symmetry.

Case	Relation between D and D^*	Frobenius-Schur test	Spinless particle	Half-spin particle
A	$D \sim D^* \sim D_r$	$\sum_a \chi(a^2) = G $	No extra degeneracy	Degeneracy doubled
B	$D \not\sim D^*$	$\sum_a \chi(a^2) = 0$	Degeneracy doubled	Degeneracy doubled
C	$D \sim D^* \not\sim D_r$	$\sum_a \chi(a^2) = - G $	Degeneracy doubled	No extra degeneracy

Table 4.6: Influence of time reversal symmetry. The representations of a group are denoted by D . A real representation is labeled by D_r .

4.3.1 Degeneracies due to Time Reversal Symmetry

In Section 4.1 we have mainly investigated spatial symmetries of a Hamiltonian H . This means that H belongs to a certain symmetry (double) group \mathcal{G} . If we suppose that the Hamiltonian H is invariant under time reversal symmetry one has also to add the time reversal operator T to the group \mathcal{G} . But here arises the basic difficulty that space symmetry operators are linear operators, whereas the operator T is antilinear. Therefore one has to generalize the results of the usual group theory to deal with a group which contains unitary as well as anti-unitary operations [91, 92].

Suppose that a set of eigenfunctions $S_1 = (\phi_1, \dots, \phi_n)$ belonging to the eigenvalue E are degenerate and form a basis for the irreducible representation of the symmetry group \mathcal{G} . Then the set of functions $S_2 = (T\phi_1, \dots, T\phi_n)$ also belongs to the eigenvalue E and one must be able to decide whether or not the new set is linearly dependent on $S_1 = (\phi_1, \dots, \phi_n)$. This can be decided by the method of Wigner [94]. It can be proved, that if a set of functions belongs to the irreducible representation D of the Hamiltonian's symmetry group \mathcal{G} , the set of time reversal conjugate functions belongs to the complex conjugate representation [87]. For the relationship between an irreducible representation and its complex conjugate three different cases may occur:

- Case A: D and D^* are equivalent to the same representation D_r by real matrices.
- Case B: D and D^* are inequivalent
- Case C: D and D^* are equivalent but not to a representation D_r by real matrices.

It is clear that in case B, an additional degeneracy is introduced by the time reversal symmetry for spinless and half-spin particles, since the set of functions $S_2 = (T\phi_1, \dots, T\phi_n)$ obtained by time reversal symmetry are linearly independent from S_1 . It turns out, that for irreducible representations which belong to case A, an extra degeneracy is only obtained for half spin-particles. For those belonging to case C, an

\bar{C}_{2v}	E	\bar{E}	C_{2z}, \bar{C}_{2z}	$\sigma_v(AC), \bar{\sigma}_v(AC)$	$\sigma_v(DB), \bar{\sigma}_v(DB)$
Γ_1	1	1	1	1	1
Γ_2	1	1	-1	1	-1
Γ_3	1	1	1	-1	-1
Γ_4	1	1	-1	-1	1
Γ_5	2	-2	0	0	0

Table 4.7: Character table for the double group \bar{C}_{2v} [95].

additional degeneracy is introduced only for spinless particles. The discussed effects of time-reversal symmetry in introducing extra degeneracies are summarized in Table 4.6 and are known as Wigner's rules. A proof of the conclusion drawn above can be found, for example, in Ref. [50].

For a finite group, one can apply the so-called *Frobenius-Schur test*, to distinguish between the cases A, B, and C by inspecting the characters of irreducible representations [50]. In this criterion, one considers the sum of the characters of the squares of the elements in this group. It can be proved that this sum takes the values $|G|$, 0, and $-|G|$, where $|G|$ is the order of the group, when the irreducible representation belongs to case A, B, or C, respectively:

$$\sum_{a \in \mathcal{G}} \chi(a^2) = \begin{cases} |G| & \text{case A} \\ 0 & \text{case B} \\ -|G| & \text{case C} \end{cases} \quad (4.18)$$

To make use of this criterion, one has to calculate the characters of the squares of the elements in this group. But for this we have to keep in mind that we are dealing with double groups. To this end one has to consider that an electron is described by a wave functions depending on both space and spin-coordinates. Therefore we have to extend ordinary group theoretical techniques. To be able to evaluate Eq. (4.18), one has to consider the transformation properties of the spin functions under the symmetry operations. In a first step, we will investigate the effect of a proper rotation R on the spin state $u = (u_+, u_-) = u_+(1, 0) + u_-(0, 1)$. The state $u' = Ru$ obtained by applying a rotation R on u can be expressed as:

$$u'_+ = (Ru)_+ = au_+ + cu_- , \quad u'_- = (Ru)_- = bu_+ + du_- .$$

The functions $(1, 0)$ and $(0, 1)$ constitutes a basis for a representation of the rotation group, in which a rotation R is represented by the matrix $\underline{\underline{\mathbf{R}}}$:

$$\underline{\underline{\mathbf{R}}} = \begin{pmatrix} a & b \\ c & d \end{pmatrix} . \quad (4.19)$$

a	E	\bar{E}	C_{2z}, \bar{C}_{2z}	$\sigma_v(AC), \bar{\sigma}_v(AC)$	$\sigma_v(DB), \bar{\sigma}_v(DB)$		
a^2	E	E	\bar{E}, \bar{E}	\bar{E}, \bar{E}	\bar{E}, \bar{E}	Σ	Case
Γ_1	1	1	1	1	1	8	A
Γ_2	1	1	1	1	1	8	A
Γ_3	1	1	1	1	1	8	A
Γ_4	1	1	1	1	1	8	A
Γ_5	2	2	-2	-2	-2	-8	C

Table 4.8: Application of the Frobenius-Schur criterion to the double group \bar{C}_{2v} .

It is known that this transformation matrix is given by [88]

$$\underline{\mathbf{R}}(\alpha, \mathbf{e}) = \begin{pmatrix} \cos(\frac{\alpha}{2}) + in \sin(\frac{\alpha}{2}) & (il + m) \sin(\frac{\alpha}{2}) \\ (il - m) \sin(\frac{\alpha}{2}) & \cos(\frac{\alpha}{2}) - in \sin(\frac{\alpha}{2}) \end{pmatrix}. \quad (4.20)$$

Equation (4.20) reveals the transformation properties of the spin functions under any proper rotation. Note in particular that any rotation of angle $\alpha = 2\pi$ changes the sign of the spin functions, as already discussed in Section 4.2. Therefore in spin space, a rotation by 2π is not equivalent to the identity operation. Only rotations by 4π or a integer multiple of 4π coincide with the identity. Consequently, as already described in Section 4.2, if one treats an eigenvalue problem with explicit inclusion of spin, one must enlarge the symmetry group \mathcal{G} by adding the symmetry element \bar{E} , corresponding to a rotation by 2π and the product of \bar{E} with all other symmetry elements of \mathcal{G} .

So far our investigations have been limited to proper rotations. To extend the theory to improper rotations, one must also consider the effect of inversion on the spin functions. It turns out that this operation results in multiplying any possible spin function by a phase factor $c = 1$ [88]. Therefore, the inversion does not change the spin states.

Illustrative Example: \bar{C}_{2v}

As an illustrative example we choose here the double group \bar{C}_{2v} . This group will be of major importance for the discussion of electronic states in QDs with a zinc blende structure.

From the character table, given in Table 4.7, we conclude that the group contains four one-dimensional irreducible representations and one two-dimensional representation. In principle it is possible, that in systems with \bar{C}_{2v} symmetry fourfold degenerate states occur due to time reversal symmetry, if the two dimensional representation Γ_5 would belong to case A or C discussed above. Thus, we have to decide, which case of Table 4.6 applies to the different representations. Since the representations $\Gamma_1, \Gamma_2, \Gamma_3$, and Γ_4 are one-dimensional and the characters are real, these representations belong to case A. Therefore double degeneracy occurs. More difficult is Γ_5 , since this representation is two dimensional. In general, a representation is of type B if and only if its character

is not real. Since the characters are real, the representation belong either to case A (double degeneracy) or to case C (no extra degeneracy). The distinction between these two alternatives can be established by the Frobenius-Schur test. The proper rotation C_{2z} is a rotation around the z axis by an angle of π . Therefore, one has to calculate $(\mathbf{R}(\alpha = \pi, \mathbf{e} = \mathbf{e}_z))^2$ from Eq. (4.20). This yields \bar{E} . Similarly, we obtain for the improper rotations $\sigma_v(AC) = IC_{2DB}$ and $\sigma_v(DB) = IC_{2AC}$, that $(\mathbf{R}(\sigma_v))^2 = \bar{E}$. Furthermore, for E and \bar{E} we deduce $E^2 = \bar{E}^2 = E$. From the characters $\chi(a^2)$ we can perform the summation required by the Frobenius-Schur test in Eq. (4.18), and we end up with Table 4.8. Therefore, the representation Γ_5 belongs to case C and no additional degeneracy occurs.

Finally, we conclude that in a system with C_{2v} symmetry, and taking the spin into account, every state should be double degenerate and no higher degeneracy should occur.

Electronic Properties of CdSe
Nanostructures with Zinc Blende
Structure

5 Introduction to Part II

Semiconductor quantum dots (QDs), epitaxially grown or chemically synthesized, are of great interest due to the possibility to study basic quantum phenomena and their potential for novel device applications. Most of the investigations of QDs involve III-V systems, such as InGaAs/GaAs and InP/GaP, which are suited for near-infrared range applications [96]. By far less work has been devoted to II-VI systems, such as CdSe/ZnSe, which are attractive for optoelectronic applications in the blue-green spectral regions [96]. For example, laser diodes with epitaxially grown CdSe QDs stacks exhibit an improved temperature stability compared to conventional laser diodes based on quantum wells [97]. Therefore these QD structures can be a real alternative to other semiconductor materials for the green spectral region. Furthermore, chemically synthesized CdSe nanocrystals also attracted great attention due to their high quantum yield and high photostability at room temperature [98]. Because of the confinement of the carriers in those systems, the emission wavelength depends strongly on the size and shape of the structure, which is defined during the synthesis. These features make them promising emitters not only for quantum information [98,99] but also for biological detection and imaging [100,101].

For a controlled use of semiconductor QDs one needs a better understanding of their electronic structure, which is rather sensitive to the actual geometrical and compositional parameters. In calculating the electronic states, one encounters the following difficulty: These systems are much larger than molecules and the most fundamental symmetry of solid state physics, namely translational invariance, is not fulfilled. Therefore, neither the standard methods of theoretical chemistry, nor those of solid state theory can immediately be applied to these systems. For example *ab initio* methods based on density functional theory (DFT) and local density approximation (LDA) would require large supercell calculations with the size of the supercell being much larger than the embedded QD or nanocrystal. However, to date such supercells are well beyond the possibility of present day computational equipment, which allows only systems with up to a few hundred atoms to be investigated in the framework of standard *ab initio* DFT methods [26–28]. Simpler models, based on a effective-mass approximation [20,102] or a multi-band $\mathbf{k} \cdot \mathbf{p}$ model [29,72,103], describe the QD by a confinement potential caused by the band offsets. Such approaches give insight into the formation of bound hole and electron states, but they are only applicable if the atomistic details of the underlying crystal structure is negligible. More suitable for a microscopic description are empirical pseudopotential methods [8,31,104,105] and empirical tight-binding (TB) models [9,32,66,106–114]. The empirical pseudopotential methods allow for a detailed variation of the wave functions on the atomic scale. This is probably the most accurate

description from a microscopic viewpoint, but it requires a large set of basis states and is therefore computationally extremely demanding and time consuming. Within a TB model, some kind of coarse graining is made and one studies spatial variations only on inter-atomic length scales. The huge advantage is that usually a small basis set is sufficient. This allows for the possibility to study larger systems. Furthermore the TB model provides a simple physical picture in terms of the atomic orbitals and on-site and inter-site hopping matrix elements between these orbitals.

Semi-empirical TB models have been used previously to describe “nearly” spherical InAs and CdSe nanocrystals, for which the dangling bonds at the surfaces are saturated by hydrogen [106–109] or organic ligands [111–113]. Also uncapped [115] and capped [9] pyramidal InAs QDs were investigated within an empirical TB framework. To model these QDs an sp^3s^* basis was used. This resulted in a $10N \times 10N$ Hamilton matrix, where N is the number of atoms, with 33 independent parameters. In this thesis we apply a similar TB model to II-VI nanostructures, namely, CdSe QDs embedded inside a ZnSe matrix, and spherical CdSe nanocrystals. We show that a smaller $s_c p_a^3$ TB basis is sufficient for a proper description of the electronic structure of these systems. This approach requires only eight independent parameters and allows for the investigation of larger nanostructures than those accessible by an sp^3s^* TB model. This advantage relies on the fact that the $s_c p_a^3$ basis set leads per se to a smaller matrix dimension and that additionally a smaller percentage of nonzero matrix elements arise. Therefore the $s_c p_a^3$ TB model is less demanding regarding both memory requirements and computational time. We find that within this approach the valence p bands for the bulk system are extremely well reproduced everywhere and the conduction s band is accurate near to the Γ point. From this we expect that also for QDs the hole states and the electron states energetically close to the gap are well reproduced. To study this accuracy of our model in more detail, we compare the results to other microscopic and macroscopic models presented in the literature. Furthermore, TB results obtained for CdSe-nanocrystals were compared to experimental results, and very good agreement is found. This demonstrates that our TB model is reliable for the reproduction of the essential electronic properties of these low dimensional nanostructures.

This part is organized as follows: Since CdSe and ZnSe crystalize in the zinc blende structure, we start with a short discussion of this crystal structure in Section 6.1. Then Section 6.2 is dedicated to the analysis of the bulk band structure of zinc blende semiconductor materials by means of group theory. The attention is mainly focused on the band structure in the vicinity of the Γ point, since the TB parameters are fitted to the characteristic features in this region. In Section 6.3 the TB model with an $s_c p_a^3$ basis is introduced. Also, the formalism used to obtain the TB parameters is described. Results for self-assembled pyramidal CdSe QDs are presented in Section 7.1. For spherical CdSe nanocrystals the results and the comparison with experimental data are given in Section 7.2.

6 Crystals with a Zinc Blende Structure

The underlying crystal structure of the system under consideration is of major importance for the calculation of the electronic structure. Therefore we will briefly introduce the zinc blende crystal structure in Section 6.1. Furthermore, to set up an appropriate tight-binding (TB) model, one has to consider special points of the bulk energy bands. Hence, Section 6.2 is dedicated to a general discussion of the band structure of zinc blende materials. Finally, the TB approach, which is used to calculate the electronic properties of zinc blende CdSe nanostructures, is addressed in Section 6.3.

6.1 Crystal Structure

By far the most common crystal structure in semiconductors is the zinc blende structure, sometimes known as sphalerite. Many important III-V compound semiconductors, such as GaAs, InAs, InP and their alloys, but also the II-VI compounds ZnS, ZnSe, CdSe and CdTe crystallize in the zinc blende structure. The corresponding conventional unit cell is depicted in Figure 6.1(a). The zinc blende structure has a face-centered cubic (fcc) lattice with a diatomic basis. In a fcc structure, one lattice point is located in the center of each of the six faces of the usual cubic unit cell. The vectors spanning the primitive unit cell are

$$\mathbf{a}_1 = \frac{a}{2}(1, 1, 0) \quad , \quad \mathbf{a}_2 = \frac{a}{2}(1, 0, 1) \quad , \quad \mathbf{a}_3 = \frac{a}{2}(0, 1, 1) \quad ,$$

where a is the lattice constant.

In the diatomic basis, the anion A is at $(0, 0, 0)$ and the cation C is at $(1, 1, 1)a/4$ relative to the lattice point. The position \mathbf{r} of the atom α can also be written in terms of the lattice vector \mathbf{R} :

$$\mathbf{r}(\mathbf{R}, \alpha) = \mathbf{R} + \alpha\boldsymbol{\tau}$$

with $\boldsymbol{\tau} = \frac{a}{4}(1, 1, 1)$ and $\mathbf{R} = n_1\mathbf{a}_1 + n_2\mathbf{a}_2 + n_3\mathbf{a}_3$ $n_1, n_2, n_3 \in \mathbb{N}$.

In this notation one has $\alpha = 0$ for the anion, and $\alpha = 1$ for the cation. Thus the cation and the anion sublattices are shifted with respect to each other by a quarter of the body diagonal of the fcc lattice. The atoms are tetrahedrally arranged, that is, each anion is bonded to four cations and vice versa. This is illustrated in Figure 6.1(b).

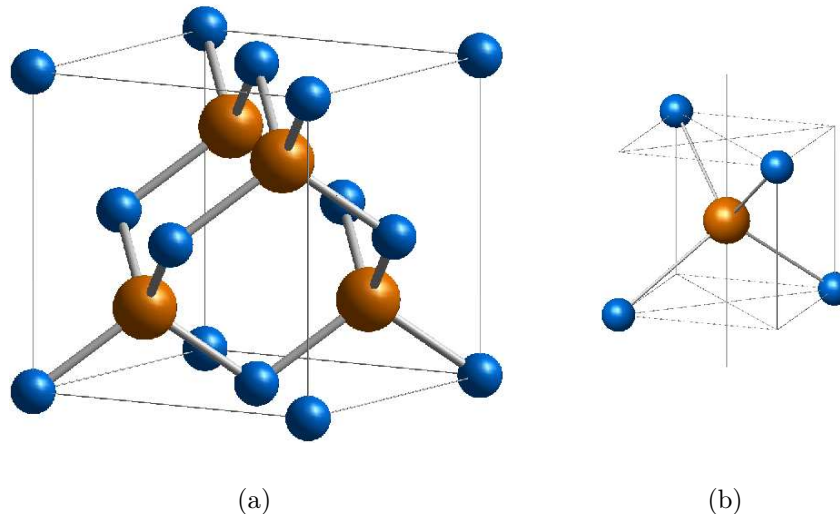


Figure 6.1: (a) Conventional unit cell of a zinc blende structure. (b) Tetrahedral bonding (sp^3 -bonding). Small spheres indicate the anions, large spheres the cations. (Figures adopted from Ref. [116]).

6.2 Symmetry Considerations and Bulk Band Structure for Zinc Blende Semiconductors

As already discussed in Chapter 3, in an empirical TB model the TB parameters are determined such that the characteristic properties of the bulk band structure are reproduced. In the following we are interested in the electronic properties of zinc blende semiconductor materials with a direct band gap. The region which is of major importance for the optical properties of these systems is the vicinity of the Γ point. Therefore, we will focus our attention on the band structure in this region. We will also introduce some group theoretical aspects in our discussion, to classify the different states. In semiconductor materials containing heavier atoms, such as CdSe and ZnSe, the spin-orbit coupling can play an important role. This is due to the fact that the magnitude of the spin-orbit splitting Δ_{so} in a semiconductor is comparable to the spin-orbit splitting of its constituent atoms, which increases with increasing atomic number [88]. Therefore, we will also discuss the influence of the spin-orbit coupling on the band structure in detail.

In a system with cubic symmetry the conduction band at the center of the Brillouin zone exhibits an s -like character [42]. The valence band states at $\mathbf{k} = 0$ consist of three p -states. For a further discussion of the bulk band structure in the vicinity of the Γ point, one can approximate the cubic symmetry in this region by a spherical one [42]. Without spin-orbit coupling, we choose the eigenfunctions of the angular momentum operator \mathbf{L} as basis states. Thus, the orbital electronic wave functions are classified according to the orbital angular momentum L as s , p , d etc. The s -like state

Γ_i	Γ_1	Γ_2	Γ_3	Γ_4	Γ_5
$\Gamma_i \times D_{1/2}$	Γ_6	Γ_7	Γ_8	$\Gamma_7 + \Gamma_8$	$\Gamma_6 + \Gamma_8$

Table 6.1: Direct products of the single group representations Γ_i with $D_{1/2}$ for the group of $\mathbf{k} = 0$ [92].

is therefore characterized by $|L = 0, m_L = 0\rangle$, where m_L is the eigenvalue of the z -component of the angular momentum operator \mathbf{L} . According to the character table of the single group of Γ given on page 38 in zinc blende type semiconductors, this state transforms like Γ_1 , since the s -state is fully symmetric. To symmetrize the p -like ($L = 1$) valence band wave functions, we make use of their similarity to the atomic p wave functions. In the absence of the spin-orbit coupling these states are three-fold degenerate. These three states can be chosen to be eigenstates of L_z , the z component of \mathbf{L} . For the p -states the eigenvalues m_L of L_z are $m_L = 1, 0, -1$. According to the group table of the single group Γ , the three-fold degenerate states $L = 1$ must belong either to the Γ_4 or Γ_5 representations. One can distinguish between the representations Γ_4 and Γ_5 by calculating the character of the representing matrix generated by $L = 1$. Because the p -states transform like x , y and z , respectively, they are changing sign under the action of the improper rotations IC_4 . Therefore, one can deduce from the character table that the $L = 1$ states belong to the Γ_4 representation.

Taking into account the spin-orbit interaction one has to consider the total angular momentum $\mathbf{J} = \mathbf{L} + \mathbf{s}$, where \mathbf{s} denotes the spin. The eigenstates of \mathbf{J} can be classified according to J and m_J , $|J, m_J\rangle$, with m_J taking $2J + 1$ values. The spin function transforms as the irreducible representation $D_{1/2}$ [50]. For $\mathbf{k} = 0$ the representation is given by $D_{1/2} = \Gamma_6$. Therefore, the *total* wave function transforms like the direct product of the single group representation with $D_{1/2}$ [88]. This direct product can be expressed in terms of the double group representations. If more than one of the double group representations appears in this decomposition, a spin-orbit splitting of the level occurs. The table of the direct products of the single group representations Γ_i with $D_{1/2}$ for the group of Γ ($\mathbf{k} = 0$) is given in Table 6.1.

The s -like conduction band is characterized by $J = 1/2$ and $m_J = \pm 1/2$. Therefore, the conduction band at the Γ point is twofold degenerate. According to Table 6.1, one obtains that the state with $J = 1/2$ belongs to the Γ_6 representation.

For the valence band states, J can take two possible values $J = 3/2$ and $J = 1/2$. Therefore the eigenstates can be classified according to J and m_J :

$$|J, m_J\rangle = \begin{cases} \left| \frac{3}{2}, \pm \frac{3}{2} \right\rangle \\ \left| \frac{3}{2}, \pm \frac{1}{2} \right\rangle \\ \left| \frac{1}{2}, \pm \frac{1}{2} \right\rangle \end{cases} \quad (6.1)$$

Since there is no six-dimensional representation in the double group of the point Γ in zinc

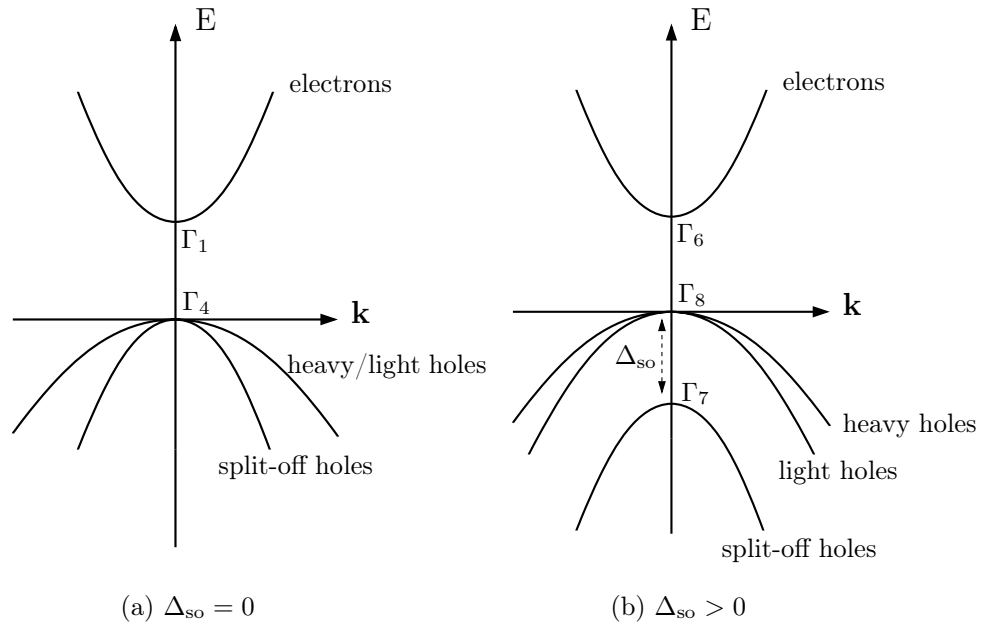


Figure 6.2: Schematic band structure of zinc blende semiconductors with conduction band and three valence bands. Without (a) and with (b) spin-orbit coupling. The spin-orbit splitting is denoted by Δ_{so} . Additionally the symmetries of the irreducible representations (Γ_i) are given.

blende type semiconductors, the spin-orbit interaction splits the states $J = 3/2$ from the states $J = 1/2$. The lifting of the degeneracy can also be confirmed by the results of Table 6.1, where the direct product $\Gamma_4 \times D_{1/2}$ is a decomposition of the representations Γ_7 and Γ_8 . The splitting between the states Γ_7 and Γ_8 is the spin-orbit splitting Δ_{so} of the valence bands at the Γ point. Furthermore one can deduce from the character table, that the four-fold degenerate $J = 3/2$ states must belong to the representation Γ_8 , because this is the only four dimensional representation. Due to the decomposition mentioned above the state $J = 1/2$ belongs to the Γ_7 representation. Finally, the Γ_8 and Γ_7 states are split by the spin-orbit component of the bulk Hamiltonian H^{bulk} . The schematic illustration of the band edges with and without spin-orbit coupling, for semiconductor materials grown in a zinc blende structure is given in Figure 6.2. Due to their different dispersions the states with $|J = 3/2, m_J \pm 3/2\rangle$ are called *heavy* holes and the states with $|J = 3/2, m_J \pm 1/2\rangle$ *light* holes. The two states ($m_J = \pm 1/2$) with $J = 1/2$, which are shifted to lower energies by the spin-orbit interaction, are called *split-off* holes.

6.3 Tight-binding Model with $s_c p_a^3$ Basis

As already discussed, the TB approach is especially useful for the description of the complicated valence band structure, since it includes the coupling between the different

bands. From the perspective of atomic orbitals and near the Γ point, the valence bands originate from the valence p orbitals while the conduction band arises from the s orbitals [117]. In polar semiconductors such as CdS, ZnSe and CdSe, the valence bands originates primarily from the anion, and the conduction band from the cation [117]. However, in non-polar semiconductors such as CdTe and GaAs, considerable mixing of the cation and anion orbitals will take place. Since we are interested in the electronic properties of CdSe/ZnSe nanostructures, we use a $s_c p_a^3$ TB model with eight basis states per elementary unit cell. This means that the set of basis states $|\nu, \alpha, \sigma, \mathbf{R}\rangle$ is given by four orbitals $\alpha = s, p_x, p_y, p_z$ with spin $\sigma = \pm\frac{1}{2}$. One s -orbital at the cation ($\nu = C$) and three p -orbitals at the anion ($\nu = A$) site in each unit cell \mathbf{R} are chosen. Such an approach has been successfully used for the investigation of optical properties in ZnSe quantum wells [118]. Furthermore, this model offers a more sophisticated description of the microscopic structure of semiconductors compared with common $\mathbf{k} \cdot \mathbf{p}$ models.

As discussed above, we choose an $s_c p_a^3$ basis set to describe the bulk semiconductor compounds CdSe and ZnSe. The TB matrix elements are given by

$$E_{\alpha, \alpha'}(\mathbf{R}' - \mathbf{R})_{\nu, \nu'} = \langle \nu', \alpha', \sigma', \mathbf{R}' | H^{\text{bulk}} | \nu, \alpha, \sigma, \mathbf{R} \rangle. \quad (6.2)$$

As the overlap of the wave functions at different sites decay rapidly it is sufficient to limit the coupling of the basis orbitals to nearest and next nearest neighbors. The spin-orbit interaction of the bulk Hamiltonian H^{bulk} is included according to the discussion given in Section 3.1.1. With the two center approximation of Slater and Koster [47] we are left with only eight independent matrix elements $E_{\alpha, \alpha'}(\mathbf{R}' - \mathbf{R})_{\nu, \nu'}$. The following abbreviations are used for the matrix elements between different orbitals:

$$\left. \begin{aligned} E_a &:= E_{xx}(000)_{AA} \\ E_c &:= E_{ss}(000)_{CC} \end{aligned} \right\} \text{orbital energies} \quad (6.3)$$

$$V := E_{sx} \left(\begin{array}{ccc} 1 & 1 & 1 \\ 2 & 2 & 2 \end{array} \right)_{CA} \quad \text{nearest neighbor hopping} \quad (6.4)$$

$$\left. \begin{aligned} t_1 &:= E_{xx}(110)_{AA} \\ t_2 &:= E_{xx}(011)_{AA} \\ t_3 &:= E_{xy}(110)_{AA} \\ U &:= E_{ss}(110)_{CC} \end{aligned} \right\} \text{second nearest neighbor hopping} \quad (6.5)$$

Here, A and C denote anions and cations, respectively. The eighth matrix element is the spin-orbit coupling parameter λ for the p orbitals at the anions. The nearest neighbor hopping is denoted by V . For the p orbitals at the anions, the overlap integrals for second nearest neighbors are given by t_1, t_2, t_3 . If one considers the cations, there is only one second nearest neighbor matrix element U . This is due to the two-center approximation discussed in Section 3.1 and the assumption of a single s orbital at the cation sites.

In \mathbf{k} space, with the basis states $|\mathbf{k}\rangle$ given in Section 3.1, the electronic properties of the pure bulk material are modeled by an 8×8 matrix $\underline{\underline{\mathbf{H}}}^{\text{bulk}}(\mathbf{k})$ for each \mathbf{k} from the first Brillouin zone. This matrix depends on the different parameters $E_{\alpha,\alpha'}(\mathbf{R}' - \mathbf{R})_{\nu,\nu'}$ and the spin-orbit parameter λ . It is explicitly given by:

$$\underline{\underline{\mathbf{H}}}^{\text{bulk}}(\mathbf{k}) = \begin{pmatrix} & |a, x, \uparrow\rangle & |a, x, \downarrow\rangle & |a, y, \uparrow\rangle & |a, y, \downarrow\rangle & |a, z, \uparrow\rangle & |a, z, \downarrow\rangle & |c, s, \uparrow\rangle & |c, s, \downarrow\rangle \\ \begin{matrix} |a, x, \uparrow\rangle \\ |a, x, \downarrow\rangle \\ |a, y, \uparrow\rangle \\ |a, y, \downarrow\rangle \\ |a, z, \uparrow\rangle \\ |a, z, \downarrow\rangle \\ |c, s, \uparrow\rangle \\ |c, s, \downarrow\rangle \end{matrix} & \begin{matrix} E_x & 0 & d_{xy} - i\lambda & 0 & d_{xz} & \lambda & d_{xs} & 0 \\ 0 & E_x & 0 & d_{xy} + i\lambda & -\lambda & d_{xz} & 0 & d_{xs} \\ d_{xy} + i\lambda & 0 & E_y & 0 & d_{yz} & -i\lambda & d_{ys} & 0 \\ 0 & d_{xy} - i\lambda & 0 & E_y & -i\lambda & d_{yz} & 0 & d_{ys} \\ d_{xz} & -\lambda & d_{yz} & i\lambda & E_z & 0 & d_{zs} & 0 \\ \lambda & d_{xz} & i\lambda & d_{yz} & 0 & E_z & 0 & d_{zs} \\ d_{xs}^* & 0 & d_{ys}^* & 0 & d_{zs}^* & 0 & E_s & 0 \\ 0 & d_{xs}^* & 0 & d_{ys}^* & 0 & d_{zs}^* & 0 & E_s \end{matrix} \end{pmatrix}$$

with the following abbreviations

$$\begin{aligned} E_\alpha &= E_A + 4t_1 \cos\left(\frac{k_\alpha a}{2}\right) \left[\cos\left(\frac{k_\gamma a}{2}\right) + \cos\left(\frac{k_\beta a}{2}\right) \right] + 4t_2 \cos\left(\frac{k_\beta a}{2}\right) \cos\left(\frac{k_\gamma a}{2}\right), \\ E_s &= E_C + 4U \left[\cos\left(\frac{k_x a}{2}\right) \cos\left(\frac{k_z a}{2}\right) + \cos\left(\frac{k_x a}{2}\right) \cos\left(\frac{k_y a}{2}\right) + \cos\left(\frac{k_y a}{2}\right) \cos\left(\frac{k_z a}{2}\right) \right], \\ d_{\alpha\beta} &= -4t_3 \sin\left(\frac{k_\alpha a}{2}\right) \sin\left(\frac{k_\beta a}{2}\right), \\ d_{\alpha s} &= 4V \left[\cos\left(\frac{k_\alpha a}{4}\right) \sin\left(\frac{k_\beta a}{4}\right) \sin\left(\frac{k_\gamma a}{4}\right) - i \sin\left(\frac{k_\alpha a}{4}\right) \cos\left(\frac{k_\beta a}{4}\right) \cos\left(\frac{k_\gamma a}{4}\right) \right], \end{aligned}$$

and the indices $\{\alpha, \beta, \gamma\} \in \{x, y, z\}$ that are pairwise unequal.

By analytical diagonalization for special \mathbf{k} directions, for example along the $\mathbf{k} = k(1, 0, 0)$ direction with $k \in [0, 2\pi/a]$, the electronic dispersion $E_n(\mathbf{k})$ is obtained as a function of the TB parameters. The index n denotes the different energy bands. Equations for the TB parameters $E_{\alpha,\alpha'}(\mathbf{R}' - \mathbf{R})_{\nu,\nu'}$ can now be deduced as a function of the Kohn-Luttinger-parameters $(\gamma_1, \gamma_2, \gamma_3)$, the energy gap E_g , the effective electron mass m_e and the spin-orbit-splitting Δ_{so} at the Γ point. The energy zero is fixed to the valence-band maximum. Doing so one obtains the following equations for the hopping matrix elements t_1, t_2, t_3 and U :

$$\begin{aligned} t_1 &= E_0 (\gamma_1 + 4\gamma_2) - \frac{V^2}{E_g}, \\ t_2 &= E_0 (\gamma_1 - 8\gamma_2) + \frac{V^2}{E_g}, \\ t_3 &= 6E_0\gamma_3 - \frac{V^2}{E_g}, \\ U &= -\frac{E_0}{m_e} + \left(\frac{E_g + \frac{2}{3}\Delta_{\text{so}}}{E_g + \Delta_{\text{so}}} \right) \frac{V^2}{E_g}. \end{aligned} \tag{6.6}$$

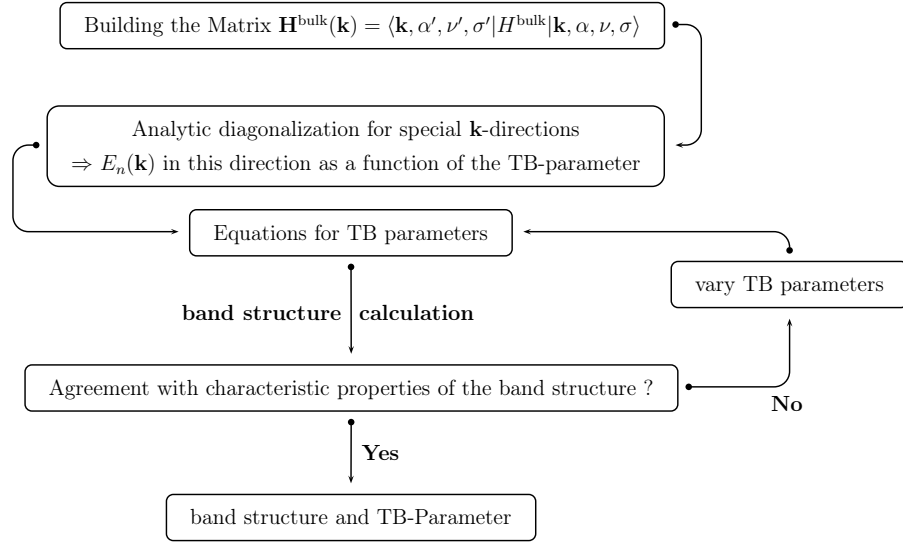


Figure 6.3: Schematic illustration for the determination of tight-binding (TB) parameters.

Here, m_e denotes the effective electron mass in units of the bare electron mass m_0 and the constant E_0 is defined by:

$$E_0 = \frac{\hbar^2}{2m_0 a^2} \approx 3.81 \text{ eV} (\text{\AA})^2 \frac{1}{a^2}.$$

The orbital energies E_C, E_A and the spin-orbit parameter λ can be deduced from the energies of the different energy bands for $\mathbf{k} = \mathbf{0}$. This yields:

$$\begin{aligned} \lambda &= \frac{\Delta_{\text{so}}}{3}, \\ E_C &= E_g + 12 \frac{E_0}{m_n} - \left(\frac{12E_g + 8\Delta_{\text{so}}}{E_g + \Delta_{\text{so}}} \right) \frac{V^2}{E_g}, \\ E_A &= -12E_0\gamma_1 + 4 \frac{V^2}{E_g} - \frac{\Delta_{\text{so}}}{3}. \end{aligned} \quad (6.7)$$

The material parameters for CdSe and ZnSe are given in Table A.1 of Appendix A. The parameter V does not affect the energy or effective masses in the vicinity of the Γ point. Therefore, this parameter can be used to reproduce the energy of the split-off band at the edge of the first Brillouin zone. This can be achieved by the following self-consistent cycle: One starts with $V = 0$ and calculates the different TB parameters according to the Eqs. (6.6) and (6.7). Then one compares the resulting energy at the L point with the corresponding value from the literature. If required the parameter V is readjusted, until convergence is reached. This self-consistent cycle is illustrated in Figure 6.3. The resulting numerical values for the different TB parameters are summarized in the Table A.2 of Appendix A.

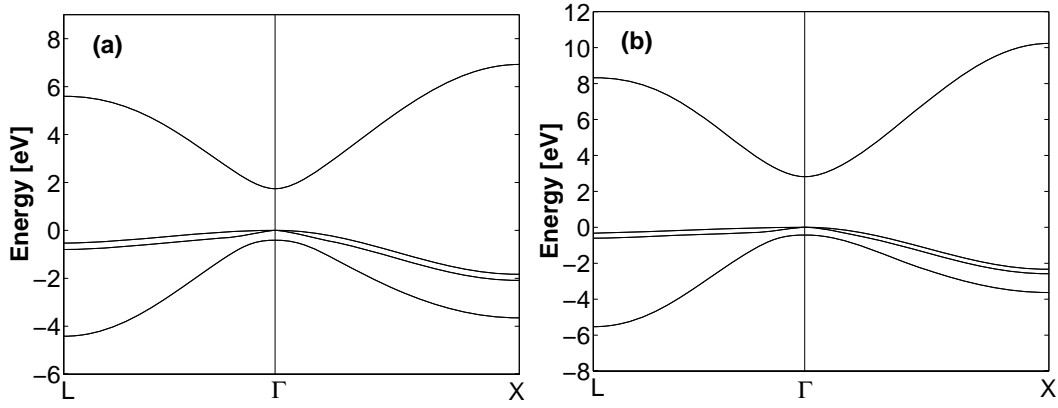


Figure 6.4: Tight-binding band structures for CdSe (a) and ZnSe (b)

The TB bands of bulk CdSe and ZnSe including spin-orbit coupling are depicted in Figure 6.4. Within our approach, the characteristic properties of the band structure in the region of the Γ point are well reproduced. Furthermore, when comparing with band structure results from the literature [119], one sees that the three valence (p -) bands are excellently reproduced everywhere. For the s -like conduction band deviations far away from the Γ -point occur. This is due to the fact that higher (unoccupied) conduction bands are neglected. The band structure can be improved by taking into account more basis states per unit cell [44, 120]. However, for a reproduction of the electronic properties in the region near the Γ -point, which is important for a proper description of the optical properties of the semiconductor materials with a direct band gap, the $s_c p_a^3$ TB model is certainly sufficient and satisfactory.

7 Results for CdSe Nanostructures

In the previous chapter, we have discussed general aspects of the sp_a^3 TB model that is used to calculate the electronic states and energies in zinc blende CdSe QDs. In this chapter, we present results for two different realizations of these nanostructures: In the following section, we will turn our attention to the self-assembled CdSe QDs, while Section 7.2 is dedicated to the chemically synthesized nanocrystals.

7.1 Results for a Pyramidal CdSe QDs Embedded in ZnSe

In this section we investigate the electronic properties of self-assembled CdSe QDs. As we have already discussed in Section 2.2, the conventional $\mathbf{k} \cdot \mathbf{p}$ approach cannot resolve atomistic details. This means that symmetry related physical effects, such as level anti-crossing, degeneracy removals and polarization anisotropy are ignored. All of these effects are naturally contained in an atomistic approach like the present TB formalism. Consequently, our microscopic TB model includes effects that can be obtained by conventional $\mathbf{k} \cdot \mathbf{p}$ or effective-mass approaches only by adding external parameters (geometry modifications, piezoelectric potentials, etc.).

7.1.1 Quantum Dot Geometry and strain

To model a self-assembled CdSe QD embedded in a ZnSe barrier material we choose a zinc blende lattice inside a box with fixed boundary conditions. In this box we consider a CdSe wetting layer (WL) of a thickness of one lattice constant a of the conventional unit cell, i.e. about two anion and two cation layers. On top of this WL resides a pyramidal QD with base length b and height $h = b/2$. The model geometry is schematically depicted in Fig 7.1. For the matrix elements corresponding to sites inside the WL or the QD we choose the TB parameters of CdSe, for all other sites those of ZnSe. We investigate embedded QDs with a base length b of $6a$, $8a$, and $10a$, where $a = 5.668 \text{ \AA}$ is the lattice constant of the bulk ZnSe material. Cells with dimensions of $18a \times 18a \times 15a$ (38 880 atoms), $20a \times 20a \times 16a$ (51 200 atoms), and $22a \times 22a \times 17a$ (65 824 atoms) are used for the calculations. We use a sufficiently large supercell, which is essential to avoid numerical artifacts for the localized QD states due to the fixed boundary conditions. To incorporate strain effects into our model the knowledge of the

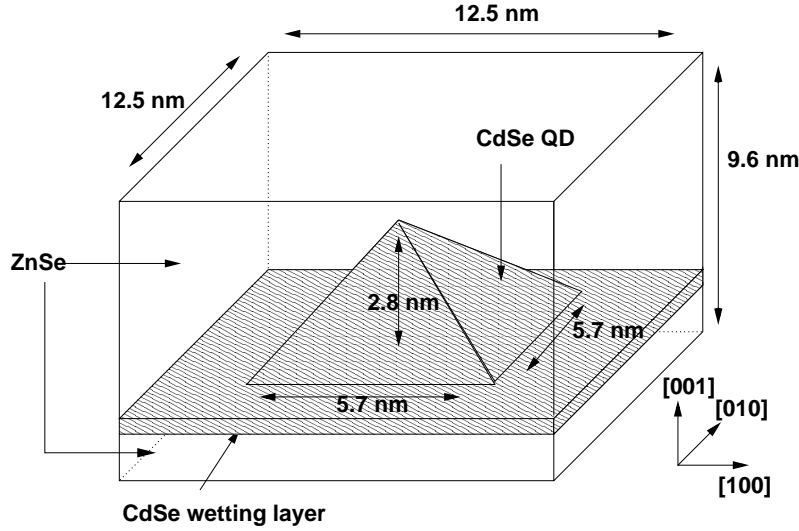


Figure 7.1: Schematic illustration of a pyramidal CdSe QD buried in a ZnSe matrix. The wetting layer has a thickness of one lattice constant ($1a$) of bulk ZnSe. The pyramidal QD has a base length b of $10a$.

strain tensor $\underline{\underline{\epsilon}}$ is necessary. The tensor $\underline{\underline{\epsilon}}$ is related to the strain dependent relative atom positions $\mathbf{d}_{\mathbf{R}'-\mathbf{R}}$ by [73]

$$\mathbf{d}_{\mathbf{R}'-\mathbf{R}} = (\underline{\underline{1}} + \underline{\underline{\epsilon}})\mathbf{d}_{\mathbf{R}'-\mathbf{R}}^0. \quad (7.1)$$

To determine the strain tensor far away from the embedded pyramid, the WL is treated as a quantum well. In the absence of a shear strain ($\epsilon_{i,j} \sim \delta_{i,j}$) for a coherently grown film, the strain components are given by [76]

$$\epsilon_{\parallel} = \epsilon_{xx} = \epsilon_{yy} = \frac{a_S - a_D}{a_D} \quad (7.2)$$

$$\epsilon_{\perp} = \epsilon_{zz} = -\frac{C_{12}}{C_{11}}\epsilon_{\parallel}. \quad (7.3)$$

Here a_D is the lattice constant of the unstrained film material and a_S denotes the parallel lattice constant of the substrate. The cubic elastic constants C_{ij} of the bulk materials are given in Table A.1 of Appendix A. Figure 7.2(a) displays a line scan of the resulting strain profile in the z -direction outside the dot. Stier *et al.* [29] obtained a similar strain profile for a pyramidal InAs/GaAs QD, because the InAs/GaAs system has the same crystal structure and approximately the same lattice mismatch as the CdSe/ZnSe system under consideration. The calculation of the strain field in the vicinity of the QD is by far more difficult. To obtain the strain profile in the region of the embedded QD we apply a model strain profile, which shows a behavior similar to the strain profile obtained by Stier *et al.* [29] for a line scan in the z direction through the tip of the pyramid. This model strain profile is displayed in Figure 7.2(b). The shear components, ϵ_{xy} , ϵ_{xz} , and ϵ_{yz} , can be neglected, at least away from the boundaries of the QD [102].

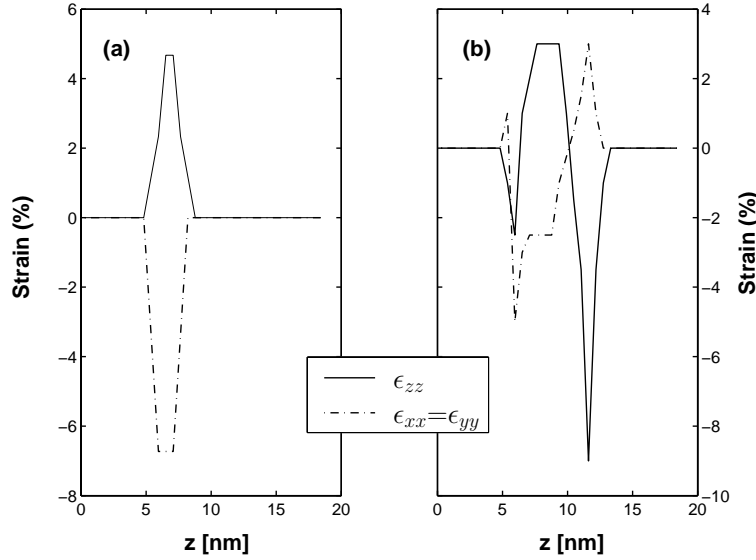


Figure 7.2: Strain distribution in and around the embedded pyramidal CdSe QD with a base length of $b = 10a$. The WL at the base of the QD is $1a$ thick. The whole structure is buried in a ZnSe matrix. Line scans along the $[001]$ direction through the WL outside the dot (a) and inside the dot through the tip of the pyramid (b) are displayed. The diagonal elements of the strain tensor $\underline{\underline{\epsilon}}$ are shown as solid (ϵ_{zz}) and dashed-dotted lines ($\epsilon_{xx} = \epsilon_{yy}$).

As discussed in Section 3.2, the strain effects are included in the TB model via the d^{-2} ansatz for the interatomic matrix elements $H_{l\mathbf{R}',m\mathbf{R}}$:

$$H_{l\mathbf{R}',m\mathbf{R}} = H_{l\mathbf{R}',m\mathbf{R}}^0 \left(\frac{d_{\mathbf{R}'-\mathbf{R}}^0}{d_{\mathbf{R}'-\mathbf{R}}} \right)^2. \quad (7.4)$$

The strained (distorted) lattice in the region of the QD may also lead to the appearance of piezoelectric potentials. These contributions are usually considered to be less important for the zinc blende structures realized in CdSe and ZnSe [72]. Furthermore, recent results of Bester *et al.* [78] indicate that the piezoelectric field in III-V semiconductors with a zinc blende structure, such as GaAs and InAs, has strong contributions from second-order effects. In particular the authors found that, for self-assembled zinc blende QDs first- and second-order terms nearly cancel each other. Consequently, the electrostatic built-in field can be neglected for the following analysis.

7.1.2 Single-Particle Properties

In this section the energy levels and wave functions of bound electron and hole states for three different QD sizes are calculated using the $s_c p_a^3$ TB model outlined and validated in the previous sections. To investigate the influence of the strain field, these calculations are done in the presence and in the absence of strain effects. For the evaluations

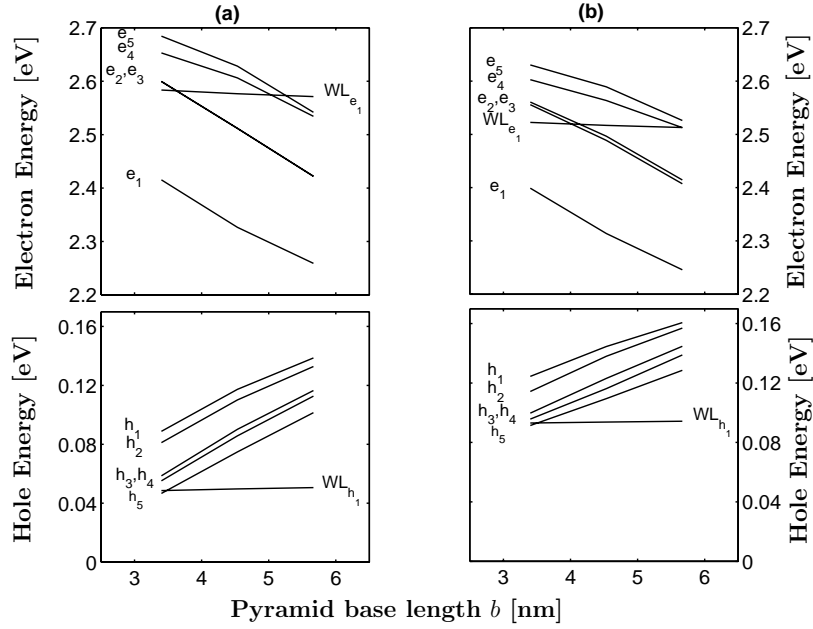


Figure 7.3: Electron and hole energies for embedded pyramidal CdSe/ZnSe QDs on a WL of thickness $1a$ (roughly 4 ML) for different base lengths of the unstrained QD (a) and with strain effects taken into account (b). For reference, the ground state energies of electrons (WL_{e_1}) and holes (WL_{h_1}) in a WL (of thickness $1a$) without a QD are also displayed.

without strain we have chosen the exponent in Eq. (7.4) to be zero. The resulting energy spectrum is shown in Figure 7.3(a). If strain is included one obtains the results depicted in Figure 7.3(b). e_1 and h_1 denote the electron and hole ground state, respectively. The first excited states are called e_2 and h_2 , and so on. All energies are measured relative to the valence-band maximum of ZnSe. Figure 7.3 also shows the size dependence of the electron and hole energy levels. The energies are compared with the ground state energies for electrons and holes in the $1a$ thick CdSe WL (WL_{e_1} and WL_{h_1} , respectively), which is calculated separately for an unstrained and a coherently strained quantum film (i.e., the WL without the QD), respectively. As expected from a naive particle-in-a-box picture, the binding of electrons and holes becomes stronger in the embedded QD when the dot size is increased. The quantum confinement causes the number of bound states to decrease when the dot size is reduced. For the embedded QDs with a base length $b = 8a$ ($b = 4.5$ nm) and $b = 10a$ ($b = 5.7$ nm) the calculated hole states are well above the WL energy (WL_{h_1}), which shows that these states are confined. This is valid both for the strain-unaffected and the strained embedded QD. For the system with $b = 6a$ ($b = 3.4$ nm) we obtain at least four bound hole states in both models. The energy splitting between the different states is slightly influenced by the strain. Furthermore we conclude from Figure 7.3 that the number of bound electron states is influenced by the strain. For the system with a base length of $b = 10a$ we obtain at least three bound-electron states when we take strain effects into account, see

Electron states for the $b = 10a$ base-length dot

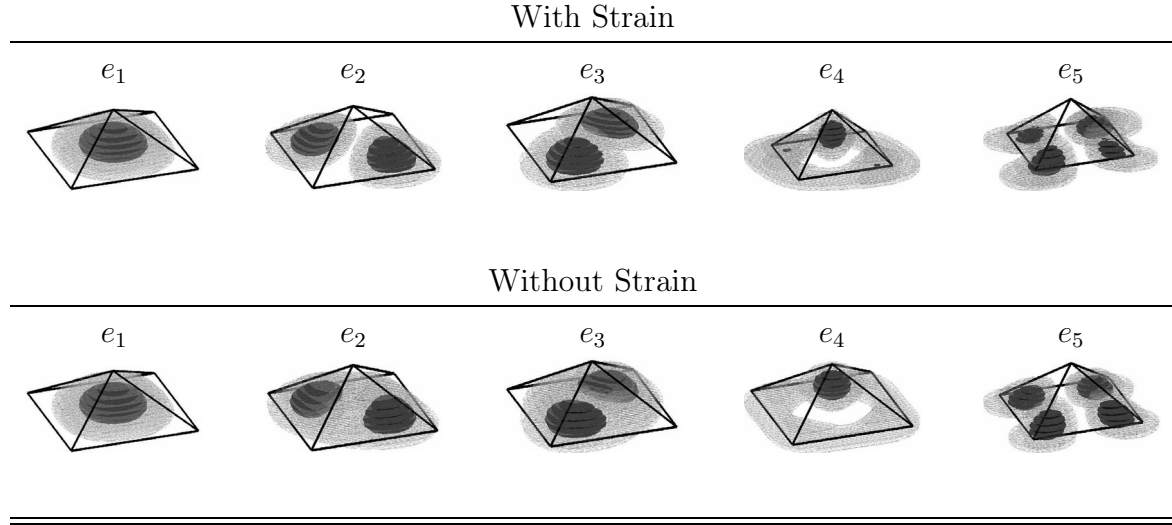


Figure 7.4: Isosurfaces of the modulus squared electron wave functions with and without strain for the embedded $b = 10a$ pyramidal QD. The light and dark surfaces correspond to 0.1 and 0.5 of the maximum probability density, respectively.

Figure 7.3 (b). Without strain effects at least five bound states are found. In conclusion, the confinement potential for the electrons is effectively reduced by the strain.

A close inspection of the two bound electron states e_2 and e_3 reveals that they are energetically non-degenerate even without strain. This arises from the C_{2v} symmetry of the system. Already from the geometry of the embedded QD system it is clear that there is no (001) mirror plane. Furthermore, if one considers a (001)-plane with sites occupied by Se anions, the nearest neighbor (cation) planes in the $\pm z$ direction are not equivalent, as for the zinc blende structure the nearest neighbors above the plane are found in the $[111]$ direction and below the plane in the $[1\bar{1}\bar{1}]$ direction. Thus for crystallographic reasons a (001) plane is not a mirror plane. Finally, if one considers the base plane of the embedded QD (or the WL) to be this anion (001) plane, there are different cations, namely Cd above and Zn below this plane. Therefore, the QD system has only a C_{2v} symmetry. In theories based on continuum models, e.g., effective-mass approximations [20, 102] or $\mathbf{k} \cdot \mathbf{p}$ models [102, 103], the discussed atomic anisotropy effects cannot be accounted for. These effects also affect the single-particle wave functions in the system. In Figure 7.4 the isosurfaces for the modulus squared electron wave functions $|\Phi_i(\mathbf{r})|^2$ are displayed with and without strain, respectively. The light and dark isosurface levels are selected as 0.1 and 0.5 of the maximum probability density, respectively. For both calculations, the lowest electron state e_1 is according to its nodal structure an s -like state. The next two states e_2 and e_3 are p -like states. These states are oriented along the $[1\bar{1}0]$ and the $[110]$ direction, respectively. Due to the different atomic structure along these directions we find a p -state splitting $\Delta_{e_2, e_3}^0 = E_{e_3} - E_{e_2}$ for the unstrained embedded QD of about 0.43 meV. In conventional $\mathbf{k} \cdot \mathbf{p}$ models [102, 103]

C_{2v}	E	C_2	$\sigma_v(xz)$	$\sigma_v(yz)$
A_1	1	1	1	1
A_2	1	1	-1	-1
B_1	1	-1	1	-1
B_2	1	-1	-1	1

(a)

C_{4v}	E	$2C_4$	C_2	$2\sigma_v$	$2\sigma_d$
A_1	1	1	1	1	1
A_2	1	1	1	-1	-1
B_1	1	-1	1	1	-1
B_2	1	-1	1	-1	1
E	2	0	-2	0	0

(b)

Table 7.1: Character table of the group C_{2v} (a) and C_{4v} (b), respectively.

an unstrained, square-based pyramidal QD is modeled with a C_{4v} symmetry. Consequently, e_2 and e_3 are degenerate in such models. In our microscopic model the resulting degeneracy is lifted and a splitting occurs as a consequence of the reduction of the C_{4v} symmetry to a C_{2v} zinc blende symmetry. This analysis is also confirmed by a group theoretical inspection of these two groups. As already discussed in Chapter 4.1, the group C_{2v} is an abelian group with four irreducible representations. The character table is again depicted in Table 7.1(a), using the notation of Section 4. From this we can deduce that each irreducible representation is one dimensional. Therefore, neglecting the spin, each state must be non-degenerate. In contrast to the group C_{2v} , the group C_{4v} is *non-abelian*. In this case we have four one dimensional representations and one two-dimensional representation. The character table of the C_{4v} group is given in Table 7.1(b). In conclusion one could expect degenerate states in systems with a C_{4v} symmetry but not in systems with an overall symmetry group of C_{2v} . Taking spin-orbit coupling into account, one has to consider the double group \bar{C}_{2v} and the additional degeneracies due to time reversal symmetry. From the analysis, given in Section 4.3.1, we conclude that each state has to be double degenerate and that no higher degeneracy occur. This is exactly the result, that we obtain from our TB calculation.

Strain splits the states e_2 and e_3 further. Due to the different atomic structure, the strain profile within each plane (perpendicular to the growth z direction) along the $[110]$ and $[\bar{1}\bar{1}0]$ direction is different [73]. This additionally contributes to the anisotropy. Due to the fact that the base is larger than the top, there is a gradient in the strain tensor between the top and the bottom of the pyramid. In the embedded QD, the cation neighbors above each anion are found in the $[111]$ direction while the cation neighbors below are found in the $[\bar{1}\bar{1}\bar{1}]$ direction. Therefore, the cations along the $[\bar{1}\bar{1}0]$ direction are systematically more stressed than the cations along the $[110]$ direction. Including strain we find a p -state splitting of $\Delta_{e_2, e_3}^{\text{strain}} = 7.1$ meV. Compared to the states e_2 and e_3 of the unstrained QD, the wave function shows a clear nodal plane in the presence of the strain field. The states e_2 and e_3 reveal nodal planes along the $[110]$ and $[\bar{1}\bar{1}0]$ directions, respectively.

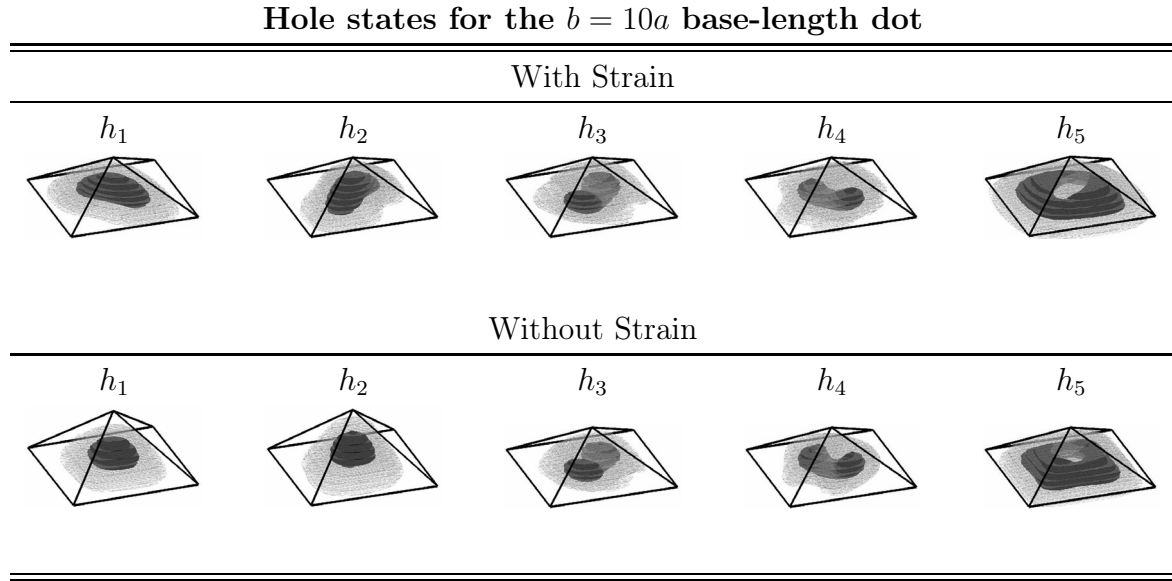


Figure 7.5: Isosurface plots of the modulus squared hole wave functions with and without strain for the embedded $b = 10a$ pyramidal QD. See the caption of Figure 7.4 for more details.

The state e_4 for the strained QD is resonant with a WL state, so the wave function is leaking into the WL. The wave function of the state e_5 is localized at the base of the pyramid but also clearly shows a finite probability density inside the WL. The states e_4 and e_5 of the unstrained QD are still mainly localized inside the dot. The classification of the state e_4 by its nodal structure is difficult. e_4 is similar to a p state which is oriented along the $[001]$ direction. The electron state e_5 is d like.

Figure 7.5 shows the isosurface plots of the modulus squared wave function $|\Phi_i(\mathbf{r})|^2$ for the lowest five hole states h_1 to h_5 with and without strain. The light and dark isosurface levels are again selected as 0.1 and 0.5 of the maximum probability density, respectively. Our atomistic calculation shows that the hole states cannot be classified as s -like, p -like, or d -like according to their nodal structures. This is the case because with and without strain the hole states are strongly affected by band mixing. Therefore the assumption of a single heavy-hole valence band for the description of the bound hole states in a QD yields even qualitatively incorrect results. In contrast to quantum well systems, the light-hole and heavy-hole bands are strongly mixed in an embedded QD. This result is in good agreement with other multi-band approaches [8,29,31,72,103–105].

From Figure 7.5 we can also analyze the influence of strain on the different hole states. Without strain the states h_1 and h_2 are only slightly elongated along the $[1\bar{1}0]$ and $[110]$ directions, respectively. Due to strain these states are clearly elongated along these directions. In contrast, the states h_3 to h_5 are only slightly affected by strain.

Another interesting result is that strain effects shift the electron states to lower energies and the hole states to higher energies as displayed in Figure 7.3. Furthermore one observes, that the WL ground state for electrons and holes is shifted in a similar way

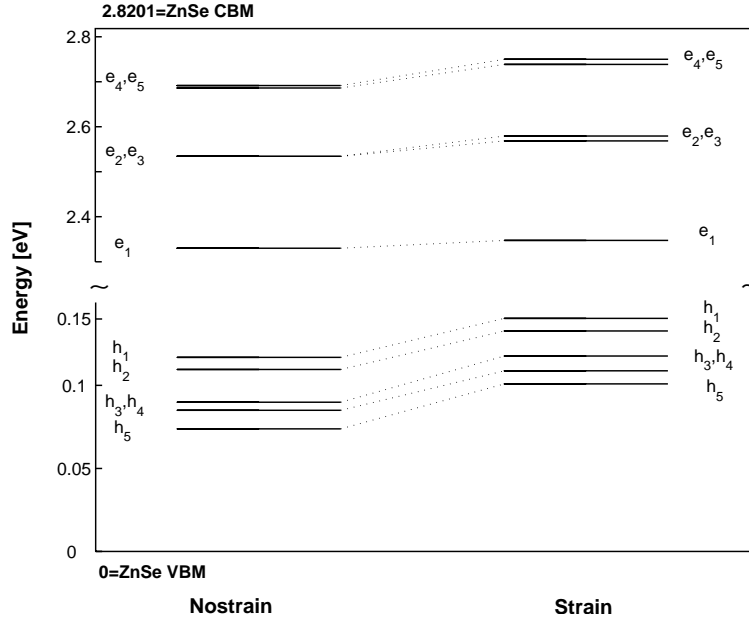


Figure 7.6: First five electron and hole state energies for the embedded pyramidal CdSe QD with $b = 10a$ and a 1 ML thick WL. On the left-hand side the results for the unstrained QD are shown. On the right-hand side the results for the strained embedded QD are displayed. All energies are measured from the valence-band maximum (VBM) of bulk ZnSe.

due to strain. We observe that strain decreases the single-particle energy gap $E_{\text{gap}}^{\text{QD}} = E_{e_1} - E_{h_1}$ by about 1.4%, lowering it from the strain-unaffected value 2.12 eV to the value 2.09 eV. For a biaxial compressive strain in a zinc blende structure, the conduction-band minimum of a bulk material is shifted to higher energies while the energy shift of the valence-band maximum depends on the magnitude of the hydrostatic and shear deformation energies [76]. Therefore, one would expect that the electron states are shifted to higher energies due to the fact that CdSe is compressively strained in the ZnSe-Matrix. This is in contradiction to the behavior we observe here.

In order to understand these results, we investigate the influence of the WL states on the one-particle spectrum. Therefore we use the same model geometry as shown in Figure 7.1 but with a considerably smaller WL thickness of only 1 ML. A 1 ML thick WL was also used before by Santoprete *et al.* [9], Stier *et al.* [29] and Wang *et al.* [31] for an InAs/GaAs embedded QD. Figure 7.6 shows the comparison of the results for a strain-unaffected and a strained pyramidal CdSe QD with a 1 ML thick WL and a base length of $b = 10a$. On the left-hand side of Figure 7.6 the first five electron and hole-state energies for an unstrained QD are displayed while the right-hand side shows the energies for the strained QD. For a 1 ML thick WL the lowest electron state is, by strain effects, shifted to higher energies. This is what one would expect for biaxial compression of the bulk material. Furthermore the splitting of the p -like states e_2 and e_3 is larger compared to the results for a 1 a thick WL. The splitting Δ_{e_2, e_3}^0 of

WL	1a		1 ML	
	No strain	Strain	No strain	Strain
Δ_{e_1,e_2} [meV]	162.8	161.5	204.1	221.2
Δ_{e_2,e_3} [meV]	0.43	7.1	0.5	10.9
Δ_{h_1,h_2} [meV]	5.76	3.7	7.25	7.66
Δ_{h_2,h_3} [meV]	16.36	12.3	19.66	15.11
$E_{\text{gap}}^{\text{QD}}$ [eV]	2.12	2.09	2.21	2.21

Table 7.2: Energy splittings for electron and hole bound-states in case of different WL thicknesses. The influence of strain effects on the splittings $\Delta_{e_1,e_2} = |E_{e_1} - E_{e_2}|$, $\Delta_{e_2,e_3} = |E_{e_2} - E_{e_3}|$, $\Delta_{h_1,h_2} = |E_{h_1} - E_{h_2}|$ and $\Delta_{h_2,h_3} = |E_{h_2} - E_{h_3}|$ is displayed together with the QD gap $E_{\text{gap}}^{\text{QD}} = E_{e_1} - E_{h_1}$. The WL thickness is $1a$ and 1 ML , respectively. The base length of the pyramid is $b = 10a$.

the unstrained embedded QD with a $1a$ thick WL is $\Delta_{e_2,e_3}^0 = 0.43 \text{ meV}$ whereas for the system with a 1 ML thick WL one has $\Delta_{e_2,e_3}^0 = 0.5 \text{ meV}$. So the splitting Δ_{e_2,e_3}^0 is increased by about 16 %. With strain-effects, the splitting for the system with 1 ML WL thickness $\Delta_{e_2,e_3}^{\text{strain}} = 10.9 \text{ meV}$ is about 54 % larger than the splitting in the system with $1a$ WL thickness $\Delta_{e_2,e_3}^{\text{strain}} = 7.1 \text{ meV}$. Also the energy splitting Δ_{e_1,e_2} between the ground state e_1 and the first excited state e_2 is strongly influenced by the WL thickness, namely $\Delta_{e_1,e_2} = 162.8 \text{ meV}$ for the unstrained system with $1a$ WL, but $\Delta_{e_1,e_2} = 204.1 \text{ meV}$ for a 1 ML WL. This means that with strain effects the splitting Δ_{e_1,e_2} is increased by about 27 % if the WL thickness is decreased from $1a$ to 1 ML . The results are summarized in Table 7.2.

These effects mainly arise from the fact, that the bound states inside the dot are also coupled to the WL states. For a $1a$ WL the wave functions of the bound states show also a probability density inside the WL. For a thinner WL the leaking of the states into the region of the WL is less pronounced. In this case, the structure inside the QD and also the strain are much more important. This explains the larger energy splittings in the case of the 1 ML WL compared to the results for a $1a$ WL.

The hole states are influenced in a similar manner. In the case of a 1 ML WL the energy spectrum of the hole states is shifted to higher energies due to the strain effects. This behavior is similar to the one obtained from the calculations for a $1a$ WL (Figure 7.6). In the 1 ML WL system the energy splittings Δ_{h_1,h_2} and Δ_{h_2,h_3} for the first three hole states are larger than the values we obtain for the system with $1a$ WL. These splittings are summarized in Tab 7.2. The WL thickness also influences the QD energy gap $E_{\text{gap}}^{\text{QD}}$. For a 1 ML WL the electron states are shifted to higher energies in contrast to the behavior of the hole states (compare Figs. 7.3 and 7.6). In the case of the 1 ML WL the gap energy $E_{\text{gap}}^{\text{QD}}$ is only slightly influenced by the strain. We observe here that

the strain has an opposite effect for electrons and hole states: electron states become shallower, approaching the conduction-band edge, while the hole states become deeper, moving away from the valence-band edge.

In this section we have analyzed the electronic states of pyramidal CdSe QDs. The knowledge of the single-particle wave functions are an important prerequisite for the examination of many-particle effects in these low dimensional systems: The single-particle states can be used as an input for the calculation of Coulomb- and dipole-matrix elements. Based on those quantities the investigation of multi-exciton emission spectra [30], carrier capture and relaxation in semiconductor quantum dot lasers [121], or a quantum kinetic description of carrier-phonon interactions [122] is possible.

7.2 Results for CdSe Nanocrystals

So far we discussed only the electronic properties of pyramidal CdSe QDs embedded in a ZnSe matrix. In this section we investigate the single-particle states and energies of chemically synthesized CdSe nanocrystals within our TB model. Furthermore, we will compare the dependence of the energy gap and the level spacing of the electronic states on the nanocrystal diameter with available experimental data.

7.2.1 Quantum Dot Geometry and Strain

Nanocrystals are chemically synthesized [16, 17]. These low dimensional systems are nearly spherical in shape [17, 123, 124] and the surface is passivated by organic ligands. Due to the flexible surrounding matrix, these nanostructures are nearly unstrained [124]. The size of the nanocrystals is typically in between 1 and 5 nm in radius [16, 35, 123, 125].

We model such a chemically synthesized nanocrystal as an unstrained, spherical crystal-lite with perfect surface passivation. For CdSe nanocrystals the zinc blende structure is assumed. In the following we concentrate on relatively large nanocrystals in the range of 2 to 5 nm. In this case, surface reconstructions [26, 28, 113] and the fact that the surface coverage with ligands is often not perfect [126], should only be of minor importance. Unlike previous works, using TB models, we investigate here in particular how the electronic structure of the nanocrystals changes with the size. The TB parameters, which describe the coupling between the dot material and the ligand molecules, are chosen to be zero. This corresponds to an infinite potential barrier at the surface and is commonly used because of the larger band gap of the surrounding material [127].

7.2.2 Single-particle Properties and Comparison with Experimental Results

We have performed TB calculations for finite, spherical, unstrained nanocrystals of a diameter between 1.82 and 4.85 nm (corresponding to $3 - 8a$, when $a \approx 0.607$ nm is the CdSe lattice constant of the conventional unit cell). For the largest nanocrystal (with a diameter of 4.85 nm) the five lowest lying electron and hole eigenstates are shown in Figure 7.7 in the form of an isosurface plot. The electron ground state e_1 has nearly spherical symmetry and can be classified as a $1s$ state. Correspondingly the second state e_2 has the form of a $2s$ state and the states $e_{3,4}$ are p states, and e_5 is d -like. Despite the spherical symmetry of the system this simple classification is no longer possible for the hole states. Even the lowest lying hole state h_1 shows no full rotational invariance, i.e., strictly speaking it cannot be classified as being an s state. This is due to the intermixing of different atomic orbitals. Similarly the higher hole states h_2 to h_4 cannot clearly be classified as an s - or p -like state. Consequently, for a proper treatment of the single-particle states a multi-band approach is required. The discussed

Electron and holes states for the nanocrystal

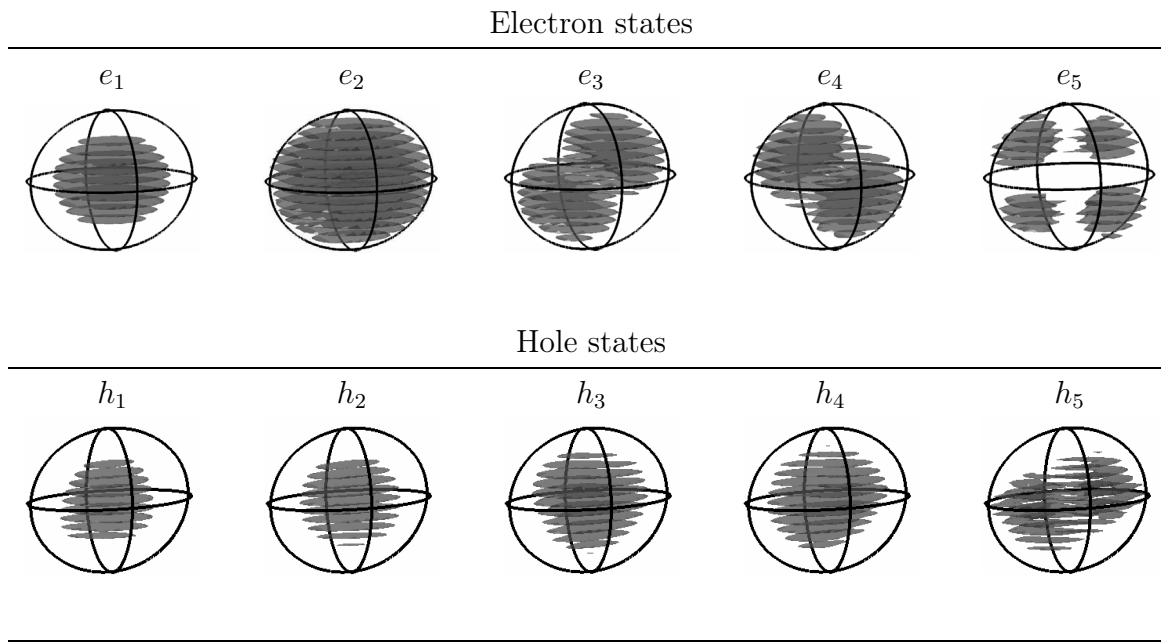


Figure 7.7: Isosurfaces (at 30 % of the maximum probability density) of the modulus squared electron and hole wave functions of spherical CdSe nanocrystals of diameter $d = 4.85$ nm for the five lowest states.

band mixing effects will also have implications in the calculation of matrix elements between these states, which for example enter selection rules for optical transitions.

In the case of an ideal zinc blende structure we do not obtain any indications of quasi-metallic behavior, i.e., of a nonvanishing (quasi-continuous) spectrum of states at the Fermi energy in contrast to previous work (assuming an ideal wurtzite structure for CdSe nanocrystals) [28, 112, 113]. This is probably due to the fact that this quasi-metallic behavior is caused by surface states in the case where no passivation and surface reconstruction is taken into account. These surface states are formed by the dangling bonds of unsaturated Se at the nanocrystal surface, which lead to the appearance of s states in the band gap region [112]. In our simplified and restricted TB $s_c p_a^3$ basis set these s orbitals at the anions (Se) are not taken into account. Therefore, these surface states, which in reality and in more realistic models are removed (i.e., energetically shifted down and filled) due to passivation and surface reconstruction, do not occur.

The discrete electronic states of semiconductor nanocrystals are experimentally accessible by scanning tunneling microscopy (STM) [35, 123, 125]. The tunnel current I between the metallic tip of the STM and the CdSe nanocrystal is measured as a function of the bias voltage V . The conductance (dI/dV) is related to the local tunneling density of states. In the dI/dV vs V diagram, several discrete peaks can be observed. These peaks correspond to the addition energies of holes and electrons. The spacing between the various peaks can be attributed to the Coulomb charging and/or charge

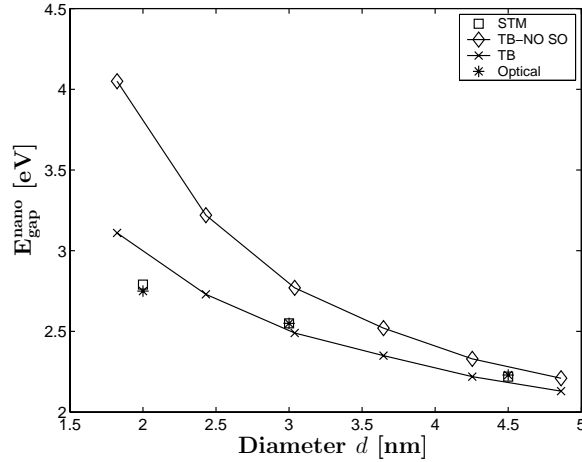


Figure 7.8: Energy gap $E_{\text{gap}}^{\text{nano}}$ as a function of the nanocrystal diameter d . Compared are the results from our TB model with (TB) and without (TB-NO SO) spin-orbit coupling, a STM (STM) [125] and an optical measurement (Optical) [125].

transfer into higher energy levels. From these measurements the energy gap $E_{\text{gap}}^{\text{nano}}$ as well as the splitting Δ_{e_1, e_2} between electron ground state e_1 and the first excited state e_2 can be determined.

Alperson *et al.* [125] investigated CdSe nanocrystals with an STM. Here we compare our calculated energy gap $E_{\text{gap}}^{\text{nano}}$, which is given by the difference between the electron and hole ground state, with the measured data. Figure 7.8 displays the results for CdSe nanocrystals with diameters from 1.82 to 4.85 nm. Alperson *et al.* [125] compare the STM results with optical spectroscopy measurements from Ekimov *et al.* [128]. The overall agreement with the TB results is very good, especially for the larger nanocrystals. Deviations in the case of the small 2 nm nanocrystal may arise from surface reconstructions [26, 28, 113] that are neglected here. To assess the impact of the spin-orbit coupling on the obtained results, the calculations were also performed in the absence of this contribution. In this case the TB parameters are re-optimized in order to reproduce the characteristic properties (band gap, effective masses) of the bulk material. The re-adjusted parameters are given in Table A.2 of Appendix A. Without spin-orbit coupling (TB-NO SO), the energy gap $E_{\text{gap}}^{\text{nano}}$ is always strongly overestimated by the TB model, in particular for smaller nanocrystals. This underlines the importance of spin-orbit interaction for a satisfactory reproduction of the experimental results.

After this discussion of the single-particle energy gap as a function of the nanocrystal diameter, we will turn our attention now to the single-particle energy spectrum. Taking into account the time reversal symmetry, the lowest electron state e_1 is twofold degenerate and s -like. This is consistent with the experimentally observed doublet [125] in the dI/dV characteristic. The next excited level is (quasi) sixfold degenerated. The

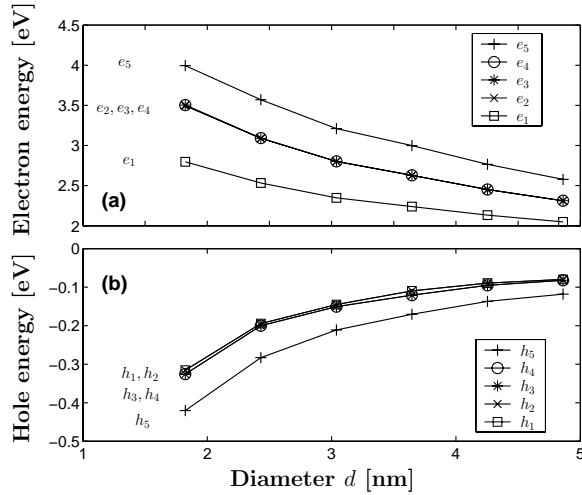


Figure 7.9: Electron (a) and hole (b) energies as a function of the nanocrystal diameter d . For electrons (e_1 to e_5) and holes (h_1 to h_5) the first five eigenvalues are displayed. Each state is twofold degenerated.

spin-orbit coupling splits this into one twofold and one fourfold degenerate state.¹ In the STM measurement Alpers *et al.* [125] observed such a high multiplicity of the second group of peaks. This behavior has also experimentally [123] and theoretically [109] been observed for InAs nanocrystals. The energy spectrum for nanocrystals of different diameters is shown in Figure 7.9(a). Here the first five electron states are displayed. Note that every state is twofold degenerated due to the time reversal symmetry, as discussed in Section 4.3.

For the hole states the situation is more complicated. Alpers *et al.* [125] observed a high density of hole states. The distinction between addition and excitation peaks is difficult, due to the large number of possible levels and the close proximity between the charging energy and the level spacing. For the holes we observe that the first two states (h_1, h_2) and (h_3, h_4) are fourfold degenerate. The energy splitting of these states is very small. These results are consistent with the observations given in Ref. [125]. Figure 7.9(b) shows the hole energy versus diameter d for the spherical CdSe nanocrystals. Obviously, the states h_1 to h_4 are almost degenerate, i.e., including time reversal symmetry there is almost an eightfold degeneracy of these states.

Furthermore the calculated splitting $\Delta_{e_1, e_2} = E_{e_2} - E_{e_1}$ between the first two electron states e_1 and e_2 is compared with experimentally observed results in Figure 7.10 as a function of the nanocrystal diameter. The influence of the spin-orbit coupling is also investigated. Once more, we have compared the calculations without (TB-NO SO) and with spin orbit-coupling (TB). The results of our TB model for the splitting

¹ Due to the spherical symmetry of the nanocrystal, and in contrast to the pyramidal QDs of the previous chapter, the symmetry of the combined system (lattice + QD geometry) is C_{4v} . According to the character table of the (double) group \bar{C}_{4v} [87], four fold degenerate states are allowed.

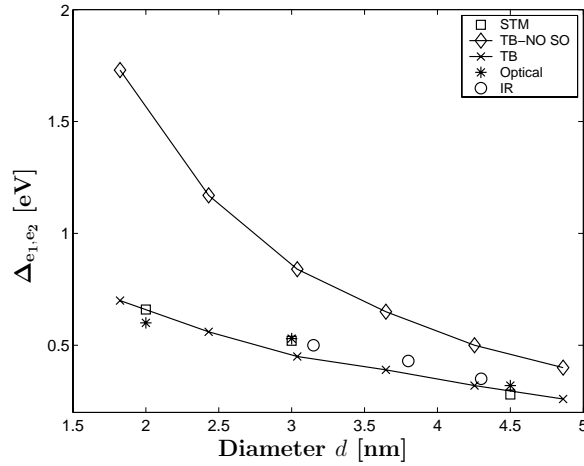


Figure 7.10: Splitting $\Delta_{e_1,e_2} = E_{e_2} - E_{e_1}$ between the lowest two electronic states as a function of the nanocrystal diameter d . The results from our TB model, with (TB) and without (TB-NO SO) spin-orbit coupling, and from a STM measurement (STM, Ref. [125]) are displayed. Besides this, results from infrared spectroscopy (IR, Ref. [129]) and optical methods (Optical, Ref. [125]) are shown.

Δ_{e_1,e_2} are also compared with results obtained by STM [125] and by optical methods (Optical) [128]. This splitting Δ_{e_1,e_2} was independently determined experimentally by Guyot-Sionnest and Hines [129] using infrared spectroscopy (IR). Again we find, that without spin-orbit coupling the TB model always overestimates the splitting Δ_{e_1,e_2} . Especially for smaller nanocrystals the spin-orbit coupling is very important in describing the electronic structure. With spin-orbit coupling the results of the TB model show good agreement with the experimentally observed results.

Electronic and Optical Properties of
Nitride Quantum Dots with a
Wurtzite Structure

8 Introduction to Part III

As a new material system, group-III nitrides are of particular interest due to their wide range of emission frequencies from red to ultraviolet [130, 131]. For the description of the electronic properties in low-dimensional heterostructures based on these materials a variety of different theoretical approaches is used. For example, models that are based on a continuum-like description of the crystal structure, like effective-mass [132, 133] and $\mathbf{k} \cdot \mathbf{p}$ [29, 134, 135] are utilized. The fundamental electronic properties are included via effective mass or Luttinger parameters of the bulk band structure. However, the applicability of one-component effective-mass theories is limited to situations where band mixing effects are of minor importance. A $\mathbf{k} \cdot \mathbf{p}$ formulation provides a more sophisticated approach, where band mixing effects can be accounted for [29] and where some but in general not all symmetry properties of the system can be included. To fully understand the influence of the underlying lattice structure on the electronic spectra of low-dimensional heterostructures, an atomistic treatment is necessary. This has recently been stressed by Bester *et al.* in case of InAs/GaAs QDs [136]. On the atomistic level, different approaches have successfully been applied in the past, namely the empirical pseudopotential method [137–139], and tight-binding (TB) models [9, 118], which include the atomistic crystal structure and provide a multi-band description of the complicated valence band structure.

The above mentioned approaches have been used to investigate the electronic and optical properties of a variety of different heterostructures, mostly QDs [9, 138, 140] and quantum well [76, 118, 141] systems. Some of the semiconductor materials of interest for optoelectronic applications, e.g., InAs, GaAs, CdSe, crystallize in the zinc blende structure, whereas some exist also in a wurtzite crystal structure, such as, CdSe. Semiconductors, like ZnO or InN, are almost exclusively found with a wurtzite structure. While for the zinc blende structure the influence of atomistic effects has previously been studied [136], for the wurtzite structure comparatively little is known.

Among the wurtzite semiconductors especially the technologically interesting group-III nitrides have recently attracted considerable attention. Quite a lot of theoretical [70, 142] and experimental [40, 143] information is available concerning GaN/AlN QD systems [40, 70, 142, 143] with emission wavelengths in the blue or ultraviolet region. Much less effort has been spent on InN/GaN QDs, which are promising to extend the emission wavelength of group-III nitride structures to the red and infrared [144]. So far, most of the theoretical work concerning InN QD structures is based on effective-mass [145, 146] and $\mathbf{k} \cdot \mathbf{p}$ calculations [147].

To provide further valuable insight into the properties of group III-nitride QDs, we investigate the optical properties of self-assembled InN/GaN quantum dots on an atomistic level by means of a TB formulation. We focus our attention on small QDs in order to minimize the quantum confined Stark effect (QCSE), which strongly reduces the emission efficiency in larger nitride-based QDs and, thus, limits their applicability as optoelectronic devices [148, 149]. We discuss how Coulomb and dipole matrix elements can be calculated from the TB single-particle wave functions and investigate the influence of the wurtzite crystal structure and the built-in electrostatic field.

The calculation of Coulomb and dipole matrix elements between the microscopically determined one-particle QD states makes the investigations of excitonic spectra by means of a configuration-interaction approach [30, 150, 151] with atomistically determined input parameters possible. As a main result, we show that for small lens-shaped InN/GaN QDs the exciton ground state emission vanishes. In contrast to an s -like state in case of the small QD, for larger QDs the twofold degenerate p -like states constitute the hole ground states. The interchanged level structure, results in nonvanishing dipole matrix elements with the electron ground state. This leads to a bright ground state exciton emission for larger QDs. However, the QCSE reduces the oscillator strengths by more than one order of magnitude.

This part is organized as follows. After a brief discussion of the wurtzite crystal structure in Section 9.1, we turn our attention to the analysis of the bulk band structure of semiconductors with a wurtzite lattice. The spontaneous polarization in such structures is discussed in Section 9.3. In the following section the TB model with an sp^3 basis is introduced. The single-particle states and the energy spectrum are presented and discussed in Section 10.1. Finally, the many-body properties, such as multi-exciton emission spectra, are investigated in Section 10.2.

9 Crystals with a Wurtzite Structure

For a microscopic description of the electronic structure in semiconductor QDs by means of an empirical TB model, the underlying crystal structure of the material systems under consideration is of essential importance. This part is dedicated to the calculation of the electronic and optical properties of InN QDs with a wurtzite structure. We will discuss the characteristics of the wurtzite crystal structure in the following section by means of group theory. Section 9.2 deals with the bulk band structure of semiconductor materials in the wurtzite phase, since the empirical parameters of the TB model are adjusted to reproduce the energy bands known from the literature. Finally, the TB model, which is used for the calculations of the electronic structure of InN/GaN QDs with a wurtzite structure is introduced in Section 9.4.

9.1 Crystal Structure

The wurtzite structure is the hexagonal analog to the zinc blende structure. Many important semiconductors crystallize in the wurtzite phase, such as GaN, AlN, InN, ZnS, CdS, CdTe and ZnO.¹

In analogy with the diamond and the zinc blende structures, the wurtzite structure can be constructed by considering to interpenetrating lattices. However, in this case they are hexagonally close packed (hcp) lattices, in contrast to the face-centered cubic lattice in zinc blende. In other words, the wurtzite structure consists of a hcp lattice with a diatomic basis. The conventional unit cell is depicted in Figure 9.1(a). The hexagonal unit cell has the axes \mathbf{a}_1 , \mathbf{a}_2 and \mathbf{a}_3 , with $|\mathbf{a}_1| = |\mathbf{a}_2| \neq |\mathbf{a}_3|$. For the angles between the different vectors one finds $\sphericalangle(\mathbf{a}_1, \mathbf{a}_2) = 120^\circ$ and $\sphericalangle(\mathbf{a}_1, \mathbf{a}_3) = \sphericalangle(\mathbf{a}_2, \mathbf{a}_3) = 90^\circ$. The basis vectors are explicitly given by

$$\mathbf{a}_1 = \left(\frac{\sqrt{3}a}{2}, \frac{-a}{2}, 0 \right), \quad \mathbf{a}_2 = (0, a, 0), \quad \mathbf{a}_3 = (0, 0, c), \quad (9.1)$$

where a is the length of a hexagonal side and c is the repeat distance along the z direction. The ratio c/a typically deviates from the ideal value $\zeta_0 = \sqrt{8/3}$, as shown in Ref. [153]. Furthermore, the wurtzite structure is often characterized by the so-called

¹ For ZnS, CdS and CdTe the crystallographic phase is temperature dependent. At high temperatures the phase is cubic whereas in the low temperature regime the phase is hexagonal [152].

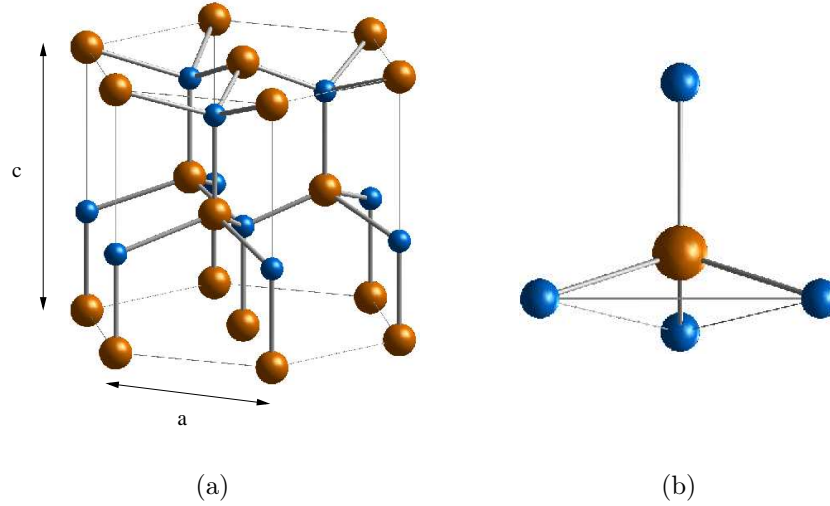


Figure 9.1: (a) Conventional unit cell of a wurtzite structure. (b) Tetrahedral bonding (sp^3 -bonding). Small spheres indicate the anions, large spheres the cations. (Figures adopted from Ref. [116])

internal parameter u defined as the anion-cation bond length along the (0001) axis in units of c . For the ideal wurtzite structure u has the value $u_0 = 3/8$. Due to the not ideal c/a ratio, in real wurtzite crystals u deviates from u_0 , e.g. for InN and GaN $u > u_0$ [154,155].

In contrast to the zinc blende structure, the wurtzite unit cell contains four atoms, two anions and two cations. The corresponding lattice vectors are given by:

$$\mathbf{R}_1 = (0, 0, 0), \quad \mathbf{R}_2 = \left(\frac{a}{\sqrt{3}}, 0, \frac{c}{2} \right), \quad \mathbf{R}_3 = \left(\frac{a}{\sqrt{3}}, 0, \frac{c}{8} \right), \quad \mathbf{R}_4 = \left(0, 0, \frac{5c}{8} \right). \quad (9.2)$$

The anions are located at \mathbf{R}_1 and \mathbf{R}_2 ; the cations are located at \mathbf{R}_3 and \mathbf{R}_4 . As in the case of zinc blende structures the atoms are tetrahedrally arranged, the cation is bonded to four anions and vice versa. The local structural environment of the atoms in the wurtzite structure is shown in Figure 9.1(b). As can be seen in Figure 6.1(b) of Section 6.1, it slightly deviates from the zinc blende structure.

To describe lattice planes and directions in a crystal the so-called *Miller indices* [156] are used. In case of the wurtzite structure, often four Miller indices are used instead of the usual three. The Miller indices are a triplet of integer numbers (hkl) , which are the reciprocal values of the axis intersections in the direct lattice. In the wurtzite structure, they are denoted as $[hkml]$. Within the (0001) plane three indices hkl are used that are related to the three vectors \mathbf{A}_1 , \mathbf{A}_2 , and \mathbf{A}_3 , shown in Figure 9.2, rotated with respect to each other by 120° . Of course the four indices are not independent, $l + h + k = 0$. Different lattice planes and directions are indicated in Figure 9.2.

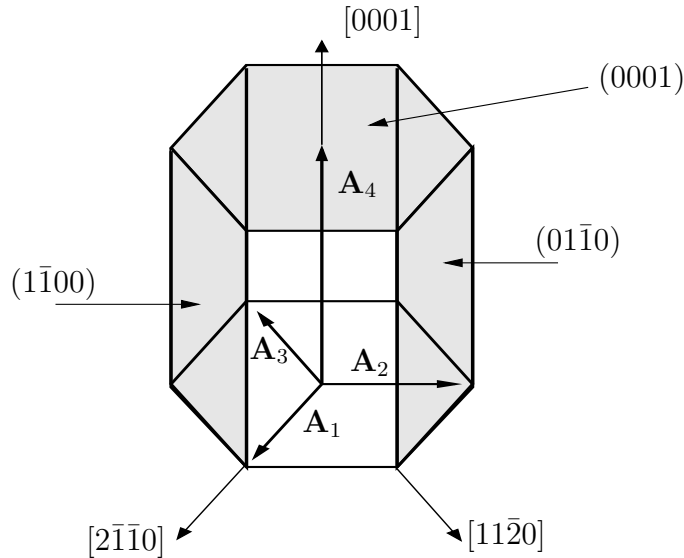


Figure 9.2: Miller indices for different lattice planes and directions in a hcp or wurtzite lattice.

9.2 Symmetry Considerations and Bulk Band Structure for Wurtzite Semiconductors

As already discussed, in an empirical TB model the TB parameters are determined such that the characteristic properties of the bulk band structure are reproduced. In the following we are interested in the electronic properties of wurtzite semiconductor materials with direct band gap, e.g., InN and GaN.

The Γ point being the region of major importance for the optical properties of these systems, we address in this section the band structure in the vicinity of the Brillouin zone center. To choose an appropriate TB model for the description of the bulk bands around the Γ point, we discuss the mixing of the states with atomic like s and p character at $\mathbf{k} = \mathbf{0}$ in the wurtzite crystal structure. For this analysis, we will also introduce group theoretical aspects in our discussion to classify the different states according to the notation which is used in the literature.

The space group of the wurtzite structure is C_{6v}^4 in contrast to tetrahedral space group T_d^2 in the case of zinc blende. Unlike the T_d^2 group, the space group C_{6v}^4 is *non-symmorphic*. A non-symmorphic space group contains glide and/or screw operations in addition to translation. The space group C_{6v}^4 comprises a six-fold screw axis, which indicates a rotation by an angle $2\pi/6$ around the c axis followed by a non-primitive translation.² As already discussed in Section 4.2, the electronic states of a crystal can be classified according to the irreducible representations of the corresponding space group [88]. Following the discussion of Section 4.2, for a given wave vector \mathbf{k} that is associated with some symmetry point in \mathbf{k} -space, one finds those operations of the point

² A non-primitive translation does not map the lattice onto itself, in contrast to primitive translation.

C_{6v}	$\{E\}$	$\{C_2\}$	$\{2C_3\}$	$\{2C_6\}$	$\{3\sigma_v\}$	$\{3\sigma_d\}$	Basis
Γ_1	1	1	1	1	1	1	$s, z, 3z^2 - r^2$
Γ_2	1	1	1	1	-1	-1	R_z
Γ_3	1	-1	1	-1	-1	1	$x^3 - 3xy^2$
Γ_4	1	-1	1	-1	1	-1	$y^3 - 3yx^2$
Γ_5	2	-2	-1	1	0	0	$(x, y), (zx, yz), (R_x, R_y)$
Γ_6	2	2	-1	-1	0	0	$(x^2 - y^2, xy)$

Table 9.1: Character table for the single group C_{6v} at Γ for a wurtzite crystal structure. Additionally, the corresponding basis functions are given [157].

group associated with the space group which transforms \mathbf{k} into itself plus a reciprocal-lattice vector. Such a set of symmetry operations forms a group called the group of the wave vector \mathbf{k} . At the Brillouin zone (BZ) center, the point group of $\mathbf{k} = \mathbf{0}$ is C_{6v} . As discussed in Section 4.2, without spin all states transform according to the *single* group representations of C_{6v} . The character table of the single group C_{6v} is given in Table 9.1. In a system with a wurtzite structure the following qualitative picture applies: The conduction band at the center of the BZ is mostly *s*-like, while the valence band states at $\mathbf{k} = \mathbf{0}$ are predominantly *p*-like [158]. According to the basis functions of the different irreducible representations of the point group C_{6v} of $\mathbf{k} = \mathbf{0}$, given in Table 9.1, we can deduce that the *s*-like conduction band belongs to the fully symmetric Γ_1 representation. Furthermore, we see from Table 9.1, that p_x - and p_y -like functions, belong to the irreducible representation Γ_5 , while the p_z -like functions belong to the representation Γ_1 . Unlike the cubic case that we discussed in Section 6.2, the three *p*-like functions no longer belong to the same irreducible representation. Degeneracies for the valence-band states are removed in the wurtzite structures by the additional crystal field splitting Δ_{cf} due to the anisotropy between the *a*- and the *c*-axis. Therefore, even without spin-orbit coupling, the valence band edge is split into a double degenerate state, corresponding to the representation Γ_5 , and into a non-degenerate state belonging to the irreducible representation Γ_1 . Here, we denote the double degenerate state by *A*, while the non-degenerate state is denoted by *C*. This is in contrast to a cubic system, where, in the absence of spin-orbit coupling, the valence band edge is three-fold degenerate at $\mathbf{k} = \mathbf{0}$.

\bar{C}_{6v}	$\{E\}$	$\{\bar{E}\}$	$\{C_2, \bar{C}_2\}$	$\{2C_3\}$	$\{2\bar{C}_3\}$	$\{2C_6\}$	$\{2\bar{C}_6\}$	$\{3\sigma_v, 3\bar{\sigma}_v\}$	$\{3\sigma_d, 3\bar{\sigma}_d\}$
Γ_7	2	-2	0	1	-1	$\sqrt{3}$	$-\sqrt{3}$	0	0
Γ_8	2	-2	0	1	-1	$-\sqrt{3}$	$\sqrt{3}$	0	0
Γ_9	2	-2	0	-2	2	0	0	0	0

Table 9.2: Additional representations, to those of Table 9.1, of the double group \bar{C}_{6v} [87].

Γ_i	Γ_1	Γ_2	Γ_3	Γ_4	Γ_5	Γ_6
$\Gamma_i \times D_{1/2}$	Γ_7	Γ_7	Γ_8	Γ_8	$\Gamma_7 + \Gamma_9$	$\Gamma_8 + \Gamma_9$

Table 9.3: Direct products of the single group representations Γ_i with $D_{1/2}$ for the group $\mathbf{k} = \mathbf{0}$.

In semiconductor materials containing heavier atoms, such as CdSe and ZnSe, the spin-orbit coupling can play an important role. This is motivated by the fact that the magnitude of the spin-orbit splitting Δ_{so} in a semiconductor is comparable to the spin-orbit splitting of its constituent atoms. Thus, we have to discuss the influence of the spin-orbit coupling on the band structure in detail. Following the discussion of Section 4.2, in the presence of spin-orbit coupling one has to deal with the *double* group \bar{C}_{6v} at $\mathbf{k} = \mathbf{0}$. The additional representations of the double group are given in Table 9.2. Following the discussion of Section 6.2, the spin function transforms as the irreducible representation $D_{1/2}$, and the *total* wave function, made up of a spatial and a spin part, transforms like the direct product of the single group representation Γ_i with $D_{1/2}$. For a rotation around an angle α , the characters $\chi^{1/2}(\alpha)$ of $D_{1/2}$ are given by [88]

$$\chi^{1/2}(\alpha) = \frac{\sin(\alpha)}{\sin(\alpha/2)}. \quad (9.3)$$

The direct product $\Gamma_i \times D_{1/2}$ can be composed in terms of the double group representations. If more than one representation of the double group appears in this decomposition, a spin-orbit splitting of the level appears. The table of the direct products of the single group representations Γ_i of Table 9.1 with $D_{1/2}$ for the group of $\mathbf{k} = \mathbf{0}$ are given in Table 9.3. From the analysis of this table, we see that the conduction band belongs to the Γ_7 representation, as does the non-degenerate valence band state C . Furthermore, the direct product $\Gamma_5 \times D_{1/2}$ is composed of the representations Γ_7 and Γ_9 . In other words, the valence band edge is split by the spin-orbit interaction in two double degenerate states. The influence of the crystal field and spin-orbit interaction is schematically illustrated in Figure 9.3.

In conclusion, the combination of the crystal field splitting and the spin-orbit interaction leads to a so-called three-edge structure in the vicinity of the Γ point, involving the top of the valence band known as the A , B and C bands in order of increasing energy. Two of these three bands are of Γ_7 and one of Γ_9 symmetry, while the lowest conduction band has Γ_7 symmetry. Typically, the topmost valence band in the wurtzite structure has Γ_9 symmetry; an exception is ZnO for which the two upper bands A (Γ_9) and B (Γ_7) are believed to be reversed [159].

The energy splittings of the valence bands A , B and C in the presence of the crystal field and the spin-orbit interaction are given by [152]

$$\Delta_{1,2} = \left(\frac{\Delta_{\text{so}} + \Delta_{\text{cf}}}{2} \right) \mp \sqrt{\left(\frac{\Delta_{\text{so}} + \Delta_{\text{cf}}}{2} \right)^2 - \frac{2}{3} \Delta_{\text{so}} \Delta_{\text{cf}}}. \quad (9.4)$$

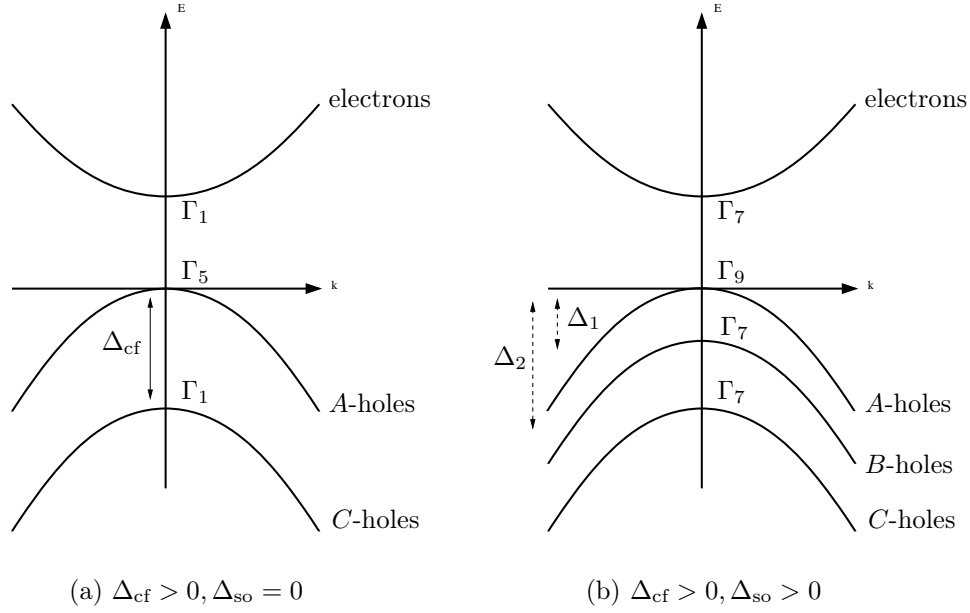


Figure 9.3: Schematic band structure of wurtzite semiconductors with conduction band and three valence bands. In the absence **(a)** and in the presence **(b)** of spin-orbit coupling. The spin-orbit and crystal field splittings are denoted as Δ_{so} and Δ_{cf} , respectively. Additionally the symmetries of the irreducible representations Γ_i are given.

It turns out that these terms are rather small in group-III nitrides. In wurtzite InN, GaN, and AlN Δ_{so} is of the order of 5-20 meV [131]. This is in strong contrast to several hundred meV found for most other III-V and II-VI semiconductor materials [160, 161]. Also the crystal field splitting Δ_{cf} in InN and GaN is only of the order of 10-40 meV [131]. In summary, compared to the II-VI and III-V materials, the contributions Δ_{so} and Δ_{cf} are negligible in case of the nitride material system with a wurtzite structure.

9.3 Spontaneous Polarization

The wurtzite crystal structure of nitride materials combined with epitaxial growth, which is usually performed in the [0001] direction, leads to the appearance of electrostatic fields and corresponding charge densities in strained materials. We have already discussed the effects of piezoelectric fields in semiconductor heterostructures in Section 3.2.2. It has been shown to affect carrier distributions, electric fields, and consequently a wide range of electronic and optical properties of nitride semiconductor materials and devices. In addition, theoretical [162] and experimental [163, 164] results have indicated that these systems exhibit a large *spontaneous* polarization. This polarization is associated with electrostatic charge densities analogous to those generated by the strain-dependent piezoelectric polarization fields. In bulk materials it is assumed that a rearrangement of surface charges counterbalances the spontaneous polarization

fields [163]. In heterostructures, however, variations in compositions are known to create nonvanishing spatially-varying spontaneous and piezoelectric polarization fields.

The existence of non-zero polarization fields in nitride semiconductors can be attributed to the lower symmetry of the wurtzite crystal structure compared to that of the cubic zinc blende, for which the spontaneous polarization vanishes [165]. The spontaneous polarization, which is denoted by $\mathbf{P}^{\text{spont}}$, represents a non-zero volume dipole moment in the crystal that exists in the absence of any external influence, such as strain or an electric field. In other words, the reason for a spontaneous polarization $\mathbf{P}^{\text{spont}}$ in wurtzite semiconductors is the static, relative shift of the positive and negative charges in the unit cell, which originates from the fact that the cell internal parameter u deviates considerably from the ideal value, as discussed in Section 9.1.

9.4 Tight-binding Model with sp^3 Basis

Following the discussion of Section 9.2, the valence bands A , B , and C originate mainly from the valence p orbitals, and, in case of the Γ_7 states, some s character. The conduction band on the other hand is predominantly s -like with some p_z character (Γ_7). Therefore, we cannot apply the $s_c p_a^3$ TB model studied in Part II, because it does not provide a mixing between s and p_z orbitals at the same atomic site. To take into account the mixing of the different orbitals, we use a TB model with an sp^3 basis $|\alpha, \mathbf{R}\rangle$, i.e., one s state ($\alpha = s$) and three p states ($\alpha = p_x, p_y, p_z$) per spin direction at each atom site \mathbf{R} . The TB matrix elements are given by

$$E_{\alpha\mathbf{R},\alpha'\mathbf{R}'} = \langle \alpha\mathbf{R} | H^{\text{bulk}} | \alpha'\mathbf{R}' \rangle, \quad (9.5)$$

where the indices \mathbf{R} and α label the lattice sites and the different types of orbitals, respectively. We include non-diagonal elements of the TB Hamiltonian matrix up to nearest neighbors and use the two-center approximation of Slater and Koster, discussed in Section 3.1, which yields nine independent TB parameters. In contrast to most other III-V and II-VI semiconductors, one can neglect spin-orbit coupling and crystal-field splitting in InN and GaN, which are of the order of 10 meV [57, 131]. In accordance with the small crystal field splitting we treat the four nearest neighbors of each atom as being equivalent. Hence the local environment is taken to be tetrahedral (T_d symmetry group) instead of C_{3v} . The influence of spin-orbit coupling and crystal field splitting on the single-particle states in InN QDs will be addressed in detail in Section 10.1.4.

In contrast to a zinc blende structure with two atoms per unit cell, the wurtzite unit cell contains four atoms, two anions and two cations. According to the discussion of Section 3.1, the electronic properties of the pure bulk materials are given by a 16×16 matrix $\underline{\mathbf{H}}^{\text{bulk}}(\mathbf{k})$ for each point in \mathbf{k} space, with the basis states $|\mathbf{k}\rangle$ [166]. This matrix

is explicitly given by

$$\underline{\underline{\mathbf{H}}}^{\text{bulk}}(\mathbf{k}) = \begin{pmatrix} \underline{\underline{\mathbf{E}_A}} & \underline{\underline{\mathbf{0}}} & \underline{\underline{\mathbf{M}_{1,3}}} & \underline{\underline{\mathbf{M}_{1,4}}} \\ \underline{\underline{\mathbf{0}}} & \underline{\underline{\mathbf{E}_A}} & \underline{\underline{\mathbf{M}_{1,4}}} & \underline{\underline{\mathbf{M}_{2,4}}} \\ \underline{\underline{\mathbf{M}_{1,3}^\dagger}} & \underline{\underline{\mathbf{M}_{1,4}^\dagger}} & \underline{\underline{\mathbf{E}_C}} & \underline{\underline{\mathbf{0}}} \\ \underline{\underline{\mathbf{M}_{1,4}^\dagger}} & \underline{\underline{\mathbf{M}_{2,4}^\dagger}} & \underline{\underline{\mathbf{0}}} & \underline{\underline{\mathbf{E}_C}} \end{pmatrix}. \quad (9.6)$$

Each element of the Hamiltonian matrix $\underline{\underline{\mathbf{H}}}^{\text{bulk}}(\mathbf{k})$ is a 4×4 matrix. The on-site matrices $\underline{\underline{\mathbf{E}_\alpha}}$ are given by

$$\underline{\underline{\mathbf{E}_\alpha}} = \begin{pmatrix} & |s, \alpha\rangle & |p_x, \alpha\rangle & |p_y, \alpha\rangle & |p_z, \alpha\rangle \\ \langle s, \alpha| & E_{s,s}^\alpha & 0 & 0 & 0 \\ \langle p_x, \alpha| & 0 & E_{p,p}^\alpha & 0 & 0 \\ \langle p_y, \alpha| & 0 & 0 & E_{p,p}^\alpha & 0 \\ \langle p_z, \alpha| & 0 & 0 & 0 & E_{p,p}^\alpha \end{pmatrix}, \quad (9.7)$$

where α denotes anions ($\alpha = A$) or cations ($\alpha = C$). The off-site matrices $\underline{\underline{\mathbf{M}_{i,j}^{\alpha,\beta}}}$ describe the coupling between the atom α and β located at positions i and j . According to the notation in Eq. (9.2), the anions are denoted by 1 and 2, while the cations are indicated by 3 and 4. The resulting matrices are given by

$$\begin{aligned} \underline{\underline{\mathbf{M}_{1,3}^{AC}}} &= F_1 \underline{\underline{\mathbf{m}_{1,3}^{AC}}}, \\ \underline{\underline{\mathbf{M}_{1,4}^{AC}}} &= F_2 \underline{\underline{\mathbf{m}_{1,4}^{AC}}}, \\ \underline{\underline{\mathbf{M}_{2,4}^{AC}}} &= F_3 \underline{\underline{\mathbf{m}_{2,4}^{AC}}}, \end{aligned}$$

with

$$F_1 = e^{-i\frac{k_x a}{3}} e^{i\frac{k_y a}{3}} e^{i\frac{k_z c}{8}}, \quad F_2 = e^{-i\frac{3k_z c}{8}}, \quad F_3 = e^{i\frac{k_x a}{3}} e^{-i\frac{k_y a}{3}} e^{i\frac{k_z c}{8}},$$

and

$$\underline{\underline{\mathbf{m}_{1,3}^{AC}}} = \begin{pmatrix} & |s, 3\rangle & |p_x, 3\rangle & |p_y, 3\rangle & |p_z, 3\rangle \\ \langle s, 1| & p_0 w_{s,s} & p_1 w_{s,x} & \frac{\sqrt{3}}{2} p_2 w_{s,x} & p_0 w_{s,z} \\ \langle p_x, 1| & p_1 w_{xs} & p_1 w_{xx} + \frac{3}{4} p_3 [w_{xx} + w_{yy}] & -\frac{\sqrt{3}}{4} p_2 [w_{xx} - w_{yy}] & p_1 w_{xz} \\ \langle p_y, 1| & \frac{\sqrt{3}}{2} p_2 w_{xs} & -\frac{\sqrt{3}}{4} p_2 [w_{xx} - w_{yy}] & p_1 w_{yy} + \frac{3}{4} p_3 [w_{xx} + w_{yy}] & \frac{\sqrt{3}}{2} p_2 w_{xz} \\ \langle p_z, 1| & p_0 w_{z,s} & p_1 w_{z,x} & \frac{\sqrt{3}}{2} p_2 w_{z,x} & p_0 w_{zz} \end{pmatrix},$$

$$\underline{\underline{\mathbf{m}_{1,4}^{AC}}} = \left(\begin{array}{c|cccc} & |s, 4\rangle & |p_x, 4\rangle & |p_y, 4\rangle & |p_z, 4\rangle \\ \hline \langle s, 1| & W_{ss} & 0 & 0 & W_{sz} \\ \langle p_x, 1| & 0 & W_{xx} & 0 & 0 \\ \langle p_y, 1| & 0 & 0 & W_{xx} & 0 \\ \langle p_z, 1| & W_{zs} & 0 & 0 & W_{zz} \end{array} \right),$$

$$\underline{\underline{\mathbf{m}_{2,4}^{AC}}} = \left(\begin{array}{c|cccc} & |s, 4\rangle & |p_x, 4\rangle & |p_y, 4\rangle & |p_z, 4\rangle \\ \hline \langle s, 2| & p_0^* w_{s,s} & -p_1^* w_{s,x} & -\frac{\sqrt{3}}{2} p_2^* w_{s,x} & p_0^* w_{s,z} \\ \langle p_x, 2| & -p_1^* w_{xs} & p_1^* w_{xx} + \frac{3}{4} p_3^* [w_{xx} + w_{yy}] & -\frac{\sqrt{3}}{4} p_2^* [w_{xx} - w_{yy}] & -p_1^* w_{xz} \\ \langle p_y, 2| & -\frac{\sqrt{3}}{2} p_2^* w_{xs} & -\frac{\sqrt{3}}{4} p_2^* [w_{xx} - w_{yy}] & p_1^* w_{yy} + \frac{3}{4} p_3^* [w_{xx} + w_{yy}] & -\frac{\sqrt{3}}{2} p_2^* w_{xz} \\ \langle p_z, 2| & p_0^* w_{z,s} & -p_1^* w_{z,x} & -\frac{\sqrt{3}}{2} p_2^* w_{z,x} & p_0^* w_{zz} \end{array} \right).$$

The different coefficients $p_i(\mathbf{k})$ read

$$\begin{aligned} p_0(\mathbf{k}) &= 1 + e^{ik_x a} + e^{-ik_y a} \quad , \quad p_1(\mathbf{k}) = e^{ik_x a} - \frac{1}{2} - \frac{1}{2} e^{-ik_y a} \\ p_2(\mathbf{k}) &= 1 - e^{-ik_y a} \quad , \quad p_3(\mathbf{k}) = 1 + e^{-ik_y a} \quad , \end{aligned}$$

where wave vector \mathbf{k} is here:

$$\mathbf{k} = k_1 \mathbf{b}_1 + k_2 \mathbf{b}_2 + k_3 \mathbf{b}_3 . \quad (9.8)$$

The reciprocal-lattice vectors are given by

$$\mathbf{b}_1 = \frac{2\pi}{a} \left(\frac{2}{\sqrt{3}}, 0, 0 \right), \quad \mathbf{b}_2 = \frac{2\pi}{a} \left(\frac{1}{\sqrt{3}}, 1, 0 \right), \quad \mathbf{b}_3 = \frac{2\pi}{c} (0, 0, 1) .$$

Furthermore, we apply the approximation that the local environment is tetrahedral to the off-diagonal elements. This corresponds to treating the four nearest-neighbor atoms equivalent. Therefore, the different tight-binding parameters W in $\underline{\underline{\mathbf{m}_{1,4}^{AC}}}$ and w in $\underline{\underline{\mathbf{m}_{2,4}^{AC}}}$ and $\underline{\underline{\mathbf{m}_{1,3}^{AC}}}$, are not independent. The relationship between the off-diagonal matrix elements of wurtzite (W 's and w 's), those of zinc blende [120] and the standard notation of Slater and Koster [47] are given in Table B.5 of Appendix B, which can also be found in Ref. [166]. From the relation between the different matrix elements one can deduce five independent parameters. Furthermore, one has to consider the four on-site terms $E_{s,s}^\alpha$ and $E_{p,p}^\alpha$, where α denotes anions or cations. Therefore, we are left with nine independent TB parameters. These parameters are empirically determined in such a way that the band gap and the energetic positions of other bands of the wurtzite bulk band structure [131, 167, 168] are reproduced at the Γ point. The resulting TB band structures are depicted in Figure 9.4 and the parameters are given in Table B.4 of Appendix B. Comparing with the literature [167, 168], the complicated valence band

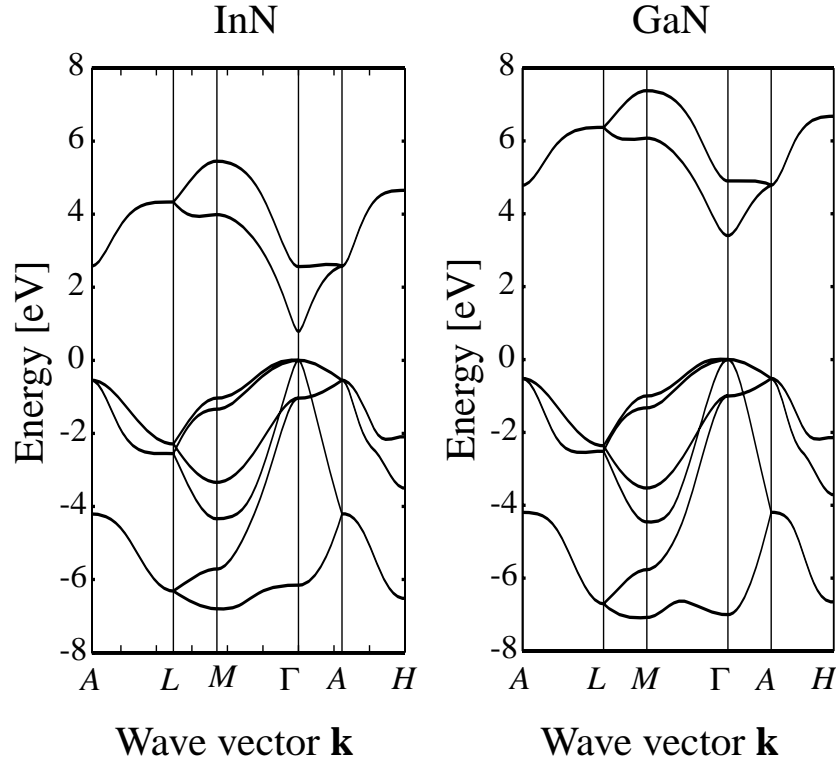


Figure 9.4: Tight-binding band structure for bulk InN and GaN. The corresponding tight-binding parameters for each material are given in Table B.4.

structure is extremely well reproduced over the whole Brillouin zone, and the s -like conduction band is accurate in the vicinity of the Γ point. For the GaN we obtain effective electron masses along the z axis of $m_{\parallel} = 0.259 m_0$ and along the x axis of $m_{\perp} = 0.256 m_0$. These values are in good agreement with the ones experimentally observed by Kasic *et al.* [169] namely $m_{\parallel} = (0.228 \pm 0.008) m_0$ and $m_{\perp} = (0.237 \pm 0.006) m_0$. For InN, we obtain an isotropic effective mass $m = m_{\parallel} = m_{\perp} = 0.069 m_0$. This value is in excellent agreement with the literature value of $m = 0.07 m_0$ [131, 170]. In principle, the conduction band structure can be improved by taking into account more basis states per unit cell [171]. However, for the discussion of the optical properties of the investigated materials, an appropriate description of the electronic structure in the region near the Γ point is sufficient. Therefore, the sp^3 TB model is adequate for our purposes, namely the calculation of optical properties for InN/GaN QDs.

10 Results for InN/GaN Quantum Dots

This chapter is dedicated to the investigation of electronic and optical properties of lens-shaped InN/GaN QDs with an underlying wurtzite structure. In Section 10.1 we will turn our attention to the single-particle states and energies of these QDs. Section 10.2 deals with the optical properties, in particular, the multi-exciton spectra of the InN nanostructures.

10.1 Single-Particle Properties

In the following sections the size dependence of the electronic properties of lens-shaped InN/GaN QDs is investigated in the framework of an empirical TB model with a sp^3 basis. The influence of the strong electrostatic built-in field on single-particle states and energies is discussed. Also the impact of the small crystal field splitting and the spin-orbit contribution is addressed.

10.1.1 Quantum Dot Geometry and Strain

Starting from the bulk TB parameters, the QD is modeled on an atomistic level. As described in detail in Section 3.2, the i th TB wave function $\psi_i(\mathbf{r})$ can be expressed in terms of the localized orbitals $\phi_{\alpha\mathbf{R}}(\mathbf{r}) = \langle \mathbf{r} | \alpha, \mathbf{R} \rangle$ at lattice site \mathbf{R} with the TB coefficients $c_{\mathbf{R}\alpha}^i$,

$$\psi_i(\mathbf{r}) = \sum_{\mathbf{R}\alpha} c_{\mathbf{R}\alpha}^i \phi_{\alpha\mathbf{R}}(\mathbf{r}) . \quad (10.1)$$

The Schrödinger equation leads to a matrix eigenvalue problem with finite dimension,

$$\sum_{\mathbf{R}\alpha} \langle \alpha' \mathbf{R}' | H | \alpha, \mathbf{R} \rangle c_{\mathbf{R}\alpha}^i - E^i c_{\mathbf{R}'\alpha'}^i = 0 , \quad (10.2)$$

where E^i is the corresponding energy eigenvalue. For the matrix elements $\langle \alpha' \mathbf{R}' | H | \alpha, \mathbf{R} \rangle$ we use the TB parameters of the bulk materials, which are given in Appendix B. We apply the sp^3 TB model introduced in Section 9.4, which neglects small contributions from crystal field splitting and spin-orbit interaction. The influence of these effects will be discussed in Section 10.1.4.

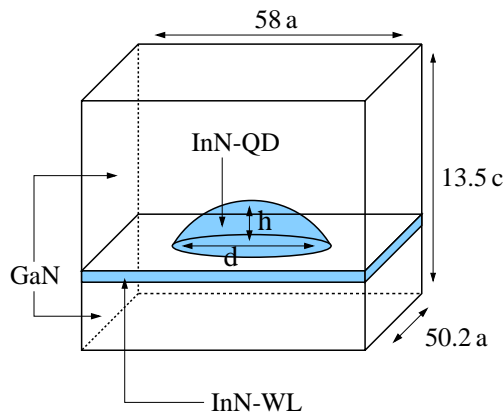


Figure 10.1: Illustration of the finite-size supercell in which the QD geometry is modeled. The investigated lens-shaped InN QDs reside on an InN wetting layer (WL) and have circular symmetry around the z axis. The InN QD-WL system is embedded in a GaN matrix.

To model an InN QD embedded in a GaN matrix, a wurtzite lattice inside a large cell with fixed boundary conditions is chosen. However, a sufficiently large supercell is required in order to avoid numerical artifacts in the localized QD states, especially artifacts due to the cubic symmetry of the boundaries. Surface effects in the finite-size supercell are removed according to Refs. [53,172]: The orbital energies and the hopping matrix elements of the surface atoms are raised to eliminate all nonphysical surface states. The parameters for each site are set according to the occupying atoms (N, In, Ga) in the InN/GaN heterostructure. At the InN/GaN interfaces averages of the TB parameters are used to take into account that the nitrogen atoms cannot unambiguously be attributed to the InN or the GaN material, respectively. The valence band offset ΔE between the two materials (InN and GaN) is included in our model by shifting the diagonal matrix elements of the bulk InN. In the past, several different values for the InN/GaN valence band offset have been reported. The theoretically calculated values, e.g. 0.3 eV (Ref. [59]) and 0.48 eV (Ref. [57]), are relatively small compared to the experimentally obtained ones of (1.05 ± 0.25) eV (Ref. [173]) or (1.26 ± 0.23) eV (Ref. [174]). A detailed discussion of this issue is given by Vurgaftman *et al.* in Ref. [131]. We choose a valence band offset of $\Delta E = 0.5$ eV, as recommended by Vurgaftman *et al.* A different value would affect the strengths of the confinement potentials for electrons and holes inside the QD structure. As a consequence the QD states might be slightly shifted in energy. However, no qualitative changes of our results are expected since only well localized states are investigated here.

We consider lens-shaped InN QDs, grown in (0001)-direction on top of an InN wetting layer (WL). The embedded QD-WL system is schematically shown in Figure 10.1. For the WL we assume a thickness of one lattice constant c . The rotational symmetry of the QD system around the z axis preserves the intrinsic C_{3v} symmetry of the underlying wurtzite crystal¹, which is important for the discussion of one-particle properties

¹ The C_{6v} symmetry of the bulk system is spoiled by the QD geometry.

and Coulomb correlations. Therefore, the symmetry group of the QD system under consideration, is different to comparable QD systems with a underlying zinc blende lattice [136]. Since inversion is not a symmetry operation for typical self-assembled QD structures, in the case of a zinc blende QD the overall system symmetry is reduced to a C_{2v} symmetry. This reduction in symmetry results in an additional splitting of otherwise degenerate one-particle energy levels, as already discussed in Part II.

In order to give a representative overview of one-particle and excitonic (optical) properties, we study three different QD sizes with diameters $d = 4.5, 5.7, 7.7$ nm and heights $h = 1.6, 2.3, 3.0$ nm, respectively. For all three QD sizes a supercell with the dimension $58a \times 50.2a \times 13.5c$ (188 181 atoms) is used in our calculations to reach convergence for the localized QD states.

The lattice mismatch between InN and GaN leads to the occurrence of a strain field in the heterostructure. This field modifies the conduction- and valence-band edge of the InN QD. Fonseca *et al.* [175] compared the electronic structure of coupled InAs/GaAs QDs for the case when the strain field is included from a microscopic calculation with the case when the strain field is modeled by a constant band-edge shift. The results for the bound electron states with inclusion of the exact strain field do not significantly differ from the results obtained with a constant band shift. However, the influence of the strain effects on the valence-band structure is more complicated. For example, in the well-studied zinc blende structure, the possible splitting of light- and heavy-hole bands depends on the sign and magnitude of the biaxial strain [176], and will therefore vary from system to system. In the present part of this thesis, we deal with an InN QD with an underlying wurtzite crystal structure for which comparable studies are rare. For this reason, we compare the bound single-particle wave functions obtained from our TB model with those of $\mathbf{k} \cdot \mathbf{p}$ calculations performed by Andreev *et al.* [70] and Fonoberov *et al.* [72] for similar QD systems (truncated hexagonal pyramidal GaN/AlN QDs), including the strain on a microscopic level. As we will discuss in Section 10.1.3, the results agree very well. Therefore, only slight changes of the one-particle states and energy levels are expected from an additional microscopic inclusion of strain effects in our model. Since we are interested in more general aspects, we neglect the influence of strain-induced displacements from the ideal atom positions. For the chosen QD geometry strain-induced displacements do not change the symmetry of the system so that our general statements (based on symmetry arguments [70]) should also hold if strain effects were more realistically included. Here we take into account only the strain-induced piezoelectric field in the structure, as described in the following section.

10.1.2 The Electrostatic Built-In Field

For the nitride-based heterostructures the electrostatic built-in field plays an important role and can significantly modify the electronic structure as well as the optical properties. In contrast to cubic III-V semiconductor heterostructures, based on InAs or GaAs, the III-V nitrides exhibit considerably larger electrostatic built-in fields for

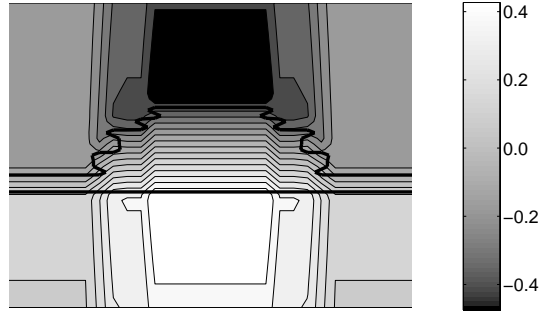


Figure 10.2: Contour plot of the electrostatic potential energy V_p . A slice in the x - z plane through the center of the QD is depicted. The result is shown for the smallest QD but is qualitatively the same for all the investigated QD sizes.

several reasons [162]. First of all the shape of the unit cell in InN and GaN differs slightly from the ideal symmetry in the wurtzite structure. Following the discussion of Section 9.3, this small aberration causes a polarization, which is referred to as the spontaneous polarization $\mathbf{P}^{\text{spont}}$. Additionally, the strain-induced piezoelectric polarization $\mathbf{P}^{\text{piezo}}$ occurs that is quite strong in InN/GaN heterostructures, compared to, e.g., cubic GaAs-based structures. Being different as for the zinc blende structure the piezoelectric tensor of the wurtzite structure has three nonvanishing independent components [177], which are several times larger than the values for other group-III-V binary compounds, and which determine the magnitude of the piezoelectric field [162].

To include these effects in our TB approach, we calculate the potential, $V_p(\mathbf{r})$, induced by the electrostatic polarizations as outlined in the following. We start from the Maxwell equation $\text{div } \mathbf{D} = \mathbf{0}$ for the displacement field \mathbf{D} , which is defined by

$$\mathbf{D} = \epsilon_0 \epsilon_r \mathbf{E} + (\mathbf{P}^{\text{spont}} + \mathbf{P}^{\text{piezo}}) = \epsilon_0 \epsilon_r \mathbf{E} + \mathbf{P}, \quad (10.3)$$

where ϵ_r is the dielectric constant, $\mathbf{P}^{\text{spont}}$ and $\mathbf{P}^{\text{piezo}}$ are the spontaneous and strain-induced polarization, respectively. The spontaneous polarization $\mathbf{P}^{\text{spont}}$ in the wurtzite crystal structure lies within growth direction: $\mathbf{P}^{\text{spont}} = P^{\text{spont}} \mathbf{e}_z$. The strain contribution $\mathbf{P}^{\text{piezo}}$ to the polarization \mathbf{P} is approximated as described in Ref. [178], $\mathbf{P}^{\text{piezo}} = P^{\text{piezo}} \mathbf{e}_z$, by

$$P^{\text{piezo}} = -2 \left(e_{33} \frac{C_{13}}{C_{33}} - e_{31} \right) \sigma_{\parallel}, \quad (10.4)$$

where e_{ij} denotes the different piezoelectric coefficients and C_{ij} the elastic constants. The (in-plane) lattice mismatch is given by σ_{\parallel} . The lattice, elastic, piezoelectric, and dielectric constants from Ref. [146] are used, as summarized in Table B.3 of Appendix B. For InN and GaN several different values have been reported for these material parameters in the literature. The relatively large variation is dominantly caused by the fact that it is difficult to grow sufficiently large bulk crystals [179, 180], and due to the different defect situation in every single sample. An overview and a discussion of the influence of different piezoelectric and elastic constants on the internal field of InN and GaN is given in Ref. [181]. In our calculations, a different value for the built-in

field would yield an overall shift in the one-particle energy levels, especially for the hole states. However, even with different values for the built-in field a similar qualitative behavior especially of the ordering of the one-particle states and its dependence on the QD size can be expected as it has already been observed for different material systems before [147]. For our chosen QD geometry, a more sophisticated inclusion of strain effects [142] will generate merely small lateral contributions to the piezoelectric field [84], which are therefore neglected in the following. Furthermore, the small thermal strain contribution is neglected [178, 182]. From the knowledge of the polarization \mathbf{P} the charge density ρ_p and the electrostatic potential ϕ_p can be obtained from the Poisson equation,

$$\operatorname{div} \mathbf{P} = -\rho_p . \quad (10.5)$$

Assuming only small contributions from image charges, the electrostatic potential ϕ_p is given by

$$\Delta \phi_p = -\frac{1}{\epsilon_0 \epsilon_r} \rho_p . \quad (10.6)$$

The resulting electrostatic potential is included in the TB model as a site-diagonal potential energy $V_p(\mathbf{r}) = -e_0 \phi_p(\mathbf{r})$. A schematic illustration of this procedure is given in Figure 3.2 on page 25. This method has been successfully applied to quantum well [83] and QD [84] structures before. With the electrostatic energy V_p , a rough estimate for the electrostatic field strength of about 5.5 MV/cm inside the QD can be obtained from a simple capacitor model.

A contour plot of the electrostatic potential energy V_p is shown in Figure 10.2 for the smallest QD. A representative picture is given because the potential inside the QD looks qualitatively the same for all the investigated QD sizes. Outside the QD, a typical dependence of the potential is reproduced as known from QW systems. To reach convergence, the calculation of the built-in field, according to Eqs. (10.5) and (10.6), is performed on a much larger area surrounding the QD-WL structure, so that the field vanishes at the supercell boundaries in z direction.

After having introduced the essential ingredients of our polarization-dependent sp^3 TB model, we will analyze the electronic structure of lens-shaped InN/GaN QDs with a wurtzite structure in the following section.

10.1.3 Single-Particle States and Energies

Figure 10.3 shows the QD geometry and the first three bound one-particle states for the largest QD for electrons and holes, respectively, including the influence of the built-in field from atop. For each state the atomic orbital character of the TB wave functions is given where the dominant contributions are highlighted. According to their nodal structure, the depicted electron states $\psi_{1,2,3}^e$ can be classified as s - and p -like states. This classification is not possible for the hole states; these states underly strong band

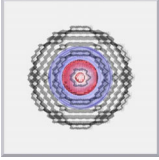
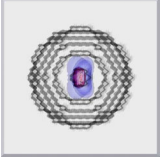
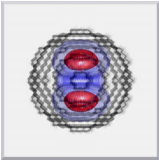
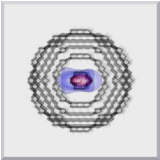
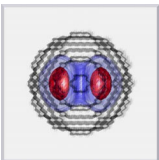
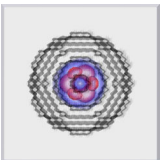
electrons	holes
$E_1^e = 1.4770\text{eV}$  $p_x : 0.044$ $p_y : 0.044$ $p_z : 0.165$ $s : \mathbf{0.747}$	$E_1^h = 0.9021\text{eV}$  $p_x : 0.162$ $p_y : \mathbf{0.820}$ $p_z : 0.012$ $s : 0.006$
$E_2^e = 1.6660\text{eV}$  $p_x : 0.039$ $p_y : 0.134$ $p_z : 0.122$ $s : \mathbf{0.706}$	$E_2^h = 0.9021\text{eV}$  $p_x : \mathbf{0.820}$ $p_y : 0.162$ $p_z : 0.012$ $s : 0.006$
$E_3^e = 1.6660\text{eV}$  $p_x : 0.134$ $p_y : 0.039$ $p_z : 0.122$ $s : \mathbf{0.706}$	$E_3^h = 0.8964\text{eV}$  $p_x : \mathbf{0.499}$ $p_y : \mathbf{0.499}$ $p_z : 0.001$ $s : 0.000$

Figure 10.3: The QD geometry is shown for the largest QD from atop. The structure is visualized and isosurfaces of the probability density for the three lowest electron (left) and hole (right) states with built-in field are included for 10 % (blue) and 50 % (red) of the maximum value. The atomistic structure and the C_{3v} symmetry of the wurtzite crystal becomes most apparent for the hole states. The corresponding energies ($E_{1,2,3}^{e,h}$) of electron and hole states, measured from the valence band maximum of bulk GaN, and the atomic orbital character for each wave function are given. The dominant contributions are highlighted.

mixing effects. Whereas only one of the p -like valence bands may contribute to the formation of the bound states in the case of QW systems [140], at least two atomic p states contribute to the formation of the QD hole states. Therefore the assumption of a single heavy-hole valence band for the description of the bound hole states in a QD even qualitatively yields incorrect results. The observation of strong band-mixing effects for the bound hole states is in agreement with results from other multi-band approaches [57, 72]. The single-particle states obtained from our TB treatment agree qualitatively very well with recent $\mathbf{k} \cdot \mathbf{p}$ calculations for truncated hexagonal pyramidal GaN/AlN QDs with a wurtzite structure [70, 72], although the strain is modeled on a microscopic level in these references. Therefore, we expect that our general statements, based on symmetry arguments, should also hold if strain effects are microscopically included in our model.

According to their degeneracy and their transformation properties under rotation by $2\pi/3$, electron as well as hole states are classified as s and p states. The two energetically degenerate states are denoted as p states, because these states transform under the action of the elements of the group C_{3v} like x and y , respectively. The non-degenerate state is invariant under a rotation by $2\pi/3$ and therefore has the properties of an s

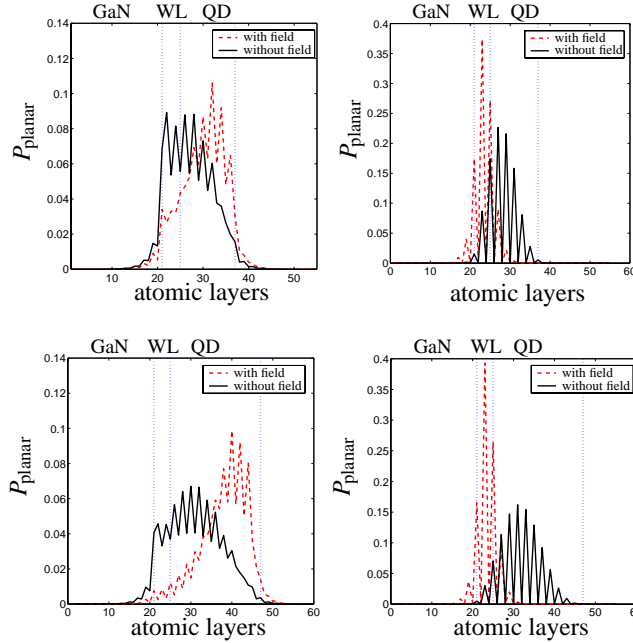


Figure 10.4: Planar-integrated probability density $P_{\text{planar}}(z)$ for the electron (left) and the hole (right) ground state, in the absence (solid lines) and in the presence (dashed lines) of the built-in field for the smallest (top) and the largest (bottom) QD.

state. As already discussed in Section 4.1, the (single) group C_{3v} is a non-abelian one. Therefore, and in contrast to the group C_{2v} of a lens-shaped QD with an underlying zinc blende structure, degeneracies in the energy spectrum could be expected in a system with a wurtzite structure. For convenience, we choose real-valued wave functions $\psi_{p_x, y}$ for the two degenerate p states of electrons and holes, respectively. However, by choosing appropriate linear combinations $\psi_{p_{\pm}} = \mp \frac{1}{\sqrt{2}}(\psi_{p_x} \pm i\psi_{p_y})$ they can be transformed into states which have the following properties under rotation by $2\pi/3$ around the z axis: $R_{\frac{2\pi}{3}}\psi_{p_{\pm}} = e^{\pm i\frac{2\pi}{3}}\psi_{p_{\pm}}$, according to the system symmetry. These states are complex-valued but are favorable for the discussion of certain properties of the Coulomb matrix elements [30, 116] as done in Section 10.2.2.

With inclusion of the built-in field, the electron states are squeezed into the cap of the QD, while the hole states are constraint to a few atomic layers at the bottom, near the wetting layer. This is illustrated in Figure 10.4 for the planar-integrated electron and hole ground state probability density $P_{\text{planar}}(z) = \sum_{i,j} |\psi(x_i, y_j, z)|^2$ in the smallest and in the largest QD. The influence of the electrostatic field on the one-particle densities is much more pronounced for the larger QD. In this case a clear spatial separation of electron and hole probability densities is observed, which lowers the direct spatial overlap of electron and hole wave functions and leads to reduced dipole matrix elements, compared to the results without built-in field. Besides the influence on the oscillator strength, the additional confinement of the electrons into the cap of the QD increases the electronic Coulomb matrix elements.

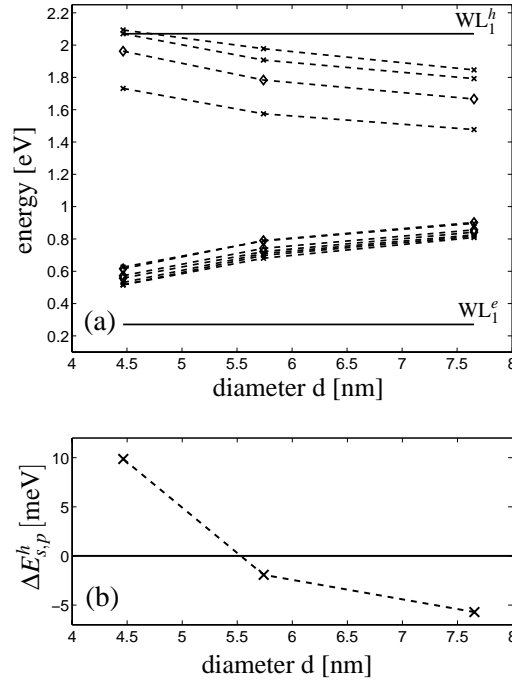


Figure 10.5: (a) The first five electron and 10 hole one-particle energy levels are shown for the three investigated QDs with increasing diameter from left to right. Results are given in the presence of the built-in field. As a consequence of the stronger quantum confinement of the carriers inside the QD structure for decreasing size, a clear blue-shift of the effective gap energy is observed. (b) The energy splitting $\Delta E_{s,p}^h = E_s^h - E_p^h$ between the s and the p shell for the holes is depicted. The splitting is positive for the smallest QD and changes sign with increasing QD diameter d , as a level reordering occurs for larger QDs. The dashed lines are included as a guide to the eye.

The dependence of the energy spectrum on the QD size for the first five electron and first 10 hole one-particle states, including the built-in field, is shown in Figure 10.5(a). All energies are measured relative to the valence-band maximum of GaN. The energies are compared with the ground state energies for electrons and holes in an InN-WL (WL_1^e and WL_1^h , respectively) of one lattice constant c thickness, which is calculated separately for the WL without the QD. As expected from a naive particle-in-a-box picture, the binding of the electrons and holes in the QD becomes stronger when the QD size is increased. For the intermediate and the largest QD, the hole ground state is formed by the twofold degenerate p states ψ_1^h and ψ_2^h . This behavior is interchanged with decreasing QD size where, for the smallest QD, the s state ψ_3^h becomes the hole ground state. This energy level-crossing with changing QD size is illustrated in terms of the energy eigenvalues in Figure 10.5(b) and has also been reported before for other QD systems [147]. To concentrate on the level crossing of the first three bound hole states, Figure 10.5(b) displays the energy splitting $\Delta E_{s,p}^h = E_s^h - E_p^h$ between the s and the p shell for the holes. The splitting is positive for the smallest QD and changes sign with increasing QD diameter d .

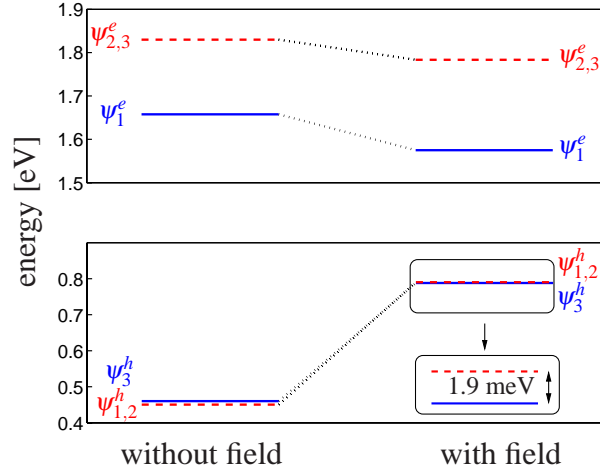


Figure 10.6: For the intermediate QD, the influence of the built-in field on the hole-state ordering is demonstrated. In the absence of the electrostatic field, the hole ground state is built by a single s -like state (solid line), whereas in the presence of the field the twofold degenerate p state (dashed line) constitutes the ground state for the holes. The dotted lines are included as a guide to the eye.

To investigate the influence of the built-in field, we compare the energies of the first three bound electron ($\psi_1^e, \psi_{2,3}^e$) and hole states ($\psi_{1,2}^h, \psi_3^h$) with and without the electrostatic field. The results for the intermediate QD size are shown in Figure 10.6. First of all, the electrostatic field shifts the electron single-particle states to lower energies, whereas the hole states are shifted to higher energies. Consequently, the built-in field leads to an overall red-shift in the single-particle energy gap. Furthermore, the electrostatic field affects the ordering of the first three bound hole states. Without the electrostatic field the hole ground state is the non-degenerate state ψ_3^h as for the largest QD in Figure 10.3. The first two excited states ψ_1^h and ψ_2^h are degenerate. The electrostatic field interchanges the ordering of the states ψ_3^h and $\psi_{1,2}^h$. In this case the hole ground state is twofold degenerate. For clarity, the splitting of 1.9 meV between ground and first excited state is displayed in the inset of Figure 10.6. The ordering of the lowest hole states has strong implications for the ground state dipole selection rules and therefore for the optical properties of the system and will be discussed in detail in Section 10.2.

10.1.4 Influence of Crystal Field Splitting and Spin-Orbit Coupling

So far we have neglected the influence of the crystal field splitting and the spin-orbit coupling. In this section we introduce these two contributions in our TB approach and investigate their effect on the single-particle states and energies.

The spin-orbit coupling is introduced as outlined in Section 3.1.1. Due to the high ionicity of the bonds in the nitride system [183], the valence band structure is dominated by the anion contributions. Therefore we introduce the spin-orbit coupling only at

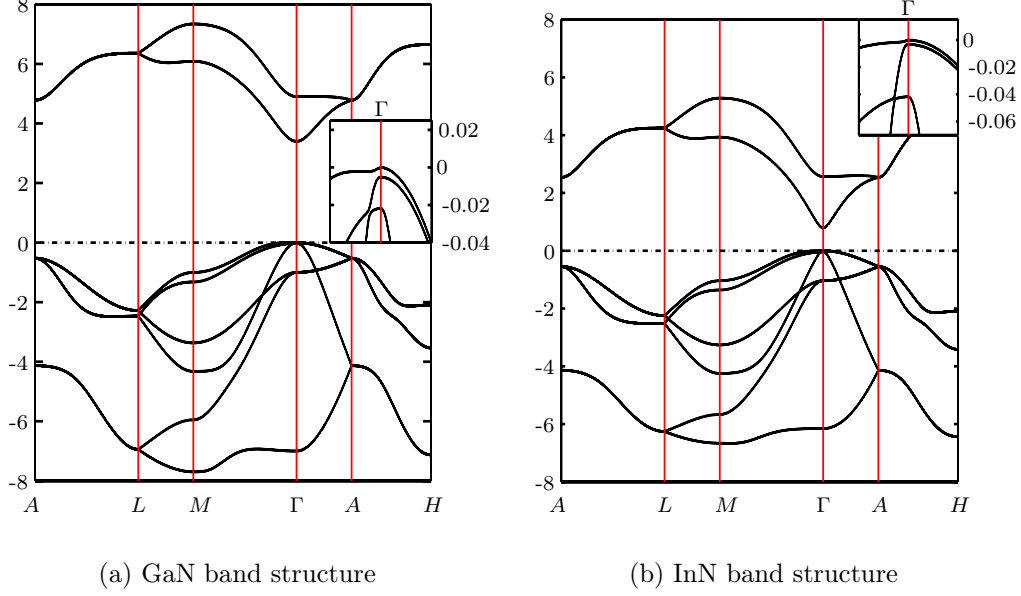


Figure 10.7: Wurtzite bulk band structure of (a) InN and (b) GaN obtained using an sp^3 TB model including crystal field splitting and spin-orbit coupling. The insets show the valence band edge in the vicinity of the Γ point.

the anion sites. As discussed in Section 9.2, the small crystal field energy Δ_{cf} of the wurtzite crystal differentiates the p_z orbital from the p_x and p_y orbitals. Our TB model considers only nearest-neighbor hopping matrix elements, whilst the bulk crystal field splitting between the A and B valence bands, schematically shown in Figure 9.3 on page 84, cannot be reproduced unless third-nearest-neighbor interactions are taken into account [184]. To reproduce the $A - B$ splitting within the sp^3 basis with nearest-neighbor coupling, we introduce on the anion sites the additional parameter E_{p_z, p_z}^A for the coupling between the p_z orbitals. According to these refinements, the anion on-site matrix of Eq. (9.7) is now given by

$$\underline{\underline{\mathbf{E}_A}} = \begin{pmatrix} & |s, A, \uparrow\rangle & |p_x, A, \uparrow\rangle & |p_y, A, \uparrow\rangle & |p_z, A, \uparrow\rangle & |s, A, \downarrow\rangle & |p_x, A, \downarrow\rangle & |p_y, A, \downarrow\rangle & |p_z, A, \downarrow\rangle \\ \langle s, A, \uparrow | & E_{s,s}^A & 0 & 0 & 0 & 0 & 0 & 0 & 0 \\ \langle p_x, A, \uparrow | & 0 & E_{p,p}^A & -i\lambda & 0 & 0 & 0 & 0 & \lambda \\ \langle p_y, A, \uparrow | & 0 & i\lambda & E_{p,p}^A & 0 & 0 & 0 & 0 & -i\lambda \\ \langle p_z, A, \uparrow | & 0 & 0 & 0 & E_{p_z, p_z}^A & -\lambda & i\lambda & 0 & 0 \\ \langle s, A, \downarrow | & 0 & 0 & 0 & 0 & E_{s,s}^A & 0 & 0 & 0 \\ \langle p_x, A, \downarrow | & 0 & 0 & 0 & -\lambda & 0 & E_{p,p}^A & i\lambda & 0 \\ \langle p_y, A, \downarrow | & 0 & 0 & 0 & -i\lambda & 0 & -i\lambda & E_{p,p}^A & 0 \\ \langle p_z, A, \downarrow | & 0 & \lambda & i\lambda & 0 & 0 & 0 & 0 & E_{p_z, p_z}^A \end{pmatrix}.$$

With four atoms per unit cell, the procedure described in Section 9.4 results in a 32×32 Hamiltonian, depending on the different TB parameters. All TB parameters are re-optimized in such a way that the band gap and the energetic positions of other bands of the wurtzite bulk band structure [131, 167, 168] at the Γ point are reproduced.

	$\Delta_{\text{so}} = 0, \Delta_{\text{cf}} = 0$	$\Delta_{\text{so}} = 0, \Delta_{\text{cf}} \neq 0$	$\Delta_{\text{so}} \neq 0, \Delta_{\text{cf}} \neq 0$
E_1^e [eV]	1.5749	1.5562	1.5554
E_2^e [eV]	1.7836	1.7635	1.7607
E_3^e [eV]	1.7836	1.7635	1.7607
E_1^h [eV]	0.7901	0.7919	0.7874
E_2^h [eV]	0.7901	0.7919	0.7861
E_3^h [eV]	0.7882	0.7905	0.7839

Table 10.1: Single-particle energies for the intermediate InN QD in the presence and absence of crystal field splitting and spin-orbit coupling. Each of the given states is two-fold degenerate due to time reversal symmetry.

The additional matrix elements λ and E_{p_z, p_z}^A are adjusted to reproduce the splittings between the different valence bands (A , B and C bands), which are determined by Eq. 9.4. Table B.4 in Appendix B summarizes the different TB parameters. The corresponding bulk band structures of GaN and InN are shown in Figure 10.7. The insets depict the valence band structure in the vicinity of the Γ point. The complicated valence band structure is in very good agreement with other TB models [171].

After having determined the TB parameters one can once again calculate the single-particle states and energies of the three different QDs discussed in the preceding section. First we focus on the single-particle energies of the intermediate QD ($d = 5.7$ nm, $h = 2.3$ nm). In Table 10.1 the energies of the first three bound electron and hole states under the influence of the built-in field are displayed. In order to assess the impact of the crystal field splitting and spin-orbit coupling, we have performed our calculations in three steps. In a first step we neglect both spin-orbit interaction and crystal field effects ($\Delta_{\text{so}} = 0, \Delta_{\text{cf}} = 0$). In this case we are left with the sp^3 TB model discussed so far. In step two we introduce only the crystal field splitting ($\Delta_{\text{so}} = 0, \Delta_{\text{cf}} \neq 0$), by including the additional parameter E_{p_z, p_z}^A in the TB model. In the final step both terms are taken into account ($\Delta_{\text{so}} \neq 0, \Delta_{\text{cf}} \neq 0$). In each step the TB parameters are re-optimized in such a way that the band gap and the energetic positions of other bands of the wurtzite bulk band structure at the Γ point are reproduced.

From Table 10.1 we obtain that the electron states are only slightly shifted to lower energies by crystal field splitting and spin-orbit coupling. Without spin-orbit coupling ($\Delta_{\text{so}} = 0$), and taking only crystal field splitting into account, $\Delta_{\text{cf}} \neq 0$, the hole states are shifted to higher energies. With spin-orbit coupling the hole energy spectrum is shifted to lower energies, compared to the case neglecting both contributions ($\Delta_{\text{cf}} = 0, \Delta_{\text{so}} = 0$). Additionally it turns out that the degeneracy of the hole states h_1 and h_2 is lifted when spin-orbit coupling is considered. Of course, each state is still twofold degenerate due to time reversal symmetry. Because of the small spin-orbit energies of the bulk materials, the splitting is also rather small (≈ 1 meV). From the splitting of the hole states h_1 and h_2 , one can deduce that the spin-orbit interaction alters the

	$\{E\}$	$\{\bar{E}\}$	$\{2C_3\}$	$\{2\bar{C}_3\}$	$\{3\sigma_v\}$	$\{3\bar{\sigma}_v\}$
Γ_1	1	1	1	1	1	1
Γ_2	1	1	1	1	-1	-1
Γ_3	2	2	-1	-1	0	0
Γ_4	2	-2	1	-1	0	0
Γ_5	1	-1	-1	1	i	$-i$
Γ_6	1	-1	-1	1	$-i$	i

Table 10.2: Character table for the double group \bar{C}_{3v} [95].

symmetry of the system. How can this be understood? Without spin-orbit coupling, the symmetry of the system is determined by the *single* group C_{3v} , as discussed in the previous sections. Including spin-orbit coupling, one has to deal with the *double* group \bar{C}_{3v} . The character table of the double group is given in Table 10.2. This group allows only two dimensional representations, even if the time reversal symmetry is included [88]. Consequently, the electron p states (e_2 and e_3) are also no longer degenerate, but in this particular case the splitting is only of the order of some μeV , and therefore not visible in Table 10.1. These findings are in agreement with a recent $\mathbf{k} \cdot \mathbf{p}$ calculations for $\text{In}_x\text{Ga}_{1-x}\text{N}$ QDs [185].

A central result of the previous section was that the strong internal electrostatic field can reverse the energetic order of the first three bound hole states. We found that, for the intermediate and the largest InN QD, in the presence of the built-in field the ground state is formed by the twofold degenerate p states ψ_1^h and ψ_2^h shown in Figure 10.3. This behavior is interchanged with decreasing QD size, where, for the smallest QD, the s state ψ_3^h becomes the hole ground state. To concentrate on this change between the hole s and p shell, the energy splitting $\Delta E_{s,p}^h = E_s^h - E_p^h$ is once more displayed in Figure 10.8 (a). In order to analyze the impact of crystal field splitting and spin-orbit coupling on the ordering of the hole level structure, we calculated the splitting $\Delta E_{s,p}^h$ when both contributions are introduced in the TB approach. Since the hole p shell is no longer degenerate, we average over the single-particle energies of the states ψ_1^h and ψ_2^h . The energy splitting $\Delta E_{s,p}^h$ with spin-orbit coupling and crystal field splitting is shown in Figure 10.8 (b). From the comparison with Figure 10.8 (a), we find that these contributions have only a negligible effect on the energy splitting $\Delta E_{s,p}^h$. Furthermore, the ordering of the first three bound hole states is not influenced by spin-orbit coupling and crystal field splitting.

In summary, the crystal field splitting alone cannot alter the symmetry of the system and leads only to an energetic shift of the first three bound electron and hole states. The spin-orbit interaction, and only this contribution, can modify the symmetry and lifts certain degeneracies. However, the splitting of the electron and hole p shell due to the spin-orbit coupling is very small compared to the level spacing of the different

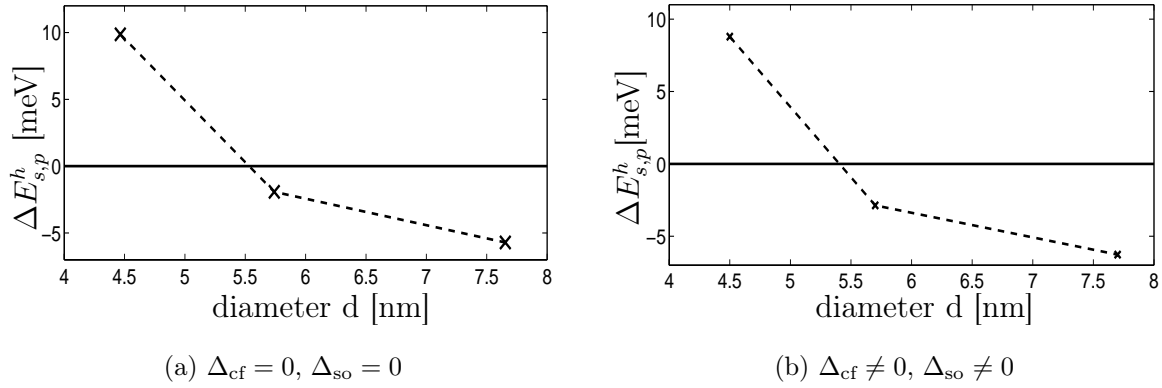


Figure 10.8: The energy splitting $\Delta E_{s,p}^h = E_s^h - E_p^h$ between the s and the p shell for the holes is shown in the absence (a) and presence (b) of crystal field Δ_{CF} and spin-orbit Δ_{so} splitting. In both cases $\Delta E_{s,p}^h$ changes sign with increasing QD diameter d , as a level reordering occurs (the dashed lines are included as a guide to the eye). The built-in field is included in the calculations.

shells. Moreover, in the presence of spin-orbit coupling and crystal field splitting, one obtains the same level ordering of the energetically lowest hole states, s - and p -shell, as in the case were these contributions are not taken into account. Therefore, it is well justified to neglect these small corrections of the crystal field splitting and the spin-orbit coupling in the following sections.

10.2 Many-Particle Properties

So far we discussed only single-particle properties, which apply strictly only for the first charge carrier occupying the dot. If more than one electron or hole is confined in the QD, the impact of the Coulomb interaction leads to distinct many-body states. In order to investigate the optical properties of semiconductor QDs, we introduce in Section 10.2.1 the many-body Hamiltonian that describes a system of interacting charge carriers. Furthermore, the basic idea of the so-called configuration interaction scheme is discussed, which enables the calculation of multi-exciton spectra. The subsequent Section 10.2.2 is dedicated to the calculation of Coulomb and dipole matrix elements from TB single-particle wave functions. These matrix elements are the essential ingredients to the many-body Hamiltonian. Results for the optical spectra based on the configuration interaction scheme are then discussed in the following sections: Excitonic emission and absorption spectra are presented in Section 10.2.3, and Section 10.2.4 deals with the emission spectrum of a QD initially filled with up to six excitons.

10.2.1 Many-Body Hamiltonian and Light-Matter Interaction

In this section we introduce the Hamiltonian H that describes a system of interacting charge carriers. The single-particle eigenstates and the corresponding eigenenergies, calculated in the previous chapter, can be used for a many-particle calculation that allows us to determine the multi-exciton spectra. The many-particle Hamiltonian H in second quantization is given by

$$H = \overbrace{\sum_i E_i^e c_i^\dagger c_i + \sum_i E_i^h h_i^\dagger h_i}^{H_0} \quad (10.7)$$

$$+ \underbrace{\frac{1}{2} \sum_{ijkl} V_{ijkl}^{ee} c_i^\dagger c_j^\dagger c_k c_l + \frac{1}{2} \sum_{ijkl} V_{ijkl}^{hh} h_i^\dagger h_j^\dagger h_k h_l - \sum_{ijkl} V_{ijkl}^{eh} h_i^\dagger e_j^\dagger e_k h_l}_{H_c} . \quad (10.8)$$

Here, creation and annihilation operators for electrons (holes) in the single-particle state $|i\rangle$ with energy $E_i^e(E_i^h)$ are denoted by $c_i^\dagger(h_i^\dagger)$ and $c_i(h_i)$, respectively. The first part H_0 , Eq. (10.7), is the non-interaction part, which contains information about the single-particle spectrum. $V_{ijkl}^{\lambda,\lambda'}$ denotes the different Coulomb matrix elements. The physical interpretation of the different terms in H_c , as given by Eq. (10.8), is the, electron-electron, hole-hole and electron-hole Coulomb interaction. Small contributions from so-called electron-hole exchange terms have been omitted [140]. The minus sign in the last term of Eq. (10.8) stems from the fact that electron and hole attract each other whereas the electron-electron and hole-hole interaction is repulsive.

If one considers only a finite number of bound single-particle states for the electrons and holes, the many-particle Hilbert space for a given number of electrons and holes has also finite dimension. Therefore, it can be solved without further approximations and the Coulomb interaction between all the different possible configurations of carriers in the considered bound states is fully taken into account. This approach is the so-called *configuration interaction* (CI) method. In order to find the eigenvalues and eigenfunctions of the interacting problem, the many-body Hamiltonian is expressed in terms of the uncorrelated many-particle basis and the resulting Hamiltonian matrix is diagonalized. This yields an expansion of the interacting eigenstates of the system for a given number of electrons and holes in terms of the uncorrelated many-body basis states. A detailed description of this approach is given in Refs [30, 150].

From the many-body states, the emission or absorption spectra between the interacting eigenstates of the QD system can be calculated using Fermi's golden rule [30]. For example the absorption intensity $I(\omega)$ is given by

$$I(\omega) = \frac{2\pi}{\hbar} |\langle \psi_f | H_d | \psi_i \rangle|^2 \delta(E_i - E_f - \hbar\omega) , \quad (10.9)$$

where the state $|\psi_i\rangle$ corresponds to the initial many-particle state with the energy E_i , while $|\psi_f\rangle$ denotes the final state with energy E_f . The light-matter interaction

Hamiltonian H_d in dipole approximation is given by

$$H_d = - \sum_{ij} \mathbf{E} \underbrace{\langle i | e \mathbf{r} | j \rangle}_{\mathbf{d}_{ij}} e_i h_j + h.c. , \quad (10.10)$$

where \mathbf{E} denotes the electric field at the position of the QD and e is the elementary charge. The matrix elements \mathbf{d}_{ij} between the single-particle states $|i\rangle$ and $|j\rangle$ are the so-called dipole matrix elements. Equation (10.10), implies that the optical field always creates or annihilates electron-hole pairs. Hence the initial and final states in Eq. (10.9) differ by exactly one electron-hole pair to yield a non-zero result. These processes correspond to the absorption and the emission of a photon, respectively.

For all practical applications the Coulomb $V_{ijkl}^{\lambda,\lambda'}$ and dipole matrix elements \mathbf{d}_{ij} between the single-particle wave functions are required. Therefore, the evaluation of these matrix elements will be the subject of the following section.

10.2.2 Matrix Elements

As emphasized above, an empirical TB model represents an atomistic approach to describe the electronic structure of low-dimensional heterostructures. However, explicit knowledge about a basis set of localized states (atomic orbitals) is not required for the calculation of one-particle energies and wave functions. Orthogonal empirical TB models are based upon a basis set of states well localized at the atomic sites of the crystal. Only the basic assumptions about these localized orbitals, i.e., symmetry, spatial orientation [47], and orthogonality, enter the TB Hamiltonian.

With the TB Hamiltonian one-particle states can be determined for electrons and holes which are localized in a semiconductor nanostructure. However, being interested in optical properties of the system, single-particle energies and wave functions are not sufficient. To study optical interband transitions, the calculation of dipole matrix elements between electron and hole wave functions and the calculation of Coulomb matrix elements is required. Besides the calculation of optical properties, the Coulomb matrix elements are of particular importance to study carrier-carrier [186] and carrier-phonon [187] scattering in InN/GaN QDs. For the calculation of these matrix elements one needs – in principle – the localized atomic basis states $\phi_{\alpha\mathbf{R}}(\mathbf{r})$ from which the one-particle eigenstates $\psi_i(\mathbf{r})$ are formed according to Eq. (10.1). In the following we describe how Coulomb and dipole matrix elements can be obtained within the empirical TB model.

Coulomb Matrix Elements

For the calculation of optical spectra, Coulomb matrix elements between the TB wave functions, Eq. (10.1), are required, which are given by

$$\begin{aligned}
 V_{ijkl} &= \sum_{\mathbf{R}_1 \mathbf{R}_2 \mathbf{R}_3 \mathbf{R}_4} \sum_{\alpha \beta \gamma \delta} c_{\mathbf{R}_1 \alpha}^{i*} c_{\mathbf{R}_2 \beta}^{j*} c_{\mathbf{R}_3 \gamma}^k c_{\mathbf{R}_4 \delta}^l \\
 &\cdot \int d^3 r d^3 r' V(\mathbf{r} - \mathbf{r}') \phi_{\alpha \mathbf{R}_1}^*(\mathbf{r}) \phi_{\beta \mathbf{R}_2}^*(\mathbf{r}') \phi_{\gamma \mathbf{R}_3}(\mathbf{r}') \phi_{\delta \mathbf{R}_4}(\mathbf{r}), \quad (10.11)
 \end{aligned}$$

with $V(\mathbf{r} - \mathbf{r}') = \frac{e_0^2}{4\pi\epsilon_0\epsilon_r|\mathbf{r} - \mathbf{r}'|}$,

where e_0 denotes the electron charge, ϵ_0 the vacuum dielectric constant, and ϵ_r the background dielectric constant of the semiconductor material. As the atomic orbitals $\phi_{\alpha \mathbf{R}}(\mathbf{r})$ are not explicitly known in an empirical TB treatment, we approximate these matrix elements by

$$V_{ijkl} = \sum_{\mathbf{R} \mathbf{R}'} \sum_{\alpha \beta} c_{\mathbf{R} \alpha}^{i*} c_{\mathbf{R}' \beta}^{j*} c_{\mathbf{R} \alpha}^k c_{\mathbf{R}' \beta}^l V(\mathbf{R} - \mathbf{R}'), \quad (10.12)$$

$$\text{with } V(\mathbf{R} - \mathbf{R}') = \frac{e_0^2}{4\pi\epsilon_0\epsilon_r|\mathbf{R} - \mathbf{R}'|} \quad \text{for } \mathbf{R} \neq \mathbf{R}'$$

$$\text{and } V(0) = \frac{1}{V_{uc}^2} \int_{uc} d^3 r d^3 r' \frac{e_0^2}{4\pi\epsilon_0\epsilon_r|\mathbf{r} - \mathbf{r}'|} \approx V_0. \quad (10.13)$$

The validity of the underlying approximations and assumptions is discussed in Appendix C. Physically this means that the variation of the Coulomb interaction is taken into account only on a larger length scale of the magnitude of lattice vectors but not within one unit cell, which is justified because of the long ranged, slowly varying behavior of the Coulomb interaction. For $|\mathbf{R} - \mathbf{R}'| = 0$ the evaluation of the integral in Eq. (10.13) can be done quasi-analytically by expansion of the Coulomb interaction in terms of spherical harmonics, following Ref. [188]. An approximation like this, leading to Eq. (10.12) is always applied in the frequently used effective-mass description of QDs, because only the spatial variation of the envelope function and no variation of the wave functions within an atomic unit cell is considered there. As shown in Appendix C, the approximations and assumptions leading to Eqs. (10.12) and (10.13) can be justified as long as $|\mathbf{R} - \mathbf{R}'|$ is larger than nearest-neighbor lattice vectors. Though the on-site and nearest-neighbor terms are absolutely the largest ones, their relative contribution to the double sum in Eq. (10.12) is less than 5%. Therefore, the possible errors in the true values of the nearest-neighbor terms are only of minor importance for the total matrix elements V_{ijkl} .

In our InN/GaN QD system under consideration, the bound states are almost completely localized inside the InN material. Therefore, in a good approximation we use the InN dielectric constant $\epsilon_r = 8.4$, taken from Ref. [146]. For the calculation of Coulomb matrix elements averaged lattice constants are used to determine $\mathbf{R} - \mathbf{R}'$ in

the whole structure, calculated from the unstrained InN and GaN lattice constants in Table B.3. Hence, we take into account that in the vicinity of the QD, where the wave functions are localized, the InN lattice structure is influenced by the surrounding GaN material and vice versa.

In the following, some basic results are summarized, regarding fundamental symmetry properties of the calculated Coulomb matrix elements. The discussion of Coulomb matrix elements is more convenient if the localized p states are chosen such that they are invariant under rotation by $2\pi/3$ up to a phase factor $\exp(i2\pi/3 \cdot m)$ as already introduced in Section 10.1.3. The integer m takes the values $m = \pm 1$ for the p states and $m = 0$ for the s state that is invariant under the rotation. For a system with full rotation invariance, as in an effective-mass approximation [30], the integer m represents the quantum number of the z component of the electronic angular momentum in each state. For our system a rotation by $2\pi/3$ transforms the Coulomb matrix elements according to

$$R_{2\pi/3}V_{ijkl} = e^{i(m_i+m_j-m_k-m_l)\frac{2\pi}{3}}V_{ijkl}. \quad (10.14)$$

As this rotation represents a symmetry operation for the chosen QD geometry and for the wurtzite lattice with discrete rotation invariance, the matrix elements must remain unchanged. Therefore the condition $(m_i + m_j - m_k - m_l) \bmod 3 = 0$ has to be fulfilled, otherwise the matrix element V_{ijkl} must vanish. This is different from the effective-mass approximation where, for circular QD geometry, each rotation is a valid symmetry transformation, and where the angular momentum conservation requires $m_i + m_j - m_k - m_l = 0$. Therefore, in our case all matrix elements with $(m_i + m_j - m_k - m_l) \bmod 3 = 0$ are, in principle, nonvanishing. However, the matrix elements that occur in addition to the result of the effective-mass approximation are small compared to the matrix elements that simply fulfill $m_i + m_j - m_k - m_l = 0$. They become even smaller for the larger QDs, where one is closer to the case of full rotation invariance, because the influence of the underlying crystal lattice becomes less important.

Although the influence of the discrete rotation invariance still allows energetic degeneracy in the p shell, differences compared to continuum-like models are found here on the level of Coulomb matrix elements between the localized states. Although this feature becomes less important for the larger QD, the aspects of band mixing, present in the multi-band formulation, remain equally important even for larger QDs. This becomes apparent in the next sections where the dipole matrix elements and selection rules are discussed in detail.

Dipole Matrix Elements

In general it is not a trivial task to incorporate electromagnetic fields into TB models, because one must pay attention that gauge invariance, conservation laws, and sum rules remain valid. In particular, in connection with the problem of lattice electrons in

Orbital α	In	Ga	N
s	$0.31 r^3 e^{-1.25r} Y_{00}$	$0.61 r^{2.7} e^{-1.35r} Y_{00}$	$6.13 r^1 e^{-1.95r} Y_{00}$
p_x	$0.31 r^3 e^{-1.25r} \frac{-1}{\sqrt{2}}(Y_{11} - Y_{1-1})$	$0.61 r^{2.7} e^{-1.35r} \frac{-1}{\sqrt{2}}(Y_{11} - Y_{1-1})$	$6.13 r^1 e^{-1.95r} \frac{-1}{\sqrt{2}}(Y_{11} - Y_{1-1})$
p_y	$0.31 r^3 e^{-1.25r} \frac{i}{\sqrt{2}}(Y_{11} + Y_{1-1})$	$0.61 r^{2.7} e^{-1.35r} \frac{i}{\sqrt{2}}(Y_{11} + Y_{1-1})$	$6.13 r^1 e^{-1.95r} \frac{i}{\sqrt{2}}(Y_{11} + Y_{1-1})$
p_z	$0.31 r^3 e^{-1.25r} Y_{10}$	$0.61 r^{2.7} e^{-1.35r} Y_{10}$	$6.13 r^1 e^{-1.95r} Y_{11}$

Table 10.3: Slater orbitals for In, Ga, and N atoms. The radial part of the wave functions is given by $R(r) = r^a e^{-br}$. The constants a and b are given by Slater's rules [189]. The angular part is given by the spherical harmonics $Y_{lm}(\varphi, \vartheta)$.

a magnetic field and the Peierls substitution [190, 191] it has been pointed out that a vector potential describing the magnetic field must be included via complex, position-dependent phase factors of the inter-site (hopping) TB matrix elements [192–196]. It has been emphasized [197] that this is the proper, unambiguous and gauge invariant way to incorporate arbitrary electromagnetic fields in the TB Hamiltonian. However, when studying weak optical fields with only a slight spatial dependence on the scale of lattice vectors, a description of the field only via a scalar potential is possible. Then at least in linear order in the field also the expansion of the matrix elements of the gauge invariant TB model leads to a coupling of the field via the dipole operator, as it is frequently used in standard effective-mass models of semiconductor physics (optics). Therefore, here we use this simplifying assumption, too. The task now is the calculation of the matrix elements of the dipole operator $e_0 \mathbf{r}$ with the TB wave functions, $\mathbf{d}_{ij}^{eh} = e_0 \langle \psi_i^e | \mathbf{r} | \psi_j^h \rangle$, which yield information about selection rules, allowed and forbidden transitions, and even relative peak heights, at least qualitatively [198].

Following the discussion of the preceding paragraph, for the calculation of optical spectra the dipole matrix elements between electron and hole wave functions are an essential ingredient. In contrast to the Coulomb matrix elements, the short-range contributions dominate the dipole matrix elements. This short-range, almost local, character of the dipole operator in real space is in accordance with the assumption of a weak \mathbf{k} dependence of the dipole matrix elements [42], which is commonly used in connection with effective-mass approaches [199]. Therefore, what turns out to be a good approximation for the Coulomb matrix elements, to neglect the precise structure of the localized orbitals, fails for the calculation of dipole matrix elements.

In accordance with the TB formulation, the position operator can be decomposed into two contributions [107, 198, 200]:

$$\mathbf{r} = \sum_{\mathbf{R}\alpha} |\mathbf{R}, \alpha\rangle \mathbf{R} \langle \mathbf{R}, \alpha| + \sum_{\mathbf{R}\alpha} \sum_{\mathbf{R}'\beta} |\mathbf{R}\alpha\rangle \langle \mathbf{R}\alpha | \tilde{\mathbf{r}} | \mathbf{R}'\beta\rangle \langle \mathbf{R}'\beta|. \quad (10.15)$$

Here, $\mathbf{R} = (X, Y, Z)$ and $\mathbf{R}' = (X', Y', Z')$ denote the discrete atomic positions and $\tilde{\mathbf{r}} = \mathbf{r} - \mathbf{R} = (\tilde{x}, \tilde{y}, \tilde{z})$ is the position within a unit cell relative to \mathbf{R} . The indices α, β label the different atomic orbitals. An optical light pulse is considered, with light polarization vector $\mathbf{e} = 1/\sqrt{2}(1, 1, 0)$. With the decomposition, Eq. (10.15), and the

TB wave functions, Eq. (10.1), the dipole matrix elements $d_{ij}^{eh} = \mathbf{e} \mathbf{d}_{ij}^{eh}$ then explicitly read

$$d_{ij}^{eh} = \frac{e_0}{\sqrt{2}} \sum_{\mathbf{R}\mathbf{R}'\alpha\beta} c_{\mathbf{R},\alpha}^{i,e*} c_{\mathbf{R}',\beta}^{j,h} \left[(X + Y) \delta_{\mathbf{R}\mathbf{R}'} \delta_{\alpha\beta} + \langle \mathbf{R}, \alpha | \tilde{x} + \tilde{y} | \mathbf{R}', \beta \rangle \right]. \quad (10.16)$$

The first part in Eq. (10.16) is the contribution to the dipole matrix elements which stems from the TB coefficients (“envelope”) which are weighted with the position of the corresponding atom site. The second part contains the matrix elements of the operator $\tilde{\mathbf{r}}$ with the localized (atomic) basis orbitals $\phi_{\alpha\mathbf{R}}(\mathbf{r})$ and is determined by their spatial variation inside the unit cell.

In the literature a variety of different approximations for the calculation of the matrix elements in Eq. (10.16) has been applied in the past [107, 111, 140, 200–203]. In some of these works, the first part, the envelope part, has been neglected [140, 203], whereas in other works parts of the second contribution, the orbital contribution, have been included in addition to the envelope contribution [107, 200, 202]. However, no general statement has been made, which part is the dominant one for which kind of system. To give a representative picture, at least for the investigated InN/GaN QD system, here we include and discuss in detail both, orbital and envelope contribution.

The first part, the envelope part, can easily be calculated from our TB wave functions as a discrete sum over all lattice sites. The result does not depend on the choice of the origin. The proper calculation of the second part, the orbital contribution, is much more involved, which is the reason why in the available literature several different approximations and assumptions have been proposed [107, 111, 140, 200, 202, 203].

In the case of the orbital part it is necessary to connect the calculated TB coefficients $c_{\mathbf{R}\alpha}^i$ directly to the underlying set of atomic basis orbitals. A commonly used approach is the use of atomic Slater orbitals [189], as given in Table 10.3 for In, Ga and N, which take into account the influence of the effective screening of inner electron densities on the effective one-particle wave functions for the bonding orbitals. These basis orbitals have been used in the past for the calculation of dipole matrix elements [106, 107]. However, previous approaches contain two shortcomings which we have improved in our calculations.

(i) While they include the correct symmetry properties underlying the TB coefficients, the Slater orbitals lack the essential assumption of orthogonality with respect to different lattice sites, since they have been developed for isolated atoms. To overcome this problem, we use numerically orthogonalized Slater orbitals, as outlined in Appendix C.1. Including the orthogonality, the Slater orbitals fulfill all basic requirements, regarding symmetry, locality, and orthogonality for the basis orbitals underlying the TB formulation.

(ii) In most approaches only on-site contributions to the dipole matrix elements have been included [107, 140, 200, 204], which results in a local dipole interaction where only the direct overlap of electron and hole wave functions is taken into. To properly treat

the slight non-locality of the dipole operator [111, 202] and in particular the anion-cation structure of the crystal, the matrix elements are calculated including up to second-nearest neighbors here.

In the past, even nearest neighbor contributions have been neglected, because the matrix elements $\langle \mathbf{R}, \alpha | \tilde{x} + \tilde{y} | \mathbf{R}', \beta \rangle$ (with \mathbf{R} and \mathbf{R}' being neighboring atom sites) are much smaller than the corresponding on-site contributions (with $\mathbf{R} = \mathbf{R}'$). However, in Eq. (10.16) not only the matrix elements alone determine the result but they are also weighted with the TB coefficients of electron, $c_{\mathbf{R},\alpha}^{i,e}$, and hole, $c_{\mathbf{R}',\beta}^{j,h}$, wave function. From an intuitive picture, having in mind the anion-cation-structure of the crystal, one might guess, that the product of the TB coefficients $c_{\mathbf{R},\alpha}^{i,e} \cdot c_{\mathbf{R}',\beta}^{j,h}$ is larger for \mathbf{R}, \mathbf{R}' labeling nearest-neighbor atom sites than for $\mathbf{R} = \mathbf{R}'$. As visualized in Figure 10.4, the main contributions to electron and hole wave functions are localized at different kinds of atoms, and therefore at different layers in the crystal, electrons at the cations and holes at the anions. Therefore it can hardly be estimated in advance which contributions will be large and which small. Furthermore, the angular momentum selection rules [140], which are valid for the on-site matrix elements in a good approximation, cannot be used for transitions between orbitals which are centered around different lattice sites.

In order to rigorously estimate the influence of the different matrix elements and in order to give further insight into the nonlocal behavior of the dipole operator we will discuss the orbital contributions in detail in the following. Afterwards the final results for the dipole matrix elements are presented.

In contrast to previous approaches all the orbital contributions have been numerically calculated. To verify the numerical calculation of dipole matrix elements between the localized atomic orbitals, it can be checked in comparison to the quasi-analytical results which can be obtained for the on-site contributions with standard Slater orbitals, without orthogonalization [107]. Matrix elements with a numerical error smaller than 1% can easily be obtained by choosing a sufficiently fine grid of quadrature points for the numerical evaluation of integrals.

We do not tabulate all the dipole matrix elements but prefer to summarize some general statements, valid for the orbital contributions to all the calculated matrix elements between the electron and hole TB wave functions. For the on-site contributions the calculations with orthogonalized and standard Slater orbitals yield similar results with up to 8% difference. This finding demonstrates that the orthogonalized orbitals are still dominated by their original character in the vicinity of the origin. For details see Appendix C.1. Without orthogonalization the nearest- and second-nearest-neighbor contributions are strongly overestimated compared to the results of the orthogonalized orbitals. With orthogonalization, the main nonlocal contribution to the dipole matrix elements stems from the nearest neighbors. The second nearest neighbors are much less important and contribute by about 5% of the on-site contributions, which is in accordance with the TB formulation where nearest-neighbor hopping is included but hopping to more distant neighbors can be neglected in a good approximation.

Our results clearly demonstrate the short-range character of the dipole operator. How-

ever, despite its short-range character, it is essential to include the nearest-neighbor contributions to properly account for the anion-cation structure of the crystal lattice. In contrast to previous approaches all the nonlocal contributions have numerically been calculated here to avoid assumptions about angular momentum selection rules, which are strictly valid only for on-site contributions but which have been extended to nearest-neighbor contributions in earlier approaches [111,202]. The previously used assumptions for nonvanishing nearest-neighbor matrix elements, $\mathbf{d} \sim \mathbf{e}_z$, are not reproduced by our numerical results. Otherwise there would be no contribution from nearest neighbors for the light polarization $\mathbf{e} = 1/\sqrt{2}(1, 1, 0)$ investigated here.

In the preceding paragraphs we have outlined how to bridge the gap between the TB coefficients of the empirical TB formulation and atomic basis orbitals, which allows us to calculate the orbital contribution to the dipole matrix elements in addition to the envelope contribution. For the investigated system the envelope contribution is found to clearly dominate the total results for the dipole matrix elements, the orbital contributions are by about a factor of 30 smaller. However, this may change in other systems or for intraband transitions [201], where the orbital contribution becomes more important. The dipole selection rules, which will be discussed in the next section, are the same for both contributions, only small differences for the ratio of different nonvanishing matrix elements are found for orbital and envelope contributions.

Dipole Selection Rules

The only relevant dipole matrix elements in our InN QD structure are $\mathbf{e}\mathbf{d}_{sp_x}^{eh} = \mathbf{e}\mathbf{d}_{sp_y}^{eh}$ and $\mathbf{e}\mathbf{d}_{p_x s}^{eh} = \mathbf{e}\mathbf{d}_{p_y s}^{eh}$, where $\mathbf{e} = 1/\sqrt{2}(1, 1, 0)$ denotes the light polarization vector. All other matrix elements are negligible due to the overall symmetry of the connected single-particle states [147, 205, 206]. The resulting optical selection rules are in strong contrast to what is known from many other III-V and II-VI heterostructures and cannot be explained within a one-component effective-mass approach [207]. Commonly used dipole matrix elements are diagonal with respect to the envelope symmetry (angular momentum) [30, 140], namely $d_{ij}^{eh} \sim \delta_{ij}$ with $i, j \in \{s, p_+, p_-\}$.

The strong band mixing in the valence band is responsible for the transformation properties of the bound hole states which strongly influences the dipole selection rules for interband transitions to the conduction band. In many other systems with different symmetry of the crystal lattice and strong spin-orbit coupling for the valence bands, the dipole operator is diagonal with respect to the envelope angular momentum as used in Refs. [30] and [140]. The dipole selection rules are important for the interpretation of the excitonic spectra in the following section.

These selection rules are, in principle, unaffected by the built-in electrostatic field. However, for the large QD the ordering of the lowest hole states is interchanged by the influence of this field as already discussed in Section 10.1.3. This has strong implication on the optical emission spectra, which will be discussed in the following section.

Furthermore, the field-induced spatial electron-hole charge separation reduces the oscillator strengths drastically, by about a factor of 2 for the smallest QD, and by more than one order of magnitude for the largest QD.

10.2.3 Excitonic Spectra

In the preceding sections we have discussed the calculation of dipole and Coulomb matrix elements. They determine the many-particle Hamiltonian in second quantization as given in Section 10.2.1 and are used in this section for the calculation of excitonic absorption spectra. To this end configuration-interaction calculations, as briefly described in Section 10.2.1, are performed. Only the s and p shell bound states for electrons and holes, are included in our calculation. This is justified by their energy separation to higher states in the structure and keeps the following discussion simple and expressive.

In Figure 10.9 excitonic absorption and emission spectra, calculated with Fermi's golden rule, are depicted for the smallest and the largest QD with (solid line) and without (dashed line) the influence of the built-in field. The two absorption lines in each spectrum correspond to the creation of an exciton in the QD. The lower energy line is dominated by contributions where the electron is excited in the s shell and the hole in the p shell, whereas the higher energy line mainly corresponds to the excitation of the hole in the s shell and the electron in the p shell. This is in accordance with the dipole selection rules discussed in the preceding section. The influence of the built-in field in the structure red-shifts the whole excitonic spectrum by about 220 meV. The oscillator strengths are merely reduced by a factor of about 2. The strong confinement of the wave functions prevents a strong spatial separation of electron and hole wave functions as it is found in the case of larger QDs. In addition to the red-shift of the spectrum and the reduced oscillator strengths, the built-in field influences the Coulomb matrix elements, which, however, does not affect the optical spectra qualitatively.

For the small QD, no emission from the excitonic ground state is observed. This is the case, because the excitonic ground state is dominated by a contribution where the electron as well as the hole is in the s shell. Since the dipole matrix element d_{ss}^{eh} vanishes, the interband transition from the electron s shell to the hole s shell is dipole forbidden, and the exciton ground state remains dark. This finding is not affected by the built-in field.

For the large QD, the excitonic absorption in the presence (solid line) and in the absence (dashed line) of the built-in field is depicted in Figure 10.9(b). Because in the large QD the spatial separation of electron and hole wave functions due to the built-in field is much larger, the red-shift in energy and the reduction of the oscillator strengths is much more pronounced than for the small QD. Furthermore, the relative oscillator strengths of the lines in the low-energy and the high-energy transitions is changed by the built-in field. As discussed in Section 10.1.3, the ground state for the holes in the large QD in the presence of the built-in field is a twofold degenerate p state. Therefore the ground state for the exciton in the large QD is dominated by a contribution for which the

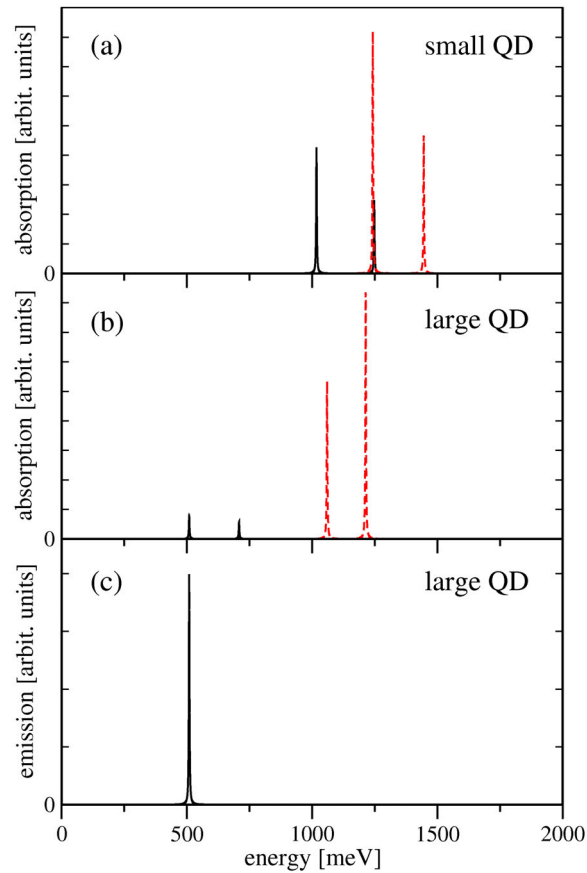


Figure 10.9: (a) Excitonic absorption for the small QD in the presence (solid line) and absence (dashed line) of the built-in field. (b) Same as (a) but for the large QD. (c) Excitonic ground state emission for the large QD including the influence of the built-in field. Without the built-in field, the ground state emission vanishes.

electron is in the s shell and, this time, the hole is in the p shell. Hence, in contrast to the small QD, for the large QD a nonvanishing exciton ground state emission can be observed. The resulting spectrum is depicted in Figure 10.9(c). In contrast, no emission is observed without the built-in field.

For the large QD the oscillator strength is drastically reduced by the field-induced spatial separation of the electron and hole wave functions. Two possible solutions to avoid the strong reduction of the oscillator strength by the built-in field in the wurtzite structure have been discussed in the past: (1) growth along a non-polar axis in the crystal lattice [149,208], or (2) growth of smaller QDs. However, our results demonstrate that the growth of smaller QDs may not be the desired solution. The small InN/GaN QD investigated here shows neither exciton nor biexciton ground state emission. Only for larger QDs the ground states become bright due to the influence of the built-in field. After this analysis of the absorption and ground state emission spectra of lens-shaped InN QDs, we will discuss in the next sections the emission spectra for an initially filling with up to six electron-hole pairs.

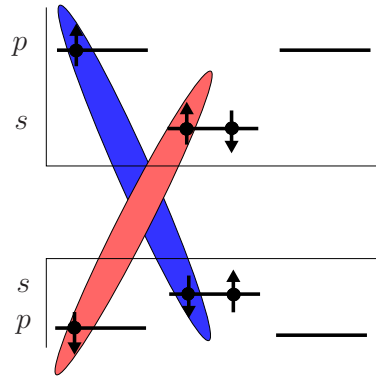


Figure 10.10: Example of a configuration with three electron hole pairs. The light (red) and dark (blue) shaded areas connect the carriers that will lead to an emission at the low- and high-energy side of the spectrum, respectively.

10.2.4 Multi-Exciton Emission Spectra

The extension of the CI calculation of the excitonic properties presented in the previous section to the more complex multi-exciton spectra is discussed here. The additionally required electron-electron and hole-hole Coulomb matrix elements can be calculated in complete analogy to the electron-hole matrix elements. The calculations of the complicated multi-exciton emission spectra have been performed in the group of Prof. Frank Jahnke, University Bremen, by Norman Baer. A detailed discussion of the different spectra are beyond the scope of this thesis and can be found in Ref. [116, 209]. Here, we present results for the small and intermediated lens-shaped InN QD.

Small QD

As discussed in the previous section the excitonic properties of the small QD are dominated by those configurations where each type of carrier is in its energetically lowest shell. Together with the fact that the dipole matrix d_{ss}^{eh} vanishes, we obtain a dark exciton ground state. Similar arguments hold for the discussion of the biexcitonic properties. Only for more than two excitons the CI calculation provides significant population of the electron and hole p shells. As mentioned above, the low- and high-energy side of the spectrum can be attributed to processes where an s electron or a p electron is dominantly involved in the recombination process, respectively. A schematic representation of the level-structure and electron-hole pairs typically involved in high- and low-energy transitions is depicted in Figure 10.10.

The emission spectra are shown in Figure 10.11 in the presence and absence of the built-in field for an initial filling with one up to six excitons. In both cases, an inspection of the emission-spectra reveals a blue-shift as the number of excitons is increased. This is in strong contrast to the results known from the InGaAs system [30, 133, 210], but can

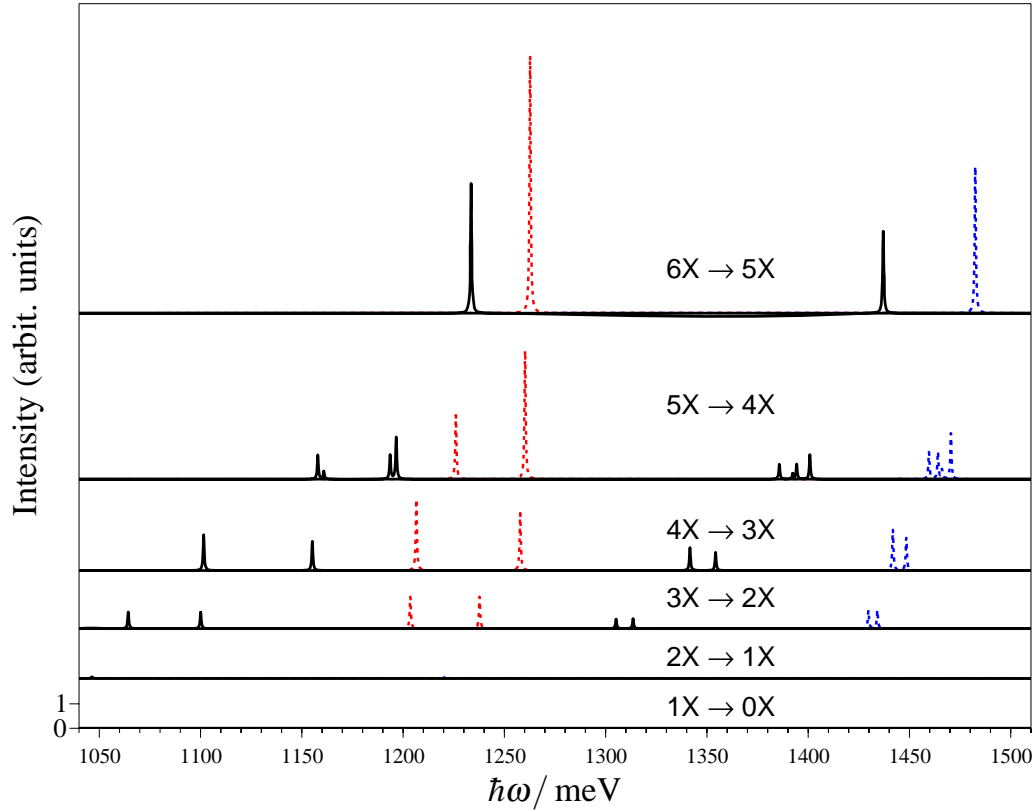


Figure 10.11: Ground state emission spectra for the smaller QD ($d = 4.5$ nm and $h = 1.6$ nm) with (solid lines) and without (dashed lines) the inclusion of the internal field. Different number of excitons with $S_z^{tot} = 0$ are chosen as initial states. For the studied system almost no ground state emission is observed for the exciton and biexciton.

already be explained by the strong Hartree contributions that arise as the envelopes for the electrons and holes are quite different. This strong deviation of the envelopes leads to Hartree-Fock terms that would at least partly cancel in the case of identical envelopes. Note, that the energetic shift with increasing number of excitons is by far more pronounced in the presence of the internal field because the stronger separation of the electron and hole wave functions is accompanied by stronger Hartree-fields. Furthermore, when the electrostatic built-in field is included in the calculation of the single-particle properties, the electron and hole wave functions are spatially separated from each other which leads to a reduction of the oscillator strength. Additionally, the single-particle gap and the Coulomb matrix elements are altered. The reduced oscillator strength and the overall red-shift of the spectra due to the QCSE are clearly visible.

Intermediate QD

Since we have seen in Section 10.2.3, that the optical properties of the lens-shaped InN QDs depend strongly on the size of these low dimensional systems, we investigate in

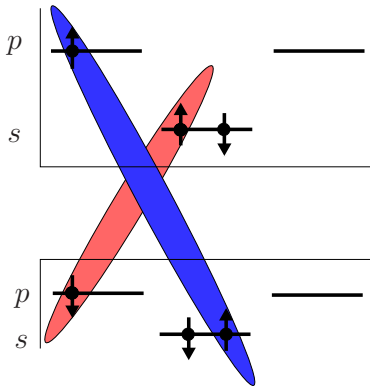


Figure 10.12: Schematic representation of a three exciton configuration. The light (red) and dark (blue) shaded areas connect the carriers that will lead to a emission at the low- and high-energy side of the spectrum, respectively.

this section the multi-exciton spectra of the intermediate QD. In this case, the energetic order of the two energetically lowest hole levels is reversed in the presence of the internal electrostatic field, as discussed in Section 10.1.3. This situation is schematically illustrated in Figure 10.12. Without the built-in field, one still has the ‘usual’ order with the s shell being lower in energy than the p shell. The resulting spectrum looks similar to those discussed in previous section and is therefore omitted. In presence of the built-in field the hole ground state consists of the two-fold degenerate p shell, which has nonvanishing dipole matrix elements with the electron s shell. This is in agreement with recent $\mathbf{k} \cdot \mathbf{p}$ calculations [147] and experimental results for CdSe QDs [206] grown in the wurtzite phase. This altered level structure results in a nonvanishing exciton and biexciton ground state emission. However, due to the strong separation of the electron and hole wave functions in this larger structure, the dipole matrix elements d_{sp}^{eh} are drastically reduced in comparison to those of the small QD.

The resulting multi-exciton spectra are shown in Figure 10.13. In contrast to the intuitive picture in which first the states with lowest single-particle energy are occupied, a strong population of the hole s shell which has a higher energy than the p shell for more than one exciton, is found. Here, the ground states are not given by those states with the lowest single-particle energy. This situation can be confirmed by a calculation that takes only Hartree Coulomb terms into account. Qualitatively this can be explained in the following way: It turns out that attractive interaction between electrons and holes being in their respective s shells is stronger than the attraction in the case of s and p shell carriers. Hence, the higher single-particle energy of the hole in s shell is compensated by attractive Coulomb interaction. Already in case of the biexciton, this effect results in an occupation of the hole s shell. As a consequence, the excitonic and biexciton lines have approximately the same oscillator strength.

From three electron-hole pairs on, the ground states are governed by configurations in which both the s shell for electrons and the s shell for holes are fully populated.

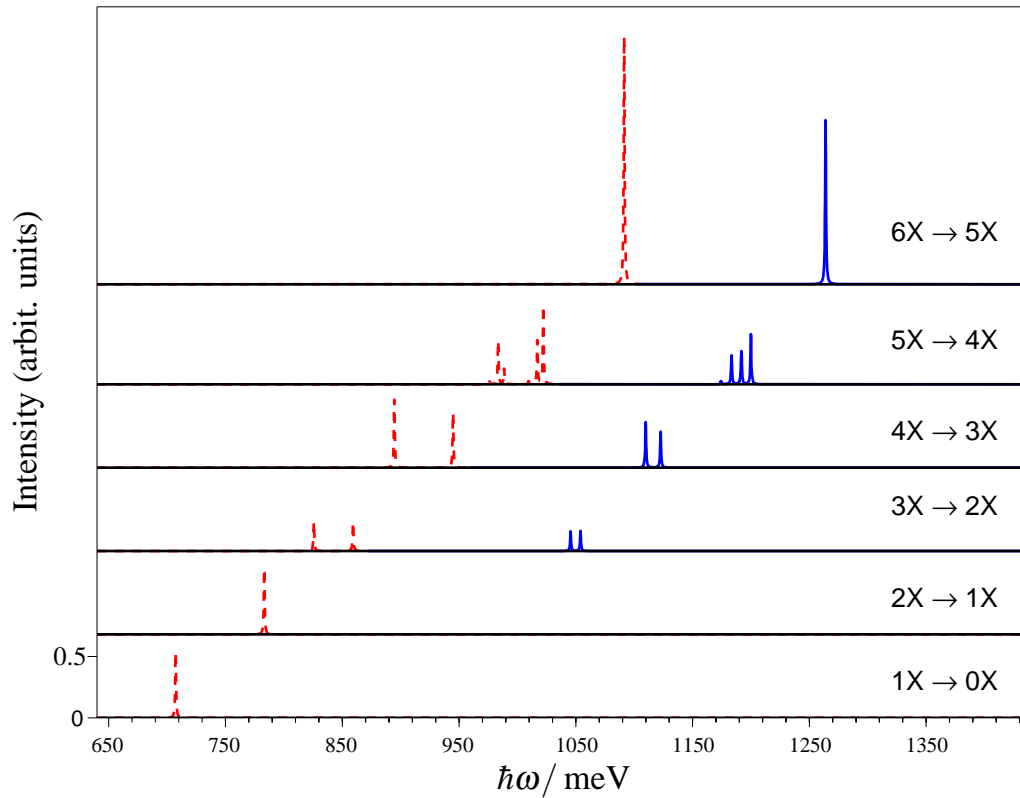


Figure 10.13: Emission spectra for a larger QD ($d = 5.7$ nm and $h = 2.3$ nm) with different number of excitons and in the presence of the internal field. For the emission of each multi-exciton complex the high-energy side is shown in blue (solid lines), the low-energy side in red (dashed lines). Due to the reversed level structure for the holes a ground state emission is observed for exciton and biexciton. As initial states the ground states with $S_z^{\text{tot}} = 0$ are chosen.

Qualitatively, one obtains the same emission spectrum as in the case of the small InN QD with the ‘normal’ ordering of the shells. However, due to the strong separation of electron and hole wave functions, the oscillator strengths are drastically reduced compared to the smaller system and here the Hartree shifts are even more pronounced.

Electronic and Optical Properties of
Zinc Blende GaN/AlN Quantum Dots

11 Introduction to Part IV

In the previous parts we have investigated the electronic and optical properties of group II-VI QDs grown in zinc blende phase as well as group III nitride QDs crystallized in a wurtzite structure. As already discussed, the nitride-based nanostructures have significantly different properties compared to QDs composed of II-VI and other III-V materials. Due to their unique characteristics, self-assembled nitride QDs attract much interest for optoelectronic applications. In particular, structures based on GaN have recently received considerable attention for applications such as blue-light emitting diodes, high-speed field-effect transistors, UV photo-detectors and high-temperature electronic devices [211, 212]. Until now, most of the GaN-based devices utilize wurtzite GaN. However, high quality self-assembled zinc blende GaN QDs have been recently made available [213–217]. These cubic GaN QDs are expected to have various advantages due to their higher crystallographic symmetry [218]. Therefore, we focus in this part on the zinc blende GaN nanostructures. Here we combine the insights gained in the investigation of zinc blende QDs and the nitride nanostructures.

High quality GaN QDs are obtained by colloidal chemical synthesis [219] or self-organization [213–217, 220]. Many of their optical properties have been investigated experimentally. In case of wurtzite GaN QDs the *polar* [0001] axis of the wurtzite lattice is often parallel to the growth direction. As detailed in the previous part, the crystal symmetry and the growth process along this direction, yields giant intrinsic electrostatic built-in fields. These fields arise in part from spontaneous and in part from strain-induced polarizations and are of the order of MV/cm [148, 221]. As a consequence, the optical properties of such low-dimensional systems are strongly influenced by these contributions [148]. For example the electrostatic built-in fields lead to a spatial separation of electrons and holes and therefore to a reduced exciton oscillator strength and enhanced radiative lifetimes [72, 148].

In contrast to wurtzite GaN/AlN nanostructures, self-assembled zinc blende QDs of these materials are often grown along the *nonpolar* [001] axis. Due to the altered lattice structure, a zinc blende GaN QD does not exhibit a spontaneous polarization. Furthermore, theoretical [72] and experimental [216] investigations reveal that the piezoelectric contributions are negligible. Moreover, GaN with a zinc blende structure offers many potential advantages over wurtzite GaN, for instance, a higher doping efficiency due to higher crystallographic symmetry, a higher carrier mobility, a smaller energy band gap, which reduces the required indium content to obtain green light emission [218].

To understand the optical properties of semiconductor QDs, the electronic structure is of major importance. In the past few years several different methods, such as pseudopo-

tential approaches [8,31,136], tight-binding theories [9,84], $\mathbf{k}\cdot\mathbf{p}$ models [29,72] as well as effective-mass approximations [20,146] have been used for calculations of the electronic states of InAs, GaAs, CdSe, etc. For GaN several authors have presented electronic structure calculations for hexagonal GaN/AlN QDs, including effects caused by strain and built-in electric-field. However, only few results have been published for zinc blende GaN QDs, and are based on continuum approaches. As we have seen in the previous parts, the underlying atomistic structure can be of great importance. Therefore we use a microscopic approach to describe the optical properties of zinc blende GaN QDs.

In the following a theoretical analysis of the electronic properties and absorption spectra of zinc blende GaN QDs by means of an empirical TB model is given. In Section 12.1.1 we discuss the geometry of the QD, which is confirmed by experimental data. Section 12.1.2 is dedicated to the strain field calculation of the QD geometry under consideration. Subsequent to this, the applied strain dependent TB model is presented. In Section 12.2.1 the Hamiltonian of the interacting charge carriers is introduced followed by a brief discussion of the calculation of Coulomb- and dipole matrix elements. The QD energy spectrum and the bound single-particle wave functions of electrons and holes are investigated in Section 13.1 and Section 13.2. The optical properties are discussed in Section 13.3.

12 Electronic and Optical Properties of GaN/AlN QDs

In this chapter we introduce the main ingredients of our theory for the calculation of electronic and optical properties of GaN QDs. These ingredients include the strain field calculation of the QD geometry under consideration, the strain dependent tight-binding (TB) model, and the evaluation of Coulomb and dipole matrix elements. In the following section we focus on the electronic structure of GaN/AlN QDs. Section 12.2 is dedicated to the many-body Hamiltonian for a system of interacting charge carriers.

12.1 Electronic Structure

For the investigation of the optical properties of semiconductor QDs the knowledge about the single-particle states is required. In order to calculate the electronic states of self-assembled QDs in the framework of an empirical strain dependent TB model, we proceed in three steps. In a first step the geometry of the QD is defined. In step two the corresponding strain field due to the lattice mismatch between the two materials is calculated. In the final step, the strain field is incorporated in our TB approach.

12.1.1 Geometry of the Quantum Dot Structure

In the previous part we have discussed the electronic and optical properties of lens-shaped InN QDs with a wurtzite structure. In this part we turn our attention to the investigation of GaN/AlN QDs with zinc blende structure. A considerable amount of experimental data is available addressing the epitaxial, structural and optical properties of cubic GaN/AlN QDs [213–217]. High resolution transmission electron microscopy [216] and atomic force microscopy [213] reveal that GaN/AlN QDs grow as truncated pyramids, nucleating on top of a wetting layer (WL). According to the literature, the extracted average QD height above the WL for zinc blende GaN is 1.6 ± 0.5 nm, and the average dot diameter is 13 nm. The WL thickness is estimated to be about 3 ML.

To model such a cubic GaN QD embedded in an AlN barrier material, we use a zinc blende lattice inside a large supercell with fixed boundary conditions. According to the experimental data, we assume a GaN WL thickness of 3 ML within this supercell, and on top of this WL a truncated pyramidal GaN QD. The height of this pyramid is $h = 4a$

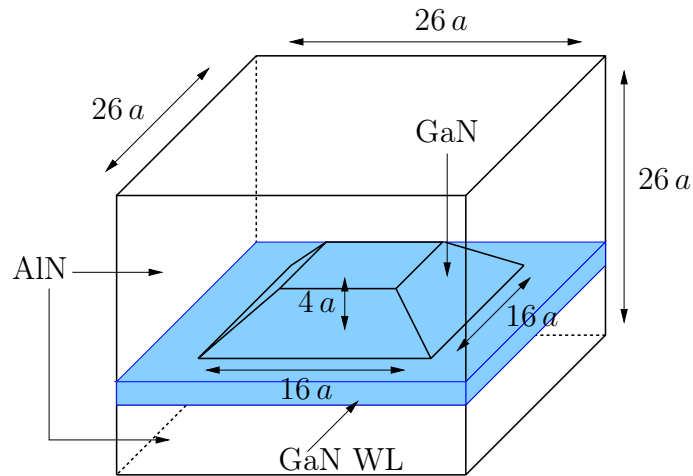


Figure 12.1: Schematic visualization of the truncated pyramidal GaN QD buried in an AlN matrix. The wetting layer has a thickness of 3 ML of GaN. The pyramidal QD has a base length b of 16 times the AlN lattice constant.

and the base diameter is $d = 16a$, where a is the AlN lattice constant $a_{\text{AlN}} = 0.438$ nm. This corresponds to $h \approx 1.75$ nm and $d = 7$ nm. The measurements of Arley *et al.* [143] and Widmann *et al.* [220] indicate that there is no intermixing between Ga and Al in wurtzite GaN QDs. Since the structural properties of zinc blende GaN/AlN QDs are found to be similar to those of hexagonal QDs [216], we take the composition of the dot and the surrounding matrix to be pure GaN and AlN, respectively. A relatively weak interdiffusion of Ga and Al atoms is observed in the WL. Since we are only interested in the bound single-particle states, which are localized inside the QD, the composition fluctuations of the WL outside the QD have only a small influence on the localized single-particle states and are therefore negligible. Figure 12.1 depicts the embedded QD with a base length b of $16a$. A cell with the dimension of $26a \times 26a \times 15a$ ($\approx 81\,000$ atoms), is used for the calculations.

Here we assume, that, initially, all atoms are placed at the lattice sites of an uniform, bulk AlN zinc blende lattice. Surely, it is reasonable to assume that far from the QD, the AlN matrix is unstrained. However, the GaN WL and QD are strongly strained due to the strain energy of the compressed GaN WL and QD, which have an unstrained bulk lattice constant $a_{\text{GaN}} = 0.45$ nm as compared to $a_{\text{AlN}} = 0.438$ nm. The following section is dedicated to the calculation of the strain field.

12.1.2 Strain Field Calculation

After having defined the QD geometry in the previous section, we calculate in this section the strain field in our structure to obtain the new positions of the atoms.

The strain tensor $\underline{\underline{\epsilon}}$ is related to the strain dependent relative positions of the atoms

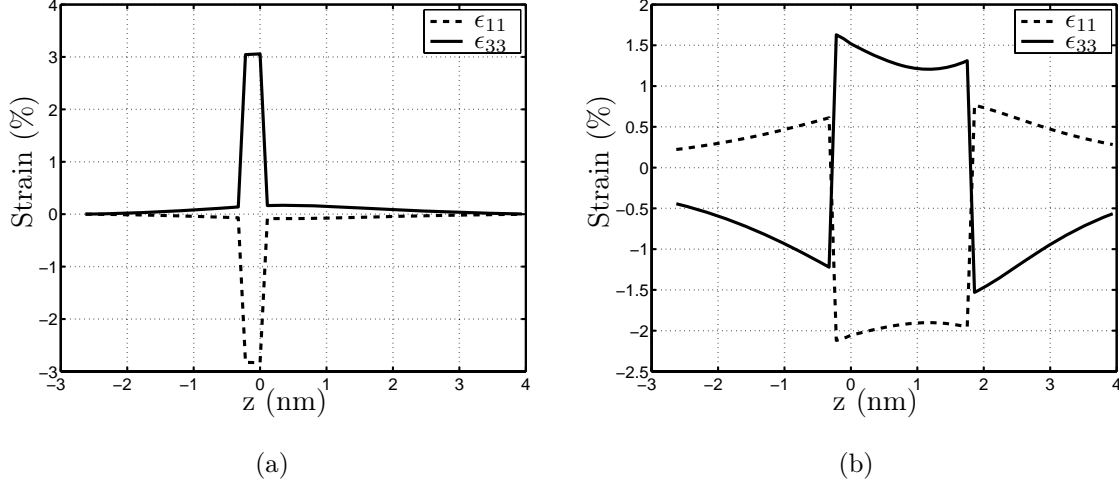


Figure 12.2: Strain distribution in and around the truncated pyramidal GaN QD with a base length of $b = 16a$. The WL at the base of the QD is 3 ML thick. The whole structure is buried in an AlN matrix. Line scans along the [001] direction through the WL outside the dot (a) and inside the dot through the center of the truncated pyramid (b) are displayed. The diagonal elements of the strain tensor $\underline{\underline{\epsilon}}$ are shown as solid (ϵ_{33}) and dashed lines ($\epsilon_{11} = \epsilon_{22}$).

$\mathbf{d}_{\mathbf{R}'-\mathbf{R}}$ by

$$\mathbf{d}_{\mathbf{R}'-\mathbf{R}} = (\underline{\underline{1}} + \underline{\underline{\epsilon}})\mathbf{d}_{\mathbf{R}'-\mathbf{R}}^0. \quad (12.1)$$

To calculate the strain tensor outside the embedded QD, the WL is treated as a quantum well (QW). In the absence of shear strain, that is $\epsilon_{i,j} \sim \delta_{i,j}$, for a coherently grown film, the strain components are given by [76]

$$\epsilon_{\parallel} = \epsilon_{11} = \epsilon_{22} = \frac{a_S - a_D}{a_D}, \quad (12.2)$$

$$\epsilon_{\perp} = \epsilon_{33} = -\frac{2C_{12}}{C_{11}}\epsilon_{\parallel}. \quad (12.3)$$

Here a_D is the lattice constant of the unstrained film material and a_S denotes the parallel lattice constant of the substrate. The cubic elastic constants C_{ij} of the bulk materials are given in Table E.6 of Appendix E. The resulting strain profile for a line scan in the z direction outside the dot is shown in Figure 12.2(a).

As discussed in Section 3.2.1, for the calculation of the strain field in a QD structure one can either apply an atomistic model or a continuum approach. The major restrictions of several continuum approaches are that these calculations assume isotropic elastic constants, that details of the underlying atomistic lattice are lost, and that calculations are limited to QDs buried inside an infinite matrix. On the other hand, the advantage of a continuum model is that the calculations are portable and quick, so that even larger systems involving many QDs can be treated with relative ease. Furthermore analytic

expressions can be obtained in continuum approaches that often provide deeper insight into the underlying physics and reveal trends and simple relations.

An elegant method to calculate the strain field of a single QD of arbitrary shape was presented by Downes *et al.* [222] as a simplification of the work of Eshelby [223]. This method, which neglects anisotropy of the elastic constants, provides analytic solutions for simple geometries such as cubic or pyramidal dots and numerical solutions for more complex geometries. Pearson and Faux [224] used this method to derive analytic solutions for the strain field of a pyramidal QD with arbitrary truncation. In the approach of Downes *et al.* [222], the stress field of a sufficiently small sphere can be extended to yield the strain distribution of an inclusion of arbitrary shape.¹ In principle, this scheme is only applicable if the QD and the surrounding material have identical elastic constants. However, Andreev *et al.* [225] compared the strain distribution of QDs in a model, which contains anisotropic contributions, to a simplified approach, in which the elastic properties are assumed to be isotropic. This analysis reveals that, both anisotropic and isotropic models give similar results if the symmetry of the QD shape is less than or equal to the cubic symmetry of the crystal. Furthermore, in our system the isotropic assumption should be a good approximation since the elastic constants of GaN and AlN are nearly equal, and their difference is smaller than the uncertainties in their values [131]. Therefore, the assumption of an isotropic elastic medium is reasonable.

According to the discussion above, we apply the approach of Person and Faux [224] to calculate the strain field induced by the GaN/AlN QD, which will be briefly discussed in the following. In a first step, we consider a small spherical QD buried in an infinite, linearly elastic and isotropic matrix, and suppose that the elastic constants are the same inside and outside the dot. The strain distribution for the inner and outer parts of this structure with radius r_0 is in spherical coordinates given by [102]:

$$\begin{aligned}\epsilon_{r,r}^{\text{in}} &= \frac{2(1-2\nu)}{3(1-\nu)}\epsilon_0 = \epsilon_{\theta,\theta}^{\text{in}} = \epsilon_{\phi,\phi}^{\text{in}} , \\ \epsilon_{r,r}^{\text{out}} &= \frac{2(1+\nu)}{3(1-\nu)}\epsilon_0 \left(\frac{r_0}{r}\right)^3 = -2\epsilon_{\theta,\theta}^{\text{out}} = -2\epsilon_{\phi,\phi}^{\text{out}} ,\end{aligned}$$

where r denotes the radius, ν the so-called *Poisson ratio* [152], and ϵ_0 the relative lattice mismatch of the dot material and the matrix. The resulting radial displacements are:

$$\begin{aligned}u_r^{\text{in}} &= \frac{2(1-2\nu)}{3(1-\nu)}\epsilon_0 r , \\ u_r^{\text{out}} &= -\frac{(1+\nu)}{3(1-\nu)}\epsilon_0 \left(\frac{r_0^3}{r^2}\right) ,\end{aligned}$$

which fulfil the so-called *shrink fit* condition [102]:

$$(u_r^{\text{in}} - u_r^{\text{out}}) |_{r=r_0} = \epsilon_0 r_0 .$$

¹ Sufficiently small means, that the initial misfit strain can be assumed uniform in this region.

Dividing the displacement by the sphere's volume, one obtains the displacement per unit volume of the inclusion. From the displacement one can derive the stress σ_{ij}^0 per unit volume [222]:

$$\begin{aligned}\sigma_{ii}^0 &= \frac{1}{4\pi} \frac{E\epsilon_0}{(1-\nu)} \frac{x_j^2 + x_k^2 - 2x_i^2}{r^5}, \\ \sigma_{ij}^0 &= -\frac{1}{4\pi} \frac{E\epsilon_0}{(1-\nu)} \left(\frac{3x_i x_j}{r^5} \right),\end{aligned}$$

where the indices i, j and k denote the Cartesian coordinates $x_1 = x$, $x_2 = y$ and $x_3 = z$. From the linear superposition of stresses [225], the stress distribution σ_{ij}^V for the arbitrary inclusion of volume V can be obtained by integrating the stress σ_{ij}^0 per unit volume over V :

$$\sigma_{ij}^V(x_1, x_2, x_3) = \int_V \sigma_{ij}^0(\mathbf{r}') d^3\mathbf{r}' = \int_V \frac{\Lambda(\delta_{ij}r'^2 - 3x'_i x'_j)}{r'^5} dV(x_1^0, x_2^0, x_3^0), \quad (12.4)$$

where, $x'_i = x_i - x_i^0$ are Cartesian coordinates. The index "0" labels the points inside the volume of the QD. The constant Λ is given by $\Lambda = \epsilon_0 E / 4\pi(1-\nu)$, where ϵ_0 is the lattice mismatch, E is the so-called *Young's modulus* [152] and ν is the Poisson ratio. As usual, δ_{ij} is the Kronecker delta and $r'^2 = \sum_i (x'_i)^2$. The strains can be calculated from the stresses according to the following expressions:

$$\epsilon_{ij} = \frac{1}{E} ((1+\nu)\sigma_{ij} - \delta_{ij}\nu\sigma_{kk}). \quad (12.5)$$

Pearson and Faux [224] derived, using Eq. (12.4), a complicated but closed expression for the stress distribution of pyramidal QDs with arbitrary truncation. These expressions are given in Appendix D. The resulting strain field distribution in and around the truncated GaN pyramid with base length $b = 16a$ and height $h = 4a$ on top of a three ML GaN WL embedded in AlN, is displayed in Figure 12.2 (b) and Figure 12.3. Several aspects of these results are of interest. From Figure 12.2 (b) we obtain that the magnitudes of the strain components are largest at the interface between QD and surrounding matrix. The strain components ϵ_{11} and ϵ_{22} are compressive everywhere inside the QD but smaller in magnitude than the initial misfit strain of 2.7% owing to strain relaxation. In the region around the nanostructure these components are tensile. Outside the dot ϵ_{33} is compressive, since the QD relaxes outwards and compresses the local environment in z direction. Inside the QD ϵ_{33} is tensile.

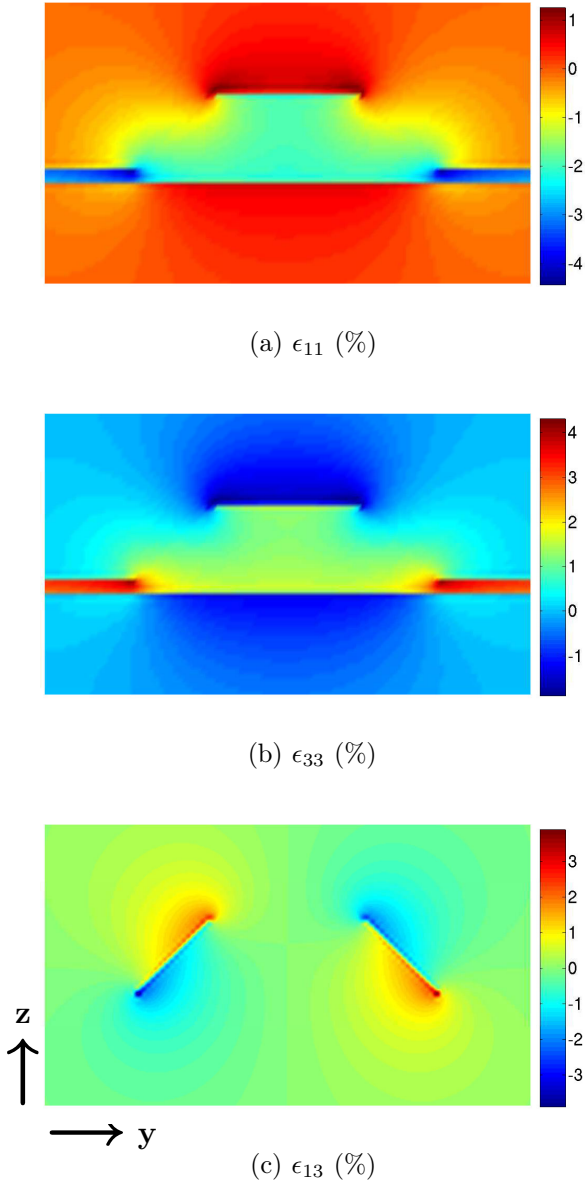


Figure 12.3: Strain distribution in and around the truncated pyramidal GaN QD with a base length of $b = 16a$. The WL at the base of the QD is 3 ML thick. The whole structure is buried in a AlN matrix. The strain tensor components ϵ_{11} (a) ϵ_{33} (b) and ϵ_{13} (c) are shown in the (100) cross section plane through the center of the truncated pyramid.

12.1.3 Tight-Binding Model

After setting up the model geometry and calculating the strain field in and around the QD structure, the tight-binding (TB) Hamiltonian matrix is constructed and the single-particle states and energies can be calculated by matrix diagonalization. Since GaN and AlN are polar semiconductors, the valence band originates mainly from the anions and the conduction band from the cations [117]. Furthermore, from the perspective of atomic orbitals and near the Brillouin zone center, the valence bands stem from the valence p orbitals and the conduction bands from the s orbitals [117]. Since we are dealing with a zinc blende structure and polar semiconductors, we apply the TB

model discussed in detail in Part II. The main points are summarized in the following paragraph.

In the TB model each anion is described by its outer valence orbitals for each spin: p_x , p_y and p_z . The cations are modeled by a single s orbital per spin direction. The coupling of the basis orbitals is restricted to nearest and second nearest neighbors. Following Ref. [51], the spin-orbit component of the bulk Hamiltonian H^{bulk} couples only p -orbitals at the same atom. The different TB parameters are chosen such that the resulting TB bands reproduce the known values of the Kohn-Luttinger-parameters $(\gamma_1, \gamma_2, \gamma_3)$, the energy gap, the effective electron-mass and the spin-orbit splitting. All these parameters are taken from Ref. [131]. Within this approach, the characteristic properties of the bulk band structure in the region of the Γ point are well reproduced. More sophisticated TB models could be used with an increased number of basis states per lattice site or hopping matrix elements at considerable additional computational cost. Including for example d orbitals can be especially important for small GaAs QDs, as demonstrated in Ref. [226], where a small energy splitting between the side valleys and the zone center is observed. Also in AlN the energy spacing between the point Γ and X is small and can lead to an indirect band gap material [167]. Under these circumstances, a strong quantum confinement may mix the side valley and the zone center states. However, we are only interested in the bound single-particle wave functions, which are mainly localized in the GaN region. The spacing between the side valley and the zone center is much larger for GaN [167]. Thus, one could expect that the localized single-particle states are dominated by contributions from near the zone center gap. Since our TB model is designed to reproduce this part of the band structure, we expect the applied TB model to give a reasonable representation for the electronic structure of zinc blende GaN QDs.

Starting from the bulk TB parameters, the QD is modeled on an atomistic level. To this end one sets the matrix elements for each lattice point according to the occupying atoms. The valence band offset ΔE_v between GaN and AlN is included in our model by shifting the diagonal matrix elements of the bulk GaN. The valence band offset ΔE_v is taken as 0.8 eV, according to the recommendations of Ref. [131].

For the strained heterostructure, the TB hopping matrix elements $H_{|\mathbf{R}'-m\mathbf{R}|}$ connecting atoms at \mathbf{R}' and \mathbf{R} , with $\mathbf{R} \neq \mathbf{R}'$, have to be recalculated at each atomic site. To incorporate the effects of changed bond angles between the sites \mathbf{R}' and \mathbf{R} , we use the Slater-Koster formulas [47] given by:

$$\begin{aligned} E_{ss}(\mathbf{d}(\boldsymbol{\epsilon}))_{\alpha',\alpha} &= V_{ss\sigma}(d(\boldsymbol{\epsilon}), \alpha', \alpha) , \\ E_{sx}(\mathbf{d}(\boldsymbol{\epsilon}))_{\alpha',\alpha} &= \cos \theta_x(\boldsymbol{\epsilon}) V_{sp\sigma}(d(\boldsymbol{\epsilon}), \alpha', \alpha) , \\ E_{xx}(\mathbf{d}(\boldsymbol{\epsilon}))_{\alpha',\alpha} &= (\cos \theta_x(\boldsymbol{\epsilon}))^2 V_{pp\sigma}(d(\boldsymbol{\epsilon}), \alpha', \alpha) + (1 - (\cos \theta_x(\boldsymbol{\epsilon}))^2) V_{pp\pi}(d(\boldsymbol{\epsilon}), \alpha', \alpha) , \\ E_{xy}(\mathbf{d}(\boldsymbol{\epsilon}))_{\alpha',\alpha} &= \cos \theta_x(\boldsymbol{\epsilon}) \cos \theta_y(\boldsymbol{\epsilon}) V_{pp\sigma}(d(\boldsymbol{\epsilon}), \alpha', \alpha) - \cos \theta_x(\boldsymbol{\epsilon}) \cos \theta_y(\boldsymbol{\epsilon}) V_{pp\pi}(d(\boldsymbol{\epsilon}), \alpha', \alpha) , \end{aligned}$$

where $\cos \theta_i = (\mathbf{R} - \mathbf{R}')\mathbf{e}_i/|\mathbf{R} - \mathbf{R}'|$ is the directional cosine of the strained material; θ_i is the angle between the $\mathbf{R} - \mathbf{R}'$ and the unit vector \mathbf{e}_i along the i^{th} axes. The different matrix elements $V_{lm}(d(\boldsymbol{\epsilon}), \alpha', \alpha)$ still depend on the bond length $d(\boldsymbol{\epsilon})$ between

		e_1 [eV]	e_2 [eV]	e_3 [eV]	h_1 [eV]	h_2 [eV]	h_3 [eV]
No Strain	$V = 0$	4.0042	4.0100	4.0100	0.4716	0.4687	0.4687
	$V \neq 0$	4.7742	4.8935	4.8967	0.3653	0.3648	0.3645
Strain	$V = 0$	3.9826	3.9887	3.9887	0.4502	0.4462	0.4462
	$V \neq 0$	4.5665	4.6030	4.6037	0.3359	0.3358	0.3353

Table 12.1: First three eigenenergies (excluding time reversal symmetry) for electrons and holes, respectively, for a three ML thick GaN QW. The calculations are done with ($V \neq 0$) and without ($V = 0$) anion-cation coupling. Furthermore results including the strain field are compared to a situation in which the strain field is artificially switched off. Note that each state is two-fold degenerate due to time reversal symmetry.

the site \mathbf{R} and \mathbf{R}' . As described in Section 3.2, a power-law scaling for the bond lengths modifications is applied. For example, the matrix element between s and p_x orbitals is expressed as

$$H_{s\mathbf{R}',p_x\mathbf{R}} = d_x(\epsilon)V_{sp\sigma} \left(\frac{d_{\mathbf{R}'-\mathbf{R}}^0}{d_{\mathbf{R}'-\mathbf{R}}} \right)^2. \quad (12.6)$$

Compared to a GaN QD with a wurtzite structure the piezoelectric field in a GaN QD with a zinc blende structure is negligible. The calculations of Fonoberov *et al.* [72] indicate, that the magnitude of the piezoelectric potential in a zinc blende GaN/AlN QD is about ten times smaller than its magnitude in a comparable wurtzite GaN/AlN QD and affects the excitonic properties of the zinc blende QD very little. Moreover, recent results of Bester *et al.* [78] show that the second order contributions to the piezoelectric potential yield further significant reduction of the piezoelectric effect. Due to these facts, the piezoelectric field is neglected in our calculations.

To examine the influence of strain effects and to inspect the symmetry of the resulting TB Hamiltonian we will first apply our model to a GaN/AlN QW.

Quantum Well Test

Before focussing on the more complicated QD systems we briefly investigate in the following the electronic structure of a quantum well (QW). This shows that the essential symmetry properties are correctly described by the strain dependent TB model.

We calculate the energy levels in a three ML thick QW in the presence and in the absence of strain. Furthermore, we artificially switch off the coupling between anion-cation sites, by setting the hopping matrix elements V equal to zero. Since we are only interested in degeneracies of eigenstates and not in the absolute values of the eigenenergies, the TB parameters are not readjusted to generate the bulk band structure. However, the parameter V is deduced to reproduce the energy of the heavy-hole valence band at the

X point. Therefore the band structure in the vicinity of the Γ point should still be meaningful. When switching off the parameter V , the symmetry of our system is \bar{C}_{4v} . For $V \neq 0$ the symmetry of the system is \bar{C}_{2v} since the QW has no inversion center. Since the calculation of the strain is based on a continuum approach and according to the character table of the group \bar{C}_{4v} [87], one expects, including time reversal symmetry, fourfold degenerate states in case of $V = 0$. This holds with and without strain. Along the same line of arguments, one can deduce that in case of $V \neq 0$ only twofold degenerate states could occur. This is exactly the result we obtain from our TB calculation, as seen in Table 12.1 which summarizes the energies of the first three (six) bound electron and hole states for the three ML thick QW. Each state is twofold degenerate due to time reversal symmetry. For $V = 0$ we obtain that the first two excited electron states e_2 and e_3 are degenerate with and without strain. The same is true for the hole states h_2 and h_3 . In case of $V \neq 0$ this symmetry is broken, and each state is only twofold degenerate due to time reversal symmetry.

In summary, the strain dependent TB model was successfully tested for a simple GaN QW system. Therefore, the approach can now be extended to the investigation of the electronic properties of GaN QDs. The results are given in Chapter 13.

12.2 Optical Properties

In the previous section we have discussed the strain dependent TB model used to calculate the single-particle wave functions and energies in zinc blende GaN QDs. In this section we address the optical properties of these QDs. Here we introduce the many-body Hamiltonian for a system of interacting charge carriers and describe the procedure to calculate the required Coulomb and dipole matrix elements.

12.2.1 Many-Body Hamiltonian, Coulomb and Dipole Matrix Elements

From the one particle states presented in the previous section the many-body Hamiltonian H can be obtained:

$$H = H_0 + H_C + H_D, \quad (12.7)$$

where

$$H_0 = \sum_i \epsilon_i^e e_i^\dagger e_i + \sum_i \epsilon_i^h h_i^\dagger h_i,$$

is the one-particle part, which is diagonal with respect to the calculated QD eigenstates,

$$H_C = \frac{1}{2} \sum_{ijkl} V_{ij,kl}^{ee} e_i^\dagger e_j^\dagger e_k e_l + \frac{1}{2} \sum_{ijkl} V_{ij,kl}^{hh} h_i^\dagger h_j^\dagger h_k h_l - \sum_{ijkl} V_{ij,kl}^{he} h_i^\dagger e_j^\dagger e_k h_l \quad (12.8)$$

describes the Coulomb interaction between the carriers and

$$H_D = \sum_{i,j} \left(\langle i | e_0 \mathbf{E} \mathbf{r} | j \rangle e_i h_j + \text{h.c.} \right) \quad (12.9)$$

denotes the coupling to an external field \mathbf{E} in dipole approximation. The creation and annihilation operators for electrons (holes) in the single-particle state $|i\rangle$ with energy $\epsilon_i^e(\epsilon_i^h)$ are denoted by $e_i^\dagger(h_i^\dagger)$ and $e_i(h_i)$, respectively. The Coulomb matrix elements are denoted by $V_{ijkl}^{\lambda,\lambda'}$. According to the discussion of Section 10.2, the $V_{ijkl}^{\lambda,\lambda'}$ are approximated by:

$$V_{ijkl}^{\lambda,\lambda'} = \sum_{\mathbf{R}(\boldsymbol{\epsilon})\mathbf{R}'(\boldsymbol{\epsilon})} \sum_{\alpha\beta\sigma\sigma'} c_{\mathbf{R}(\boldsymbol{\epsilon})\alpha\sigma}^{\lambda,i*} c_{\mathbf{R}'(\boldsymbol{\epsilon})\beta\sigma'}^{\lambda',j*} c_{\mathbf{R}'(\boldsymbol{\epsilon})\beta\sigma'}^{\lambda',k} c_{\mathbf{R}(\boldsymbol{\epsilon})\alpha\sigma}^{\lambda,l} V(\mathbf{R}(\boldsymbol{\epsilon}) - \mathbf{R}'(\boldsymbol{\epsilon})), \quad (12.10)$$

with

$$V(\mathbf{R}(\boldsymbol{\epsilon}) - \mathbf{R}'(\boldsymbol{\epsilon})) = \frac{e_0^2}{4\pi\epsilon_0\epsilon_r|\mathbf{R}(\boldsymbol{\epsilon}) - \mathbf{R}'(\boldsymbol{\epsilon})|} \quad \text{for } \mathbf{R}(\boldsymbol{\epsilon}) \neq \mathbf{R}'(\boldsymbol{\epsilon}), \quad (12.11)$$

and

$$V(0) = \frac{1}{V_{uc}^2} \int_{uc} d^3r d^3r' \frac{e_0^2}{4\pi\epsilon_0\epsilon_r|\mathbf{r} - \mathbf{r}'|} \approx V_0. \quad (12.12)$$

In contrast to the discussion in Section 10.2, the atomic positions are modified according to the strain field $\underline{\boldsymbol{\epsilon}}$, which is explicitly included here. For the operator \mathbf{r} in the dipole Hamiltonian, Eq. (12.9), we use the approximation

$$\begin{aligned} \mathbf{r} &= \sum_{\mathbf{R}(\boldsymbol{\epsilon})\alpha\sigma} |\mathbf{R}(\boldsymbol{\epsilon}), \alpha, \sigma\rangle \mathbf{R}(\boldsymbol{\epsilon}) \langle \mathbf{R}(\boldsymbol{\epsilon}), \alpha, \sigma| \\ &+ \sum_{\mathbf{R}(\boldsymbol{\epsilon})\alpha\sigma} \sum_{\mathbf{R}'(\boldsymbol{\epsilon})\beta\sigma'} |\mathbf{R}(\boldsymbol{\epsilon}), \alpha, \sigma\rangle \langle \mathbf{R}(\boldsymbol{\epsilon}), \alpha, \sigma | \tilde{\mathbf{r}} | \mathbf{R}'(\boldsymbol{\epsilon}), \beta, \sigma' \rangle \langle \mathbf{R}'(\boldsymbol{\epsilon}), \beta, \sigma'|, \end{aligned} \quad (12.13)$$

where $\tilde{\mathbf{r}}$ denotes the position inside a unit cell relative to $\mathbf{R}(\boldsymbol{\epsilon})$. The expansion coefficients $c_{\alpha,\mathbf{R}(\boldsymbol{\epsilon})}^i$ are related to the i^{th} one-particle wave function

$$\Phi_i(\mathbf{r}) = \sum_{\alpha,\mathbf{R}(\boldsymbol{\epsilon})\sigma} c_{\alpha,\mathbf{R}(\boldsymbol{\epsilon})\sigma}^i \phi_{\alpha,\mathbf{R}(\boldsymbol{\epsilon})\sigma}(\mathbf{r}) \quad (12.14)$$

where $\phi_{\alpha,\mathbf{R}(\boldsymbol{\epsilon})\sigma}(\mathbf{r})$ denotes the atomic wave functions localized at the lattice site $\mathbf{R}(\boldsymbol{\epsilon})$.

In addition to the Coulomb matrix elements, one has to calculate the matrix elements $\mathbf{d}_{ij}^{eh} = e_0 \langle \psi_i^e | \mathbf{r} | \psi_j^h \rangle$ of the dipole operator $e_0 \mathbf{r}$ using the TB wave functions $\Phi_i(\mathbf{r})$. This expression gives information on selection rules, allowed and forbidden transitions, and oscillator strengths [198]. With the decomposition of the operator \mathbf{r} , Eq. (12.13), and

the TB wave functions, Eq. (12.14), the dipole matrix elements $d_{ij}^{eh} = \mathbf{e} \mathbf{d}_{ij}^{eh}$ explicitly read

$$d_{ij}^{eh} = e_0 \sum_{\mathbf{R}(\epsilon) \mathbf{R}'(\epsilon) \alpha \beta \sigma \sigma'} c_{\mathbf{R}(\epsilon), \alpha, \sigma}^{i, e*} c_{\mathbf{R}'(\epsilon), \beta, \sigma'}^{j, h} \cdot \left[\mathbf{e} \mathbf{R}(\epsilon) \delta_{\mathbf{R}(\epsilon) \mathbf{R}'(\epsilon)} \delta_{\alpha \beta} \delta_{\sigma \sigma'} + \langle \mathbf{R}(\epsilon), \alpha, \sigma | \mathbf{e} \tilde{\mathbf{r}} | \mathbf{R}'(\epsilon), \beta, \sigma' \rangle \right]. \quad (12.15)$$

The first part in Eq. (12.15) stems from the TB coefficients (“envelope”) weighted with the position of the corresponding atom site. The second part contains the matrix elements of the operator $\tilde{\mathbf{r}}$ with the localized (atomic) basis orbitals $\phi_{\alpha \mathbf{R}}(\mathbf{r})$ and is determined by their spatial dependence inside the unit cell. Following the discussion of Section 10.2, this orbital part must be calculated using orthogonalized Slater orbitals. In order to estimate the importance of the orbital part, we performed the calculation in the absence of strain. It turns out that the orbital part, for light polarizations [110], $[1\bar{1}0]$, and [001], respectively, is negligible compared to the envelope part. Therefore, the dipole matrix elements d_{ij}^{eh} , Eq. (12.15), are approximated in the following by:

$$d_{ij}^{eh} \approx e_0 \sum_{\mathbf{R}(\epsilon) \mathbf{R}'(\epsilon) \alpha \beta \sigma \sigma'} c_{\mathbf{R}(\epsilon), \alpha, \sigma}^{i, e*} c_{\mathbf{R}'(\epsilon), \beta, \sigma'}^{j, h} \left[\mathbf{e} \mathbf{R}(\epsilon) \delta_{\mathbf{R}(\epsilon) \mathbf{R}'(\epsilon)} \delta_{\alpha \beta} \delta_{\sigma \sigma'} \right]. \quad (12.16)$$

Similar to the bulk systems, a separation of the orbital α and spin part σ is prohibited by the spin-orbit coupling. Furthermore, and in contrast to the bulk case, there is strong band mixing. This prevents a strict classification of QD single-particle states according to their angular momentum. Therefore, even total angular momentum selection rules are no longer applicable. Consequently, any treatment of many-body effects in QDs based on strict selection rules for the total angular momentum yields inaccurate predictions of level degeneracies, because it ignores the band mixing characteristics of zero-dimensional structures. Nevertheless it turns out that the basic pattern of the exciton structure is governed by the total angular momentum while the band mixing introduces a perturbation.

An often discussed quantity in QD systems with a zinc blende structure is the so-called *light-polarization anisotropy* λ . The light-polarization anisotropy is defined as the ratio of the absorption for light polarized along the $[1\bar{1}0]$ and $[110]$ axes [31]:

$$\lambda = \frac{P_{[1\bar{1}0]}}{P_{[110]}} = \frac{|\langle \psi_{e1} | r_{[1\bar{1}0]} | \psi_{h1} \rangle|^2}{|\langle \psi_{e1} | r_{[110]} | \psi_{h1} \rangle|^2}. \quad (12.17)$$

The polarization anisotropy λ can deviate from unity for three different reasons: (i) The geometric dimensions of the QD are different along the $[110]$ and $[1\bar{1}0]$ direction. (ii) The underlying zinc blende structure makes the $[110]$ and $[1\bar{1}0]$ directions inequivalent. (iii) A piezoelectric field breaks the symmetry. As discussed in Section 12.1.3, we neglect the piezoelectric field. Furthermore, the results of Fonoberov *et al.* [72] indicate that the built-in field for a truncated pyramidal GaN QDs does not break the symmetry. Consequently, in a square-based pyramid, where the geometric factor does not

contribute, a $\mathbf{k} \cdot \mathbf{p}$ model neglecting piezoelectricity produces $\lambda = 1$. This is because the $\mathbf{k} \cdot \mathbf{p}$ approach neglects the atomistic details, except for small asymmetry effects introduced by an atomistic strain field, and treats the square-based pyramid as having the same symmetry along $[110]$ and $[\bar{1}\bar{1}0]$ direction. For this reason, such an approach can only account for the geometrical factor. In an atomistic approach, such as TB models or pseudopotential calculations, both contributions are naturally included. Therefore, even in a square-based pyramidal QD, one could expect deviations from unity.

This section was devoted to the many-body Hamiltonian and the calculation of Coulomb and dipole matrix elements. Furthermore, we have introduced the so-called light-polarization anisotropy λ . In the following chapter we discuss the single-particle states and energies of the truncated pyramidal GaN QD and analyze the excitonic absorption spectrum with regard to λ .

13 Results for Truncated Pyramidal GaN Quantum Dots

In Section 12.1 the strain-dependent TB model for the calculation of single-particle states and energies was outlined. To address many-body effects, the Hamiltonian for a system of interacting charge carriers was introduced in Section 12.2. The following chapter focuses on the calculation of electronic and optical properties of a truncated pyramidal GaN QD. In a first step we will discuss the bound single-particle states for electrons and holes. Subsequently, the excitonic absorption spectrum of the GaN QD will be analyzed.

13.1 Electron Single-Particle States and Energies

Figure 13.1 shows the calculated probability density for the electron wave functions of the truncated pyramidal GaN/AlN QDs in the presence and absence of the strain field. Here only the first four bound states are displayed. For each state the orbital contributions to the TB single-particle wave functions are given. The dominant contributions are highlighted. Due to time reversal symmetry, each state is twofold degenerate.

Without taking the strain field into account, we obtain the following results: The first state e_1 is commonly described as *s*-like as it shows no nodes. The states e_2 and e_3 are *p*-like with nodal planes (110) and (1 $\bar{1}$ 0), whereas the state e_4 is commonly described as *d*-like. Due to the underlying zinc blende lattice, the \bar{C}_{4v} symmetry is reduced to \bar{C}_{2v} . Hence, the states e_1 to e_4 correspond to the A_1 , B_1 , B_2 and A_2 irreducible representations of the double group \bar{C}_{2v} . The \bar{C}_{2v} symmetry of the system results in a splitting Δ_{e_2,e_3} of the *p* states e_2 and e_3 . Furthermore, in accordance with the underlying zinc blende structure the states e_2 and e_3 are aligned along the [1 $\bar{1}$ 0] and [110] directions, respectively.

Including strain, the electron ground state e_1 is slightly elongated along the [1 $\bar{1}$ 0] direction. Since the atomic structure along [110] and [1 $\bar{1}$ 0] is different in a zinc blende lattice, the strain field emphasizes this anisotropy even more. This effect is clearly visible by comparing the state e_4 with and without strain field. The wave functions of the states e_2 and e_3 are only slightly affected by strain.

The values of the e_1 - e_2 and e_3 - e_4 energy spacings without strain are denoted by Δ_{e_1,e_2}^0 and Δ_{e_3,e_4}^0 , respectively. From our calculation we derive the values $\Delta_{e_1,e_2}^0 = 128.6$ meV

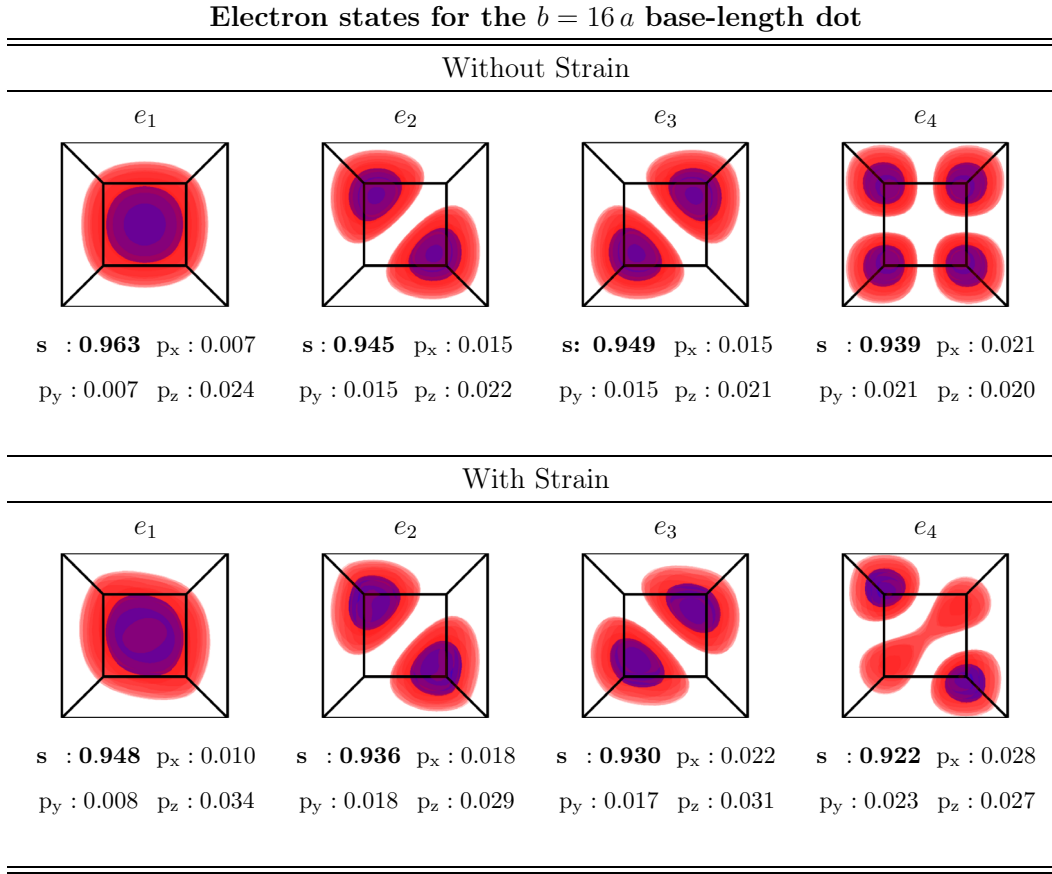


Figure 13.1: Isosurfaces of the modulus squared electron wave functions with and without strain for the embedded $b = 16a$ truncated pyramidal GaN QD. The light and dark surfaces correspond to 0.1 and 0.5 of the maximum probability density, respectively.

and $\Delta_{e_3,e_4}^0 = 112.95$ meV. The splitting of the two p states is $\Delta_{e_2,e_3}^0 = 0.21$ meV. Including strain, the corresponding quantities are denoted by Δ_{e_1,e_2} , Δ_{e_3,e_4} and Δ_{e_2,e_3} . In this case we obtain $\Delta_{e_1,e_2} = 115.93$ meV, $\Delta_{e_3,e_4} = 96.77$ meV and $\Delta_{e_2,e_3} = 30.35$ meV. Due to the strain field, the splitting of the p states is drastically increased. The splittings

	Electrons		
	Δ_{e_1,e_2} [meV]	Δ_{e_2,e_3} [meV]	Δ_{e_3,e_4} [meV]
No Strain	128.6	0.21	112.95
Strain	115.93	30.35	96.77

Table 13.1: Influence of strain-effects on the level spacings $\Delta_{e_1,e_2} = |E_{e_1} - E_{e_2}|$, $\Delta_{e_2,e_3} = |E_{e_2} - E_{e_3}|$, for electrons in a truncated pyramidal GaN QD. The base length of the truncated pyramid is $b = 16a$.

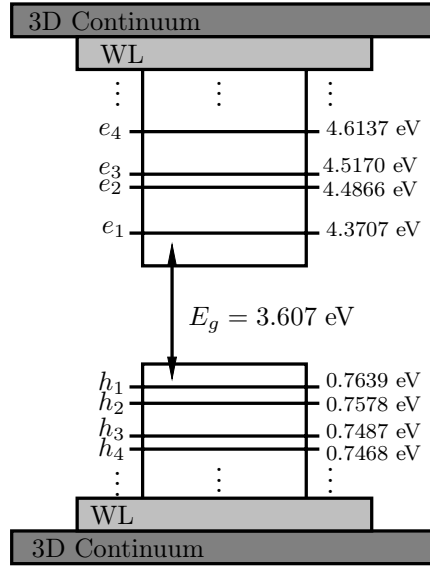


Figure 13.2: Schematic illustration of the electronic structure of the truncated pyramidal GaN QD, deduced from our strain dependent $s_c p_a^3$ TB model. The energies are shown relative to the top of the AlN valence band. WL denotes the GaN wetting layer 2D continuum, below (above) the bulk AlN barrier 3D continuum.

are summarized in Table 13.1, and the energy levels of the truncated pyramidal GaN QD including strain are schematically depicted in Figure 13.2. All energies are given relative to the AlN valence band edge.

13.2 Hole Single-Particle States and Energies

In Figure 13.3 the first four calculated modulus squared hole wave functions in the presence as well as in the absence of the strain field are shown. In contrast to the electron states, the hole states cannot be approximated by the solution of a single band Hamiltonian. Instead, there is strong mixing between the different orbitals. In contrast to QW systems, where the formation of bound hole states is dominated by only one of the p -like valence bands [140], at least two atomic p states lead to the formation of QD hole states, as indicated in Figure 13.3. Therefore a multi-band approach is required to describe the single-particle hole states of a truncated pyramidal GaN QD. The larger effective mass for the holes results in an increased quantum confinement of the hole states and consequently in a larger number of bound states. The single-particle hole states are only slightly affected by the strain field. This can be attributed to the fact that the confined hole states have less “contact” with the interface than the electron states and the fact that the strain contribution is higher in this region.

From the one-particle energies, we obtain a single-particle energy gap $E_g = e_1 - h_1$ in the absence of strain of $E_g^0 = 3.689$ eV and of $E_g = 3.607$ eV in presence of the

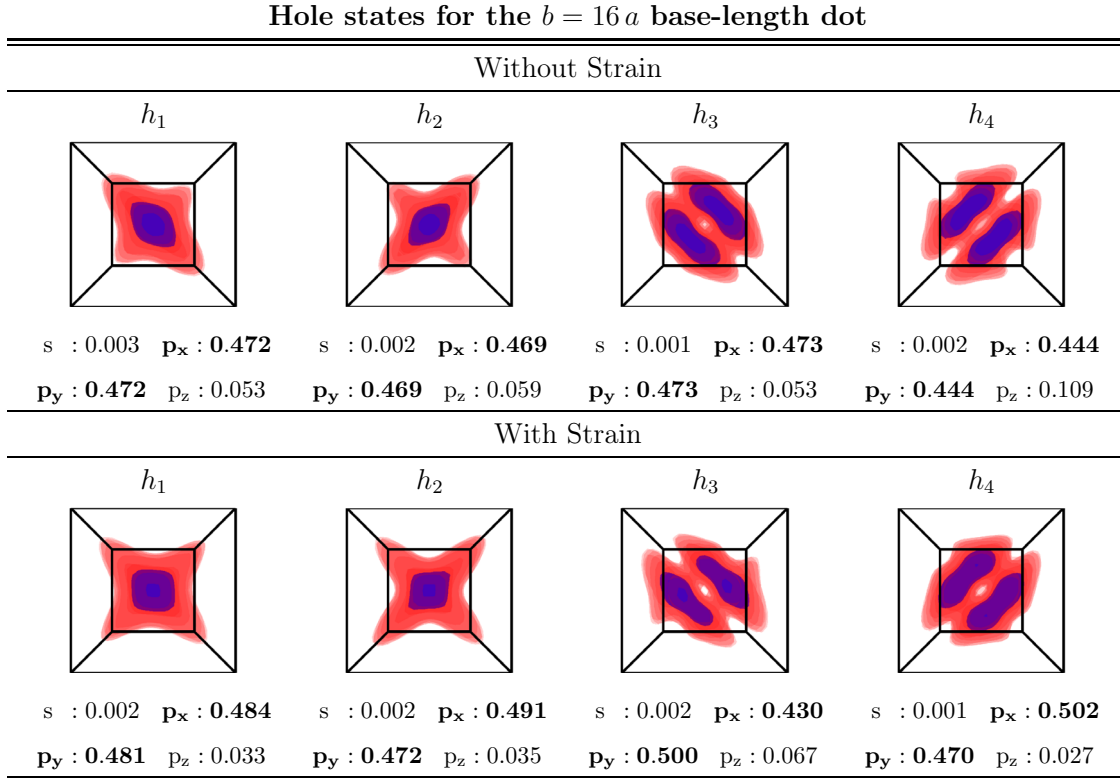


Figure 13.3: Isosurfaces plots of the modulus squared hole wave functions with and without strain for the embedded $b = 16a$ truncated pyramidal GaN QD. See caption of Figure 13.1 for more details.

strain field. The level spacing $h_1 - h_2$, $h_2 - h_3$ and $h_3 - h_4$ without taking strain into account are denoted by Δ_{h_1, h_2}^0 , Δ_{h_2, h_3}^0 and Δ_{h_3, h_4}^0 , respectively. The calculated values are $\Delta_{h_1, h_2}^0 = 6.148$ meV, $\Delta_{h_2, h_3}^0 = 6.0$ meV, and $\Delta_{h_3, h_4}^0 = 4.539$ meV. Including strain effects one finds $\Delta_{h_1, h_2} = 6.094$ meV, $\Delta_{h_2, h_3} = 9.132$ meV, and $\Delta_{h_3, h_4} = 1.831$ meV. Table 13.2 summarizes the energy splittings, and the hole level structure including strain is schematically shown in Figure 13.2. Due to the larger effective mass of the holes, the level spacings are much smaller than the spacings of the electrons. In the $\mathbf{k} \cdot \mathbf{p}$ calculation of Fonoberov *et al.* [72] for a truncated pyramidal GaN QD with a zinc blende structure, the first two hole states are degenerate. This is a clear shortcoming of the $\mathbf{k} \cdot \mathbf{p}$ model, since it cannot resolve the atomistic structure of the underlying zinc blende lattice. Here, even without strain, the states h_1 and h_2 are split due to the \bar{C}_{2v} of the system. This splitting leads to a polarization anisotropy and additional lines in the excitonic absorption spectrum, as we will see in the following section.

13.3 Excitonic Absorption Spectra

Starting from the calculated single-particle wave functions the dipole and Coulomb matrix elements are obtained from Eq. (12.10) and Eq. (12.16). The calculation of

	Holes		
	Δ_{h_1, h_2} [meV]	Δ_{h_2, h_3} [meV]	Δ_{h_3, h_4} [meV]
No Strain	6.15	6.0	4.54
Strain	6.09	9.13	1.83

Table 13.2: Influence of strain-effects on the level spacings $\Delta_{h_1, h_2} = |E_{h_1} - E_{h_2}|$ and $\Delta_{h_2, h_3} = |E_{h_2} - E_{h_3}|$ for holes in a truncated pyramidal GaN QD. The base length of the truncated pyramid is $b = 16a$.

excitonic absorption spectra in this section can directly be performed starting from the many-particle Hamiltonian in second quantization as given in Section 12.2. For the localized states configuration-interaction calculations are applied. To keep the discussion simple, only the first three bound states for electrons and holes are included in the calculation. This can be justified by their energy separation to higher states in the structure. The excitonic absorption spectra are calculated using Fermi's golden rule, given in Eq. (10.9).

Figure 13.4 a) shows the excitonic absorption spectra of the “artificially” unstrained truncated pyramidal QD without Coulomb interaction, while Figure 13.4 b) displays the spectrum with Coulomb interaction and strain. The excitonic absorption spectra of the QD are calculated for different light polarizations ($\mathbf{e} \sim (x, \pm y, 0)$, $\mathbf{e} \sim (0, 0, z)$). The different absorption lines in each spectrum correspond to the excitation of an exciton in the QD. With and without Coulomb interaction, there is a strong anisotropy between the [001] and the in-plane polarization directions, and a weaker anisotropy between $[1\bar{1}0]$ and $[110]$ directions. The latter reflects the \bar{C}_{2v} symmetry of the single-particle wave functions. Without Coulomb interaction, the two peaks on the low energy side correspond to transitions where the electron is in the ground state e_1 and the hole in state h_1 and h_2 , respectively. The states h_1 and h_2 are split by about 6 meV due to the C_{2v} symmetry of the underlying zinc blende structure. In the $\mathbf{k} \cdot \mathbf{p}$ calculation of Fonoberov *et al.* [72], the states h_1 and h_2 are degenerate. Therefore only one line is expected in such a model. The two bright lines for the polarizations $[1\bar{1}0]$ and $[110]$ on the high energy side correspond to the transitions $h_3 - e_2$ and $h_3 - e_3$. These lines are energetically separated due to the small splitting of electron p -states of about 0.21 meV. The magnitudes of the oscillator strength for the $[110]$ and $[1\bar{1}0]$ directions follow from the orientations of the single-particle states displayed in Figure 13.1 and Figure 13.3. For example, the electron ground state without strain is nearly isotropic. The hole ground state is aligned along the $[1\bar{1}0]$ direction. Therefore the transition $e_1 - h_1$ is favored by the $[1\bar{1}0]$ polarization.

Including Coulomb interaction and strain, the absorption lines shift to lower energies due to the red-shift in the single-particle band gap and the attractive interaction between electron and hole. This demonstrates that the strain introduces mainly energetic corrections with respect to the spectrum without strain, which is also reflected in the

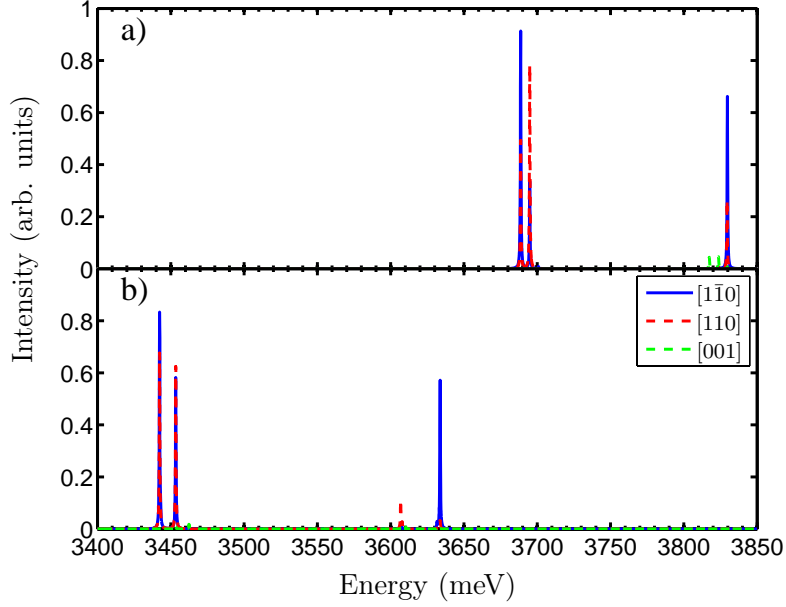


Figure 13.4: (Color online). Excitonic absorption spectrum of a truncated pyramidal GaN QD for different light polarizations. a) Spectrum without Coulomb interaction and strain. b) Spectrum with Coulomb interaction and strain.

small modifications of the single-particle wave functions. According to the CI calculation, the two lines on the low energy side are dominated by contributions where the electron is in state e_1 and the hole in state h_1 and h_2 , respectively.

Since the states h_2 and h_3 are only slightly elongated along the $[1\bar{1}0]$ and $[110]$ direction, respectively, the polarization anisotropy is weaker compared to the results without strain field. The large splitting of the two lines on the high energy side can be attributed to the splitting $\Delta_{e_2, e_3} = 30.4$ meV of the electron p states e_2 and e_3 .

The ratios of the dipole matrix elements for light polarized along the $[1\bar{1}0]$ and $[110]$ directions are calculated from Eq. (12.17). In case of the $h_1 - e_1$ transition, we find a polarization anisotropy ratio of $\lambda = 1.34$ for this truncated pyramidal GaN QD. Again, the magnitude of the ratios reflects the orientation of the single-particle states displayed in Figure 13.1 and Figure 13.3. To the best of our knowledge, there has been no measurements of the polarization anisotropy in cubic GaN QDs. In InAs/GaAs, Yang *et al.* measured this anisotropy for $e_i - h_i$ excitonic recombination in QDs formed by four $\{136\}$ faceted planes and a height to base ratio of 4:1, which is similar to the aspect ratio of our truncated pyramid. The authors obtained a polarization anisotropy ratio of $\lambda_{e_1, h_1} = 1.2$. Yang *et al.* [227] performed $\mathbf{k} \cdot \mathbf{p}$ calculations for an elongated dot geometry, which include the geometric factor but not the atomic factor discussed in Section 12.2. A polarization anisotropy of $\lambda = 1.8$ is found. The pseudopotential calculation of Wang *et al.* [31] for a square-based pyramidal InAs QD leads to a value of $\lambda = 1.26$. These investigations as well as ours reveal, that the major part of a polarization anisotropy λ can already be explained by a square-based pyramidal QD.

In other words, even without a deformation of the pyramid (“geometrical factor”) an atomistic approach yields a distinct polarization anisotropy λ . Therefore, the geometric shape anisotropy of a QD cannot be deduced using $\mathbf{k}\cdot\mathbf{p}$ calculations to fit the measured polarization anisotropy, as suggested by Yang *et al.* [227], since the $\mathbf{k}\cdot\mathbf{p}$ simulations lack the atomistic symmetries. This comparison emphasizes the importance of an atomistic simulation for a detailed description of the optical properties of semiconductor QDs.

Part V

Summary and Outlook

In this thesis, different tight-binding (TB) models including strain and built-in electric fields have been applied to the calculations of electronic and optical properties of semiconductor quantum dots (QDs) and nanocrystals. The great advantage of the presented approach is the use of a theoretical model, which takes into account the atomistic structure of the QD. In other words, symmetry related physical effects are naturally included. Furthermore, the TB approach allows for a realistic description of the geometrical shape of the nanostructure. The predictive power of a TB model for QD structures is assured by the choice of the material parameters for the bulk semiconductors: Given that the calculated TB bulk band structure describes the band structure sufficiently well in the region of interest, a proper description of the electronic states in QDs is achieved. Based on the electronic structure emission and absorption spectra were calculated. A coherent computational framework was established and the accuracy has been validated by comparison with experiments and other theoretical methods.

In the first part of this thesis, an empirical $s_c p_a^3$ TB model was applied for the calculation of the electronic properties of group II-VI pyramidal semiconductor QDs and spherical nanocrystals with a zinc blende structure. For the pyramidal QD systems the numerical diagonalization yields a discrete spectrum of bound electron (hole) states localized in the region of the embedded QD. These discrete states are energetically below (above) the continuum of the wetting layer states. The dependence of the bound eigenenergies and their degeneracy on strain and on the thickness of the WL have been discussed. Furthermore the influence of the spin-orbit coupling has been investigated. Our atomistic approach automatically lifts certain degeneracies and leads consequently to a splitting between, for instance, the first and the second excited electron state, whereas a comparable 8-band- $\mathbf{k} \cdot \mathbf{p}$ model yields degenerate eigenenergies for the corresponding states. Looking at the states themselves, one finds that electron states can be roughly classified as s -like, p -like, etc. states. In contrast, the hole states cannot be classified according to such simple symmetries because they are dominated by a mixing between the different (anion) p orbitals. This emphasizes the importance of a multi band approach for a proper treatment of the electronic properties. These band mixing effects have also consequences, e.g., for the calculation of dipole matrix elements between electron and hole states, which determine the selection rules for optical transitions. In spite of the spherical symmetry of the CdSe nanocrystals the hole states do not have a simple s, p, d symmetry as one might be expect but are intermixtures of atomic

p orbitals. The results obtained from the TB model agree very well with experimental data obtained by STM measurements.

In addition to CdSe QDs, also electronic and optical properties of lens-shaped InN/GaN QDs were investigated. The wurtzite crystal structure of the underlying lattice is fully included in the formulation. Dipole and Coulomb matrix elements have been calculated which allow the investigation of multi-exciton spectra with microscopically determined input parameters. The calculations reveal the strong influence of band-mixing effects on the optical transitions between the Coulomb correlated electron-hole states. The inclusion of the built-in field for the strained wurtzite crystal structure leads to a quantum confined Stark effect which creates a strong red-shift of the one-particle gap. Additionally, the Coulomb matrix elements are modified and the oscillator strengths are strongly reduced due to the spatial separation of electron and hole wave functions. As an important consequence for future optoelectronic applications, we predict vanishing exciton and biexciton ground state emission for small lens-shaped InN/GaN QDs. In strong contrast to conventional III-V system, the emission from InN QDs is dominated by 'skew' excitons, which give rise to completely different multi-exciton emission spectra. For larger QDs, we found that the internal electric field can reverse the energetic order of the lowest hole states, which results in a bright ground state emission but with drastically reduced oscillator strengths caused by the quantum confined Stark effect.

In the last part, the electronic and optical properties of truncated pyramidal GaN/AlN QDs with a zinc blende structure are discussed by means of a strain dependent $s_c p_a^3$ TB model. The analysis of the electronic structure reveals that, while the bound electron states are essentially derived from the s -orbitals, the hole states show massive band mixing. Consequently, in contrast to the electron states it is impossible to classify the different hole states as s , p , and d states. Therefore, the optical properties of such a dot cannot be interpreted by using a simplified description that includes only heavy-hole states or only light-hole states. Furthermore, our atomistic approach naturally captures the C_{2v} symmetry of the system. This leads, for instance, to a splitting of the p -like electron states and the first two hole states, which are degenerate in a $\mathbf{k} \cdot \mathbf{p}$ model. This splitting of the hole states results in two distinct lines in the excitonic absorption spectrum. Furthermore the lowest interband transition has a very different intensity along the $[110]$ and $[1\bar{1}0]$ direction. This anisotropy exists even in the absence of strain, reflecting both the underlying C_{2v} symmetry of the QD system and the band mixing. Such an anisotropy is absent in conventional $\mathbf{k} \cdot \mathbf{p}$ models for square-based pyramidal QDs.

The TB framework presented in this thesis for the investigation of electronic and optical properties of semiconductor QDs can be extended in several directions. For example, a combination with ab-initio calculations is possible by determining the TB parameters from a first-principles band structure calculation of the bulk material. For the nitride QDs, a direct theory-experiment comparison would be favorable. In addition to isolated QDs one could, starting from the accurate TB description of the single-particle states and followed by a configuration interaction approach, also analyze the optical properties of laterally [228] or vertically coupled [229, 230] QDs. In such molecules one has the

additional possibility of tailoring the optical properties by varying the distance between the dots.

The microscopic description of the electronic and optical properties of modern low-dimensional systems is an important step towards an understanding and improving of nanostructure based devices.

Appendix

A Parameters for CdSe and ZnSe

	CdSe	ZnSe
E_g [eV]	1.74 [161]	2.8201 [161]
Δ_{so} [eV]	0.41 [161]	0.43 [161]
m_e	0.12 [161]	0.147 [231]
γ_1	3.33 [161]	2.45 [231]
γ_2	1.11 [161]	0.61 [231]
γ_3	1.45 [161]	1.11 [231]
C_{12} [GPa]	46.3 [232]	50.6 [232]
C_{11} [GPa]	66.7 [232]	85.9 [232]

Table A.1: Properties of the CdSe and ZnSe band structures. The lattice constants are given by 6.077 Å and 5.668 Å, respectively. E_g denotes the band gap, Δ_{so} the spin-orbit coupling and m_e the effective electron mass. The Kohn-Luttinger-Parameters are γ_1, γ_2 and γ_3 . The C_{ij} are the elements of the elastic stiffness tensor.

Parameter	ZnSe		CdSe	
	TB	TB-NO SO	TB	TB-NO SO
$E_{xx}(000)_{aa}$	-1.7277	-2.0413	-1.2738	-1.7805
$E_{ss}(000)_{cc}$	7.0462	12.1223	3.6697	10.8053
$E_{sx}(\frac{1}{2}\frac{1}{2}\frac{1}{2})_{ac}$	1.1581	0.2990	1.1396	0.4260
$E_{xx}(110)_{aa}$	0.1044	0.2185	0.1512	0.3120
$E_{xx}(011)_{aa}$	0.1874	0.0732	0.1738	0.0129
$E_{xy}(110)_{aa}$	0.3143	0.4285	0.1512	0.3120
$E_{ss}(110)_{cc}$	-0.3522	-0.7752	-0.1608	-0.7554
λ	0.1433	0	0.1367	0

Table A.2: Tight-binding parameters (in eV) with (TB) and without (TB-NO SO) spin-orbit coupling for ZnSe and CdSe, using the notation of Ref. [47].

B Parameters for InN and GaN

	InN	GaN
a [Å]	3.545	3.189
c [Å]	5.703	5.185
e_{31} [C/m ²]	-0.23	-0.20
e_{33} [C/m ²]	0.39	0.29
C_{13} [GPa]	9.4	11.4
C_{33} [GPa]	20.0	38.1
P^{spont} [C/m ²]	-0.042	-0.034

Table B.3: Parameters for lattice, piezoelectric e_{ij} , elastic C_{ij} , and spontaneous polarization P^{spont} constants for wurtzite InN and GaN, taken from Ref. [146].

Parameter	InN [eV]			GaN [eV]		
	$\Delta_{\text{cf}} = 0$	$\Delta_{\text{cf}} \neq 0$	$\Delta_{\text{cf}} \neq 0$	$\Delta_{\text{cf}} = 0$	$\Delta_{\text{cf}} \neq 0$	$\Delta_{\text{cf}} \neq 0$
	$\Delta_{\text{so}} = 0$	$\Delta_{\text{so}} = 0$	$\Delta_{\text{so}} \neq 0$	$\Delta_{\text{so}} = 0$	$\Delta_{\text{so}} = 0$	$\Delta_{\text{so}} \neq 0$
E(s,a)	-6.791	-6.5134	-6.6046	-11.012	-8.9893	-8.5282
E(p,a)	0.000	0.0000	0.0000	0.005	0.0015	-0.0024
E(p _z ,a)	0.000	-0.0418	-0.0400	0.005	-0.0203	-0.0208
E(s,c)	-3.015	-3.3923	-3.3500	1.438	0.7851	0.6945
E(p,c)	8.822	8.8220	8.8203	10.896	10.0986	10.0996
V(s,s)	-5.371	-5.5267	-5.5330	-5.318	-5.6918	-5.6808
V(x,x)	0.022	0.0156	0.1221	-0.222	-0.1223	-0.0699
V(x,y)	6.373	6.3794	6.2772	7.136	6.7902	6.7328
V(sa,pc)	0.370	0.9576	0.9307	0.628	0.2641	1.3633
V(pa,sc)	7.5	7.5574	7.4136	7.279	8.0324	7.7173
λ	0	0	0.0016	0	0	0.0023

Table B.4: Tight-binding parameters (in eV) for the nearest neighbors of wurtzite InN and GaN. The notation of Ref. [166] is used.

wurtzite	zinc blende	Slater-Koster
$4W_{ss}$	$V(s, s)$	$4V(ss\sigma)$
$\left(\frac{4}{3}\right) [W_{zz} + 2W_{xx}]$	$V(x, x)$	$\left(\frac{4}{3}\right) [V(pp\sigma) + 2V_{pp\pi}]$
$\left(\frac{4}{3}\right) [W_{zz} - W_{xx}]$	$V(x, y)$	$\left(\frac{4}{3}\right) [V(pp\sigma) - V_{pp\pi}]$
$-\left(\frac{4}{\sqrt{3}}\right) W_{sz}$	$V(sa, pc)$	$\left(\frac{4}{\sqrt{3}}\right) V(sp\sigma)$
$w_{ss} - W_{ss}$	0	0
$\left(\frac{1}{3}\right) [w_{xx} + w_{yy} + w_{zz}] - \left(\frac{1}{3}\right) [2W_{xx} + W_{zz}]$	0	0
$\left(\frac{1}{2}\right) [w_{xx} + w_{yy} - 2w_{zz}] - \left(\frac{1}{3}\right) [W_{zz} - W_{xx}]$	0	0
$\left(\frac{3}{8}\right) [w_{xx} - w_{yy}] - \left(\frac{1}{3}\right) [W_{zz} - W_{xx}]$	0	0
$\sqrt{3}w_{sz} + \left(\frac{1}{\sqrt{3}}\right) W_{sz}$	0	0
$-\sqrt{3}w_{zs} - \left(\frac{1}{\sqrt{3}}\right) W_{zs}$	0	0
$\frac{\sqrt{6}}{4}w_{sx} + \left(\frac{1}{\sqrt{3}}\right) W_{sz}$	0	0
$-\frac{\sqrt{6}}{4}w_{xs} - \left(\frac{1}{\sqrt{3}}\right) W_{zs}$	0	0
$\left(\frac{3\sqrt{2}}{4}\right) w_{zx} - \left(\frac{1}{3}\right) [W_{zz} - W_{xx}]$	0	0
$\left(\frac{3\sqrt{2}}{4}\right) w_{xz} - \left(\frac{1}{3}\right) [W_{zz} - W_{xx}]$	0	0

Table B.5: Relationships between the parameters of the TB model used in Part III, the zinc blende notation [120] and Slater-Koster notation [47].

From relationships above, one can determine the following equations for the different wurtzite TB parameters w 's and W 's, respectively:

$$\begin{aligned}
 W_{ss} &= \frac{1}{4}V(s, s) \quad , \quad W_{sz} = -\frac{\sqrt{3}}{4}V(sa, pc) \quad , \\
 W_{zs} &= \frac{\sqrt{3}}{4}V(pa, sc) \quad , \quad W_{zz} = \frac{1}{4}(V(x, x) + 2V(x, y)) \quad , \\
 W_{xx} &= \frac{1}{4}(V(x, x) - V(x, y)) \quad , \quad w_{ss} = W_{ss} \quad , \\
 w_{sz} &= -\frac{1}{3}W_{sz} \quad , \quad w_{sx} = -\frac{2\sqrt{2}}{3}W_{sz} \quad , \\
 w_{zs} &= -\frac{1}{3}W_{zs} \quad , \quad w_{zz} = \frac{1}{4}V(x, x) - \frac{1}{6}V(x, y) \quad , \\
 w_{zx} &= \frac{1}{3\sqrt{2}}V(x, y) \quad , \quad w_{xs} = -\frac{2\sqrt{2}}{3}W_{zs} \quad , \\
 w_{xz} &= -\frac{1}{3\sqrt{2}}V(x, y) \quad , \quad w_{xx} = \frac{1}{9}(W_{xx} + 8W_{zz}) \quad , \\
 w_{yy} &= W_{xx}
 \end{aligned}$$

With the knowledge of the TB parameters $E_{p,p}^a$, $E_{s,s}^a$, $E_{s,s}^c$, $E_{p,p}^c$, $V(s, s)$, $V(x, x)$, $V(x, y)$, $V(sa, pc)$ and $V(pa, sc)$ all other parameters can be obtained.

C Coulomb Matrix Elements

In this appendix we summarize the approximations that yield the Coulomb matrix elements in the form used in Eq. (10.12), and we point out in more detail on which assumptions these matrix elements are based. Furthermore, the quasi-analytic calculation of the on-site matrix elements is briefly outlined. The discussion in this appendix is supposed to deepen the understanding of approaches to the Coulomb matrix elements in semiconductor quantum dots (QDs) as already used in earlier works [140].

Starting point is the Coulomb matrix element as given in Eq. (10.11):

$$V_{ijkl} = \sum_{\mathbf{R}_1 \mathbf{R}_2 \mathbf{R}_3 \mathbf{R}_4} \sum_{\alpha \beta \gamma \delta} c_{\mathbf{R}_1 \alpha}^{i*} c_{\mathbf{R}_2 \beta}^{j*} c_{\mathbf{R}_3 \gamma}^k c_{\mathbf{R}_4 \delta}^l \cdot \int d^3 r d^3 r' V(\mathbf{r} - \mathbf{r}') \phi_{\mathbf{R}_1 \alpha}^*(\mathbf{r}) \phi_{\mathbf{R}_2 \beta}^*(\mathbf{r}') \phi_{\mathbf{R}_3 \gamma}(\mathbf{r}') \phi_{\mathbf{R}_4 \delta}(\mathbf{r}),$$

In principle, the Coulomb matrix elements involve four atomic orbitals $\phi_{\mathbf{R}\alpha}(\mathbf{r})$. According to Ref. [188] we take only two-center contributions into account. Off-site exchange integrals, with $\mathbf{R}_1 = \mathbf{R}_3$ and $\mathbf{R}_2 = \mathbf{R}_4$, decrease quickly as the distance between the atomic sites increases, due to the orthogonality and the localization of the atomic orbitals [107]. Therefore, terms with exchange character are also neglected. In this approximation, the Coulomb matrix elements are given by

$$V_{ijkl} \approx \sum_{\mathbf{R}\mathbf{R}'} \sum_{\alpha \beta \gamma \delta} c_{\mathbf{R}\alpha}^{i*} c_{\mathbf{R}'\beta}^{j*} c_{\mathbf{R}'\gamma}^k c_{\mathbf{R}\delta}^l \int_{\text{uc}} d^3 \tilde{r} d^3 \tilde{r}' \frac{e_0^2 \phi_{\mathbf{R}\alpha}^*(\tilde{\mathbf{r}}) \phi_{\mathbf{R}'\beta}^*(\tilde{\mathbf{r}}') \phi_{\mathbf{R}'\gamma}(\tilde{\mathbf{r}}') \phi_{\mathbf{R}\delta}(\tilde{\mathbf{r}})}{4\pi\epsilon_0\epsilon_r |\mathbf{R} + \tilde{\mathbf{r}} - \mathbf{R}' - \tilde{\mathbf{r}}'|}.$$

We have decomposed the position operators \mathbf{r} and \mathbf{r}' into the positions \mathbf{R} and \mathbf{R}' of the lattice sites and the positions $\tilde{\mathbf{r}}$ and $\tilde{\mathbf{r}}'$ inside each unit cell. For sites which are far enough apart from each other the exact structure of the localized orbitals is not important. The long-range contributions are dominated by the monopole interaction of two charge densities localized at different lattice sites which leads to the approximation:

$$V_{ijkl} \approx \sum_{\mathbf{R}\mathbf{R}'} \sum_{\alpha \beta \gamma \delta} c_{\mathbf{R}\alpha}^{i*} c_{\mathbf{R}'\beta}^{j*} c_{\mathbf{R}'\gamma}^k c_{\mathbf{R}\delta}^l V(\mathbf{R} - \mathbf{R}') \int d^3 \tilde{r} \phi_{\mathbf{R}\alpha}^*(\tilde{\mathbf{r}}) \phi_{\mathbf{R}\delta}(\tilde{\mathbf{r}}) \int d^3 \tilde{r}' \phi_{\mathbf{R}'\beta}^*(\tilde{\mathbf{r}}') \phi_{\mathbf{R}'\gamma}(\tilde{\mathbf{r}}').$$

Due to the orthogonality of the atomic orbitals, the final result for the Coulomb matrix elements is then given by

$$\begin{aligned} V_{ijkl} &= \sum_{\mathbf{R}\mathbf{R}'} \sum_{\alpha \beta} c_{\mathbf{R}\alpha}^{i*} c_{\mathbf{R}'\beta}^{j*} c_{\mathbf{R}'\beta}^k c_{\mathbf{R}\alpha}^l V(\mathbf{R} - \mathbf{R}') \\ &= \sum_{\mathbf{R}\mathbf{R}'} \sum_{\alpha \beta} c_{\mathbf{R}\alpha}^{i*} c_{\mathbf{R}'\beta}^{j*} c_{\mathbf{R}'\beta}^k c_{\mathbf{R}\alpha}^l \frac{e_0^2}{4\pi\epsilon_0\epsilon_r |\mathbf{R} - \mathbf{R}'|}. \end{aligned} \quad (\text{C.1})$$

The on-site contributions for $|\mathbf{R} - \mathbf{R}'| = 0$ can be calculated by integration of the Coulomb interaction over the volume of one unit cell:

$$V(0) = \frac{1}{V_{\text{uc}}^2} \int_{\text{uc}} d^3 r d^3 r' V(\mathbf{r} - \mathbf{r}'). \quad (\text{C.2})$$

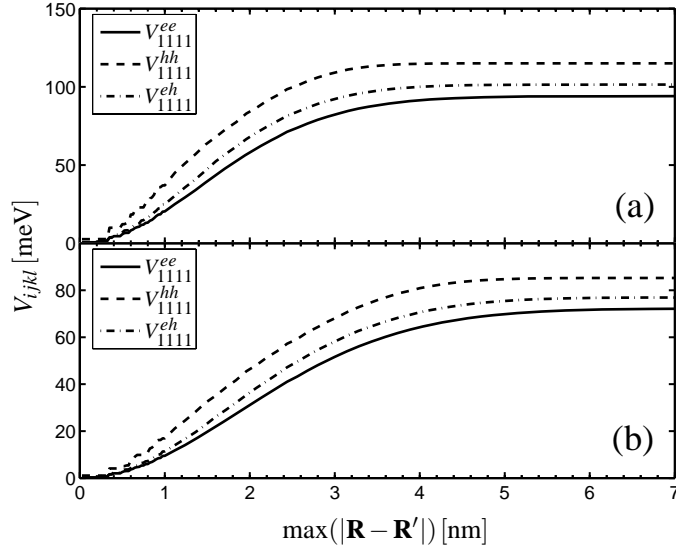


Figure C.1: Coulomb matrix elements calculated with a cut-off radius R_0 with $|\mathbf{R}-\mathbf{R}'| < R_0$ in the sum of Eq. (C.1). Results are shown for the direct electron-electron (solid line), hole-hole (dashed line) and electron-hole (dashed-dotted line) Coulomb matrix elements for the ground state wave functions without the influence of the built-in field. (a) Small QD. (b) Large QD.

As already mentioned in Section 10.2.2, the evaluation of the integral (including the Coulomb singularity) can be done quasi-analytically by expansion of the Coulomb interaction in terms of spherical harmonics following the guidelines given in Ref. [188]. The calculations yield meaningful values of about ~ 16 eV for the unscreened on-site matrix elements. These values are in accordance with other calculations [188]. However, the exact values are not crucial for the QD Coulomb matrix elements since the screened on-site contributions are small compared to the long-range part.

The final result for the Coulomb matrix elements can be interpreted in an intuitive way as already outlined in Section 10.2.2. In Eq. (C.1) the atomic orbitals underlying the TB formulation do no longer enter the calculation of Coulomb matrix elements. Since the on-site and nearest-neighbor contributions – which are mostly affected by the above approximations – are small compared to the total Coulomb matrix elements, only small overall mistakes are made. Nearest-neighbor contributions are underestimated but only small additional contributions would apply to the long-range-dominated Coulomb matrix elements, at least for constant background screening, which is in accordance with the commonly used effective-mass approaches [30].

For illustration purposes, in Figure C.1 results for the Coulomb interaction, Eq. (C.1), are shown which demonstrate that only rather minor contributions to the total matrix elements for our system originate from on-site and nearest-neighbor contributions. Results are depicted for the direct electron-electron, hole-hole, and electron-hole interaction in the smallest (upper panel) and the largest (lower panel) QD for the one-particle ground states without the influence of the built-in field. Similar results are found for all the investigated QD sizes as well as for the excited electron and hole states. The

long-range part of the Coulomb interaction clearly dominates the results for which the treatment applied here can be justified. However, for different material systems or materials with an indirect band-gap, results may change especially for the electron-hole exchange interaction [106] which has not been subject of this thesis.

C.1 Orthogonalized Slater orbitals

In this appendix we give the details concerning the atomic basis orbitals $\phi_{\alpha\mathbf{R}}(\mathbf{r})$. They are required to calculate the optical dipole matrix elements with electron and hole wave functions $\psi_i(\mathbf{r})$ which are evaluated in terms of the empirical TB model. The overlap matrix of the atomic orbitals is given by

$$S_{\alpha\beta}^{\mathbf{R}\mathbf{R}'} = \langle \alpha, \mathbf{R} | \beta, \mathbf{R}' \rangle = \int d^3r \phi_{\alpha}^*(\mathbf{r} - \mathbf{R}) \phi_{\beta}(\mathbf{r} - \mathbf{R}'), \quad (\text{C.3})$$

with the position vectors \mathbf{R}, \mathbf{R}' of the atoms at which the two orbitals $\alpha, \beta \in \{p_x, p_y, p_z, s\}$ are centered. For the original Slater orbitals, part of the overlap matrix, $S_{\alpha\beta}^{0\mathbf{R}'}$, is shown in Figure C.2 for a nitrogen atom in the origin $\mathbf{R} = 0$ in an InN crystal structure. The overlap for the four different nitrogen orbitals $\alpha \in \{p_x, p_y, p_z, s\}$ with neighboring orbitals is stacked in the vertical direction and is visualized by the color coding. Contributions from different neighbors \mathbf{R}' and their different orbitals β are given on the horizontal axis with increasing distance $|\mathbf{R}'|$ to the center nitrogen atom from left to right. The entries one to four on the horizontal axis show the overlap of the normalized orbitals with themselves, which is unity by definition. Contributions five to 20 correspond to the overlap to nearest neighbors (indium) with an averaged overlap of ≈ 0.427 for each neighboring orbital. The overlap 21 to 68 represents the overlap to second nearest neighbor (nitrogen) orbitals, with an averaged overlap of ≈ 0.008 . Elements 69 to 92 give the overlap to third nearest neighbor (indium) orbitals, with an averaged overlap ≈ 0.081 . Within an orthogonal basis this overlap matrix becomes the unit matrix which is a basic assumption for the TB model.

We apply a natural method to obtain an orthogonal set of atomic basis states which fulfill all the basic assumptions underlying the TB formulation in a good approximation. We start with the original Slater orbitals (given in Table 10.3) localized at the atom sites in the wurtzite crystal structure. The overlap matrix $\underline{\underline{\mathbf{S}}}$ is calculated for a finite neighborhood surrounding a central atom (here, up to third nearest neighbors). The aim is to construct a set of orthogonal basis states for which the overlap matrix becomes the unit matrix $\underline{\underline{\mathbf{1}}}$, therefore we are looking for a transformation matrix $\underline{\underline{\mathbf{X}}}$ which fulfills $\underline{\underline{\mathbf{1}}} = \underline{\underline{\mathbf{X}}}^\dagger \underline{\underline{\mathbf{S}}} \underline{\underline{\mathbf{X}}}$. One specific choice for the transformation matrix is obviously given by $\underline{\underline{\mathbf{X}}} = \underline{\underline{\mathbf{S}}}^{-1/2}$. The *non-unitary* transformation matrix $\underline{\underline{\mathbf{X}}}$ which transforms the overlap matrix S into a unit matrix is obtained by $\underline{\underline{\mathbf{X}}} = \underline{\underline{\mathbf{S}}}^{-1/2} = \underline{\underline{\mathbf{T}}} \underline{\underline{\mathbf{s}}}^{-1/2} \underline{\underline{\mathbf{T}}}^\dagger$. Here $\underline{\underline{\mathbf{T}}}$ is the unitary transformation matrix which brings $\underline{\underline{\mathbf{S}}}$ into diagonal form $\underline{\underline{\mathbf{s}}} = \underline{\underline{\mathbf{T}}}^\dagger \underline{\underline{\mathbf{S}}} \underline{\underline{\mathbf{T}}}$. The new (orthogonal) basis states C' are then obtained by the transformation $C' = XC$. This way, new basis orbitals are obtained which are centered around the atom in the center

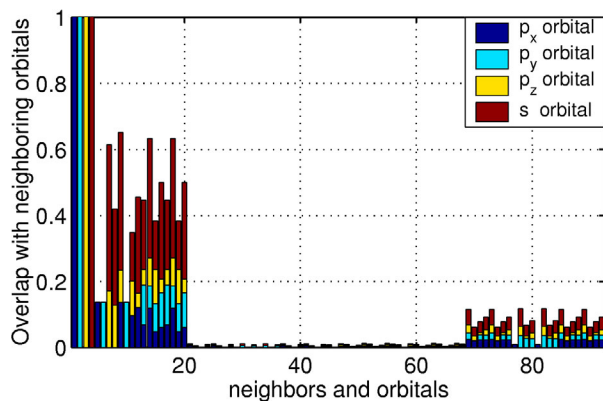


Figure C.2: Overlap matrix $S_{\alpha\beta}^{0\mathbf{R}'}$ for a nitrogen atom to the atomic orbitals centered at the atom sites \mathbf{R}' in the neighborhood up to third-nearest neighbors. The results are calculated with the original Slater orbitals. The overlap for the four different nitrogen orbitals $\alpha \in \{p_x, p_y, p_z, s\}$ is stacked in vertical direction and is visualized by the color coding. Contributions from different neighbors and their different orbitals β are given on the horizontal axis with increasing distance $|\mathbf{R}'|$ to the center nitrogen atom from left to right.

of the chosen neighborhood. The orthogonality to the new orbitals which are centered at atoms up to third nearest neighbors can be checked by calculation of the overlap matrix with the new orbitals as is visualized in Figure C.3 for the example of a nitrogen atom. The corresponding result without orthogonalization is shown in Figure C.2. The averaged overlap is reduced to ≈ 0.013 for nearest neighbor orbitals, to ≈ 0.005 for second nearest neighbor orbitals, and to ≈ 0.009 for third nearest neighbor orbitals. Examples for the basis orbitals which are centered at a nitrogen atom in the crystal lattice are depicted in Figure C.4 without orthogonalization (top) and orthogonalization up to third nearest neighbors (bottom). Two isosurfaces of the probability density are included with 20 % (inner surface) and 0.001 % (outer surface) of the maximum value, respectively. The sum of the non-diagonal overlap matrix elements is reduced by at

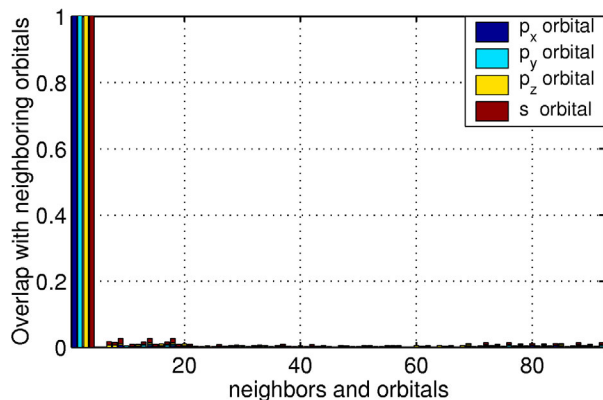


Figure C.3: Same as Figure C.2 but calculated with the orthogonalized Slater orbitals.

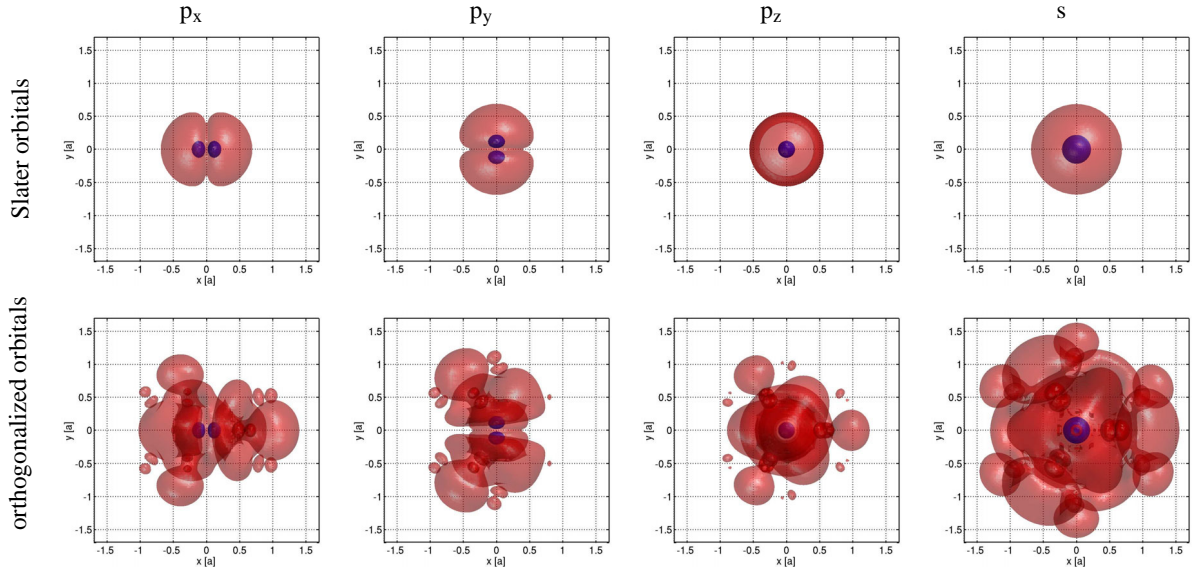


Figure C.4: Nitrogen basis orbitals (Slater orbitals) without (top) and with (bottom) orthogonalization up to third nearest neighbors. The depicted orbitals are from left to right: p_x , p_y , p_z , and s . The viewpoint is on the z -axis. Two isosurfaces of the probability density are included with 20 % (inner surface) and 0.001 % (outer surface) of the maximum value, respectively.

least one order of magnitude for orthogonalization up to third nearest neighbors. The figures, Figures C.2 and C.3, demonstrate that the new basis states are orthogonal in a good approximation. Additionally, they mostly show the original symmetries of atomic orbitals which underly the TB Hamiltonian and are still rather well localized states at a certain atom site, Figure C.4. Only small contributions at the neighboring atom sites are found which are essential to obtain orthogonality. The added orthogonality now justifies the direct connection to the TB coefficients $c_{\mathbf{R}\alpha}^i$ since the orbitals fulfill all basic assumptions underlying an empirical TB model. Therefore the procedure demonstrated here, to obtain an orthogonal set of atomic basis orbitals, helps to improve earlier approaches for the calculation of optical properties from TB calculations.

D Strain Field Equations

The analytic solution of Eq. (12.4) and simplification can be performed using an algebraic software package such as *Maple* or *Mathematica*. The diagonal terms σ_{11} and σ_{22} of the stress tensor are found to be [224]

$$\sigma_{11} = -4\pi\Lambda\chi + \Lambda \sum_{\substack{p=\pm 1 \\ q=\pm 1 \\ n=2,3}} H_1(-1)^n \left[aB \ln(\gamma) - hq \arctan\left(\frac{\beta_{11}}{\alpha_{11}}\right) + \frac{aq}{2} \ln(\alpha_{11}^2 + \beta_{11}^2) \right] ,$$

$$\sigma_{22} = -4\pi\Lambda\chi + \Lambda \sum_{\substack{p=\pm 1 \\ q=\pm 1 \\ n=2,3}} H_2(-1)^n \left[bA \ln(\gamma) - hq \arctan\left(\frac{\beta_{22}}{\alpha_{22}}\right) + \frac{b}{2} \ln(\alpha_{22}^2 + \beta_{22}^2) \right] ,$$

with

$$\begin{aligned} \alpha_{11} &= \frac{X_n C_{11} + Z_n D_{11}}{X_n^2 + Z_n^2} , & \beta_{11} &= \frac{Z_n C_{11} - X_n D_{11}}{X_n^2 + Z_n^2} , \\ \alpha_{22} &= \frac{Y_n C_{22} + Z_n D_{22}}{Y_n^2 + Z_n^2} , & \beta_{22} &= \frac{Z_n C_{22} - Y_n D_{22}}{Y_n^2 + Z_n^2} , \\ C_{11} &= X_1 X_n + Y_1 (Y_n + S) , & C_{22} &= Y_1 Y_n + X_1 (X_n + pS) , \\ D_{11} &= X_1 Z_n + \left(\frac{qbx_1 - pax_2}{h} \right) (Y_n + S) , & D_{22} &= Y_1 Z_n - \left(\frac{qbx_1 - pax_2}{h} \right) (X_n + pS) , \\ H_1 &= \frac{h}{(a^2 + h^2)} , & H_2 &= \frac{h}{(b^2 + h^2)} , \\ A &= \frac{a}{\sqrt{a^2 + b^2 + h^2}} , & B &= \frac{b}{\sqrt{a^2 + b^2 + h^2}} , \\ X_1 &= x_1 + pa \left(1 - \frac{x_3}{h} \right) , & X_2 &= x_1 + pa(1 - f) , \\ Y_1 &= x_2 + qb \left(1 - \frac{x_3}{h} \right) , & Y_2 &= x_2 + qb(1 - f) , \\ X_3 &= x_1 + pa , & Y_3 &= x_2 + qb , \\ Z_2 &= x_3 - hf , & Z_3 &= x_3 , \\ \gamma &= -pAX_n - qBY_n - \frac{hZ_n}{\sqrt{a^2 + b^2 + h^2}} + S , & S &= \sqrt{X_n^2 + Y_n^2 + Z_n^2} . \end{aligned}$$

The quantity χ is equal to 1 inside the volume of the QD and zero outside. The stress component σ_{33} can be deduced from the relation for the hydrostatic stress, σ_h , which is given by

$$\sigma_h = \sigma_{11} + \sigma_{22} + \sigma_{33} = 8\pi\Lambda .$$

This equation reflects that in the isotropic limit the sum of the plane stresses is proportional to the lattice mismatch ϵ_0 inside the QD and zero outside. The three shear stress components σ_{12} , σ_{13} and σ_{23} are given by

$$\begin{aligned}\sigma_{12} &= \Lambda \sum_{\substack{p=\pm 1 \\ q=\pm 1 \\ n=2,3}} \frac{pqh}{\sqrt{a^2 + b^2 + h^2}} (-1)^n \ln(\gamma) , \\ \sigma_{13} &= \Lambda \sum_{\substack{p=\pm 1 \\ q=\pm 1 \\ n=2,3}} p H_1 (-1)^n \left[hB \ln(\gamma) + a \arctan\left(\frac{\beta_{13}}{\alpha_{13}}\right) - \frac{h}{2} \ln(\alpha_{13}^2 + \beta_{13}^2) \right] , \\ \sigma_{23} &= -\Lambda \sum_{\substack{p=\pm 1 \\ q=\pm 1 \\ n=2,3}} H_2 (-1)^n \left[hAq \ln(\gamma) + b \arctan\left(\frac{\beta_{23}}{\alpha_{23}}\right) + \frac{hq}{2} \ln(\alpha_{23}^2 + \beta_{23}^2) \right] ,\end{aligned}$$

with

$$\begin{aligned}\alpha_{23} &= \frac{Y_n C_{23} + Z_n D_{23}}{Y_n^2 + Z_n^2} , & \beta_{23} &= \frac{Z_n C_{23} - Y_n D_{23}}{Y_n^2 + Z_n^2} , \\ \alpha_{13} &= \frac{X_n C_{13} + Z_n D_{13}}{X_n^2 + Z_n^2} , & \beta_{13} &= -p \frac{Z_n C_{13} - X_n D_{13}}{X_n^2 + Z_n^2} , \\ C_{13} &= X_1 X_n + Y_1 (Y_n - qS) , & C_{23} &= Y_1 Y_n + X_1 (X_n + pS) \\ D_{23} &= Y_1 Z_n - \left(\frac{qbx_1 - pax_2}{h} \right) (X_n + pS) , & D_{13} &= X_1 Z_n + \left(\frac{qbx_1 - pax_2}{h} \right) (Y_n - qS) .\end{aligned}$$

E Parameters for Cubic GaN and AlN

	GaN	AlN
E_g [eV]	3.26	4.9
Δ_{so} [eV]	0.017	0.019
m_e	0.15	0.25
γ_1	2.67	1.92
γ_2	0.75	0.47
γ_3	1.10	0.85
C_{12} [GPa]	293	304
C_{11} [GPa]	159	160

Table E.6: Properties of the cubic GaN and AlN band structures. The lattice constants are given by 4.50 Å and 4.38 Å, respectively. E_g denotes the band gap, Δ_{so} the spin-orbit coupling and m_e the effective electron mass. The Kohn-Luttinger-Parameters are γ_1, γ_2 and γ_3 . The C_{ij} are the elements of the elastic stiffness tensor. All parameters are taken from Ref. [72].

Parameter	AlN	GaN
$E_{xx}(000)_{aa}$	-1.4812	-2.0940
$E_{ss}(000)_{cc}$	5.1420	6.5123
$E_{sx}(\frac{1}{2}\frac{1}{2}\frac{1}{2})_{ac}$	1.9490	1.7919
$E_{xx}(110)_{aa}$	-0.0205	0.0818
$E_{xx}(011)_{aa}$	0.4098	0.3585
$E_{xy}(110)_{aa}$	0.2376	0.2568
$E_{ss}(110)_{cc}$	-0.0202	-0.2710
λ	0.0063	0.0057

Table E.7: Tight-binding parameters (in eV) for cubic AlN and GaN, using the notation of Ref. [47].

List of Figures

2.1	Schematic band edge diagram for two materials with different energy gaps.	2
2.2	Density of states $D(E)$ for systems with different dimensionality.	3
2.3	Schematically illustration of the two different types of QDs and sizes produced by different techniques.	4
3.1	Nonzero hopping matrix elements in case of an sp -bonding	14
3.2	Flowchart for the calculation of the piezoelectric potential	25
3.3	Schematic illustration of the folded spectrum method.	27
4.1	Schematic representation of C_{2v} and C_{3v} symmetry.	30
6.1	Conventional unit cell of a zinc blende structure.	52
6.2	Schematic band structure of semiconductors with a zinc blende structure.	54
6.3	Schematic illustration for the determination of tight-binding parameters.	57
6.4	Tight-binding band structures for CdSe and ZnSe.	58
7.1	Schematic illustration of a pyramidal CdSe QD buried in a ZnSe matrix.	60
7.2	Strain distribution in and around the embedded pyramidal CdSe QD. .	61
7.3	Electron and hole energies for pyramidal CdSe QDs with different base lengths.	62
7.4	Isosurfaces of the modulus squared electron wave functions for a pyramidal CdSe QD.	63
7.5	Isosurfaces of the modulus squared hole wave functions for a pyramidal CdSe QD.	65
7.6	Single-particle energies for the pyramidal CdSe QD with a 1 ML thick WL.	66
7.7	Isosurfaces of the probability density for electron and hole wave functions of spherical CdSe nanocrystal.	70

7.8	Energy gap $E_{\text{gap}}^{\text{nano}}$ as a function of the nanocrystal diameter.	71
7.9	Electron and hole energies as a function of the nanocrystal diameter d	72
7.10	Energy splitting Δ_{e_1, e_2} between the lowest two electronic states as a function of the nanocrystal diameter.	73
9.1	Conventional unit cell of a wurtzite structure.	80
9.2	Miller indices for different lattice planes and directions in a wurtzite lattice.	81
9.3	Schematic band structure of a semiconductor with a wurtzite structure.	84
9.4	Tight-binding band structure for bulk InN and GaN.	88
10.1	Schematic illustration of the lens-shaped InN QD buried in a GaN matrix.	90
10.2	Contour plot of the electrostatic potential energy V_p	92
10.3	Isosurfaces of the probability densities of the three lowest electron and holes states for the largest InN QD.	94
10.4	Planar-integrated probability density $P_{\text{planar}}(z)$ for the electron and the hole ground state for smallest and largest InN QD.	95
10.5	Single-particle energy levels for the three investigated InN QD sizes.	96
10.6	Intermediate InN QD: Influence of the built-in field on the hole-state ordering.	97
10.7	Wurtzite bulk band structure of InN and GaN including crystal field splitting and spin-orbit coupling.	98
10.8	Energy splitting $\Delta E_{s,p}^h$ with and without crystal field and spin-orbit splitting.	101
10.9	Excitonic absorption for InN QDs in the presence and absence of the built-in field.	111
10.10	Example of a configuration with three electron hole pairs.	112
10.11	Ground state emission spectra for the small InN QD with and without the inclusion of the internal field.	113
10.12	Schematic representation of a three exciton configuration.	114
10.13	Emission spectra for the intermediate InN QD with different number of excitons and in the presence of the internal field.	115
12.1	Schematic visualization of the truncated pyramidal GaN QD buried in an AlN matrix.	122
12.2	Strain distribution in and around the truncated pyramidal GaN QD	123
12.3	Strain tensor components ϵ_{11} , ϵ_{33} and ϵ_{13} shown in the (100) cross section plane through the center of the truncated pyramidal GaN QD.	126

13.1	Isosurfaces of the modulus squared electron wave functions with and without strain for a truncated pyramidal GaN QD.	134
13.2	Schematic illustration of the electronic structure of the truncated pyramidal GaN QD.	135
13.3	Isosurfaces of the modulus squared hole wave functions with and without strain for a truncated pyramidal GaN QD.	136
13.4	Excitonic absorption spectrum of a truncated pyramidal GaN QD for different light polarizations	138
C.1	Coulomb matrix elements as function of a cut-off radius R_0	153
C.2	Overlap matrix for a nitrogen atom calculated with standard Slater orbitals.	155
C.3	Overlap matrix for a nitrogen atom calculated with the orthogonalized Slater orbitals.	155
C.4	Nitrogen Slater orbitals without and with orthogonalization.	156

List of Tables

4.1	Multiplication table for the C_{2v} group.	31
4.2	Multiplication table for the C_{3v} group.	32
4.3	Character table of the group C_{2v} and C_{3v}	33
4.4	Character table and commonly used notations for the irreducible representations of the T_d point group.	38
4.5	Character table of the double group \bar{T}_d	39
4.6	Additional degeneracies due to time reversal symmetry.	43
4.7	Character table for the double group \bar{C}_{2v}	44
4.8	Application of the Frobenius-Schur criterion to the double group \bar{C}_{2v}	45
6.1	Direct products of the single group representations Γ_i with $D_{1/2}$ for the T_d point group.	53
7.1	Character tables for the groups C_{2v} and C_{4v}	64
7.2	Energy splittings for electron and hole bound-states in case of different wetting layer thicknesses.	67
9.1	Character table for the single group C_{6v}	82
9.2	Additional representations of the double group \bar{C}_{6v}	82
9.3	Direct products of the single group representations Γ_i of C_{6v} with $D_{1/2}$	83
10.1	Single-particle energies for the intermediate InN QD in the presence and absence of crystal field splitting and spin-orbit coupling.	99
10.2	Character table for the double group \bar{C}_{3v}	100
10.3	Slater orbitals for In, Ga, and N atoms.	106
12.1	Single-particle energies of a GaN quantum well.	128
13.1	Energy splittings for electron states in a truncated pyramidal GaN QD.	134

13.2	Energy splittings for hole states in a truncated pyramidal GaN QD. . .	137
A.1	Properties of the CdSe and ZnSe band structures.	149
A.2	Tight-binding parameters for ZnSe and CdSe.	149
B.3	Properties of wurtzite InN and GaN band structures.	150
B.4	Tight-binding parameters for wurtzite InN and GaN.	150
B.5	Relationships between the parameters of the tight-binding model used in Part III, the zinc blende notation and Slater-Koster notation.	151
E.6	Properties of the cubic GaN and AlN band structures.	159
E.7	Tight-binding parameters for cubic AlN and GaN,	159

Bibliography

- [1] P. Michler. *Single Quantum Dots: Fundamentals, Applications, and New Concepts*. Topics in Applied Physics (Springer, Berlin, 2003).
- [2] I. N. Stranski and L. Krastanow. *Zur Theorie der orientierten Ausscheidung von Ionenkristallen aufeinander*. Akademie der Wissenschaften Wien Klasse IIb **146**, 797 (1938).
- [3] Y.-W. Mo, D. E. Savage, B. S. Swartzentruber, and M. G. Lagally. *Kinetic pathway in Stranski-Krastanow growth of Ge on Si(001)*. Phys. Rev. Lett. **65**, 1020 (1990).
- [4] D. J. Eaglesham and M. Cerullo. *Dislocation-free Stranski-Krastanow growth of Ge on Si(100)*. Phys. Rev. Lett. **64**, 1943 (1990).
- [5] M. Bayer. *One at a time, please*. Nature **418**, 597 (2002).
- [6] A. Zrenner, E. Beham, S. Stuffer, F. Findeis, M. Bichler, and G. Abstreiter. *Coherent properties of a two-level system based on a quantum-dot photodiode*. Nature **418**, 612 (2002).
- [7] R. D. Schaller and V. I. Klimov. *High Efficiency Carrier Multiplication in PbSe Nanocrystals: Implications for Solar Energy Conversion*. Phys. Rev. Lett. **92**, 186601 (2004).
- [8] L. W. Wang, A. J. Williamson, A. Zunger, H. Jiang, and J. Singh. *Comparison of the $\mathbf{k} \cdot \mathbf{p}$ and direct diagonalization approaches to the electronic structure of InAs/GaAs quantum dots*. Appl. Phys. Lett. **76**, 339 (2000).
- [9] R. Santoprete, B. Koiller, R. B. Capaz, P. Kratzer, Q. K. K. Liu, and M. Scheffler. *Tight-Binding study of the influence of the strain on the electronic properties of InAs/GaAs quantum dots*. Phys. Rev. B **68**, 235311 (2003).
- [10] M. Schwab, H. Kurtze, T. Auer, T. Berstermann, M. Bayer, J. Wiersig, N. Baer, C. Gies, F. Jahnke, J. P. Reithmaier, A. Forchel, M. Benyoucef, and P. Michler. *Radiative emission dynamics of quantum dots in a single cavity micropillar*. Phys. Rev. B **74**, 045323 (2006).
- [11] C. B. Murray, D. J. Norris, and M. G. Bawendi. *Synthesis and Characterization of Nearly Monodisperse CdE ($E=S, Se, Te$) Semiconductor Nanocrystallites*. J. Am. Chem. Soc. **115**, 8706 (1993).

- [12] W. G. van der Wiel, S. De Franceschi, J. M. Elzerman, T. Fujisawa, S. Tarucha, and L. P. Kouwenhoven. *Electron transport through double quantum dots*. Rev. Mod. Phys. **75**, 1 (2003).
- [13] J. L. Merz, S. Lee, and J. K. Furdyna. *Self-organized growth, ripening and optical properties of wide-band gap II-VI quantum dots*. J. Cryst. Growth **184**, 228 (1998).
- [14] Yi Yang, D. Z. Shen, J. Y. Zhang, X. W. Fan, B. S. Li, Y. M. Lu, Y. C. Liu, and Y. N. Liu. *The formation mechanism of self-assembled CdSe quantum dots*. J. Cryst. Growth **233**, 785 (2001).
- [15] B. P. Zhang, D. D. Manh, K. Wakatsuki, and Y. Segawa. *Nanostructures formed on CdSe/ZnSe surfaces*. J. Cryst. Growth **227**, 645 (2001).
- [16] B. S. Kim, M. A. Islam, L. E. Brus, and I. P. Herman. *Interdot interactions and band gap changes in CdSe nanocrystal arrays at elevated pressure*. J. Appl. Phys. **89**, 8127 (2001).
- [17] A. A. Guzelian, U. Banin, A. V. Kadavanich, X. Peng, and A. P. Alivisatos. *Colloidal chemical synthesis and characterization of InAs nanocrystal quantum dots*. Appl. Phys. Lett. **69**, 1432 (1996).
- [18] L. Manna, E. C. Scher, and A. P. Alivisatos. *Synthesis of Soluble and Processable Rod-, Arrow-, Teardrop-, and Tetrapod-Shaped CdSe Nanocrystals*. J. Am. Chem. Soc. **122**, 12700 (2000).
- [19] C. B. Murray, S. Sun, W. Gaschler, H. Doyle, T. A. Betley, and C. R. Kagan. *Colloidal synthesis of nanocrystals and nanocrystal superlattices*. IBM J. Res. & Dev. **45**, 47 (2001).
- [20] A. Wojs, P. Hawrylak, S. Fafard, and L. Jacak. *Electronic structure and magneto-optics of self-assembled quantum dots*. Phys. Rev. B **54**, 5604 (1996).
- [21] K. Kowalik, O. Krebs, A. Lemaître, S. Laurent, P. Senellart, P. Voisin, and J. A. Gaj. *Influence of an in-plane electric field on exciton fine structure in InAs-GaAs self-assembled quantum dots*. Appl. Phys. Lett. **86**, 041907 (2005).
- [22] P. W. Fry, I. E. Itskevich, D. J. Mowbray, M. S. Skolnick, J. J. Finley, J. A. Barker, E. P. O'Reilly, L. R. Wilson, I. A. Larkin, P. A. Maksym, M. Hopkinson, M. Al-Khafaji, J. P. R. David, A. G. Cullis, G. Hill, and J. C. Clark. *Inverted Electron-Hole Alignment in InAs-GaAs Self-Assembled Quantum Dots*. Phys. Rev. Lett. **84**, 733 (2000).
- [23] S. Ruvimov, P. Werner, K. Scheerschmidt, U. Gösele, J. Heydenreich, U. Richter, N. N. Ledentsov, M. Grundmann, D. Bimberg, V. M. Ustinov, A. Yu. Egorov, P. S. Kop'ev, and Zh. I. Alferov. *Structural characterization of (In,Ga)As quantum dots in a GaAs matrix*. Phys. Rev. B **51**, 14766 (1995).
- [24] H. Eisele, O. Flebbe, T. Kalka, C. Preinesberger, F. Heinrichsdorff, A. Krost, D. Bimberg, and M. Dähne-Prietsch. *Cross-sectional scanning-tunneling microscopy of stacked InAs quantum dots*. Appl. Phys. Lett. **75**, 106 (1999).

- [25] J. Shumway, A. J. Williamson, Alex Zunger, A. Passaseo, M. DeGiorgi, R. Cingolani, M. Catalano, and P. Crozier. *Electronic structure consequences of In/Ga composition variations in self-assembled $In_xGa_{1-x}As/GaAs$ alloy quantum dots*. Phys. Rev. B **64**, 125302 (2001).
- [26] P. Deglmann, R. Ahlrichs, and K. Tsereteli. *Theoretical studies of ligand-free cadmium selenide and related semiconductor clusters*. J. Chem. Phys. **116**, 1585 (2002).
- [27] P. Sarkar and M. Springborg. *Density-functional study of size-dependent properties of Cd_mSe_m* . Phys. Rev. B **68**, 235409 (2003).
- [28] A. Puzder, A. J. Williamson, F. Gygi, and G. Galli. *Self-Healing of CdSe Nanocrystals: First-Principle Calculations*. Phys. Rev. Lett. **92**, 217401 (2004).
- [29] O. Stier, M. Grundmann, and D. Bimberg. *Electronic and optical properties of strained quantum dots modeled by $8\mathbf{k}\cdot\mathbf{p}$ theory*. Phys. Rev. B **59**, 5688 (1999).
- [30] N. Baer, P. Gartner, and F. Jahnke. *Coulomb effects in semiconductor quantum dots*. Eur. Phys. J. B **42**, 231 (2004).
- [31] L. W. Wang, J. Kim, and A. Zunger. *Electronic structures of $[110]$ -faceted self-assembled pyramidal $InAs/GaAs$ quantum dots*. Phys. Rev. B **59**, 5678 (1999).
- [32] T. Saito and Y. Arakawa. *Electronic structure of piezoelectric $In_{0.2}Ga_{0.8}N$ quantum dots in GaN calculated using a tight-binding method*. Physica E (Amsterdam) **15**, 169 (2002).
- [33] E. O. Kane. *Energy band structure in p-type germanium and silicon*. J. Chem. Phys. Solids **1**, 82 (1956).
- [34] C. R. Pidgeon and R. N. Brown. *Interband Magneto-Absorption and Faraday Rotation in $InSb$* . Phys. Rev. **146**, 575 (1966).
- [35] U. Banin, C. J. Lee, A. A. Guzelian, A. V. Kadavanich, A. P. Alivisatos, W. Jaskolski, G. W. Bryant, Al. L. Efros, and M. Rosen. *Size-dependent electronic level structure of $InAs$ nanocrystal quantum dots: Test of multiband effective-mass theory*. J. Chem. Phys. **109**, 2306 (1998).
- [36] Lin-Wang Wang and A. Zunger. *Solving Schrödinger's equation around a desired energy: Application to silicon quantum dots*. J. Chem. Phys. **100**, 2394 (1994).
- [37] A. Di Carlo. *Microscopic theory of nanostructured semiconductor devices: beyond the envelope-function approximation*. Semicond. Sci. Technol. **18**, R1 (2003).
- [38] L. W. Wang and A. Zunger. *Linear combination of bulk bands method for large-scale electronic structure calculations on strained nanostructures*. Phys. Rev. B **59**, 15806 (1999).
- [39] D. M. Bruls, P. M. Koenraad, H.W. M. Salemink, J. H. Wolter, M. Hopkinson, and M. S. Skolnick. *Stacked low-growth-rate $InAs$ quantum dots studied at the atomic level by cross-sectional scanning tunneling microscopy*. Appl. Phys. Lett. **82**, 3758 (2003).

- [40] V. Chamard, T. Schüllli, M. Sztucki, T. H. Metzger, E. Sarigiannidou, J.-L. Rouvière, M. Tolan, C. Adelman, and B. Daudin. *Strain distribution in nitride quantum dot multilayers*. Phys. Rev. B **69**, 125327 (2004).
- [41] G. Czycholl. *Theoretische Festkörperphysik* (Vieweg, Braunschweig/Wiesbaden, 2000).
- [42] H. Haug and S. W. Koch. *Quantum Theory of the Optical and Electronic Properties of Semiconductors* (World Scientific, Singapore, 1993).
- [43] F. Cleri and V. Rosato. *Tight-binding potentials for transition metals and alloys*. Phys. Rev. B **48**, 22 (1993).
- [44] T. B. Boykin. *Improved fits of the effective masses at Γ in the spin-orbit, second-nearest-neighbor sp^3s^* model: Results from analytic expressions*. Phys. Rev. B **56**, 9613 (1997).
- [45] D. Porezag, Th. Frauenheim, Th. Köhler, G. Seifert, and R. Kaschner. *Construction of tight-binding-like potentials on the basis of density-functional theory: Application to carbon*. Phys. Rev. B **51**, 12947 (1995).
- [46] P. O. Löwdin. *On the non-orthogonality problem connected with the use of atomic wave functions in the theory of molecules and crystals*. J. Chem. Phys. **18**, 365 (1950).
- [47] J. C. Slater and G. F. Koster. *Simplified LCAO Method for Periodic Potential Problem*. Phys. Rev. **94**, 1498 (1954).
- [48] P. Y. Yu and M. Cardona. *Fundamentals of Semiconductors*. Physics and Material Properties (Springer, Berlin, 1999).
- [49] F. Schwabl. *Quantenmechanik für Fortgeschrittene* (Springer, Berlin, 2000).
- [50] H. W. Streitwolf. *Gruppentheorie in der Festkörperphysik* (Akademische Verlagsgesellschaft Geest & Portig K.G., Leipzig, 1967).
- [51] D. J. Chadi. *Spin-orbit splitting in crystalline and compositionally disordered semiconductors*. Phys. Rev. B **16**, 790 (1977).
- [52] T. B. Boykin. *More complete treatment of spin-orbit effects in tight-binding models*. Phys. Rev. B **57**, 1620 (1998).
- [53] S. Sapra and D. D. Sarma. *Evolution of the electronic structure with size in II-VI semiconductor nanocrystals*. Phys. Rev. B **69**, 125304 (2004).
- [54] C. G. Van de Walle and J. Neugebauer. *Universal alignment of hydrogen levels in semiconductors, insulators and solutions*. Nature **423**, 626 (2003).
- [55] S. Lakes, T. Reisinger, B. Hahn, C. Meier, M. Meier, and W. Gebhardt. *Composition dependent determination of band offsets in ZnCdSe/ZnSe and ZnSe/ZnSSe SQW by optical means*. J. Cryst. Growth **159**, 480 (1996).
- [56] E. Kurtz, M. Schmidt, M. Baldauf, S. Wachter, M. Grün, H. Kalt, and C. Klingshirn. *Suppression of lateral fluctuations in CdSe-based quantum wells*. Appl. Phys. Lett. **79**, 1118 (2001).

-
- [57] S.-H. Wei and A. Zunger. *Valence band splittings and band offsets of AlN, GaN, and InN*. Appl. Phys. Lett. **69**, 2719 (1996).
- [58] S. H. Wei and A. Zunger. *Calculated natural band offsets of all II-VI and III-V semiconductors: Chemical trends and the role of cation d orbitals*. Appl. Phys. Lett. **72**, 2011 (1998).
- [59] C. G. Van de Walle and J. Neugebauer. *Small valence-band offsets at GaN/InGaN heterojunctions*. Appl. Phys. Lett. **70**, 2577 (1997).
- [60] J. M. Jancu, R. Scholz, F. Beltram, and F. Bassani. *Empirical spds* tight-binding calculation for cubic semiconductors: General method and material parameters*. Phys. Rev. B **57**, 6493 (1998).
- [61] T. B. Boykin, G. Klimeck, R. C. Bowen, and F. Oyafuso. *Diagonal parameter shifts due to nearest-neighbor displacements in empirical tight-binding theory*. Phys. Rev. B **66**, 125207 (2002).
- [62] C. Priester, G. Allan, and M. Lannoo. *Band-edge deformation potentials in a tight-binding framework*. Phys. Rev. B **37**, 8519 (1988).
- [63] S. Froyen and W. A. Harrison. *Elementary prediction of linear combination of atomic orbitals matrix elements*. Phys. Rev. B **20**, 2420 (1979).
- [64] S. Sapra, N. Shanthi, and D. D. Sarma. *Realistic tight-binding model for the electronic structure of II-VI semiconductors*. Phys. Rev. B **66**, 205202 (2002).
- [65] D. Bertho, D. Boiron, A. Simon, C. Jouanin, and C. Priester. *Calculation of hydrostatic and uniaxial deformation potentials with a self-consistent tight-binding model for Zn-cation-based II-VI compounds*. Phys. Rev. B **44**, 6118 (1991).
- [66] S. Lee, O. L. Lazarenkova, P. von Allmen, F. Oyafuso, and G. Klimeck. *Effect of wetting layers on the strain and electronic structure of InAs self-assembled quantum dots*. Phys. Rev. B **70**, 125307 (2004).
- [67] W. G. Cady. *Piezoelectricity* (McGraw-Hill, New York, 1946).
- [68] T. Hidaka. *Theory of the Piezoelectricity of Zinc Blende-Type and Wurtzite-Type Crystals*. Phys. Rev. B **5**, 4030 (1972).
- [69] W. A. Harrison. *Effective charges and piezoelectricity*. Phys. Rev. B **10**, 767 (1974).
- [70] A. D. Andreev and E. P. O'Reilly. *Theory of the electronic structure of GaN/AlN hexagonal quantum dots*. Phys. Rev. B **62**, 15851 (2000).
- [71] A. S. Saada. *Elasticity: theory and applications* (Pergamon Press, Florida, 1974).
- [72] V. A. Fonoberov and A. A. Baladin. *Excitonic properties of strained wurtzite and zinc blende GaN/Al_xGa_{1-x}N*. J. Appl. Phys. **94**, 7178 (2003).
- [73] C. Pryor, J. Kim, L. W. Wang, A. J. Williamson, and A. Zunger. *Comparison of two methods for describing the strain profiles in quantum dots*. J. Appl. Phys. **83**, 2548 (1998).

- [74] P. N. Keating. *Effect of Invariance Requirements on the Elastic Strain Energy of Crystals with Application to the Diamond Structure*. Phys. Rev. **145**, 637 (1966).
- [75] R. M. Martin. *Elastic Properties of ZnS Structure Semiconductors*. Phys. Rev. B **1**, 4005 (1970).
- [76] S. L. Chuang. *Physics of optoelectronic devices*. Wiley series in pure and applied optics (Wiley-Interscience publication, New York, 1995).
- [77] S.-H. Park, S.-L. Chuang, and D. Ahn. *Piezoelectric effects on many-body optical gain of zinc blende and wurtzite GaN/AlGaN quantum-well lasers*. Appl. Phys. Lett. **75**, 1354 (1999).
- [78] G. Bester, X. Wu, D. Vanderbilt, and A. Zunger. *Importance of Second-Order Piezoelectric Effects in Zinc Blende Semiconductors*. Phys. Rev. Lett. **96**, 187602 (2006).
- [79] Soohaeng Cho, A. Majerfeld, A. Sanz-Hervás, J. J. Sánchez, J. L. Sánchez-Rojas, and I. Izpura. *Determination of the pyroelectric coefficient in strained InGaAs/GaAs quantum wells grown on (111)B GaAs substrates*. J. Appl. Phys. **90**, 915 (2001).
- [80] J. J. Sánchez, J. I. Izpura, J. M. G. Tijero, E. Muñoz, Soohaeng Cho, and A. Majerfeld. *Confirmation of the pyroelectric coefficient of strained $In_xGa_{1-x}As$ /GaAs quantum well structures grown on (111)B GaAs by differential photocurrent spectroscopy*. J. Appl. Phys. **91**, 3002 (2002).
- [81] M. Sabathil, S. Hackenbuchner, S. Birner, J. A. Majewski, P. Vogl, and J. J. Finley. *Theory of vertical and lateral Stark shifts of excitons in quantum dots*. phys. stat. sol (c) **4**, 1181 (2003).
- [82] M. Povolotskyi, A. Di Carlo, and S. Birner. *Electronic and optical properties of [N11] grown nanostructures*. phys. stat. sol (c) **6**, 1511 (2004).
- [83] F. D. Sala, A. D. Carlo, P. Lugli, F. Bernardini, V. Fiorentini, R. Scholz, and J. M. Jancu. *Free-carrier screening of polarization fields in wurtzite GaN/InGaN laser structures*. Appl. Phys. Lett. **74**, 2002 (1999).
- [84] T. Saito and Y. Arakawa. *Electronic structure of piezoelectric $In_{0.2}Ga_{0.8}N$ quantum dots in GaN calculated using a tight-binding method*. Physica E (Amsterdam) **15**, 169 (2002).
- [85] <http://www.caam.rice.edu/software/ARPACK>.
- [86] <http://jumpdoc.fz-juelich.de>.
- [87] J. F. Cornwell. *Group Theory and electronic energy bands in solids* (North-Holland Publishing Company, Amsterdam, 1969).
- [88] F. Bassani and G. Pastori Parravicini. *Electronic states and optical transitions in solids* (Pergamon Press, New York, 1975).
- [89] I. N. Bronstein, K. A. Semendjajew, G. Musiol, and H. Mühlig. *Taschenbuch der Mathematik* (Verlag Harri Deutsch, Frankfurt am Main, 1997).

-
- [90] J. R. Chelikowsky, T. J. Wagener, J. H. Weaver, and A. Jin. *Valence- and conduction-band densities of states for tetrahedral semiconductors: Theory and experiment*. Phys. Rev. B **40**, 9644 (1989).
- [91] Conyers Herring. *Effect of Time-Reversal Symmetry on Energy Bands of Crystals*. Phys. Rev. **52**, 361 (1937).
- [92] R. J. Elliott. *Spin-Orbit Coupling in Band Theory—Character Tables for Some "Double" Space Groups*. Phys. Rev. **96**, 280 (1954).
- [93] A. S. Davydov. *Quantum mechanics* (Pergamon Press, Oxford, 1965).
- [94] V. Heine. *Group theory in quantum mechanics : An introduction to its present usage* (Pergamon Press, Oxford, 1970).
- [95] E. Kartheuser and S. Rodriguez. *Group-Theoretical Study of Double Acceptors in Semiconductors under Uniaxial Stress*. Phys. Rev. B **8**, 1556 (1973).
- [96] T. Passow, K. Leonardi, H. Heinke, D. Hommel, D. Litvinov, A. Rosenauer, D. Gerthsen, J. Seufert, G. Bacher, and A. Forchel. *Quantum dot formation by segregation enhanced CdSe reorganization*. J. Appl. Phys. **92**, 6546 (2002).
- [97] M. Klude, T. Passow, H. Heinke, and D. Hommel. *Electro-Optical Characterization of CdSe Quantum Dot Laser Diodes*. phys. stat. sol. (b) **229**, 1029 (2002).
- [98] X. Brokmann, E. Giacobino, M. Dahan, and J. P. Hermier. *Highly efficient triggered emission of single photons by colloidal CdSe/ZnS nanocrystals*. Appl. Phys. Lett. **85**, 712 (2004).
- [99] X. Peng, L. Manna, W. Yang, J. Wickham, E. Scher, A. Kadavanich, and A. P. Alivisatos. *Shape control of CdSe nanocrystals*. Nature **404**, 59 (2000).
- [100] P. Alivisatos. *The use of nanocrystals in biological detection*. Nature Biotechnology **22**, 47 (2004).
- [101] J. K. Jaiswal and S. M. Simon. *Potentials and pitfalls of fluorescent quantum dots for biological imaging*. Trends in Cell Biology **14**, 497 (2004).
- [102] M. Grundmann, O. Stier, and D. Bimberg. *InAs/GaAs pyramidal quantum dots: Strain distribution, optical phonons, and electronic structure*. Phys. Rev. B **52**, 11969 (1995).
- [103] C. Pryor. *Eight-band calculations of strained InAs/GaAs quantum dots compared with one-, four-, and six-band approximations*. Phys. Rev. B **57**, 7190 (1998).
- [104] A. J. Williamson, L. W. Wang, and A. Zunger. *Theoretical interpretation of the experimental electronic structure of lens-shaped self-assembled InAs/GaAs quantum dots*. Phys. Rev. B **62**, 12963 (2000).
- [105] J. Kim, L. W. Wang, and A. Zunger. *Comparison of the electronic structure of InAs/GaAs pyramidal quantum dots with different facet orientations*. Phys. Rev. B **57**, R9408 (1998).

- [106] S. Lee, L. Jönsson, J. W. Wilkins, G. W. Bryant, and G. Klimeck. *Electron-hole correlations in semiconductor quantum dots with tight-binding wave functions*. Phys. Rev. B **63**, 195318 (2001).
- [107] S. Lee, J. Kim, L. Jönsson, J. W. Wilkins, G. W. Bryant, and G. Klimeck. *Many-body levels of optically excited and multiply charged InAs nanocrystals modeled by semiempirical tight binding*. Phys. Rev. B **66**, 235307 (2002).
- [108] G. Allan, Y. M. Niquet, and C. Delerue. *Quantum confinement energies in zinc blende III-V and group IV semiconductors*. Appl. Phys. Lett. **77**, 639 (2000).
- [109] Y. M. Niquet, C. Delerue, M. Lannoo, and G. Allan. *Single-particle tunneling in semiconductor quantum dots*. Phys. Rev. B **64**, 113305 (2001).
- [110] N. A. Hill and K. B. Whaley. *A theoretical study of the influence of the surface on the electronic structure of CdSe nanoclusters*. J. Chem. Phys. **100**, 2831 (1994).
- [111] K. Leung, S. Pokrant, and K. B. Whaley. *Exciton fine structure in CdSe nanoclusters*. Phys. Rev. B **57**, 12291 (1998).
- [112] K. Leung and K. B. Whaley. *Surface relaxation in CdSe nanocrystals*. J. Chem. Phys. **100**, 11012 (1999).
- [113] S. Pokrant and K. B. Whaley. *Tight-binding studies of surface effects on electronic structure of CdSe nanocrystals: the of organic ligands, surface reconstruction, and inorganic capping shells*. Eur. Phys. J. D **6**, 255 (1999).
- [114] J. Schrier and K. B. Whaley. *Tight-binding g-factor calculations of CdSe nanostructures*. Phys. Rev. B **67**, 235301 (2003).
- [115] T. Saito, J. N. Schulman, and Y. Arakawa. *Strain distribution and electronic structure of InAs pyramidal quantum dots with uncovered surfaces: Tight-binding analysis*. Phys. Rev. B **57**, 13016 (1998).
- [116] N. Baer. *Optical and Electronic Properties of InGaAs and Nitride Quantum Dots* (Universität Bremen, Bremen, 2006).
- [117] J. C. Phillips. *Bonds and bands in semiconductors* (Academic Press, New York, 1973).
- [118] H. Dierks and G. Czycholl. *Tight-Binding calculation of linear excitonic absorption spectra of single quantum wells*. J. Cryst. Growth **185**, 877 (1998).
- [119] M. L. Cohen and J. R. Chelikowski. *Electronic Structure and Optical Properties of Semiconductors* (Springer Series in Solid-State Sciences 75, Second Edition, Berlin, 1989).
- [120] P. Vogl, H. P. Hjalmarson, and J. D. Dow. *A semi-empirical tight-binding theory of the electronic structure of semiconductors*. J. Phys. Chem. Solids **44**, 365 (1983).
- [121] T. R. Nielsen, P. Gartner, and F. Jahnke. *Many-body theory of carrier capture and relaxation in semiconductor quantum-dot lasers*. Phys. Rev. B **69**, 235314 (2004).

-
- [122] J. Seebeck, T. R. Nielsen, P. Gartner, and F. Jahnke. *Polarons in semiconductor quantum dots and their role in the quantum kinetics of carrier relaxation*. Phys. Rev. B **71**, 125327 (2005).
- [123] U. Banin, C. YunWei, D. Katz, and O. Millo. *Identification of atomic-like electronic states in indium arsenide nanocrystal quantum dots*. Nature **400**, 542 (1999).
- [124] A. P. Alivisatos. *Semiconductor Clusters, Nanocrystals, and Quantum Dots*. Science **271**, 933 (1996).
- [125] B. Alpers, I. Rubinstein, G. Hodes, D. Porath, and O. Millo. *Energy level tunneling spectroscopy and single electron charging in individual CdSe quantum dots*. Appl. Phys. Lett. **75**, 1751 (1999).
- [126] J. Taylor, T. Kippeny, and S. J. Rosenthal. *Surface Stoichiometry of CdSe Nanocrystals Determined by Rutherford Backscattering Spectroscopy*. J. Cluster Sci. **12**, 571 (2002).
- [127] P. E. Lippens and M. Lannoo. *Calculation of the band gap for small CdS and ZnS crystallites*. Phys. Rev. B **39**, 10935 (1989).
- [128] A. I. Ekimov, F. Hache, M. C. Schanne-Klein, D. Ricard, C. Flytzanis, I. A. Kudryavtsev, T. V. Yazeva, A. V. Rodina, and Al. L. Efros. *Absorption and intensity-dependent photoluminescence measurements on CdSe quantum dots: assignment of first electronic transitions*. J. Opt. Soc. Am. B **10**, 100 (1993).
- [129] P. Guyot-Sionnest and M. A. Hines. *Intraband transitions in semiconductor nanocrystals*. Appl. Phys. Lett. **72**, 686 (1998).
- [130] S. C. Jain, M. Willander, J. Narayan, and R. V. Overstraeten. *III-nitrides: Growth, characterization, and properties*. J. Appl. Phys. **87**, 965 (2000).
- [131] I. Vurgaftman and J. R. Meyer. *Band parameters for nitrogen-containing semiconductors*. J. Appl. Phys. **94**, 3675 (2003).
- [132] J. Y. Marzin and G. Bastard. *Calculation of the energy-levels in InAs/GaAs quantum dots*. Solid State Comm. **92**, 437 (1994).
- [133] M. Bayer, O. Stern, P. Hawrylak, S. Fafard, and A. Forchel. *Hidden symmetries in the energy levels of excitonic 'artificial atoms'*. Nature **405**, 923 (2000).
- [134] R. Heitz, O. Stier, I. Mukhametzhanov, A. Madhukar, and D. Bimberg. *Quantum size effect in self-organized InAs/GaAs quantum dots*. Phys. Rev. B **62**, 11017 (2000).
- [135] E. P. Pokatilov, V. A. Fonoberov, V. M. Fomin, and J. T. Devreese. *Development of an eight-band theory for quantum dot heterostructures*. Phys. Rev. B **64**, 245328 (2001).
- [136] G. Bester and A. Zunger. *Cylindrically shaped zinc blende semiconductor quantum dots do not have cylindrical symmetry: Atomistic symmetry, atomic relaxation, and piezoelectric effects*. Phys. Rev. B **71**, 045318 (2005).
- [137] L.-W. Wang and A. Zunger. *Pseudopotential calculations of nanoscale CdSe quantum dots*. Phys. Rev. B **53**, 9579 (1995).

- [138] A. Franceschetti, H. Fu, L. W. Wang, and A. Zunger. *Many-body pseudopotential theory of excitons in InP and CdSe quantum dots*. Phys. Rev. B **60**, 1819 (1999).
- [139] G. Bester, S. Nair, and A. Zunger. *Pseudopotential calculation of the excitonic fine structure of million-atom self-assembled $\text{In}_{1-x}\text{Ga}_x\text{As}/\text{GaAs}$ quantum dots*. Phys. Rev. B **67**, 161306(R) (2003).
- [140] W. Sheng, S. J. Cheng, and P. Hawrylak. *Multiband theory of multi-exciton complexes in self-assembled quantum dots*. Phys. Rev. B **71**, 035316 (2005).
- [141] G. Khitrova, H. M. Gibbs, F. Jahnke, M. Kira, and S. W. Koch. *Nonlinear optics of normal-mode-coupling semiconductor microcavities*. Rev. Mod. Phys. **71**, 1591 (1999).
- [142] A. D. Andreev and E. P. O'Reilly. *Optical transitions and radiative lifetime in GaN/AlN self-organized quantum dots*. Appl. Phys. Lett. **79**, 521 (2001).
- [143] M. Arlery, J. L. Rouviere, F. Widmann, B. Daudin, G. Feuillet, and H. Mariette. *Quantitative characterization of GaN quantum-dot structures in AlN by high-resolution transmission electron microscopy*. Appl. Phys. Lett. **74**, 3287 (1999).
- [144] F. Demangeot, J. Frandon, C. Pinguier, M. Caumont, O. Briot, B. Maleyre, S. Clur-Ruffenach, and B. Gil. *Raman scattering in large single indium nitride dots: Correlations between morphology and strain*. Phys. Rev. B **68**, 245308 (2003).
- [145] R. W. Martin and K. P. O'Donnell. *Calculation of optical transition energies for self-formed InGaN quantum dots*. phys. stat. sol. (b) **216**, 441 (1999).
- [146] J.-J. Shi and Z.-Z. Gan. *Effects of piezoelectricity and spontaneous polarization on localized excitons in self-formed InGaN quantum dots*. J. Appl. Phys. **94**, 407 (2003).
- [147] A. Bagga, P. K. Chattopadhyay, and S. Ghosh. *Dark and bright excitonic states in nitride quantum dots*. Phys. Rev. B **71**, 115327 (2005).
- [148] J. Simon, N. T. Pelekanos, C. Adelman, E. Martinez-Guerrero, R. Andre, B. Daudin, Le Si Dang, and H. Mariette. *Direct comparison of recombination dynamics in cubic and hexagonal GaN/AlN quantum dots*. Phys. Rev. B **68**, 035312 (2003).
- [149] N. Garro, A. Cros, J. A. Budagosky andd A. Cantarero, A. Vinattieri, M. Gurioli, S. Founta, H. Mariette, and B. Daudin. *Reduction of the internal electric field in wurtzite a-plane GaN self-assembled quantum dots*. Appl. Phys. Lett. **87**, 011101 (2005).
- [150] A. Barenco and M. A. Dupertuis. *Quantum many-body states of excitons in a small quantum dot*. Phys. Rev. B **52**, 2766 (1995).
- [151] S. M. Ulrich, M. Benyoucef, P. Michler, N. Baer, P. Gartner, F. Jahnke, M. Schwab, H. Kurtze, M. Bayer, S. Fafard, Z. Wasilewski, and A. Forchel. *Correlated photon-pair emission from a charged single quantum dot*. Phys. Rev. B **71**, 235328 (2005).
- [152] M. Grundmann. *The Physics of Semiconductors: An Introduction Including Devices and Nanophysics* (Springer, Berlin, 2006).
- [153] P. Lawaetz. *Stability of the Wurtzite Structure*. Phys. Rev. B **5**, 4039 (1972).

-
- [154] F. Grosse and J. Neugebauer. *Limits and accuracy of valence force field models for $In_xGa_{1-x}N$ alloys*. Phys. Rev. B **63**, 085207 (2001).
- [155] P. Rinke, M. Scheffler, A. Qteish, M. Winkelnkemper, D. Bimberg, and J. Neugebauer. *Band gap and band parameters of InN and GaN from quasiparticle energy calculations based on exact-exchange density-functional theory*. Appl. Phys. Lett. **89**, 161919 (2006).
- [156] W. Demtröder. *Experimentalphysik 3: Atome, Moleküle und Festkörper* (Springer, Berlin, 2000).
- [157] G. F. Koster, J. O. Dimmock, R. G. Wheeler, and H. Statz. *Properties of thirty-two point groups* (M.I.T. Press, Massachusetts, 1969).
- [158] T. Uenoyama and M. Suzuki. *Valence subband structures of wurtzite $GaN/AlGaN$ quantum wells*. Appl. Phys. Lett. **67**, 2527 (1995).
- [159] W. R. L. Lambrecht, A. V. Rodina, S. Limpijumnong, B. Segall, and B. K. Meyer. *Valence-band ordering and magneto-optic exciton fine structure in ZnO* . Phys. Rev. B **65**, 075207 (2002).
- [160] I. Vurgaftman, J. R. Meyer, and L. R. Ram-Mohan. *Band parameters for III-V compound semiconductors and their alloys*. J. Appl. Phys. **89**, 5815 (2001).
- [161] Y. D. Kim, M. V. Klein, S. F. Ren, Y. C. Chang, H. Luo, N. Samarth, and J. K. Furdyna. *Optical properties of zinc blende $CdSe$ and $Zn_xCd_{1-x}Se$ films grown on $GaAs$* . Phys. Rev. B **49**, 7262 (1994).
- [162] F. Bernardini, V. Fiorentini, and D. Vanderbilt. *Spontaneous polarization and piezoelectric constants of III-V nitrides*. Phys. Rev. B **56**, R10024 (1997).
- [163] A. Hangleiter. *Optical properties and polarization fields in the nitrides*. Journal of Luminescence **87-89**, 130 (2000).
- [164] J. Simon, R. Langer, A. Barski, and N.T. Pelekanos. *Spontaneous polarization effects in $GaN/Al_xGa_{1-x}N$ quantum wells*. Phys. Rev. B **61**, 7211 (2000).
- [165] S. Yoshida. *Growth of cubic III-nitride semiconductors for electronics and optoelectronics application*. Physica E (Amsterdam) **7**, 907 (2000).
- [166] A. Kobayashi, O. F. Sankey, S. M. Volz, and J. D. Dow. *Semiempirical tight-binding band structures of wurtzite semiconductors: AlN , CdS , $CdSe$, ZnS , and ZnO* . Phys. Rev. B **28**, 935 (1983).
- [167] D. Fritsch, H. Schmidt, and M. Grundmann. *Band dispersion relations of zinc blende and wurtzite InN* . Phys. Rev. B **69**, 165204 (2004).
- [168] G. L. Zhao, D. Bagayoko, and T. D. Williams. *Local-density-approximation prediction of electronic properties of GaN , Si , C , and RuO_2* . Phys. Rev. B **60**, 1563 (1999).
- [169] A. Kasic, M. Schubert, S. Einfeldt, D. Hommel, and T. E. Tiwald. *Free-carrier and phonon properties of n - and p -type hexagonal GaN films measured by infrared ellipsometry*. Phys. Rev. B **62**, 7365 (2000).

- [170] J. Wu, W. Walukiewicz, W. Shan, K. M. Yu, J. W. Ager, E. E. Haller, Hai Lu, and William J. Schaff. *Effects of the narrow band gap on the properties of InN*. Phys. Rev. B **66**, 201403 (2002).
- [171] J.-M. Jancu, F. Bassani, F. D. Salla, and R. Scholz. *Transferable tight-binding parametrization for the group-III nitrides*. Appl. Phys. Lett. **81**, 4838 (2002).
- [172] S. Lee, F. Oyafuso, P. von Allmen, and G. Klimeck. *Boundary conditions for the electronic structure of finite-extent embedded semiconductor nanostructures*. Phys. Rev. B **69**, 045316 (2004).
- [173] G. Martin, A. Botchkarev, A. Rockett, and H. Morko \check{c} . *Valence-band discontinuities of wurtzite GaN, AlN, and InN heterojunctions measured by x-ray photoemission spectroscopy*. Appl. Phys. Lett. **68**, 2541 (1996).
- [174] Ch. Manz, M. Kunzer, H. Obloh, A. Ramakrishnan, and U. Kaufmann. *In_xGa_{1-x}N/GaN band offsets as inferred from the deep, yellow-red emission band in In_xGa_{1-x}N*. Appl. Phys. Lett. **74**, 3993 (1999).
- [175] L. R. C. Fonseca, J. L. Jimenez, and J. P. Leburton. *Electronic coupling in InAs/GaAs self-assembled stacked double-quantum-dot systems*. Phys. Rev. B **58**, 9955 (1998).
- [176] M. A. Cusack, P. R. Briddon, and M. Jaros. *Electronic structure of InAs/GaAs self-assembled quantum dots*. Phys. Rev. B **54**, R2300 (1996).
- [177] V. A. Fonoberov and A. A. Balandin. *Optical properties of wurtzite and zinc blende GaN/AlN quantum dots*. J. Vac. Sci. Technol. B **22**, 2190 (2004).
- [178] S. De Rinaldis, I. D'Amico, and F. Rossi. *Intrinsic electric field effects on few-particle interactions in coupled GaN quantum dots*. Phys. Rev. B **69**, 235316 (2004).
- [179] B. Monema, P. P. Paskov, and A. Kasi. *Optical properties of InN – the band gap question*. Superlattices and Microstructures **38**, 38 (2005).
- [180] B. Monema. *Basic III-V nitride research - past, present and future*. J. Cryst. Growth **189/190**, 1 (1998).
- [181] U. M. E. Christmas, A. D. Andreev, and D. A. Faux. *Calculation of electric field and optical transitions in InGaN/GaN quantum wells*. J. Appl. Phys. **98**, 073522 (2005).
- [182] S. De Rinaldis, I. D'Amico, and F. Rossi. *Exciton-exciton interaction engineering in coupled GaN quantum dots*. Appl. Phys. Lett. **81**, 4236 (2002).
- [183] A. Yoshikawa and K. Xu. *Polarity selection process and polarity manipulation of GaN in MOVPE and RF-MBE growth*. Thin Solid Films **412**, 38 (2002).
- [184] M. Murayama and T. Nakayama. *Chemical trend of band offsets at wurtzite/zinc blende heterocrystalline semiconductor interfaces*. Phys. Rev. B **49**, 4710 (1994).
- [185] M. Winkelnkemper, A. Schliwa, and D. Bimberg. *Interrelation of structural and electronic properties in In_xGa_{1-x}N/GaN quantum dots using an eight-band $\mathbf{k} \cdot \mathbf{p}$ model*. Phys. Rev. B **74**, 155322 (2006).

-
- [186] T. R. Nielsen, P. Gartner, M. Lorke, J. Seebeck, and F. Jahnke. *Coulomb scattering in nitride-based self-assembled quantum-dot systems*. Phys. Rev. B **72**, 235311 (2005).
- [187] J. Seebeck, T. R. Nielsen, P. Gartner, and F. Jahnke. *Quantum kinetic theory of phonon-assisted carrier transitions in nitride-based quantum-dot systems*. Eur. Phys. J. B **49**, 167 (2006).
- [188] I. Schnell, G. Czycholl, and R. C. Albers. *Hubbard- U calculations for Cu from first-principle Wannier functions*. Phys. Rev. B **65**, 075103 (2002).
- [189] J. C. Slater. *Atomic Shielding Constants*. Phys. Rev. **36**, 57 (1930).
- [190] R. E. Peierls. *Zur Theorie des Diamagnetismus von Leitungselektronen*. Z. Phys. **80**, 763 (1933).
- [191] J. M. Luttinger. *The Effect of a Magnetic Field on Electrons in a Periodic Potential*. Phys. Rev. **84**, 814 (1951).
- [192] D. R. Hofstadter. *Energy levels and wave functions of Bloch electrons in rational and irrational magnetic fields*. Phys. Rev. B **14**, 2239 (1976).
- [193] A. Rauh, G. H. Wannier, and G. Obermair. *Bloch electrons in irrational magnetic fields*. phys. stat. sol. (b) **63**, 215 (1974).
- [194] G. H. Wannier. *Invariance properties of a proposed Hamiltonian for Bloch electrons in a magnetic field*. phys. stat. sol. (b) **70**, 727 (1975).
- [195] G. M. Obermair and G. H. Wannier. *Bloch electrons in magnetic fields. Rationality, irrationality, degeneracy*. phys. stat. sol. (b) **76**, 217 (1976).
- [196] G. Czycholl and W. Ponischowski. *The recursion method for a two-dimensional electron system in a strong magnetic field*. Z. Phys. B **73**, 343 (1988).
- [197] M. Graf and P. Vogl. *Electromagnetic fields and dielectric response in empirical tight-binding theory*. Phys. Rev. B **51**, 4940 (1995).
- [198] G. W. Bryant and W. Jaskolski. *Tight-binding theory of quantum-dot quantum wells: Single-particle effects and near-band-edge structure*. Phys. Rev. B **67**, 205320 (2003).
- [199] S. Schumacher, G. Czycholl, F. Jahnke, I. Kudyk, L. Wischmeier, I. Rückmann, T. Voss, J. Gutowski, A. Gust, and D. Hommel. *Coherent Propagation of Polaritons in Semiconductor Heterostructures: Nonlinear Pulse Transmission in Theory and Experiment*. Phys. Rev. B **72**, 081308(R) (2005).
- [200] K. Leung and K. B. Whaley. *Electron-hole interactions in silicon nanocrystals*. Phys. Rev. B **56**, 7455 (1997).
- [201] H. Jiang and J. Singh. *Self-Assembled Semiconductor Structures: Electronic and Optoelectronic Properties*. IEEE J. Quantum Electron. **34**, 1188 (1998).
- [202] J. Perez-Conde and A. K. Bhattacharjee. *Exciton states and optical properties of CdSe nanocrystals*. Phys. Rev. B **63**, 245318 (2001).

- [203] J. G. Diaz, J. Planelles G. W. Bryant, and J. Aizpurua. *Tight-binding meethod and multiband effective mass theory appliedd to CdS Nanocrystals: Single-particle effects and optical spectra fine structure*. J. Phys. Chem. B **108**, 17800 (2004).
- [204] S. J. Sun and Y. C. Chang. *Modeling self-assembled quantum dots by effective bond-orbital method*. Phys. Rev. B **62**, 13631 (2000).
- [205] A. Bagga, P. K. Chattopadhyay, and S. Ghosh. *Energy levels of nitride quantum dots: Wurtzite versus zinc blende structure*. Phys. Rev. B **68**, 155331 (2003).
- [206] M. Nirmal, D. J. Norris, M. Kuno, M. G. Bawendi, A. L. Efros, and M. Rosen. *Observation of the “Dark Exciton” in CdSe Quantum Dots*. Phys. Rev. Lett. **75**, 3728 (1995).
- [207] J. Li and J.-B. Xia. *Exciton states and optical spectra in CdSe nanocrystallite quantum dots*. Phys. Rev. B **61**, 15880 (2000).
- [208] S. Founta, F. Rol, E. Bellet-Amalric, J. Bleuse, B. Daudin, B. Gayral, H. Mariette, and C. Moisson. *Optical properties of GaN quantum dots grown on nonpolar (11-20) SiC by molecular-beam epitaxy*. Appl. Phys. Lett. **86**, 171901 (2005).
- [209] N. Baer, S. Schulz, P. Gartner, S. Schumacher, G. Czycholl, and F. Jahnke. *Influence of symmetry and Coulomb-correlation effects on the optical properties of nitride quantum dots*. submitted, arXiv.org:cond-mat/0612353 .
- [210] E. Dekel, D. Gershoni, E. Ehrenfreund, J. M. Garcia, and P. M. Petroff. *Carrier-Carrier correlations in an optically excited single semiconductor quantum dot*. Phys. Rev. B **61**, 11009 (2000).
- [211] C. H. Qiu, W. Melton, M. W. Leksono, J. I. Pankove, B. P. Keller, and S. P. DenBaars. *Photocurrent decay in n-type GaN thin films*. Appl. Phys. Lett. **69**, 1282 (1996).
- [212] H. Morkoc, S. Strite, G. B. Gao, M. E. Lin, B. Sverdlov, and M. Burns. *Large-band-gap SiC, III-V nitride, and II-VI ZnSe-based semiconductor device technologies*. J. Appl. Phys. **76**, 1363 (1994).
- [213] E. Martinez-Guerrero, C. Adelman, F. Chabuel, J. Simon, N. T. Pelekanos, Guido Mula, B. Daudin, G. Feuillet, and H. Mariette. *Self-assembled zinc blende GaN quantum dots grown by molecular-beam epitaxy*. Appl. Phys. Lett. **77**, 809 (2000).
- [214] C. Adelman, E. Martinez Guerrero, F. Chabuel, J. Simon, B. Bataillou, G. Mula, Le Si Dang, N. T. Pelekanos, B. Daudin, G. Feuillet, and H. Mariette. *Growth and characterisation of self-assembled cubic GaN quantum dots*. Materials and Engineering B **82**, 212 (2001).
- [215] B. Daudin, G. Feuillet, H. Mariette, G. Mula, N. Pelekanos, E. Molva, J. L. Rouviere, C. Adelman, E. Martinez Guerrero, J. Barjon, F. Chabuel, B. Bataillou, and J. Simon. *Self-assembled GaN Quantum Dots Grown by Plasma-Assisted Molecular Beam Epitaxy*. Jpn. J. Appl. Phys. **40**, 1892 (2001).

- [216] N. Gogneau, F. Enjalbert, F. Fossard, Y. Hori, C. Adelman, J. Brault, E. Martinez-Guerrero, J. Simon, E. Bellet-Almaric, D. Jalabert, N. Pelekanos, J.-L. Rouviere, B. Daudin, Le Si Dang, H. Mariette, and E. Monroy. *Recent progress in the growth and physics of GaN/AlN quantum dots*. phys. stat. sol. (c) **1**, 1445 (2004).
- [217] J.P. Garayt, J.M. Gerard, F. Enjalbert, L. Ferlazzo, S. Founta, E. Martinez-Guerrero, F. Rol, D. Araujo, R. Cox, B. Daudin, B. Gayral, Le Si Dang, and H. Mariette. *Study of isolated cubic GaN quantum dots by low-temperature cathodoluminescence*. Physica E (Amsterdam) **26**, 203 (2005).
- [218] Hui Yang, L. X. Zheng, J. B. Li, X. J. Wang, D. P. Xu, Y. T. Wang, X. W. Hu, and P. D. Han. *Cubic-phase GaN light-emitting diodes*. Appl. Phys. Lett. **74**, 2498 (1999).
- [219] O. I. Micic, S. P. Ahrenkiel, D. Bertram, and A. J. Nozik. *Synthesis, structure, and optical properties of colloidal GaN quantum dots*. Appl. Phys. Lett. **75**, 478 (1999).
- [220] F. Widmann, B. Daudin, G. Feuillet, Y. Samson, J. L. Rouviere, and N. Pelekanos. *Growth kinetics and optical properties of self-organized GaN quantum dots*. J. Appl. Phys. **83**, 7618 (1998).
- [221] F. Widmann, J. Simon, B. Daudin, G. Feuillet, J. L. Rouvière, N. T. Pelekanos, and G. Fishman. *Blue-light emission from GaN self-assembled quantum dots due to giant piezoelectric effect*. Phys. Rev. B **58**, R15989 (1998).
- [222] J. R. Downes, D. A. Faux, and E. P. O'Reilly. *A simple method for calculating strain distributions in quantum dot structures*. J. Appl. Phys. **81**, 6700 (1997).
- [223] J. D. Eshelby. *The Determination of the elastic field of an ellipsoidal inclusion, and related problems*. Proc. R. Soc. London Ser. A **241**, 376 (1957).
- [224] G. S. Pearson and D. A. Faux. *Analytic solutions for strain in pyramidal quantum dots*. J. Appl. Phys. **88**, 730 (2000).
- [225] A. D. Andreev, J.R. Downes, D. A. Faux, and E. P. O'Reilly. *Strain distributions in quantum dots of arbitrary shape*. J. Appl. Phys. **86**, 297 (1999).
- [226] J. G. Díaz and G. W. Bryant. *Electronic and optical fine structure of GaAs nanocrystals: The role of d orbitals in a tight-binding approach*. Phys. Rev. B **73**, 075329 (2006).
- [227] W. Yang, H. Lee, T. J. Johnson, P. C. Sercel, and A. G. Norman. *Electronic structure of self-organized InAs/GaAs quantum dots bounded by {136} facets*. Phys. Rev. B **61**, 2784 (2000).
- [228] G. J. Beirne, C. Hermannstadter, L. Wang, A. Rastelli, O. G. Schmidt, and P. Michler. *Quantum Light Emission of Two Lateral Tunnel-Coupled (In,Ga)As/GaAs Quantum Dots Controlled by a Tunable Static Electric Field*. Phys. Rev. Lett. **96**, 137401 (2006).
- [229] M. Bayer, P. Hawrylak, K. Hinzer, S. Fafard, M. Korkusinski, Z. R. Wasilewski, O. Stern, and A. Forchel. *Coupling and Entangling of Quantum States in Quantum Dot Molecules*. Science **291**, 451 (2001).

- [230] M. Pi, A. Emperador, M. Barranco, F. Garcias, K. Muraki, S. Tarucha, and D. G. Austing. *Dissociation of Vertical Semiconductor Diatomic Artificial Molecules*. Phys. Rev. Lett. **87**, 066801 (2001).
- [231] H. W. Hölscher, A. Nöthe, and Ch. Uihlein. *Investigation of band masses and g values of ZnSe by two-photon magnetoabsorption*. Phys. Rev. B **31**, 2379 (1985).
- [232] V. Pellegrini, R. Atanasov, A. Tredicucci, F. Beltram, C. Amzulini, L. Sorba, L. Vanzetti, and A. Franciosi. *Excitonic properties of Zn_{1-x}Cd_xSe/ZnSe strained quantum wells*. Phys. Rev. B **51**, 5171 (1995).

List of Publication

- *Tight-binding model for semiconductor nanostructures*
S. Schulz and G. Czycholl,
Phys. Rev. B 72, 165317 (2005).
- *Optical properties of self-organized wurtzite InN/GaN quantum dots: A combined atomistic tight-binding and full configuration interaction calculation*
N. Baer, S. Schulz, S. Schumacher, P. Gartner, G. Czycholl and F. Jahnke,
Appl. Phys. Lett. 87, 231114 (2005).
- *Electronic states in nitride semiconductor quantum dots: A tight-binding approach*
S. Schulz and G. Czycholl ,
phys. stat. sol. (c) 3 , 1675 (2006).
- *Tight-binding model for semiconductor quantum dots with a wurtzite crystal structure: From one-particle properties to Coulomb correlations and optical spectra*
S. Schulz, S. Schumacher and G. Czycholl,
Phys. Rev. B 73, 245327 (2006).
- *Microscopic tight-binding description for electronic and optical properties of InN/GaN quantum dots*
S. Schulz, N. Baer, S. Schumacher, P. Gartner, F. Jahnke and G. Czycholl,
phys. stat. sol. (c) 3, 3631 (2006).
- *Semiconductor nanocrystals and embedded quantum dots: Electronic and optical properties*
S. Schulz, S. Schumacher and G. Czycholl,
phys. stat. sol. (b) 244, 2399 (2007).
- *InN/GaN quantum dots: Electronic and optical properties*
S. Schulz, S. Schumacher and G. Czycholl,
AIP Conference Proceedings 893, 897 (2007).
- *Influence of symmetry and Coulomb-correlation effects on the optical properties of nitride quantum dots*
N. Baer, S. Schulz, P. Gartner, S. Schumacher, G. Czycholl and F. Jahnke,
Phys. Rev. B 76, 075310 (2007).

List of Conference Contributions

- Workshop of the DFG Research Group “Physics of nitride-based nanostructured light-emitting devices”, Barendorf (2003)
Tight-Binding models for semiconductor quantum dots,
S. Schulz and G. Czycholl.
- DPG Frühjahrstagung des Arbeitskreises Festkörperphysik, Regensburg (2004)
Tight-Binding Modellierung von Halbleiterquantenpunkten,
S. Schulz and G. Czycholl.
- Workshop of the DFG Research Group “Physics of nitride-based nanostructured light-emitting devices”, Riezlern (2004)
Tight-Binding models of electronic states in quantum dots,
S. Schulz and G. Czycholl.
- DPG Frühjahrstagung des Arbeitskreises Festkörperphysik, Berlin (2005)
Untersuchung der elektronischen Zustände von Halbleiterquantenpunkten im Rahmen von Tight-Binding-Modellen,
S. Schulz and G. Czycholl.
- Workshop of the DFG Research Group “Physics of nitride-based nanostructured light-emitting devices”, Bad Bederkesa (2005)
Electronic and optical properties of self-organized InN/GaN quantum dots,
S. Schulz, N. Baer, S. Schumacher, P. Gartner, F. Jahnke and G. Czycholl.
- 6th International Conference on Nitride Semiconductors (ICNS-6), Bremen (2005)
Electronic states in nitride semiconductor quantum dots: A tight-binding approach,
S. Schulz and G. Czycholl.
- DPG Frühjahrstagung des Arbeitskreises Festkörperphysik, Dresden (2006)
Optical properties of self-organized wurtzite InN/GaN quantum dots: A combined atomistic tight-binding and full configuration interaction calculation,
S. Schulz, N. Baer, S. Schumacher, P. Gartner, F. Jahnke and G. Czycholl.
- DPG Frühjahrstagung des Arbeitskreises Festkörperphysik, Dresden (2006)
Engineering the multi-exciton spectra in wurtzite InN/GaN quantum dots,
N. Baer, S. Schulz, S. Schumacher, P. Gartner, F. Jahnke and G. Czycholl.

- 28th International Conference on the Physics of Semiconductors (ICPS-28), Wien (2006)
InN/GaN quantum dots: Electronic and optical properties,
S. Schulz, S. Schumacher and G. Czycholl.
- Conference on lasers and electro-optics/ Quantum electronic & laser-science conference (CLEO/QELS), Long Beach (2006)
Electronic and optical properties of self-assembled InN/GaN quantum dots,
S. Schumacher, N. Baer, S. Schulz, P. Gartner, G. Czycholl and F. Jahnke.
- 4th International Conference on Quantum Dots, Chamonix-Mont Blanc (2006)
Microscopic tight-binding description for electronic optical properties of InN/GaN quantum dots,
S. Schulz, N. Baer, S. Schumacher, P. Gartner, F. Jahnke and G. Czycholl.
- Workshop of the DFG Research Group “Physics of nitride-based nanostructured light-emitting devices”, Riezlern (2006)
Electronic and optical properties of self-assembled InN/GaN quantum dots,
S. Schulz, N. Baer, S. Schumacher, P. Gartner, F. Jahnke and G. Czycholl.
- XXX International Conference of Theoretical Physics: Electron Correlations in Nano- and Makrosystems, Ustron (2006)
Electronic and optical properties of semiconductor quantum dots,
G. Czycholl and S. Schulz.

Danksagung

Mein herzlicher Dank geht an alle diejenigen, die diese Arbeit mit ihrem Interesse und ihrer Initiative unterstützt haben.

Herrn Prof. Dr. Gerd Czycholl möchte ich für die gute Betreuung meiner Arbeit danken. Ich möchte mich sowohl für die Gelegenheit bedanken, meine eigenen Vorstellungen umsetzen zu können, als auch die Möglichkeit, die erzielten Ergebnisse auf verschiedenen Konferenzen präsentieren zu dürfen.

Bei Herrn Prof. Dr. Frank Jahnke möchte ich mich dafür bedanken, dass er sich bereit erklärt hat das zweite Gutachten zu erstellen, sowie für die angenehme und produktive Zusammenarbeit.

Besonderer Dank gilt Norman Baer für das sehr aufmerksame und engagierte Korrekturlesen dieser Arbeit. Insbesondere möchte ich mich bei ihm für die eine oder andere “Expresslieferung” von Korrekturvorschlägen bedanken, als auch dafür, dass er immer bereit war überarbeitete Passagen erneut zu lesen. Auch möchte ich ihm für die angenehme und freundschaftlich Zusammenarbeit und für die immer unterhaltsamen Diskussionen und Gespräche danken.

Ebenfalls möchte ich mich an dieser Stelle bei Stefan Schumacher für viele anregende Diskussionen, eine sehr produktive Zusammenarbeit, die Durchsicht meines Manuskripts sowie für die sehr angenehme und freundschaftlich Arbeitsatmosphäre in unserem gemeinsamen Büro bedanken.

Paul Gartner danke ich für seine Bereitschaft immer und überall physikalische Sachverhalte zu diskutieren. Bedanken möchte ich mich besonders für die Einblicke in gruppentheoretische Aspekte von Halbleiter-Quantenpunkten.

Christopher Gies möchte ich an dieser Stelle dafür danken, dass er Teile dieser Arbeit kritisch kommentiert hat und für Diskussionen jeder Art zur Verfügung stand. Danken möchte ich ihm auch für die eine oder andere entspannte und unterhaltsame Kaffeepause.

Bei Jan Seebeck and Michael Lorke möchte ich mich für das Korrekturlesen dieser Arbeit bedanken.

Bei allen Mitgliedern der Arbeitsgruppen *Theoretische Festkörperphysik* und *Theoretische Halbleiterphysik* bedanke ich mich für die angenehme Arbeitsatmosphäre.

Ein ganz besonderer Dank gilt meiner Freundin Christine. Ich möchte mich bei ihr dafür bedanken, dass sie mich ertragen hat, ich immer bei ihr Rückhalt finden konnte und sie mich in schwierigen Phasen immer liebevoll unterstützt und mir Mut zugesprochen hat.